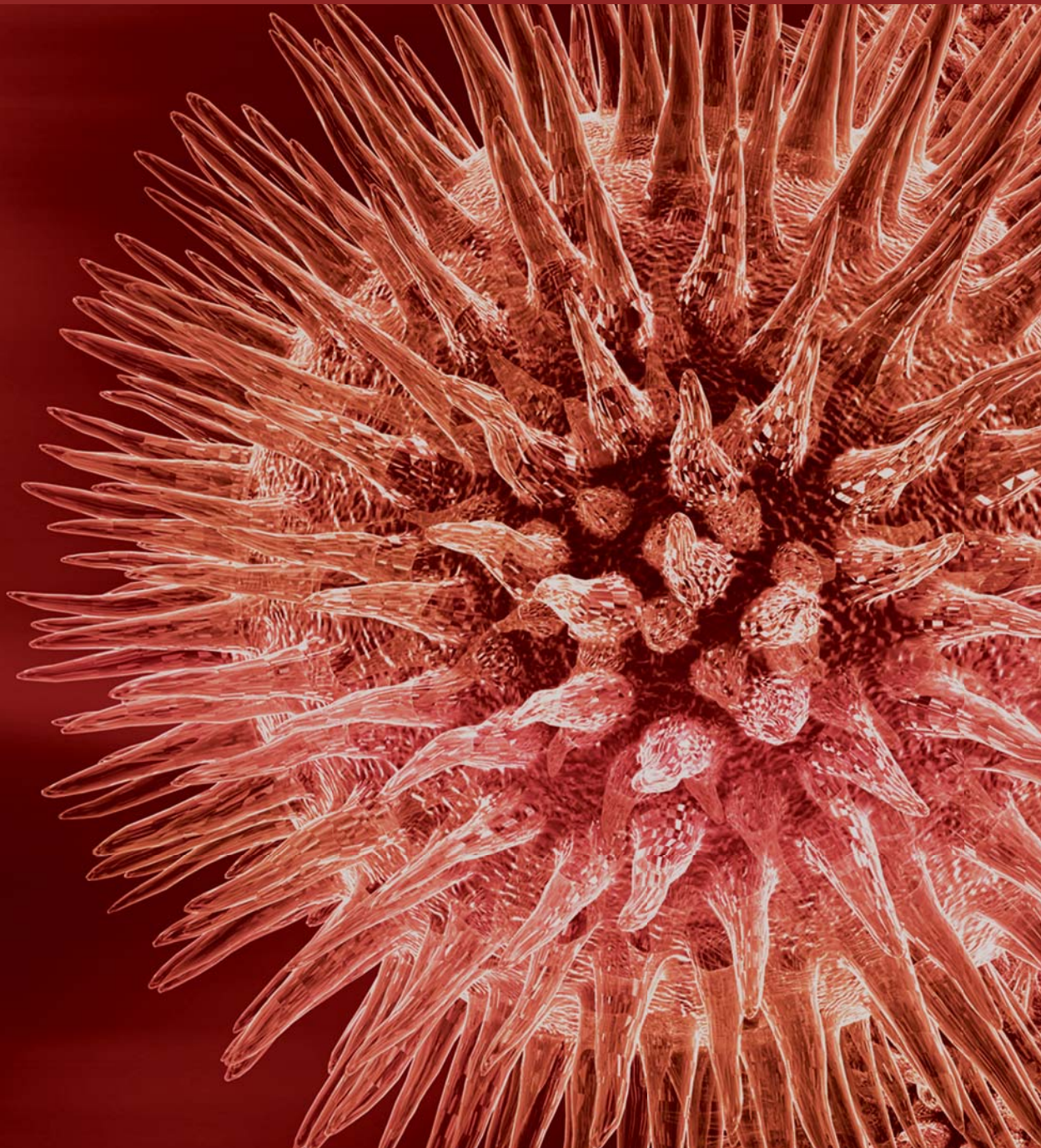# Molecular Image-Guided Theranostic and Personalized Medicine

Guest Editors: David J. Yang, Hong Zhang, Mei Tian, Carrio Ignasi, Zhen Cheng, and Lie-Hang Shen

Molecular Image-Guided Theranostic and Personalized Medicine

Molecular Image-Guided Theranostic and Personalized Medicine

Guest Editors: David J. Yang, Hong Zhang, Mei Tian, Carrio Ignasi, Zhen Cheng, and Lie-Hang Shen

Biophysics

Miguel Castanho, Portugal
P. Bryant Chase, USA
Kuo-Chen Chou, USA
Rizwan Khan, India

Ali A. Khraibi, Saudi Arabia
Rumiana Koynova, USA
Serdar Kuyucak, Australia
Jianjie Ma, USA

S. B. Petersen, Denmark
Peter Schuck, USA
Claudio M. Soares, Portugal

Cell Biology

Omar Benzakour, France
Sanford I. Bernstein, USA
Phillip I. Bird, Australia
Eric Bouhassira, USA
Mohamed Boutjdir, USA
Chung-Liang Chien, Taiwan
Richard Gomer, USA
Paul J. Higgins, USA
Pavel Hozak, Czech Republic

Xudong Huang, USA
Anton M. Jetten, USA
Seamus J. Martin, Ireland
Manuela Martins-Green, USA
Shoichiro Ono, USA
George Perry, USA
M. Piacentini, Italy
George E. Plopper, USA
Lawrence Rothblum, USA

Michael Sheetz, USA
James L. Sherley, USA
G. S. Stein, USA
Richard Tucker, USA
Thomas van Groen, USA
Andre Van Wijnen, USA
Steve Winder, UK
Chuanyue Wu, USA
Bin-Xian Zhang, USA

Genetics

Adewale Adeyinka, USA
Claude Bagnis, France
J. Birchler, USA
Susan Blanton, USA
Barry J. Byrne, USA
R. Chakraborty, USA
Domenico Coviello, Italy
Sarah H. Elsea, USA
Celina Janion, Poland

J. Spencer Johnston, USA
M. Ilyas Kamboh, USA
Feige Kaplan, Canada
Manfred Kayser, The Netherlands
Brynn Levy, USA
Xiao Jiang Li, USA
Thomas Liehr, Germany
James M. Mason, USA
Mohammed Rachidi, France

Raj S. Ramesar, South Africa
Elliot D. Rosen, USA
Dharambir K. Sanghera, USA
Michael Schmid, Germany
Markus Schuelke, Germany
Wolfgang Arthur Schulz, Germany
Jorge Sequeiros, Portugal
Mouldy Sioud, Norway
Rongjia Zhou, China

Genomics

Vladimir Bajic, Saudi Arabia
Margit Burmeister, USA
Settara Chandrasekharappa, USA
Yataro Daigo, Japan
J. Spencer Johnston, USA

Vladimir Larionov, USA
Thomas Lufkin, Singapore
Joakim Lundeberg, Sweden
John L. McGregor, France
John V. Moran, USA

Yasushi Okazaki, Japan
Gopi K. Podila, USA
Momiao Xiong, USA

Immunology

Hassan Alizadeh, USA
Peter Bretscher, Canada
Robert E. Cone, USA
Terry L. Delovitch, Canada
Anthony L. DeVico, USA
Nick Di Girolamo, Australia
Don Mark Estes, USA
Soldano Ferrone, USA
Jeffrey A. Frelinger, USA
John Robert Gordon, Canada

James D. Gorham, USA
Silvia Gregori, Italy
Thomas Griffith, USA
Young S. Hahn, USA
Dorothy E. Lewis, USA
Bradley W. McIntyre, USA
R. Mosley, USA
Marija Mostarica-Stojković, Serbia
Hans Konrad Muller, Australia
Ali Ouaissi, France

Kanury V. S. Rao, India
Yair Reisner, Israel
Harry W. Schroeder, USA
Wilhelm Schwaeble, UK
Nilabh Shastri, USA
Yufang Shi, China
Piet Stinissen, Belgium
Hannes Stockinger, Austria
J. W. Tervaert, The Netherlands
Graham R. Wallace, UK

Microbial Biotechnology

Jozef Anné, Belgium
Yoav Bashan, Mexico
Marco Bazzicalupo, Italy
Nico Boon, Belgium
Luca Simone Cocolin, Italy

Peter Coloe, Australia
Daniele Daffonchio, Italy
Han de Winde, The Netherlands
Yanhe Ma, China
Bernd H. A. Rehm, New Zealand

Angela Sessitsch, Austria
Effie Tsakalidou, Greece
J. Wiegel, USA

Microbiology

D. Beighton, UK
Steven R. Blanke, USA
Stanley Brul, The Netherlands
Isaac K. O. Cann, USA
Peter Dimroth, Switzerland
Stephen K. Farrand, USA
Alain Filloux, UK

Gad Frankel, UK
Roy Gross, Germany
Hans-Peter Klenk, Germany
Tanya Parish, UK
Gopi K. Podila, USA
Frederick D. Quinn, USA
Didier A. Raoult, France

Isabel Sá-Correia, Portugal
P. L. C. Small, USA
Lori Snyder, UK
Michael Thomm, Germany
H. C. van der Mei, The Netherlands
Schwan William, USA

Molecular Biology

Rudi Beyaert, Belgium
Michael Bustin, USA
Douglas Cyr, USA
K. Iatrou, Greece
Lokesh Joshi, Ireland
David W. Litchfield, Canada

Wuyuan Lu, USA
Patrick Matthias, Switzerland
John L. McGregor, France
S. L. Mowbray, Sweden
Elena Orlova, UK
Yeon-Kyun Shin, USA

William S. Trimble, Canada
Lisa Wiesmuller, Germany
Masamitsu Yamaguchi, Japan

Virology

Nafees Ahmad, USA
Edouard Cantin, USA
Ellen Collisson, USA
Kevin M. Coombs, Canada
Norbert K. Herzog, USA
Tom Hobman, Canada
Shahid Jameel, India

Fred Kibenge, Canada
Fenyong Liu, USA
Éric Rassart, Canada
Gerald G. Schumann, Germany
Y.-C. Sung, Republic of Korea
Gregory Tannock, Australia

Ralf Wagner, Germany
Jianguo Wu, China
Decheng Yang, Canada
Jiing-Kuan Yee, USA
Xueping Zhou, China
Wen-Quan Zou, USA

Contents

Editorial

Molecular Image-Guided Theranostic and Personalized Medicine

Hong Zhang,[1] Mei Tian,[2] Carrio Ignasi,[3] Zhen Cheng,[4] Lie-Hang Shen,[5] and David J. Yang[2]

[1] *The Second Affiliated Hospital of Zhejiang University, Hangzhou, Zhejiang 310009, China*
[2] *The University of Texas MD Anderson Cancer Center, Houston, TX 77030, USA*
[3] *Nuclear Medicine Department, Hospital Sant Pau, 08025 Barcelona, Spain*
[4] *Molecular Imaging Program at Stanford and Bio-X Program, Stanford University, Stanford, CA 94305, USA*
[5] *Institute of Nuclear Energy Research, Taoyuan 32546, Taiwan*

Correspondence should be addressed to David J. Yang, dyang@mdanderson.org

The growing use of molecular imaging helps to control and monitor dosage for increased safety and effectiveness. Molecular imaging agents become the scientific tools for moving a concept from bench work to clinic product development. This special issue provides original research and review of new trends in molecular imaging agent development.

Among clinic molecular imaging modalities, radionuclide imaging technique is the most sensitive and could provide target-specific information. The radiotracer could noninvasively assess disease treatment endpoints which used to rely almost exclusively on biopsies and histopathological assays.

L.-H. Shen et al. (Taiwan) reviewed molecular imaging in the diagnosis and management of CNS disorders. F.-L. Kong et al. (USA), N. Tsao et al. (USA), and C.-L. Ho et al. (Taiwan) report pharmacokinetics and dosimetry of molecular imaging compounds in oncology. M.-H. Liao et al. (Taiwan), X. Wang et al. (China), C. Wu et al. (China) and M. Tian et al. (USA) reported that molecular imaging techniques play a major role in the development of novel therapies since they measure target expressions (apoptosis, glycolysis) as well as function, pathway activities, and cell migration in the intact organism. Y.-F. Wang et al. and M.-Y. Chao et al. (Taiwan) described the kit probe for ^{99m}Tc-labeling which is crucial for centralized drug process. The kit probe may allow theranostic concept. A theranostic agent would be more accurate in the evaluation of patient response to treatment. The radiotracer could also be used for radionuclide therapy as reported by C. Wang et al. (China). Hybrid molecular imaging modalities (PET/CT, SPECT/CT) provide high-sensitivity functional and high-resolution anatomical imaging which are important in design-personalized treatment. M.-C. Chen et al. (Taiwan) reported the value of using I-131 NP-59 SPECT/CT to diagnose patients with subclinical or atypical features of primary aldosteronism. To proof of concept for molecular biology findings using different imaging modalities (optical, sonography) were described by Z. Pu et al. (China).

In summary, molecular imaging enables the comprehensive characterization of therapeutic intervention and can be used in preclinical studies, pharmacokinetic studies, dose-finding studies, and proof-of-concept studies. Molecular imaging technologies promote the discovery and development of personalized medicine.

Hong Zhang
Mei Tian
Carrio Ignasi
Zhen Cheng
Lie-Hang Shen
David J. Yang

Review Article

The Role of Molecular Imaging in the Diagnosis and Management of Neuropsychiatric Disorders

Lie-Hang Shen,[1] Yu-Chin Tseng,[1] Mei-Hsiu Liao,[1, 2] and Ying-Kai Fu[1, 3]

[1] *Institute of Nuclear Energy Research, Lungtan, Taoyuan 325, Taiwan*
[2] *Institute of Pharmacology, School of Medicine, National Yang-Ming University, Taipei 112, Taiwan*
[3] *Department of Chemistry, Chung Yuan Christian University, Chung-Li 320, Taiwan*

Correspondence should be addressed to Ying-Kai Fu, fufrank@iner.gov.tw

Neuropsychiatric disorders are becoming a major socioeconomic burden to modern society. In recent years, a dramatic expansion of tools has facilitated the study of the molecular basis of neuropsychiatric disorders. Molecular imaging has enabled the noninvasive characterization and quantification of biological processes at the cellular, tissue, and organism levels in intact living subjects. This technology has revolutionized the practice of medicine and has become critical to quality health care. New advances in research on molecular imaging hold promise for personalized medicine in neuropsychiatric disorders, with adjusted therapeutic doses, predictable responses, reduced adverse drug reactions, early diagnosis, and personal health planning. In this paper, we discuss the development of radiotracers for imaging dopaminergic, serotonergic, and noradrenergic systems and β-amyloid plaques. We will underline the role of molecular imaging technologies in various neuropsychiatric disorders, describe their unique strengths and limitations, and suggest future directions in the diagnosis and management of neuropsychiatric disorders.

1. Introduction

Modern neuroimaging offers tremendous opportunities for gaining insights into the molecular basis of neuropsychiatric disorders. Molecular imaging shows how specific tissues are functioning. This contrasts with conventional diagnostic imaging procedures, which simply provide anatomical or structural pictures of organs and tissues. Several techniques including functional magnetic resonance imaging (fMRI) and nuclear medicine imaging can measure regional changes in cerebral activity; however, nuclear medicine imaging is the only tool for direct measurements of neurotransmitter levels and the distribution, density, and activity of receptors or transporters. In contrast to fMRI, nuclear medicine imaging involves the administration of radioactively labeled tracers, which decay over time by emitting gamma rays that can be detected by a positron emission tomography (PET) or single photon emission computed tomography (SPECT) scanner. The radioisotopes used in PET can reach a more stable configuration by the emission of positrons, which travel a short distance and collide with electrons. The

annihilation of positron and electron produces 2 gamma rays, 511 keV each, which are emitted in opposite directions. In PET, annihilation coincidence detection is used in lieu of absorptive collimation to determine the directionality of the detected photons; this partially explains the greater spatial resolution and sensitivity of PET. However, compared with SPECT, PET is more expensive and less readily available. The most commonly used radioisotopes for labeling PET radiopharmaceuticals are ^{11}C and ^{18}F. ^{11}C has a short half-life of approximately 20 min, which allows multiple studies in the same day. In contrast, ^{18}F has a half-life of nearly 2 h, which allows shipment of tracers over considerable distances to PET centers that do not have a cyclotron. SPECT radiotracers typically have longer physical half-lives than most PET tracers; this may partially compensate for their disadvantages, particularly when measurements over several hours are required to eliminate nonspecific binding and reach equilibrium.

A major advantage of nuclear medicine imaging is the extraordinarily high sensitivity (10^{-9} to 10^{-12} M), many orders of magnitude greater than the sensitivities available

with MRI (10^{-4} M). Because many molecules relevant to neuropsychiatric disorders are present at concentrations below 10^{-8} M, nuclear medicine imaging is currently the only available *in vivo* method capable of quantifying subtle cerebral pathophysiological changes that might occur before neurostructural abnormalities take place [1].

PET and SPECT can measure biological processes, like glucose consumption and regional cerebral blood flow (rCBF), which may change in various neuropsychiatric disorders. In PET imaging, ^{18}F-fluorodeoxyglucose (^{18}F-FDG) is the most commonly used radiopharmaceutical. Active neurons have higher metabolic rates and higher glucose uptake rates than less active neurons. Similarly, active brain regions have higher regional cerebral blood flow (rCBF) compared to less active brain regions. With PET, intravenous ^{15}O-H$_2$O can be administered to measure rCBF. In SPECT imaging, ^{99m}Tc-hexamethylpropyleneamine oxime (^{99m}Tc-HMPAO) is the most commonly used radiopharmaceutical.

Radioligands must fulfill several criteria for successful PET or SPECT imaging, including stability of labeling, sufficient affinity and high selectivity for the specific receptor, combined with low nonspecific binding to brain tissues that do not contain the receptor of interest, and rapid permeation through the blood-brain barrier to permit tracers access to receptors [2]. Selective radioligands are available for various transmitter systems; these enable the visualization of receptor distributions in the normal brain and the detection of changes in receptor binding during various physiologic activities or under pathologic conditions. Quantitative imaging has gained clinical importance for measuring the activities of several receptors/transporters and molecular targets, for example, quantification of dopamine transporters for detecting loss of functional dopaminergic neuron terminals in the striatum, quantification of dopamine D2 receptors for studies of movement disorders and for assessments of receptor occupancy by neuroleptic drugs, quantification of serotonin (5-hydroxytryptamine, or 5-HT) receptors in affective disorders, quantification of serotonin and norepinephrine transporters for assessment of occupancy of antidepressants, and quantification of β-amyloid and acetylcholinesterase as markers of cognitive and memory impairments. The clinical and experimental relevance of these findings should not be underestimated. Neuroprotective and disease-modifying drug research has intensified, and results rely heavily on accurate, early diagnoses.

New advances in neuroimaging offer the promise of more personalized treatment for individuals with neuropsychiatric disorders. Molecular imaging can provide patient-specific information that allows treatment to be tailored to the specific biological attributes of both the disease and the patient. The eventual success of experimental therapies rests on understanding the mechanisms of the various neuropsychiatric disorders, early and accurate diagnoses, and noninvasive approaches for monitoring the progression of disease and the response to treatment.

Although nuclear imaging is a promising technique, several barriers must be addressed to facilitate its successful application to neuropsychiatric disorders. The major barrier to nuclear medicine imaging of molecular targets may be the difficulty in developing radiotracers. Another barrier is the lack of current evidence to support the use of molecular imaging as a diagnostic tool in clinical practice. The radiotracers used as biomarkers in neuropsychiatric disorders must have both biologic relevance and a strong linkage to the clinical outcome of interest. Despite the development of a large number of radioactive ligands for receptors, most do not fulfill the criteria for a good label, and only a few have been applied in clinical nuclear medicine. Physical barriers include limited anatomic resolution and the need for higher sensitivity. However, recent developments in improved detector crystals and three-dimensional image acquisition have markedly enhanced both sensitivity and resolution. Radiotracer imaging with PET and, to a lesser extent, with SPECT is ideally suited for *in vivo* applications, due to its superior anatomic resolution.

2. Parkinson's Disease and Related Disorders

Parkinson's disease (PD), the second most common neurodegenerative disorder, is characterized by severe loss of nigrostriatal neurons, which results in a deficiency of the neurotransmitter, dopamine [3]. Clinical diagnosis of PD relies on the presence of characteristic motor symptoms, including bradykinesia, rigidity, and resting tremors. In addition, nonmotor features have been increasingly recognized as early symptoms [4, 5]. Nonetheless, an early differential diagnosis can be difficult, particularly because the initial presentation may include overlapping clinical features, like essential tremor, vascular parkinsonism, drug-induced parkinsonism, and atypical parkinsonian syndrome (i.e., multiple system atrophy and progressive supranuclear palsy). Often, the clinical diagnosis of PD is supported by a positive response to dopaminergic drugs, particularly levodopa. However, some patients with pathologically confirmed PD respond poorly to levodopa; conversely, other patients with early multiple system atrophy or progressive supranuclear palsy respond well to drug treatment. Previously, the rate of misdiagnosis of idiopathic PD was as high as 24% [6, 7].

The evolution of neuroimaging techniques over the past several years has yielded unprecedented information about the degenerative processes in PD and other movement disorders. PET and SPECT techniques have been successfully employed in identifying dopaminergic dysfunction in PD by detecting changes in brain levodopa, glucose metabolism, and dopamine transporter binding. Several tracers can be employed to assess the integrity of dopamine terminals in PD. First, dopa decarboxylase activity and dopamine turnover can both be measured with ^{18}F-FDOPA PET. Second, the availability of presynaptic dopamine transporters (DATs) can be assessed with various tracers, which are typically tropane based. Third, vesicle monoamine density in dopamine terminals can be evaluated with ^{11}C-dihydrotetrabenazine PET [8, 9].

The uptake of ^{18}F-FDOPA reflects both the density of the axonal terminal plexus and the activity of the striatal aromatic amino acid decarboxylase (AADC), the
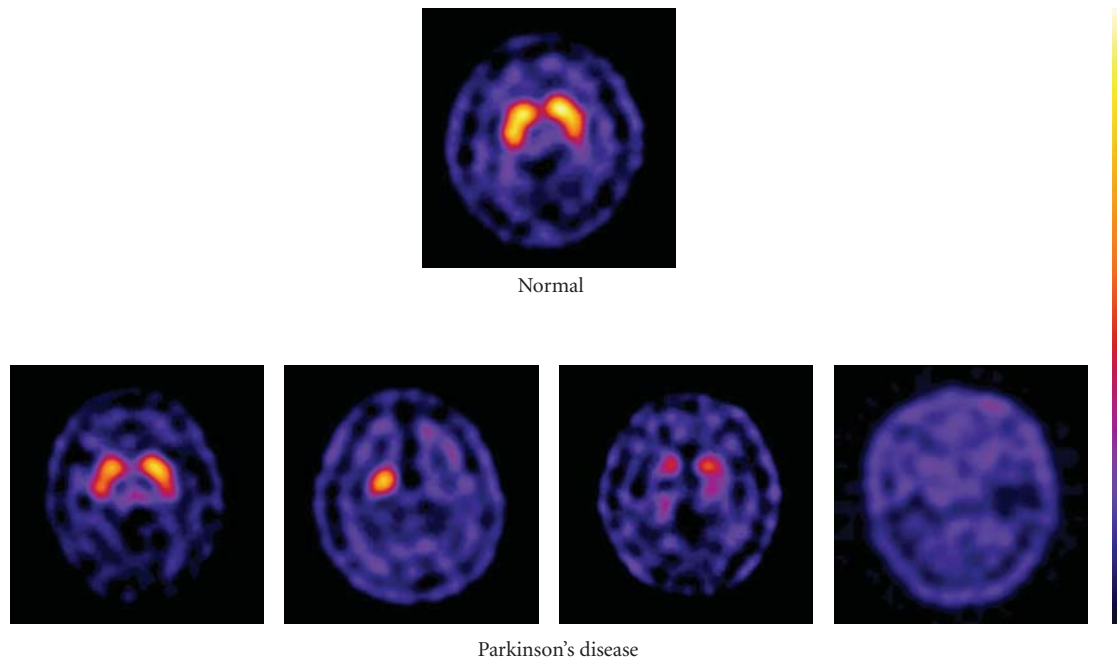
FIGURE 1: ^{99m}Tc-TRODAT-1 imaging on four patients with Parkinson's disease at different stage and one normal control. The differentiation between normal and PD is primarily based on shape that reflects differences of uptake intensity.

enzyme responsible for the conversion of ^{18}F-FDOPA to ^{18}F-dopamine [3, 10]. Therefore, particularly in the early stages of disease, ^{18}F-FDOPA PET may underestimate the degenerative process, due to the compensatory upregulation of AADC in the remaining terminals. Moreover, because AADC is present in the terminals of all monoaminergic neurons, measurements of ^{18}F-FDOPA uptake into extrastriatal areas provide an index of the density of the serotonergic, noradrenergic, and dopaminergic terminals [3, 10].

DAT is a protein complex located in presynaptic dopaminergic nerve terminals, which serves as the primary means for removing monoaminergic neurotransmitters from the synaptic cleft. It is therefore a potential marker of the integrity of nigrostriatal projections. Several PET ligands (^{11}C-CFT, ^{18}F-CFT, ^{18}F-FP-CIT, and ^{11}C-PE2I) and SPECT tracers (^{123}I-β-CIT, ^{123}I-FP-CIT, ^{123}I-altropane, ^{123}I-PE2I, and ^{99m}Tc-TRODAT-1) are now available to measure DAT availability [10, 11]. The technetium-based ^{99m}Tc-TRODAT-1 has the advantage of being relatively inexpensive and available in kit form [12]. However, its specific signal is lower than the ^{123}I-based SPECT tracers. In general, all the DAT markers have shown efficacy in PD similar to that achieved with ^{18}F-FDOPA PET; all are able to differentiate patients with early PD from healthy subjects with a sensitivity and specificity of approximately 90% [13–15]. A multicenter, phase III trial conducted at Institute of Nuclear Energy Research (INER) indicated that patients with PD were easily distinguished from healthy volunteers with the ^{99m}Tc-TRODAT-1 SPECT, which had a sensitivity of 97.2% and a specificity of 92.6% (unpublished data). Figure 1 depicts the typical dopamine transporter images in

4 patients with PD for different stage and a healthy control. The differentiation between normal and Parkinson's disease is primarily based on shape, which reflects differences of uptake intensity. The high sensitivity and specificity of DAT images make them useful in both the clinical diagnosis of PD and preclinical screening for asymptomatic individuals. To date, only DaTSCAN (^{123}I-FP-CIT) and ^{99m}Tc-TRODAT-1 are available on the market and licensed for detecting loss of functional dopaminergic neuron terminals in the striatum. In contrast to ^{18}F-FDOPA, the striatal uptake of DAT ligands in early PD may overestimate the reduction in terminal density due to the relative downregulation of DAT in the remaining neurons as a response to nigral neuron loss; this is a compensatory mechanism that acts to maintain synaptic dopamine levels. DAT binding falls with age in healthy subjects, but striatal ^{18}F-FDOPA uptake does not appear to be age dependent [3, 12, 16].

Dopaminergic neurotransmission plays an important role in regulating several aspects of basic brain function, including motor behavior, motivation, and working memory. Dopaminergic systems are also a central element in the brain reward system that controls learning. There are five subtypes of dopamine receptors, D_1, D_2, D_3, D_4, and D_5. D_1 and D_5 receptors are members of the D_1-like family of dopamine receptors, and D_2, D_3, and D_4 receptors are members of the D_2-like family. The assessment of D_1-like receptors has not achieved clinical significance; therefore, in the past, many investigations have focused on the D_2-like receptor system. Positron-emitting ligands, like ^{11}C-raclopride, ^{18}F-spiperone, and ^{18}F-methyl-benperidol have been developed for the visualization of dopamine

D_2 receptors *in vivo* with PET; alternatively, single-proton emitting ligands, like ^{123}I-iodobenzamide (^{123}I-IBZM), ^{123}I-epidrpride, and ^{123}I-IBF have been developed for SPECT imaging. ^{11}C-raclopride, a derivative of benzamide, is currently the gold standard PET tracer for D_2 receptors [17].

It is important to discriminate between idiopathic Parkinson's disease (IPD) and other neurodegenerative parkinsonian syndromes (non-IPS), because there are marked differences in the prognoses and therapies. DAT imaging with ^{99m}Tc-TRODAT-1 SPECT has proven successful in the differential diagnosis between PD and vascular parkinsonism; patients with PD displayed a significant decrease in striatal ^{99m}Tc-TRODAT-1 uptake compared to patients with vascular parkinsonism ($P < .01$) [18]. Higher diagnostic accuracy in the differential diagnosis of parkinsonism may be achieved by combining pre- and postsynaptic quantitative information about the dopaminergic system. Previous imaging studies with the most commonly used dopamine D_2 receptor tracers, ^{11}C-raclopride and ^{123}I-IBZM, have consistently shown that DATs, which represent the integrity of the nigrostriatal neurons, are downregulated in patients with early IPD, but D_2 receptors are normal or even upregulated. In contrast, patients with multiple system atrophy (MSA) typically show reductions in both DAT and D_2 binding [19, 20]. However, with progression of PD, striatal D_2 receptor activity returns to normal or may fall below normal levels [2], and the small differences in D_2 binding make it difficult to distinguish between PD, IPD, and healthy control groups (unpublished data).

Gradually, we have attained a broader understanding of the genetic linkages among different aspects of parkinsonism. Approximately 20% of patients with PD have genetic mutations [21]. Several genes, including *PINK1, SNCA, parkin, UCHL1, DJ1*, and *LRRK2*, have been associated with familial parkinsonism and/or sporadic early onset Parkinson's disease (EOPD). A ^{99m}Tc-TRODAT-1 scan showed that patients with the *PINK1* mutation displayed a rather even, symmetrical reduction of dopamine uptake; in contrast, patients with late-onset Parkinson's disease (LOPD) displayed a dominant decline in dopamine uptake in the putamen [22]. In addition, ^{99m}Tc-TRODAT-1 SPECT revealed that the dopamine transporter concentration was significantly reduced in patients with Machado-Joseph Disease and in asymptomatic gene carriers compared to healthy volunteers ($P < .001$). This indicated that the brain SPECT was capable of detecting early alterations in dopamine neurons of the striatal region [23].

Molecular imaging is also a major tool for the evaluation of new experimental therapeutic strategies in PD, particularly for those that aim to restore or protect striatal dopaminergic innervation. Neuroprotective and disease-modifying drug research has intensified, and the results rely heavily on accurate early diagnosis [24]. Several teams of investigators have reported the results from double-blind, placebo-controlled trials of human embryonic dopaminergic tissue transplantation for the treatment of PD. Evaluations with ^{18}F-FDOPA scans have shown that significant declines in the motor scores over time after transplantation ($P < .001$), based on the Unified Parkinson Disease Rating Scale (UPDRS), were associated with increases in putamen ^{18}F-FDOPA uptake at 4-year posttransplantation followups ($P < .001$). Furthermore, posttransplantation changes in putamen PET signals and clinical outcomes were significantly intercorrelated ($P < .02$) [25, 26]. Current imaging biomarkers may be a valuable adjunct to clinical data for assessing both the mechanism and efficacy of neuroprotective agents. To date, functional imaging studies in these trials have failed to demonstrate a clear-cut neuroprotective effect on nigrostriatal degeneration. In addition, discordance between clinical and imaging outcomes has been reported in studies that compared a dopamine agonist versus levodopa [10, 27].

Gene therapy may be potentially useful for ameliorating the motor symptoms of PD and the motor complications of PD treatments. Several gene therapy studies in humans investigated transductions (with various viral vectors) of glial-derived neurotrophic factor (GDNF), neurturin (NTN), AADC, or glutamic acid decarboxylase (GAD) [28]. Brain imaging with ^{18}F-FDODA PET, ^{18}F-FFMT, or ^{18}F-FDG PET was used to evaluate clinical outcomes adjunct to the UPDRS scores [29–33].

3. Alzheimer's Disease

Alzheimer's disease (AD) is the most common form of dementia. AD is characterized by progressive impairments in cognitive function and behavior [34]. Data suggest that the number of patients with AD worldwide will increase from 26.6 million in 2006 to 106.8 million in 2050 [35, 36]. Beta amyloid (Aβ 1–42) is considered a primary cause of AD, but there are numerous other ongoing processes, including oxidative stress, inflammatory reactions, microglial activation, tau phosphorylation, and neurotransmitter impairments, that can lead to cognitive impairments [36, 37]. Some methods have shown promise as diagnostic tools for AD, including MRI measurements of medial temporal lobe atrophy, PET imaging of glucose metabolism and Aβ deposits, and cerebral spinal fluid (CSF) biomarkers. A substantial number of studies have shown that MRI measurements of hippocampal atrophy can distinguish between subjects with AD and older subjects with normal cognition with 80–90% accuracy [34, 38].

PET tracers have been developed for studies of functional activity, neurotransmitter activity, and pathologic processes in different dementia disorders. PET imaging with ^{18}F-FDG has shown that AD was associated with metabolic deficits in the neocortical association areas, but normal activity was observed in the basal ganglia, thalamus, cerebellum, primary sensory motor cortex, and visual cortex [39]. During disease progression, glucose metabolism continues to decline, and this is associated with declining scores on cognitive tests [40]. A large multicenter study showed 93% sensitivity and specificity for distinguishing between individuals with AD and normal individuals [34]. This indicated that ^{18}F-FDG PET can serve as a biomarker in clinical trials [36].

Imaging techniques that include radiolabeled PET tracers that can bind to aggregated Aβ peptides in Aβ plaques have

the potential of directly assessing relative brain Aβ plaque pathology. Several research groups have applied the small-molecule approach to the development of tracers suitable for amyloid imaging; for example, derivatives of Congo red, thioflavin, stilbene, chrysamine-G, and acridine were developed for PET and SPECT imaging. This opens up new possibilities for early diagnosis and provides new tools for monitoring antiamyloid therapy in AD [36, 41–44].

^{18}F-FDDNP was the first PET tracer used *in vivo* for detecting cerebral amyloid plaques. Increased ^{18}F-FDDNP binding was observed in the temporal, parietal, and frontal regions of the AD brain, compared with brains from older control subjects with no cognitive impairments. ^{18}F-FDDNP binds to both neuritic plaques and neurofibrillary tangles [45]. Pittsburgh compound B (^{11}C-PIB), a derivative of thioflavin-T, binds with high affinity and high specificity to neuritic Aβ plaques, but it shows no binding to diffuse plaques or neurofibrillary tangles [46]. ^{11}C-PIB PET is presently the most used amyloid PET ligand; it has been studied in over 2000 subjects [39, 40]. Imaging with ^{11}C-PIB PET showed significantly higher retention in the frontal, temporal, parietal, and occipital cortices and the striatum of patients with AD compared to healthy controls (1.9- to 1.5-fold differences). Interestingly, the increase in ^{11}C-PIB retention observed in mild AD patients relative to age-matched healthy controls was larger than the decrease in ^{18}F-FDG uptake in AD patients relative to controls [47]. Figure 2 illustrates cerebral glucose metabolism as assessed by ^{18}F-FDG PET and amyloid plaque burden as assessed by ^{11}C-PIB PET in two AD patients and a healthy control [43].

The memory predominant subtype, amnestic mild cognitive impairment (MCI), has been suggested to constitute a transitional stage between normal aging and AD [34]. Clinical studies suggested that about 12% of patients with the amnestic form of MCI progressed to AD within one year and up to 80% progressed to AD after 6 y [48]. Glucose metabolism is a sensitive measure of change in cognition and functional ability, both in AD and in MCI; therefore, accurate detection of changes in glucose metabolism has value in predicting future cognitive decline [49]. Clinical follow-up studies have shown that patients with MCI who converted to AD showed significantly higher ^{11}C-PIB retention than those with MCI that did not convert; this suggested the possibility of identifying prodromal AD with β-amyloid imaging [36, 50].

To date, ^{11}C-PIB PET is the most widely used imaging approach for the visualization of Aβ. Although ^{11}C-PIB can be used for academic studies, the 20-minute half-life of ^{11}C and limited manufacturing access makes the molecule unsuitable for widespread use as a routine diagnostic agent. [18]F, with a half-life of 110 minutes, offers much better potential for manufacturing and distribution. In addition to ^{18}F-FDDNP, several ^{18}F-labeled Aβ tracers have been successfully investigated in clinical trials, including ^{18}F-PIB (^{18}F-flutemetamol), ^{18}F-AV-1 (^{18}F-BAY94-9172), and ^{18}F-AV-45 (Florbetapir F-18). ^{18}F-AV-45, a derivative of stilbene, has demonstrated high binding to the Aβ aggregates in patients with AD. In a pilot study, patients with AD and healthy controls displayed averages of 1.67 ± 0.18 and 1.25 ± 0.18, respectively, in standard uptake value ratios (SUVRs) of ^{18}F-AV-45 for the cortical area relative to the cerebellum [51]. The interim results of a phase III study demonstrated that the ^{18}F-AV-45 PET images correlated strongly with the postmortem histopathology findings. The PET images correctly identified subjects that had β-amyloid deposits and showed where in the brain the deposits had accumulated. Recently, a marketing application for Florbetapir was submitted to the FDA.

In the regions of the highest retention, the specific signal from ^{18}F-FDDNP was only 0.3 times that of the reference tissue; this contrasts with the 1.5–2.0-fold specific signal with respect to the reference tissue that was associated with the ^{11}C-PIB [47] and ^{11}C-SB13 tracers [52]. Visual assessment of ^{11}C-PIB PET images demonstrated promise as a supportive diagnostic marker for AD with both sensitivity and specificity values of 0.95. Additionally, ^{18}F-PIB showed promise as an AD biomarker with both sensitivity and specificity values of 0.93; in contrast, ^{18}F-FDDNP PET images showed only moderate accuracy, with a sensitivity of 0.81 and a specificity of 0.72 [53, 54].

Development of amyloid probes applicable to both PET and SPECT in AD may provide a cost-effective approach, particularly when effective antiamyloid therapy becomes available. Accurate and early diagnoses of dementias will become increasingly important as new therapies are introduced. The presently available imaging ligands will be valuable for monitoring any reduction in Aβ plaques. Ongoing studies with antiamyloid therapies, including a vaccination, an Aβ fibrillization inhibitor, or a secretase modulator, have described some difficulties in the assessment of drug effects at autopsy. Assessments of the efficacy of antiamyloid therapy could be greatly facilitated with the visualization of amyloid plaques in the brains of living patients with AD [55].

One hypothesis holds that there is a cholinergic mechanism underlying AD; this hypothesis proposes that degeneration of cholinergic neurons in the basal forebrain nuclei causes disturbances in presynaptic cholinergic terminals in the hippocampus and neocortex, which are important for memory disturbances and other cognitive symptoms [34]. The most important degrading enzyme for acetylcholine in the human cortex is acetylcholinesterase, which is present in cholinergic axons. The PET tracers, ^{11}C-PMP and ^{11}C-MP4A, have been used to measure acetylcholinesterase activity. These tracers showed a decline in acetylcholinesterase activity in patients with AD compared to healthy controls. Reduction in acetylcholinesterase activity has also been reported in patients with MCI, particularly in those that later converted to AD. This suggested that acetylcholinesterase changes might precede the development of clinical AD [56]. The inhibition of acetylcholinesterase with specific therapeutic drugs, like donepezil, can also be measured with these tracers [57].

4. Affective Disorders

Serotonin (5-hydroxy-tryptamine, 5-HT) is a modulatory neurotransmitter in the human brain that regulates mood,

(a)

Control, 63 years   AD, 62 years   AD, 75 years
MMSE 30/30   MMSE 28/30   MMSE 25/30

(b)
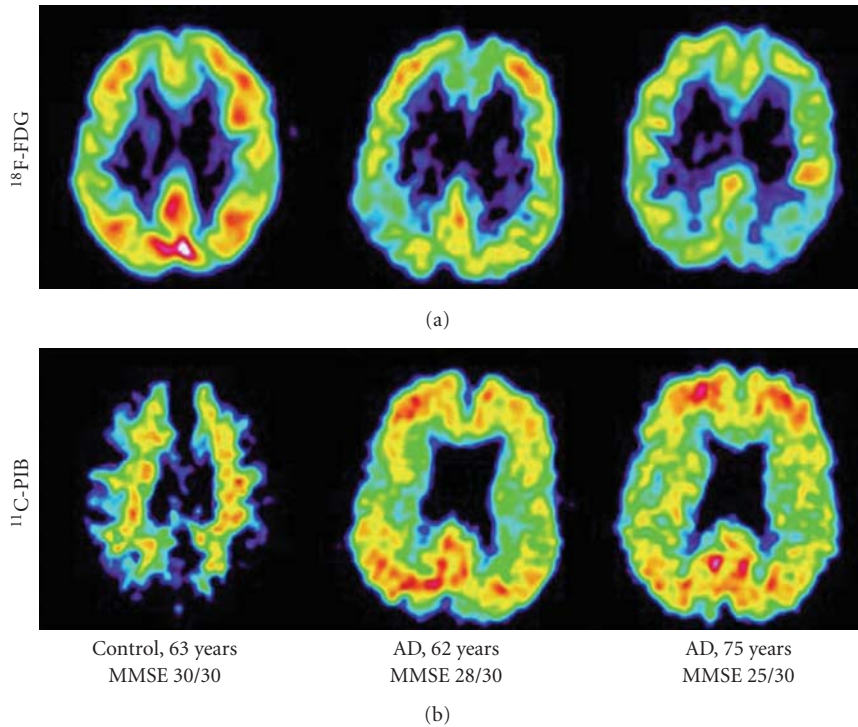
FIGURE 2: Cerebral glucose metabolism (^{18}F-FDG) and ^{11}C-PIB amyloid imaging in two AD patients and one healthy control. The PET scans show ^{18}F-FDG and ^{11}C-PIB at a sagittal section. MMSE: Mini Mental State Examination. Adapted from [43].

anger, reward, aggression, and appetite [58]. Serotonergic neurotransmission is altered in many neuropsychiatric disorders, including depression, anxiety disorders, biopolar disorders (BD), compulsive disorders, autism, schizophrenia, AD, and PD [2, 59].

There is broad heterogeneity in the postsynaptic serotonin receptors; however, the only suitable radioligands available are for 5-HT$_{1A}$ and 5-HT$_{2A}$ receptors [2]. For visualization of brain 5-HT$_{1A}$ receptor activity, the ^{11}C-WAY-100635 (WAY) and ^{18}F-labeled analogs of WAY (^{18}F-trans-FCWAY) exhibited high affinity. 5-HT$_{1A}$ receptors are present in high density in the hippocampus, septum, amygdala, hypothalamus, and neocortex of the human brain. PET imaging with ^{18}F-FCWAY demonstrated that abnormalities of 5-HT$_{1A}$ receptors were present in affective disorders, particularly in depression and panic disorder [60–62]. However, there were only small differences between the study population and the healthy control groups; this may indicate considerable overlap between groups, which would impede a clear diagnostic cutoff. 5-HT$_{2A}$ receptors are present in all neocortical regions, with lower densities in the hippocampus, basal ganglia, and thalamus. 5-HT$_{2A}$ receptors have been quantified with ^{18}F-altanserin, ^{18}F-setoperone, and ^{123}I-2-ketanserin [58]. ^{18}F-setoperone showed specific binding in the cortex, reversibility, and a favorable ratio of specific binding to nonspecific binding and unbound label [63]. PET studies with ^{18}F-Setoperone showed significantly decreased 5-HT$_{2A}$ receptor densities in neuroleptic-naïve patients with schizophrenia and in patients with AD [64, 65].

The serotonin transporter (SERT, 5-HTT) plays an important role in modulating presynaptic serotonergic function. It removes serotonin from the synaptic cleft and terminates its function [66]. SERT is the primary target for selective serotonin reuptake inhibitors (SSRIs), which are commonly used for treatment of psychiatric disorders, and as the first-line treatment for major depression and anxiety disorders. SERT imaging provides information on the integrity of serotonergic neurotransmission *in vivo*. ^{123}I-β-CIT was the first SERT marker to be applied; however, it binds all the monoamine transporters, including SERT, DAT, and norepinephrine transporters (NETs). The first PET radiotracer that was selective for brain SERT was ^{11}C-McN5652 [67, 68]. Subsequently, two excellent PET tracers were developed for visualization of SERT in human brains; these are known as ^{11}C-DASB and ^{11}C-MADAM, and both exhibit high affinity and selectivity for SERT [69]. Alternatively, a promising SPECT tracer was also developed for visualization of SERT in humans; this ^{123}I-ADAM, a derivative of 403U76, displays high affinity and selectivity for SERT. ^{123}I-ADAM was efficiently taken up in the hypothalamus, brain stem, pons, and medial temporal lobe [70]. Compared with previous radioligands, ^{11}C-DASB offers both high selectivity and a favorable ratio of specific binding relative to free and nonspecific binding. Therefore, ^{11}C-DASB PET imaging is considered as the state-of-the-art method for quantifying SERT in humans.

In vivo imaging studies of SERT have generally been conducted in patients with acute depression; however, the

results have been somewhat inconsistent [71]. Parsey et al. used ^{11}C-McN5652 PET in unmedicated patients with major depression. Those patients had lower SERT binding potential in the amygdala and midbrain region compared to healthy subjects [72]. In a study with ^{11}C-DASB PET, brain SERT density was investigated in subjects with a history of major depressive episodes (MDEs). Those patients displayed no regional differences in SERT binding potential compared to healthy subjects [73, 74]. Newberg et al. used ^{123}I-ADAM SPECT and found reduced SERT binding potential in the midbrain regions of patients with depression compared to healthy volunteers [75]; however another study with ^{123}I-ADAM SPECT found no difference between similar groups [76]. Dysfunction in serotonin neurotransmission is likely to play a critical role in BD [77]. BD is defined on the basis of manic symptoms of varying severity. Bipolar I disorder (BD I) is defined by a full-blown episode of mania, whereas bipolar II disorder (BD II) is defined by hypomanic episodes and depressive episodes [78]. Assessment of SERT binding in the midbrain with ^{123}I-ADAM SPECT demonstrated no differences in brain SERT binding between healthy controls and patients with BD that were in a euthymic state. However, the SERT binding was lower in patients with BD I compared to those with BD II. Furthermore, the decreased specific uptake ratios (SURs) in BD I patients were well correlated with the duration of the illness ($R = -0.742, P = .014$) [79]. In addition to the serotonin system, the *DAT* gene was also shown to play a role in the etiology of both adult and pediatric BD. Using ^{99m}Tc-TRODAT-1 SPECT, Chang et al. found that striatal DAT availability was significantly higher in patients with euthymic BD than in healthy volunteers [80].

Aggression is one of the most extensively studied areas of human behavior. Central serotoninergic function has been linked to both normal and pathological aggressiveness. Because hostility shares some similarities with aggression, it is possible that central serotonin activity is also related to hostility. ^{123}I-ADAM SPECT imaging indicates that central serotoninergic activities may play a role in hostility. The hostile attribution subscore was negatively correlated with SERT availability ($r = -0.71, P < .05$) [81].

Although imaging of the serotonin system has many potential clinical uses, currently, serotonin imaging is not used for the routine diagnosis of any neuropsychiatric diseases. Perhaps one of the most valuable current uses of molecular imaging technology is the determination of the *in vivo* brain occupancy of a putative pharmaceutical at the target of interest when developing a pharmaceutical treatment for depression. Currently, there is no other method available for *in vivo* determinations of receptor occupancy in humans [58]. Drug concentrations in plasma may vary by over tenfold when identical doses are administered to different patients. Therapeutic drug monitoring can reduce the number of nonresponders and decrease the risk for developing side effects by identifying patients with either insufficient or excess serum concentrations of the drug [82]. The first SSRI occupancy study with ^{11}C-DASB PET found 80% striatal occupancy in multiple regions after 4 weeks of antidepressant treatment, with doses of paroxetine and citalopram known to have clinical effects distinct from
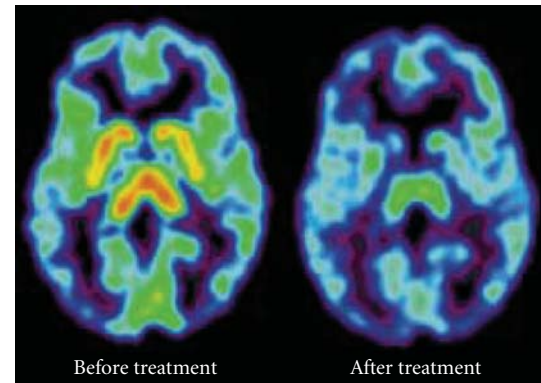
(a)
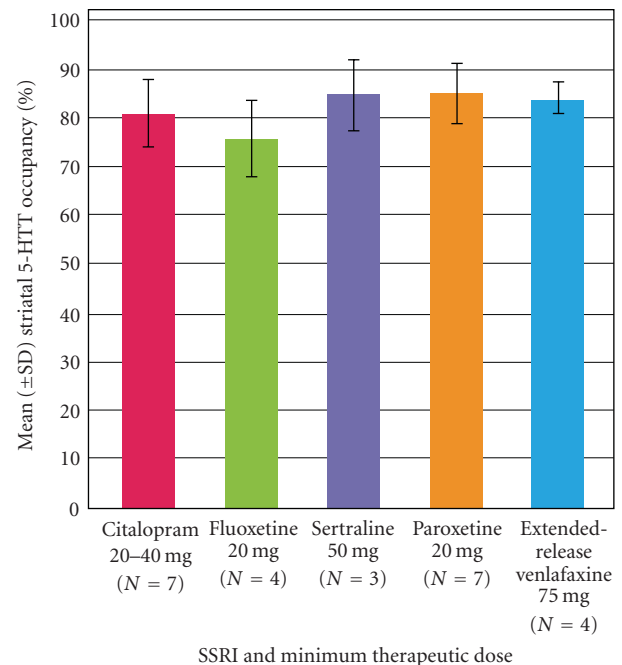
(b)

Figure 3: (a) Effect of citalopram on ^{11}C-DASB PET scan of the serotonin transporter in a depressed subject. Treatment was with 20 mg/day of citalopram for 4 weeks. Adapted from [73]. (b) Striatal serotonin transporter (5-HTT) occupancy in depressed subjects after 4 weeks of treatment at minimum therapeutic doses of five SSRIs. Adapted from [74].

placebo [73]. Thereafter, occupancy measurements of citalopram, fluoxetine, sertraline, paroxetine, or venlafaxine with ^{11}C-DASB PET suggested that 80% occupancy of the SERT was a necessary minimum for SSRI efficacy for depressive episodes. Moreover, occupancy increased as the dose or plasma level increased, and occupancy reached a plateau at saturating doses [74]. Figure 3(a) illustrates a typical occupancy study of citalopram on the serotonin transporters with ^{11}C-DASB PET scan in a depressed subject [73]. Figure 3(b) summaries the striatal SERT occupancy in depressed subjects after 4 weeks of treatment at minimum therapeutic doses of five SSRIs [74]. Given the association between the clinically

relevant dose and SERT occupancy for all SSRIs, it is now generally believed that an 80% SERT occupancy with an SSRI is therapeutically useful. Consequently, antidepressant drug development aims for 80% serotonin transporter occupancy. This practical approach can be applied in phase I trials to assess whether potential new antidepressant drugs can adequately penetrate the brain and in phase II clinical trials to guide dosing selections [69].

NETs are responsible for the reuptake of norepinephrine into presynaptic nerves, and they are a primary target of antidepressants. With the development of NET tracers, like ^{18}F-FMeNER-D$_2$ [83] and ^{11}C-MRB [84], it is currently possible to investigate NET occupancy for antidepressants that are selective norepinephrine reuptake inhibitors (SNRIs). In an investigation with ^{18}F-FMeNER-D$_2$, the NET occupancy of nortriptyline was 16% to 41%, which corresponded to a dose of 10–75 mg [83]. In addition to NET, antidepressants also target DAT. Bupropion is thought to exert its antidepressive effect by blocking the DAT and NET with an efficacy comparable to that of SSRIs. With bupropion treatment, the average DAT occupancy was 20.84%, measured by ^{99m}Tc-TRODAT-1 SPECT [85]. To achieve SNRI efficacy, the optimal and minimal occupancies of NET remain to be determined.

For antipsychotic drugs, it was shown that the occupancy of dopamine D$_2$-like receptors was better correlated to plasma concentrations than to the doses administered [82]. In association with the analysis of clinical effects, Farde et al. established the concept that at least 60–70% dopamine receptor occupancy was necessary for treating positive symptoms of schizophrenia. However, occupancies above 80% were associated with extrapyramidal side effects [82, 86].

5. Conclusions and Future Directions

With the appropriate radioligands, molecular imaging enables the visualization of presynaptic and postsynaptic sites in the dopaminergic system. This can provide crucial information for the assessment and monitoring of neuroprotective agents, gene therapies, and stem cell strategies for the treatment of PD. Future studies are needed in the development of new radiotracers to target nondopaminergic brain pathways and the glial reaction to disease.

Accurate and early differentiation of dementias will become increasingly important as new therapies are introduced. Recently, reliable PET tracers for assessing the Aβ burden in the brain have been introduced; these tracers may be valuable for early diagnosis of the presymptomatic stages of AD. The measurement of β-amyloid *in vivo* will greatly facilitate our understanding of the underlying pathophysiological mechanisms of AD; in addition, these measurements will promote the testing of new antiamyloid drugs and therapies. Although early studies were performed with ^{11}C-PIB, several groups have developed fluorinated compounds for widespread and routine diagnostic uses.

Although serotonin imaging has many potential clinical applications, currently, serotonin imaging is not used for the routine diagnosis of any neuropsychiatric diseases. Perhaps

one of the most valuable current uses of molecular imaging technology is the determination of *in vivo* brain occupancy of a putative pharmaceutical agent when developing a treatment for depression. Finally, to achieve SNRI efficacy, the optimal and minimal occupancies of NET remain to be determined.

In the future, the role of molecular imaging may become more significant in guiding therapy. Enhancements in image resolution and specific molecular tags will permit accurate diagnoses of a wide range of diseases, based on both structural and molecular changes in the brain. For widespread application, advances in molecular imaging should include the characterization of new radiotracers, application of modeling techniques, standardization and automation of image-processing techniques, and appropriate clinical settings in large multicenter trials. The growing field of molecular imaging is helping nuclear medicine physicians identify pathways into personalized patient care.

Acknowledgments

References

[1] M. Fumita and R. B. Innis, "In vivo molecular imaging: ligand development and research applications," in *Neuropsychopharmacology: The Fifth Generation of Progress*, pp. 411–425, 2000.

[2] W. D. Heiss and K. Herholz, "Brain receptor imaging," *Journal of Nuclear Medicine*, vol. 47, no. 2, pp. 302–312, 2006.

[3] N. Pavese, L. Kiferle, and P. Piccini, "Neuroprotection and imaging studies in Parkinson's disease," *Parkinsonism and Related Disorders*, vol. 15, no. 4, pp. S33–S37, 2010.

[4] D. J. Gelb, E. Oliver, and S. Gilman, "Diagnostic criteria for Parkinson disease," *Archives of Neurology*, vol. 56, no. 1, pp. 33–39, 1999.

[5] E. Tolosa, G. Wenning, and W. Poewe, "The diagnosis of Parkinson's disease," *Lancet Neurology*, vol. 5, no. 1, pp. 75–86, 2006.

[6] A. J. Hughes, S. E. Daniel, S. Blankson, and A. J. Lees, "A clinicopathologic study of 100 cases of Parkinson's disease," *Archives of Neurology*, vol. 50, no. 2, pp. 140–148, 1993.

[7] A. H. Rajput, B. Rozdilsky, and A. Rajput, "Accuracy of clinical diagnosis in Parkinsonism—a prospective study," *Canadian Journal of Neurological Sciences*, vol. 18, no. 3, pp. 275–278, 1991.

[8] C. Sioka, A. Fotopoulos, and A. P. Kyritsis, "Recent advances in PET imaging for evaluation of Parkinson's disease," *European Journal of Nuclear Medicine and Molecular Imaging*, vol. 37, pp. 1594–1603, 2010.

[9] D. J. Brooks, K. A. Frey, K. L. Marek et al., "Assessment of neuroimaging techniques as biomarkers of the progression of

Parkinson's disease," *Experimental Neurology*, vol. 184, no. 1, pp. S68–S79, 2003.

[10] N. Pavese and D. J. Brooks, "Imaging neurodegeneration in Parkinson's disease," *Biochimica et Biophysica Acta*, vol. 1792, no. 7, pp. 722–729, 2009.

[11] M. J. Ribeiro, M. Vidailhet, C. Loc'h et al., "Dopaminergic function and dopamine transporter binding assessed with positron emission tomography in Parkinson disease," *Archives of Neurology*, vol. 59, no. 4, pp. 580–586, 2002.

[12] S. K. Meegalla, K. Plössl, M. P. Kung et al., "Synthesis and characterization of technetium-99m-labeled tropanes as dopamine transporter-imaging agents," *Journal of Medicinal Chemistry*, vol. 40, no. 1, pp. 9–17, 1997.

[13] P. D. Mozley, J. S. Schneider, P. D. Acton et al., "Binding of [^{99m}Tc]TRODAT-1 to dopamine transporters in patients with Parkinson's disease and in healthy volunteers," *Journal of Nuclear Medicine*, vol. 41, no. 4, pp. 584–589, 2000.

[14] W. S. Huang, Y. H. Chiang, J. C. Lin, Y. H. Chou, C. Y. Cheng, and R. S. Liu, "Crossover study of ^{99m}Tc-TRODAT-1 SPECT and ^{18}F-FDOPA PET in Parkinson's disease patients," *Journal of Nuclear Medicine*, vol. 44, no. 7, pp. 999–1005, 2003.

[15] Y. H. Weng, T. C. Yen, M. C. Chen et al., "Sensitivity and specificity of ^{99m}Tc-TRODAT-1 SPECT imaging in differentiating patients with idiopathic Parkinson's disease from healthy subjects," *Journal of Nuclear Medicine*, vol. 45, no. 3, pp. 393–401, 2004.

[16] E. Nurmi, H. M. Ruottinen, J. Bergman et al., "Rate of progression in Parkinson's disease: a 6-[^{18}F]fluoro-L-dopa PET study," *Movement Disorders*, vol. 16, no. 4, pp. 608–615, 2001.

[17] L. Farde, S. Pauli, H. Hall et al., "Stereoselective binding of 11C-raclopride in living human brain - A search for extrastriatal central D2-dopamine receptors by PET," *Psychopharmacology*, vol. 94, no. 4, pp. 471–478, 1988.

[18] K. Y. Tzen, C. S. Lu, T. C. Yen, S. P. Wey, and G. Ting, "Differential diagnosis of Parkinson's disease and vascular parkinsonism by [^{99m}Tc]-TRODAT-1," *Journal of Nuclear Medicine*, vol. 42, no. 3, pp. 408–413, 2001.

[19] W. Koch, C. Hamann, P. E. Radau, and K. Tatsch, "Does combined imaging of the pre- and postsynaptic dopaminergic system increase the diagnostic accuracy in the differential diagnosis of parkinsonism?" *European Journal of Nuclear Medicine and Molecular Imaging*, vol. 34, no. 8, pp. 1265–1273, 2007.

[20] M. Plotkin, H. Amthauer, S. Klaffke et al., "Combined ^{123}I-FP-CIT and I-IBZM SPECT for the diagnosis of parkinsonian syndromes: study on 72 patients," *Journal of Neural Transmission*, vol. 112, no. 5, pp. 677–692, 2005.

[21] R. Pahwa and K. E. Lyons, "Early diagnosis of Parkinson's disease: recommendations from diagnostic clinical guidelines," *The American Journal of Managed Care*, vol. 16, pp. S94–99, 2010.

[22] Y. H. Weng, Y. H. W. Chou, W. S. Wu et al., "PINK1 mutation in Taiwanese early-onset parkinsonismml: clinical, genetic, and dopamine transporter studies," *Journal of Neurology*, vol. 254, no. 10, pp. 1347–1355, 2007.

[23] T. C. Yen, K. Y. Tzen, M. C. Chen et al., "Dopamine transporter concentration is reduced in asymptomatic Machado-Joseph disease gene carriers," *Journal of Nuclear Medicine*, vol. 43, no. 2, pp. 153–159, 2002.

[24] A. Antonini, "Imaging for early differential diagnosis of parkinsonism," *The Lancet Neurology*, vol. 9, no. 2, pp. 130–131, 2010.

[25] C. R. Freed, P. E. Greene, R. E. Breeze et al., "Transplantation of embryonic dopamine neurons for severe Parkinson's disease," *New England Journal of Medicine*, vol. 344, no. 10, pp. 710–719, 2001.

[26] Y. Ma, C. Tang, T. Chaly et al., "Dopamine cell implantation in Parkinson's disease: long-term clinical and ^{18}F-FDOPA PET outcomes," *Journal of Nuclear Medicine*, vol. 51, no. 1, pp. 7–15, 2010.

[27] A. E. Lang, S. Gill, N. K. Patel et al., "Randomized controlled trial of intraputamenal glial cell line-derived neurotrophic factor infusion in Parkinson disease," *Annals of Neurology*, vol. 59, no. 3, pp. 459–466, 2006.

[28] A. L. Berry and T. Foltynie, "Gene therapy: a viable therapeutic strategy for Parkinson's disease?" *Journal of Neurology*, vol. 258, pp. 179–188, 2010.

[29] W. J. Marks Jr., J. L. Ostrem, L. Verhagen et al., "Safety and tolerability of intraputaminal delivery of CERE-120 (adeno-associated virus serotype 2-neurturin) to patients with idiopathic Parkinson's disease: an open-label, phase I trial," *The Lancet Neurology*, vol. 7, no. 5, pp. 375–376, 2008.

[30] M. G. Kaplitt, A. Feigin, C. Tang et al., "Safety and tolerability of gene therapy with an adeno-associated virus (AAV) borne GAD gene for Parkinson's disease: an open label, phase I trial," *Lancet*, vol. 369, no. 9579, pp. 2097–2105, 2007.

[31] J. L. Eberling, W. J. Jagust, C. W. Christine et al., "Results from a phase I safety trial of hAADC gene therapy for Parkinson disease," *Neurology*, vol. 70, no. 21, pp. 1980–1983, 2008.

[32] L. Leriche, T. Björklund, N. Breysse et al., "Positron emission tomography imaging demonstrates correlation between behavioral recovery and correction of dopamine neurotransmission after gene therapy," *Journal of Neuroscience*, vol. 29, no. 5, pp. 1544–1553, 2009.

[33] S. I. Muramatsu, K. I. Fujimoto, S. Kato et al., "A phase I study of aromatic L-amino acid decarboxylase gene therapy for Parkinson's disease," *Molecular Therapy*, vol. 18, pp. 1731–1735, 2010.

[34] K. Blennow, M. J. de Leon, and H. Zetterberg, "Alzheimer's disease," *Lancet*, vol. 368, pp. 387–403, 2006.

[35] R. Brookmeyer, E. Johnson, K. Ziegler-Graham, and H. M. Arrighi, "Forecasting the global burden of Alzheimer's disease," *Alzheimer's and Dementia*, vol. 3, no. 3, pp. 186–191, 2007.

[36] A. Kadir and A. Nordberg, "Target-specific PET probes for neurodegenerative disorders related to dementia," *Journal of Nuclear Medicine*, vol. 51, no. 9, pp. 1418–1430, 2010.

[37] M. P. Mattson, "Pathways towards and away from Alzheimer's disease," *Nature*, vol. 430, no. 7000, pp. 631–639, 2004.

[38] W. Jagust, "Positron emission tomography and magnetic resonance imaging in the diagnosis and prediction of dementia," *Alzheimer's and Dementia*, vol. 2, no. 1, pp. 36–42, 2006.

[39] D. H. S. Silverman, G. W. Small, and M. E. Phelps, "Clinical value of neuroimaging in the diagnosis of dementia. Sensitivity and specificity of regional cerebral metabolic and other parameters for early identification of Alzheimer's disease," *Clinical Positron Imaging*, vol. 2, no. 3, pp. 119–130, 1999.

[40] H. Engler, A. Forsberg, O. Almkvist et al., "Two-year follow-up of amyloid deposition in patients with Alzheimer's disease," *Brain*, vol. 129, no. 11, pp. 2856–2866, 2006.

[41] A. Nordberg, "PET imaging of amyloid in Alzheimer's disease," *Lancet Neurology*, vol. 3, no. 9, pp. 519–527, 2004.

[42] A. Nordberg, "Amyloid imaging in Alzheimer's disease," *Neuropsychologia*, vol. 46, no. 6, pp. 1636–1641, 2008.

[43] A. Nordberg, "Amyloid plaque imaging in vivo: current achievement and future prospects," *European Journal of*

Nuclear Medicine and Molecular Imaging, vol. 35, no. 1, pp. S46–S50, 2008.

[44] V. Valotassiou, S. Archimandritis, N. Sifakis, J. Papatriantafyllou, and P. Georgoulias, "Alzheimer's disease: SPECT and PET tracers for beta-amyloid imaging," *Current Alzheimer Research*, vol. 7, no. 6, pp. 477–486, 2010.

[45] K. Shoghi-Jadid, G. W. Small, E. D. Agdeppa et al., "Localization of neurofibrillary tangles and beta-amyloid plaques in the brains of living patients with alzheimer disease," *American Journal of Geriatric Psychiatry*, vol. 10, no. 1, pp. 24–35, 2002.

[46] C. A. Mathis, B. J. Bacskai, S. T. Kajdasz et al., "A lipophilic thioflavin-T derivative for positron emission tomography (PET) imaging of amyloid in brain," *Bioorganic and Medicinal Chemistry Letters*, vol. 12, no. 3, pp. 295–298, 2002.

[47] W. E. Klunk, H. Engler, A. Nordberg et al., "Imaging Brain Amyloid in Alzheimer's Disease with Pittsburgh Compound-B," *Annals of Neurology*, vol. 55, no. 3, pp. 306–319, 2004.

[48] R. C. Petersen, G. E. Smith, S. C. Waring, R. J. Ivnik, E. G. Tangalos, and E. Kokmen, "Mild cognitive impairment: clinical characterization and outcome," *Archives of Neurology*, vol. 56, no. 3, pp. 303–308, 1999.

[49] S. M. Landau, D. Harvey, C. M. Madison et al., "The Alzheimer's Disease Neuroimaging Initiative. Associations between cognitive, functional, and FDG-PET measures of decline in AD and MCI," *Neurobiology of Aging*. In press.

[50] A. Forsberg, H. Engler, O. Almkvist et al., "PET imaging of amyloid deposition in patients with mild cognitive impairment," *Neurobiology of Aging*, vol. 29, no. 10, pp. 1456–1465, 2008.

[51] D. F. Wong, P. B. Rosenberg, Y. Zhou et al., "In vivo imaging of amyloid deposition in Alzheimer disease using the radioligand 18F-AV-45 (flobetapir F 18)," *Journal of Nuclear Medicine*, vol. 51, no. 6, pp. 913–920, 2010.

[52] N. P. L. G. Verhoeff, A. A. Wilson, S. Takeshita et al., "In-vivo imaging of Alzheimer disease β-amyloid with [^{11}C]SB-13 PET," *American Journal of Geriatric Psychiatry*, vol. 12, no. 6, pp. 584–595, 2004.

[53] N. Tolboom, W. M. Van Der Flier, J. Boverhoff et al., "Molecular imaging in the diagnosis of Alzheimer's disease: visual assessment of [11C]PIB and [18F]FDDNP PET images," *Journal of Neurology, Neurosurgery and Psychiatry*, vol. 81, no. 8, pp. 882–884, 2010.

[54] R. Vandenberghe, K. Van Laere, A. Ivanoiu et al., "18F-flutemetamol amyloid imaging in Alzheimer disease and mild cognitive impairment: a phase 2 trial," *Annals of Neurology*, vol. 68, pp. 319–329, 2010.

[55] J. Hardy and D. J. Selkoe, "The amyloid hypothesis of Alzheimer's disease: progress and problems on the road to therapeutics," *Science*, vol. 297, no. 5580, pp. 353–356, 2002.

[56] A. Kadir, N. Andreasen, O. Almkvist et al., "Effect of phenserine treatment on brain functional activity and amyloid in Alzheimer's disease," *Annals of Neurology*, vol. 63, no. 5, pp. 621–631, 2008.

[57] D. E. Kuhl, S. Minoshima, K. A. Frey, N. L. Foster, M. R. Kilbourn, and R. A. Koeppe, "Limited donepezil inhibition of acetylcholinesterase measured with positron emission tomography in living Alzheimer cerebral cortex," *Annals of Neurology*, vol. 48, no. 3, pp. 391–395, 2000.

[58] R. V. Parsey, "Serotonin receptor imaging: clinically useful?" *Journal of Nuclear Medicine*, vol. 51, no. 10, pp. 1495–1498, 2010.

[59] S. Sobczak, A. Honig, M. A. van Duinen, and W. J. Riedel, "Serotonergic dysregulation in bipolar disorders: a literature review of serotonergic challenge studies," *Bipolar Disorders*, vol. 4, no. 6, pp. 347–356, 2002.

[60] A. Neumeister, E. Bain, A. C. Nugent et al., "Reduced serotonin type 1 receptor binding in panic disorder," *Journal of Neuroscience*, vol. 24, no. 3, pp. 589–591, 2004.

[61] W. C. Drevets, E. Frank, J. C. Price et al., "PET imaging of serotonin 1A receptor binding in depression," *Biological Psychiatry*, vol. 46, no. 10, pp. 1375–1387, 1999.

[62] W. C. Drevets, E. Frank, J. C. Price, D. J. Kupfer, P. J. Greer, and C. Mathis, "Serotonin type-1A receptor imaging in depression," *Nuclear Medicine and Biology*, vol. 27, no. 5, pp. 499–507, 2000.

[63] J. Blin, G. Sette, M. Fiorelli et al., "A method for the in vivo investigation in the serotonergic 5-HT$_2$ receptors in the human cerebral cortex using positron emission tomography and ^{18}F-labeled setoperone," *Journal of Neurochemistry*, vol. 54, no. 5, pp. 1744–1754, 1990.

[64] J. Blin, J. C. Baron, B. Dubois et al., "Loss of brain 5-HT$_2$ receptors in Alzheimer's disease. In vivo assessment with positron emission tomography and [^{18}F]setoperone," *Brain*, vol. 116, no. 3, pp. 497–510, 1993.

[65] E. T. C. Ngan, L. N. Yatham, T. J. Ruth, and P. F. Liddle, "Decreased serotonin 2A receptor densities in neuroleptic-naive patients with schizophrenia: a pet study using [^{18}F]setoperone," *American Journal of Psychiatry*, vol. 157, no. 6, pp. 1016–1018, 2000.

[66] W. A. Wolf and D. M. Kuhn, "Modulation of serotonin release: interactions between the serotonin transporter and autoreceptors," *Annals of the New York Academy of Sciences*, vol. 604, pp. 505–513, 1990.

[67] M. Suehiro, U. Scheffel, H. T. Ravert, R. F. Dannals, and H. N. Wagner, "[11C](+)McN5652 as a radiotracer for imaging serotonin uptake sites with PET," *Life Sciences*, vol. 53, no. 11, pp. 883–892, 1993.

[68] S. Hesse, H. Barthel, J. Schwarz, O. Sabri, and U. Müller, "Advances in in vivo imaging of serotonergic neurons in neuropsychiatric disorders," *Neuroscience and Biobehavioral Reviews*, vol. 28, no. 6, pp. 547–563, 2004.

[69] J. H. Meyer, "Imaging the serotonin transporter during major depressive disorder and antidepressant treatment," *Journal of Psychiatry and Neuroscience*, vol. 32, no. 2, pp. 86–102, 2007.

[70] K. J. Lin, C. Y. Liu, S. P. Wey et al., "Brain SPECT imaging and whole-body biodistribution with [^{123}I]ADAM—a serotonin transporter radiotracer in healthy human subjects," *Nuclear Medicine and Biology*, vol. 33, no. 2, pp. 193–202, 2006.

[71] Z. Bhagwagar, N. Murthy, S. Selvaraj et al., "5-HTT binding in recovered depressed patients and healthy volunteers: a positron emission tomography study with [^{11}C]DASB," *American Journal of Psychiatry*, vol. 164, no. 12, pp. 1858–1865, 2007.

[72] R. V. Parsey, R. S. Hastings, M. A. Oquendo et al., "Lower serotonin transporter binding potential in the human brain during major depressive episodes," *American Journal of Psychiatry*, vol. 163, no. 1, pp. 52–58, 2006.

[73] J. H. Meyer, A. A. Wilson, N. Ginovart et al., "Occupancy of serotonin transporters by paroxetine and citalopram during treatment of depression: a [^{11}C]DASB PET imaging study," *American Journal of Psychiatry*, vol. 158, no. 11, pp. 1843–1849, 2001.

[74] J. H. Meyer, S. Houle, S. Sagrati et al., "Brain serotonin transporter binding potential measured with [^{11}C]DASB positron emission tomography: effects of major depressive episodes and severity of dysfunctional attitudes," *Archives of General Psychiatry*, vol. 61, no. 12, pp. 1271–1279, 2004.

[75] A. B. Newberg, J. D. Amsterdam, N. Wintering et al., "[123]I-ADAM binding to serotonin transporters in patients with major depression and healthy controls: a preliminary study," *Journal of Nuclear Medicine*, vol. 46, no. 6, pp. 973–977, 2005.

[76] N. Herold, K. Uebelhack, L. Franke et al., "Imaging of serotonin transporters and its blockade by citalopram in patients with major depression using a novel SPECT ligand [^{123}I]-ADAM," *Journal of Neural Transmission*, vol. 113, no. 5, pp. 659–670, 2006.

[77] S. Sobczak, A. Honig, M. A. van Duinen, and W. J. Riedel, "Serotonergic dysregulation in bipolar disorders: a literature review of serotonergic challenge studies," *Bipolar Disorders*, vol. 4, no. 6, pp. 347–356, 2002.

[78] G. Murray and S. L. Johnson, "The clinical significance of creativity in bipolar disorder," *Clinical Psychology Review*, vol. 30, pp. 721–732, 2010.

[79] Y. H. Chou, S. J. Wang, C. L. Lin, W. C. Mao, S. M. Lee, and M. H. Liao, "Decreased brain serotonin transporter binding in the euthymic state of bipolar I but not bipolar II disorder: a SPECT study," *Bipolar Disorders*, vol. 12, no. 3, pp. 312–318, 2010.

[80] T. T. Chang, T. L. Yeh, N. T. Chiu et al., "Higher striatal dopamine transporters in euthymic patients with bipolar disorder: a SPECT study with [99mTc] TRODAT-1," *Bipolar Disorders*, vol. 12, no. 1, pp. 102–106, 2010.

[81] Y. K. Yang, W. J. Yao, T. L. Yeh, I. H. Lee, K. C. Chen, and R. B. Lu, "Association between serotonin transporter availability and hostility scores in healthy volunteers—a single photon emission computed tomography study with [^{123}I] ADAM," *Psychiatry Research*, vol. 154, no. 3, pp. 281–284, 2007.

[82] C. Hiemke, "Therapeutic drug monitoring in neuropsychopharmacology: does it hold its promises?" *European Archives of Psychiatry and Clinical Neuroscience*, vol. 258, no. 1, supplement, pp. 21–27, 2008.

[83] M. Sekine, R. Arakawa, H. Ito et al., "Norepinephrine transporter occupancy by antidepressant in human brain using positron emission tomography with (S,S)-[18F]FMeNER-D," *Psychopharmacology*, vol. 210, pp. 331–336, 2010.

[84] Y. S. Ding, T. Singhal, B. Planeta-Wilson et al., "PET imaging of the effects of age and cocaine on the norepinephrine transporter in the human brain using (S,S)-[11C]O-methylreboxetine and HRRT," *Synapse*, vol. 64, no. 1, pp. 30–38, 2010.

[85] M. Árgyelán, Z. Szabó, B. Kanyó et al., "Dopamine transporter availability in medication free and in bupropion treated depression: a 99mTc-TRODAT-1 SPECT study," *Journal of Affective Disorders*, vol. 89, no. 1-3, pp. 115–123, 2005.

[86] L. Farde, F. A. Wiesel, C. Halldin, and G. Sedvall, "Central D2-dopamine receptor occupancy in schizophrenic patients treated with antipsychotic drugs," *Archives of General Psychiatry*, vol. 45, no. 1, pp. 71–76, 1988.

Research Article

Synthesis and Evaluation of Amino Acid-Based Radiotracer ^{99m}Tc-N4-AMT for Breast Cancer Imaging

Fan-Lin Kong, Mohammad S. Ali, Yinhan Zhang, Chang-Sok Oh, Dong-Fang Yu, Mithu Chanda, and David J. Yang

Department of Experimental Diagnostic Imaging, The University of Texas M. D. Anderson Cancer Center, 1515 Holcombe Boulevard, Houston, TX 77030, USA

Correspondence should be addressed to Fan-Lin Kong, fanlin.kong@mdanderson.org

Purpose. This study was to develop an efficient synthesis of ^{99m}Tc-O-[3-(1,4,8,11-tetraazabicyclohexadecane)-propyl]-α-methyl tyrosine (^{99m}Tc-N4-AMT) and evaluate its potential in cancer imaging. *Methods.* N4-AMT was synthesized by reacting N4-oxalate and 3-bromopropyl AMT (N-BOC, ethyl ester). *In vitro* cellular uptake kinetics of ^{99m}Tc-N4-AMT was assessed in rat mammary tumor cells. Tissue distribution of the radiotracer was determined in normal rats at 0.5–4 h, while planar imaging was performed in mammary tumor-bearing rats at 30–120 min. *Results.* The total synthesis yield of N4-AMT was 14%. Cellular uptake of ^{99m}Tc-N4-AMT was significantly higher than that of ^{99m}Tc-N4. Planar imaging revealed that ^{99m}Tc-N4-AMT rendered greater tumor/muscle ratios than ^{99m}Tc-N4. *Conclusions.* N4-AMT could be synthesized with a considerably high yield. Our *in vitro* and *in vivo* data suggest that ^{99m}Tc-N4-AMT, a novel amino acid-based radiotracer, efficiently enters breast cancer cells, effectively distinguishes mammary tumors from normal tissues, and thus holds the promise for breast cancer imaging.

1. Introduction

^{18}F-fluoro-deoxy-glucose (FDG), an ^{18}F-labeled glucose analog, is the most common radiotracer for positron emission tomography (PET) in cancer diagnosis [1]. However, FDG-PET has several limitations in practice, for example, FDG cannot distinguish tumor tissues from inflammatory or normal brain tissues. Therefore, ^{18}F-labeled amino acid-based radiotracers have been reported as an alternative, which is based on the fact that tumor cells take up and consume more amino acids to maintain their sustained fast growth. Among those radiotracers, ^{18}F-labeled alpha-methyl tyrosine (AMT) has shown high tumor uptake and great ability to differentiate tumor tissue from inflammatory sites in brain tumors and squamous cell carcinoma [2]. ^{18}F-AMT enters the tumor cells via L-type amino acid transporters (LAT), which is the only system that can transport large neutral amino acids with aromatic rings [3]. LAT, especially its subtype LAT1, was reported to be highly expressed in many cancer cell lines and positively correlates with tumor growth [4, 5]. So far, ^{18}F-AMT is the most suitable amino acid transporter-targeting radiotracer for tumor imaging, regardless of low synthesis yield and requirement of an on-site cyclotron to produce ^{18}F.

Although PET has emerged as an advanced imaging tool for cancer diagnosis, only limited facilities around the world can afford complete armamentarium of PET and cyclotron for the local production of short-lived positron-emitting radionuclides such as ^{11}C and ^{18}F. Therefore, mature technologies, that is, single photon emission computed tomography (SPECT) or its combination with computed tomography (CT), still play important and irreplaceable roles in nuclear imaging area [6]. The most common radionuclide for SPECT is technetium-99m (^{99m}Tc, $t_{1/2} = 6.02$ h), which is produced by in-house generator and does not require the cyclotron [7]. Due to their similar chemistry, the diagnostic radioisotope ^{99m}Tc and the therapeutic radioisotope rhenium-188 (^{188}Re) could be labeled to the same ligand, which leads to the diagnostic/therapeutic matched pair. Unlike most of the cyclotron-produced radionuclides that utilize the covalent chemistry for labeling, ^{99m}Tc requires a "chelator" to conjugate the radionuclide with the target ligand. The nitrogen,

oxygen, and sulfur combinations have been shown to be stable chelators for ^{99m}Tc such as N$_4$ (e.g., DOTA, cyclam-14), N$_3$S (e.g., MAG-3), N$_2$S$_2$ (e.g., ECD), NS$_3$, S$_4$ (e.g., sulfur colloid), diethylenetriamine pentaacetic acid (DTPA), O$_2$S$_2$ (e.g., DMSA), and hydrazinonicotinamide (HYNIC) [8–13].

Here, we report the synthesis of precursor O-[3-(1,4,8,11-tetraazacyclotetradecan)-propyl]-α-methyl tyrosine (N$_4$-AMT) and its radiolabeling with ^{99m}Tc. *In vitro* cellular uptake kinetics and planar scintigraphic imaging of ^{99m}Tc-N4-AMT were also evaluated.

2. Materials and Methods

All chemicals of analytical grade and solvents of HPLC grade for compound synthesis were purchased from Sigma-Aldrich (St. Louis, MO). ^{1}H-, ^{13}C-NMR spectra were performed on Bruker 300 MHz spectrometer in CDCl$_3$, CD$_3$OD, and D$_2$O. Tetramethylsilane was used as an external standard. Chemical shifts were reported in δ (ppm) and J values in hertz. Sodium pertechnetate (Na^{99m}TcO$_4$) was obtained from ^{99}Mo/^{99m}Tc generator in Mallinckrodt (Houston, TX).

2.1. Synthesis of Precursor N4-AMT

2.1.1. α-Methyl Tyrosine Ethylester 2. The synthetic strategies for precursor N$_4$-AMT are demonstrated in Figure 1. Thionyl chloride (10 mL; 137.42 mmol) was added to a solution of α-methyltyrosine 1 (10.00 g; 51.22 mmol) in anhydrous ethanol (60 mL) at 0°C, and then heated at 78°C for 4 h while stirring. After cooling, the reaction mixture was reduced to 20 mL, and then 10 mL of triethylamine was added into it. The mixture was poured into 100 mL of water and extracted with chloroform. The combined organic layers were dried over MgSO$_4$ and evaporated. The desired compound was obtained as white solid. Yield: 9.00 g (40.32 mmol, 78.75%). ^{1}H-NMR (CDCl$_3$) δ = 7.02 (d, 2H, J = 8.4 Hz), 6.70 (d, 2H, J = 8.4 Hz), 4.22 (dd, 2H, J = 7.2 Hz, J = 7.8 Hz), 3.14 (dd, 2H, J = 13.5 Hz, J = 13.5), 1.42 (s, 3H), 1.33 (t, 3H, J = 16.2 Hz) ppm. ^{13}C-NMR δ = 175.47, 156.36, 130.66, 126.39, 114.87, 61.05, 58.65, 45.29, 24.08, 13.07 ppm, MS: m/z = 224.23 [M]$^+$.

2.1.2. N-t-Butoxycarbonyl-α-Methyl Tyrosine Ethylester 3. Compound 2 (2.09 g; 9.36 mmol) was dissolved in 40 mL of anhydrous DMF under nitrogen and treated with triethylamine (2.78 mL; 20 mmol) while stirring. Ditertiarbutyl dicarbonate (3.27 g; 15 mmol) was added to the reaction mixture and stirred over night at room temperature. The solvent was removed under reduced pressure to yield a residue, which was extracted with ethyl acetate and dried with anhydrous MgSO$_4$. The extraction was filtered and evaporated to give yellow oil which was purified by column chromatography on silica gel and eluted with hexane: ethyl acetate (5 : 1.5 v/v). After evaporation of the solvent, yellow oil 3 was obtained. Yield: 2.00 g (6.18 mmol, 66.20%). ^{1}H-NMR (CDCl$_3$) δ = 6.97 (d, 2H, J = 8.4 Hz), 6.75 (d, 2H, J = 8.7 Hz), 4.22 (dd, 2H, J = 2.7 Hz, J = 7.2 Hz),

3.32 (dd, 2H, J = 15.0 Hz, J = 13.5), 1.55 (s, 3H), 1.48 (s, 9H), 1.32 (t, 3H, J = 18.0 Hz) ppm. ^{13}C-NMR δ = 174.16, 155.04, 154.51, 131.16, 128.50, 115.14, 77.25, 61.64, 60.54, 40.99, 28.39, 23.55, 14.77 ppm, MS: m/z = 324.36 [M]$^+$.

2.1.3. N-t-Butoxycarbonyl-O-[3-Hydroxypropyl]-α-Methyl Tyrosine Ethylester 4. Sodium metal (0.09 g; 14.02 mmol) was dissolved in 30 mL of anhydrous ethanol with stirring under nitrogen. Compound 3 (1.00 g; 3.09 mmol) was dissolved in 50 mL of anhydrous ethanol and treated with sodium ethoxide solution and refluxed for 2.5 h at 70°C. 3-Bromopropanol (0.56 mL; 6.18 mmol) was added and continued heating over night. The ethanol was removed under reduced pressure and replaced with 40 mL of ethyl acetate, washed with water, and dried over MgSO$_4$. After removal of the solvent, it was purified by silica gel column chromatography (hexane: ethylacetate 2 : 1), giving 0.83 g (2.17 mmol, 71% yield) of the product as clear yellow oil. ^{1}H-NMR (CDCl$_3$) δ = 7.01 (d, 2H, J = 6.3 Hz), 6.81 (d, 2H, J = 6.6 Hz), 4.20 (dd, 2H, J = 5.1 Hz, J = 5.1 Hz), 4.12 (t, 2H, J = 15.0 Hz), 3.86 (t, 2H, J = 10.2 Hz), 3.16 (dd, J = 13.5 Hz, J = 12.9 Hz), 2.06 (m, 2H), 1.54 (s, 3H), 1.47 (s, 9H), 1.31 (t, 3H, J = 12.3 Hz) ppm. ^{13}C-NMR δ = 174.01, 171.91, 157.73, 154.35, 131.07, 128.65, 114.14, 79.39, 65.65, 61.54, 60.40, 60.24, 40.79, 32.01, 28.39, 23.58, 14.15 ppm, MS: m/z = 381.033 [M]$^+$.

2.1.4. N-t-Butoxycarbonyl-O-[3-Br-Propyl]-α-Methyl Tyrosine Ethylester 5. A solution of 4 (5.44 g; 16.82 mmol) and 1,3-dibromopropane (136.74 g; 677.30 mmol) in 100 mL acetone was purged with nitrogen for 15 min. Potassium carbonate (22.62 g; 163.69 mmol) was added to the reaction mixture, the mixture was then refluxed for 12 h at 75°C. After the removal of solvents and excessive reagents under reduced pressure, the residue was dissolved in chloroform, washed with water, and dried in anhydrous magnesium sulfate. A yellow liquid was purified by silica gel flash chromatography (hexane: ethylacetate, 2 : 1) to furnish compound 5 as pale yellow liquid. Yield: 4.80 g (7.52 mmol, 64.69%). ^{1}H-NMR (CDCl$_3$) δ = 7.02 (d, 2H, J = 9.00 Hz), 6.82 (d, 2H, J = 9.00 Hz), 4.23 (dd, 2H, J = 27.00), 4.09 (t, 2H, J = 12.00 Hz), 3.61 (t, 2H, J = 12.00 Hz), 3.32, 3.16 (d, 2H, J = 15.00, 12.00 Hz), 2.34 (dd, J = 24.00 Hz), 1.54 (s, 3H), 1.47 (s, 9H), 1.32 (t, 3H, J = 15.0 Hz) ppm. ^{13}C-NMR δ = 173.96, 157.63, 154.32, 131.09, 128.78, 114.18, 77.48, 65.24, 61.51, 60.35, 40.80, 30.00, 28.40, 23.60, 14.19 ppm. MS: m/z = 446.3 [M]$^+$.

2.1.5. N^1, N^4-Dioxylyl-1,4,8,11-Tetraazabicyclotetradecane (N^1,N^4-Cyclooxamide) 6. 1,4,8,11-tetraazacyclotetradecane (cyclam) (15.00 g; 74.88 mmol) was dissolved in 150 mL of anhydrous ethanol, and diethyl oxalate (10.94 g; 74.88 mmol) was added. The reaction mixture was refluxed 18 h at 75°C. The solvent was rotary evaporated, and the crude product was recrystallized in acetone: ethanol to yield white crystals of N^1,N^4-dioxylyl-1,4,8,11-1,5,8,12-tetraazabicyclotetradecane (N^1,N^4-cyclooxamide) 6. Yield: 13.64 g (17.31 mmol, 72.00%). ^{1}H-NMR (CDCl$_3$) δ = 4.35 (m, 2H), 375 (m, 2H), 3.40 (m, 2H), 2.77 (m, 2H), 2.68 (m, 2H), 2.54 (m, 2H), 2.43 (m, 4H), 1.75 (m, 2H),
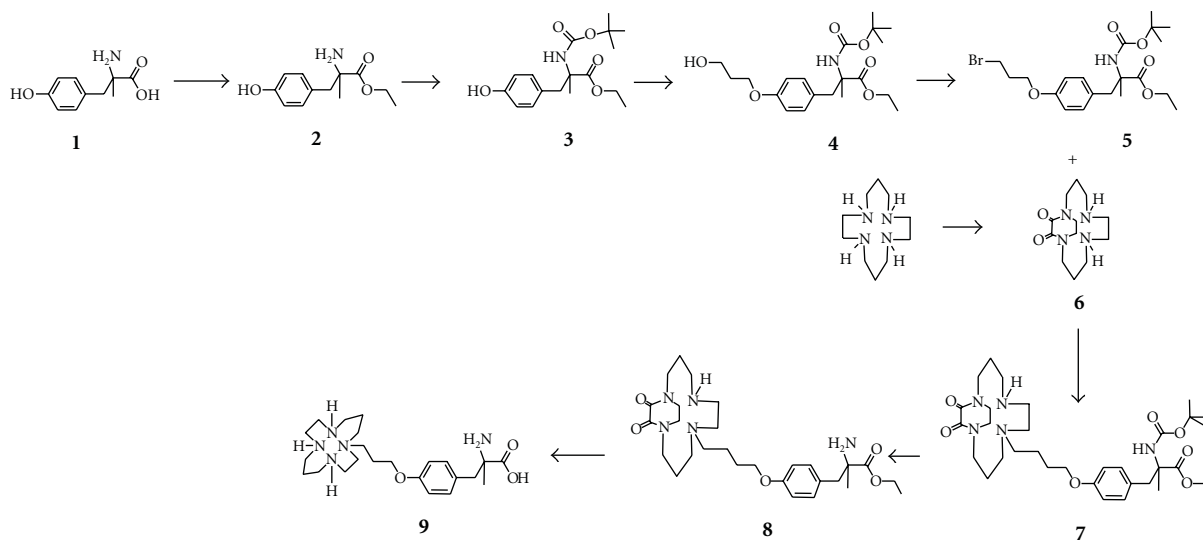
Figure 1: Synthetic scheme of precursor N4-AMT.

1.24 (m, 2H)) ppm. ^{13}C-NMR δ = 158.55, 49.92, 49.38, 47.73, 44.13, 25.42 ppm. MS: m/z = 255.33 $[M]^+$.

2.1.6. N-t-Butoxycarbonyl-O-[3-(N^1,N^4-Dioxylyl-1,4,8,11-Tetraazabicyclotetradecane)-Propyl]-α-Methyl Tyrosine Ethylester 7.

Compound 6 (1.00 g; 3.93 mmol) was dissolved in 20 mL of anhydrous DMF and treated with a solution of N-t-Butoxycarbonyl-O-[3-Br-propyl]-α-methyl tyrosine ethylester 5 (1.74 g; 3.93 mmol) in 40 mL of DMF under nitrogen atmosphere. The reaction mixture was heated to reflux for 18 h at 75°C and then allowed to cool down to room temperature. The solvent was removed *in vacuo*. The residue was dissolved in chloroform (30 mL), washed with water and 1 M Na$_2$CO$_3$, (12 mL), and then separated for the organic layer. It was dried with anhydrous Magnesium sulfate, filtered, and evaporated. The crude compound was purified by silica gel column chromatograph (chloroform: methanol 9 : 1). Yield: 1.00 g (1.63 mmol, 42.00%). ^{1}H-NMR (CDCl$_3$) δ = 7.00 (d, 2H, J = 9.00 Hz), 6.79 (d, 2H, J = 9.00 Hz), 4.56 (m, 2H), 4.22 (t, 2H, J = 12.0 Hz), 3.95 (m, 2H), 3.67 (m, 2H), 3.55 (t, 2H, J = 15.0 Hz), 3.30 (m, 4H), 2.81 (m, 12H), 1.88 (m, 6H), 1.54 (s, 3H), 1.47 (s, 9H), 1.32 (t, 3H, J= 15.0 Hz) ppm. ^{13}C-NMR δ = 173.97, 158.65, 158.06, 157.91, 154.31, 131.01, 128.34, 114.04, 79.38, 77.27, 66.01, 61.50, 60.26, 53.76, 52.76, 49.20, 48.41, 47.54, 46.15, 45.83, 44.50, 42.60, 40.84, 28.40, 26.39, 23.57, 23.36, 23.07, 14.14 ppm. MS: m/z = 618.38 $[M]^+$.

2.1.7. O-[3-(N^1,N^4-Dioxylyl-1,4,8,11-Tetraazabicyclotetradecane)-Propyl]-α-Methyltyrosine Ethylester 8.

Compound 7 (0.25 g; 0.40 mmol) was dissolved in dichloromethane (10 mL), and trifluoroacetic acid (1.0 mL) was added to it. The solution was stirred over night at room temperature, and volatiles were removed *in vacuo*. The crude compound was purified by chromatography over silica gel (chloroform: methanol 9 : 1) as white solid. Yield: 0.20 g (0.39 mmol; 95.69%). ^{1}H-NMR (CD$_3$OD) δ = 7.14 (d, 2H, J = 9.0 Hz),

6.94 (d, 2H), 4.33 (m, 4H), 4.05 (t, 2H, J = 9.0 Hz), 3.85 (m, 2H), 3.71 (m, 2 H), 3.26 (m, 13H), 2.07 (m, 6H), 1.58 (s, 3H), 1.33 (t, 3H, J = 15.0 Hz) ppm. ^{13}C-NMR δ = 170.65, 161.87, 161.42, 159.70, 159.02, 158.67, 131.01, 125.14, 118.79, 114.65, 65.34, 62.47, 60.33, 56.92, 52.16, 51.26, 45.64, 45.31, 44.50, 43.20, 42.05, 24.31, 22.00, 21.39, 21.03, 16.96, 12.90 ppm, MS: m/z = 517.63 $[M]^+$.

2.1.8. O-[3-(1,4,8,11-Tetraazabicyclohexadecane)-Propyl]-α-Methyl Tyrosine (N_4-AMT) 9.

To a solution of compound 8 (0.20 g; 0.39 mmol) in a 5 mL of water, 10 N NaOH (2 mL) was added, stirred, and refluxed over night at 90°C. The solvent was evaporated under vacuum, giving white solid, which was dissolved in 5 mL of water and neutralized with 5 N HCl solution to pH = 7. It was lyophilized and obtained as white solid. The solid was stirred in 25 mL anhydrous methanol, filtered, and evaporated to afford an off white solid. Yield: 0.20 g (0.46 mmol: 99.0%). ^{1}H-NMR (D$_2$O) δ = 7.21 (d, 2H, J = 9.00 Hz), 7.00 (d, 2H, J = 9.00 Hz), 4.14 (t, 2H, J = 12.0 Hz), 3.10 (m, 5H), 2.94 (m, 2H), 2.84 (m, 13H), 1.95 (m, 6H), 1.33 (s, 3H) ppm.^{13}C-NMR δ = 180.69, 163.42, 163.16, 162.88, 162.60, 157.06, 131.40, 129.19, 117.57, 115.26, 115.10, 112.93, 66.25, 60.73, 53.69, 51.46, 49.88, 49.26, 48.04, 47.84, 46.60, 45.42, 45.07, 43.94, 24.71, 24.32, 23.62, 22.55 ppm. MS: m/z = 436.327 $[M]^+$.

2.2. Radiosynthesis of ^{99m}Tc-N4-AMT.

Radiolabeling of N4-AMT with ^{99m}Tc was performed in a standard manner [14]. Briefly, radiosynthesis of ^{99m}Tc-N4-AMT was achieved by adding a required amount of sodium pertechnetate into a vial containing precursor N4-AMT and SnCl$_2$ (100 μg). Radiochemical purity was assessed by high-performance liquid chromatography (HPLC), equipped with NaI and UV detector (274 nm), and was performed using a C-18 reverse column with a mobile phase of acetonitrile : water (7 : 3) at a flow rate of 0.5 mL/min.

(a)

(b)
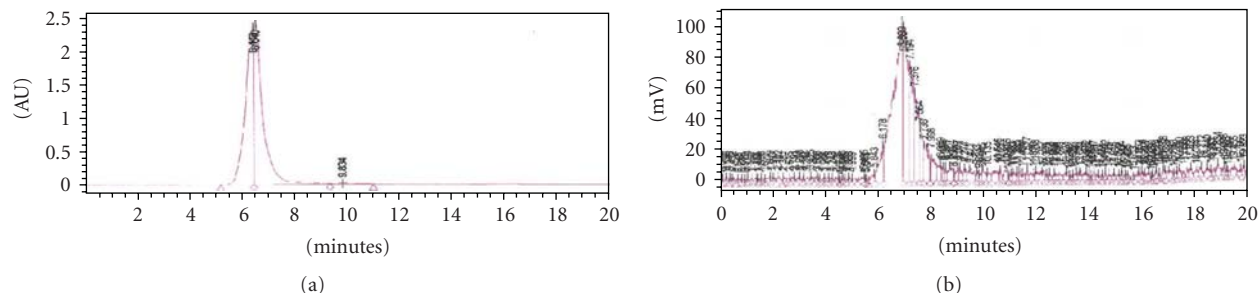
FIGURE 2: HPLC analysis of ^{99m}Tc-N4-AMT at a flow rate of 0.5 mL/min using a C-18 reverse column under UV absorbance of 274 nm.
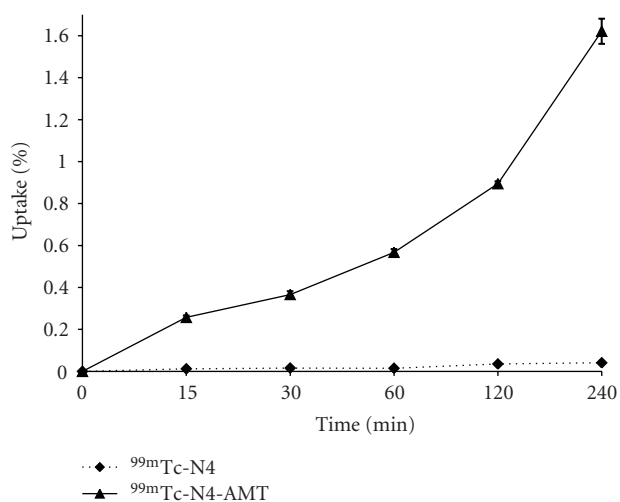
FIGURE 3: *In vitro* cellular uptake of ^{99m}Tc-N4-AMT. The cellular uptake kinetics of ^{99m}Tc-N4-AMT and ^{99m}Tc-N4 was conducted in the rat breast tumor cell line 13762. Data were expressed in mean ± S.D. percent of cellular uptake (%Uptake).

2.3. In Vitro Cellular Uptake of ^{99m}Tc-N4-AMT. Rat mammary tumor cell line 13762 was obtained from American Type Culture Collection (Rockville, MD). The same cell line was used to create the animal model for *in vivo* evaluation. Cells were maintained at 37°C in a humidified atmosphere containing 5% CO_2 in Dulbecco's modified Eagle's medium and nutrient mixture F-12 Ham (DMEM/F12; GIBCO, Grand Island, NY). Cells were plated to 6-well tissue culture plates (2×10^5 cells/well) for two days before the study, and incubated with ^{99m}Tc-N4-AMT (0.05 mg/well, 8 uCi/well) or ^{99m}Tc-N4 chelator itself (0.025 mg/well, 8 uCi/well) for 15 min–4 h. After incubation, cells were washed with ice-cold PBS twice and detached by adding 0.5 mL of trypsin. Cells were then collected and the radioactivity was measured with gamma counter (Cobra Quantum; Packard, MN). Data was expressed in mean ± S.D. percent of cellular uptake.

2.4. In Vivo Tissue Distribution Studies. All animal work was carried out in the Small Animal Imaging Facility (SAIF) at University of Texas MD Anderson Cancer Center under the protocol approved by Institutional Animal Care and Use

Committee (IACUC). Tissue distribution studies of ^{99m}Tc-N4-AMT (study I, $n = 9$) or ^{99m}Tc-N4 (study II, $n = 9$) were conducted by using normal female Fischer 344 rats (150 ± 25 g, $n = 18$) (Harlan Sprague-Dawley, Indianapolis, IN). For each radiotracer, nine rats were divided into three groups for three time intervals (0.5, 2, 4 h). The injection activity was $25 \pm 0.5 \mu$Ci/rat intravenously. At each time interval, the rats were sacrificed, and the selected tissues were excised, weighed, and measured for radioactivity by gamma counter. Data from each sample were represented as the percentage of the injected dose per gram of tissue wet weight (%ID/g). Counts from a diluted sample of the original injection were used as the reference.

2.5. Planar Scintigraphic Imaging Studies of ^{99m}Tc-N4-AMT. Female Fischer 344 rats were inoculated subcutaneously with 0.1 mL of 13762 rat mammary tumor cell suspension (10^5 cells/rat) into the right posterior legs using 22-gauge needles. Imaging studies were performed 14 to 17 days after inoculation when tumors reached approximately 1 cm in diameter. The anesthetized rats were injected intravenously with ^{99m}Tc-N4-AMT (0.3 mg/rat, 300μCi/rat; $n = 3$) or with ^{99m}Tc-N4 (0.15 mg/rat, 300μCi/rat; $n = 3$), respectively. Planar scintigraphic images were obtained using M-CAM (Siemens Medical Solutions, Hoffman Estates, IL) equipped with a Low-Energy High-Resolution collimator at 30–120 min. The field of view was 53.3 cm $\times$ 38.7 cm. The intrinsic spatial resolution was 3.2 mm and the pixel size was from 19.18 mm (32×32, zoom = 1) to 0.187 mm (1024×1024, zoom = 3.2). Computer outlined regions of interest (ROI) (counts per pixel) of tumors, and normal muscle tissues at symmetric sites were used to calculate tumor-to-muscle (T/M) ratios.

3. Results and Discussion

3.1. Chemistry. N4-AMT was synthesized via an eight-step procedure (Figure 1). Commercially available α-methyl tyrosine **1** was converted into corresponding acid chloride, then to ethyl ester by reacting with thionyl chloride in ethanol. The amine in α-methyl tyrosine ethyl ester **2** was protected as its Boc-derivative N-t-butoxycarbonyl-α-methyl tyrosine ethylester **3** with triethylamine and di-t-butyldicarbonate in DMF. The chain at the –OH group was extended when compound
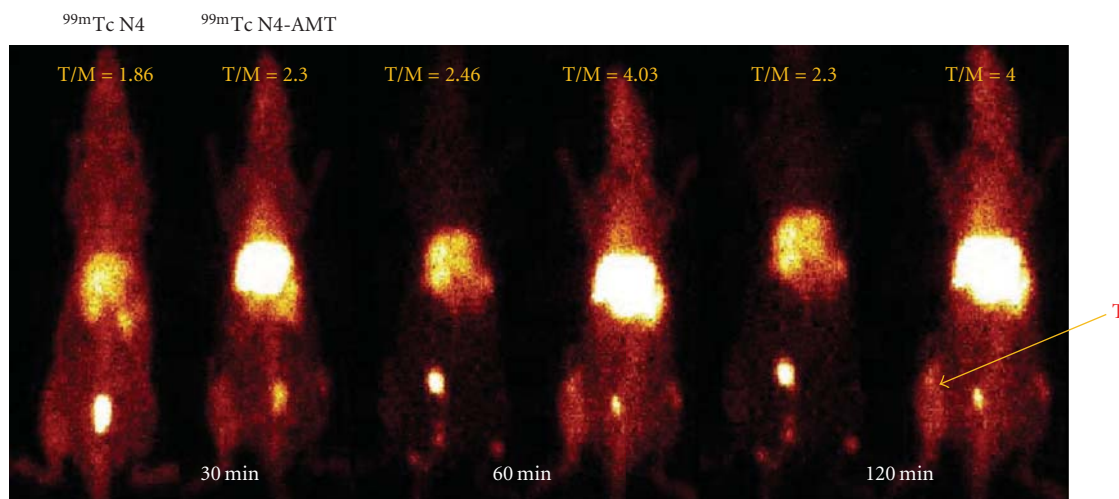
FIGURE 4: Planar scintigraphic imaging studies of ^{99m}Tc-N$_4$-AMT. Scintigraphic images of Fisher 344 tumor bearing rats were acquired, and computer outlined regions of interest (counts per pixel) in the tumors (T) and the symmetrical muscle tissues (M) were used to determine T/M count density ratios.

3 was treated with 1, 3-dibromopropane and obtained as N-t-butoxycarbonyl-O-[3-bromopropyl]-α-methyl tyrosine ethylester **4**. Acylation of 1,4,8,11-tetraazacyclo-tetradecane (cyclam) with diethyloxalate led to N^1,N^4-dioxalyl 1,4,8,11-tetraazacyclotetradecane (N^1,N^4-cyclamoxamide) **5**. Under SN^2 condition **4** and **5** were efficiently converted to alkylated compound N-t-butoxycarbonyl-O-[3-(N^1,N^4-dioxalyl-1,4, 8,11-tetraazacyclotetradecane)-propyl]-α-methyl tyrosine ethylester **6**. Exposure of **6** to trifluoroacetic acid in CH$_2$Cl$_2$ caused qualitative de-t-butoxycarboxylation to yield O-[3-(N^1, N^4-dioxalyl 1,4,8,11-tetraazacyclotetradecane)-propyl]-α-methyl tyrosine ethylester **7**. 10 N NaOH in water at 75°C promoted the hydrolysis of ester to acid and a simultaneous deoxalation of **7** to yield the final compound O-[3-(1,4,8,11-tetraazacyclotetradecan)-propyl]-α-methyl tyrosine (N$_4$-AMT) **8**. The total synthesis yield was 14%, which can be adapted to industrial manufacturing. The structure and purity of the compounds at each step were validated by ^{1}H- and ^{13}C-NMR, mass spectra, and HPLC.

3.2. Radiosynthesis. As shown in Figure 2, precursor N4-AMT could be labeled with ^{99m}Tc successfully in a high radiochemical purity (>96%). The retention time of ^{99m}Tc-N4-AMT was 6.899 min. Given that ^{99m}Tc-N4-AMT is a kit-product and labeled without any further purification, the radiochemical yield was assumed to be identical to its radiochemical purity. In this study, we labeled amino acid α-methyltyrosine AMT with ^{99m}Tc using cyclam N4 as the chelator because of its stable chelating ability and fast renal clearance. ^{99m}Tc was selected as the radionuclide due to its favorable physical characteristics, suitable half-life, and cost-effectiveness.

3.3. In Vitro Cellular Uptake of ^{99m}Tc-N4-AMT. The cellular uptake kinetics of ^{99m}Tc-N4-AMT and ^{99m}Tc-N4 in rat breast tumor cell line 13762 is shown in Figure 3. There was a drastically increased uptake for ^{99m}Tc-N4-AMT in the tumor cells at 15–240 min, but not for ^{99m}Tc-N4 chelator. These findings suggest that by adding the amino acid AMT, ^{99m}Tc-N$_4$-AMT can enter and accumulate into tumor cells effectively and rapidly. To further investigate the transport mechanisms of ^{99m}Tc-N$_4$-AMT, the competitive inhibition study using various types of transporter inhibitors will be conducted in the future.

3.4. In Vivo Evaluation of ^{99m}Tc-N$_4$-AMT. The result of the *in vivo* biodistribution studies in the normal Fischer rats at 0.5, 2, and 4 hours after intravenous administration of ^{99m}Tc-N4-AMT is shown in Table 1. Planar scintigraphic images of ^{99m}Tc-N4-AMT and ^{99m}Tc-N4 at 30, 60, and 120 min in breast tumor-bearing rats are shown in Figure 4. T/M ratios of ^{99m}Tc-N4-AMT were 2.3–4.0, whereas those of ^{99m}Tc-N4 were 1.9–2.5, respectively. Tumors could be clearly visualized by ^{99m}Tc-N4-AMT, but not by ^{99m}Tc-N4. In addition, the rat kidneys showed intense activity of ^{99m}Tc-N4-AMT in the planar images, which was consistent with the results from the *in vivo* biodistribution studies in the normal rats. This may be due to the nature of AMT, an inhibitor of tyrosine hydroxylase that cannot be excreted from kidneys and hence crystallized in the proximal tubules because of its poor solubility at the hydrogen ion concentrations of body fluids (pH 5–8) [15]. In the future, *in vivo* uptake blocking study using the unlabeled AMT will be performed to ascertain whether accumulation of ^{99m}Tc-N4-AMT in the kidney is attributed to AMT module.

4. Conclusion

In conclusion, efficient synthesis of N4-AMT was achieved. *In vitro* cellular uptake and *in vivo* imaging findings collectively suggest that ^{99m}Tc-N4-AMT is a potential radiotracer for breast cancer imaging. In compliance with the chelating

TABLE 1: Biodistribution of ^{99m}Tc-N4-AMT in Normal Fischer 344 Rats.

	30 MIN	120 MIN	240 MIN
blood	0.74 ± 0.024	0.28 ± 0.010	0.18 ± 0.008
heart	0.18 ± 0.013	0.08 ± 0.006	0.05 ± 0.003
lung	0.44 ± 0.029	0.22 ± 0.004	0.13 ± 0.008
thyroid	0.57 ± 0.040	0.31 ± 0.015	0.24 ± 0.012
pancreas	0.18 ± 0.006	0.09 ± 0.005	0.06 ± 0.002
liver	1.40 ± 0.077	0.83 ± 0.045	0.60 ± 0.023
spleen	0.24 ± 0.004	0.19 ± 0.002	0.18 ± 0.011
kidney	5.77 ± 0.355	5.32 ± 0.180	4.74 ± 0.332
stomach	0.50 ± 0.029	0.42 ± 0.031	0.43 ± 0.026
intestine	0.33 ± 0.019	0.18 ± 0.010	0.13 ± 0.006
uterus	0.34 ± 0.014	0.14 ± 0.023	0.08 ± 0.004
muscle	0.09 ± 0.007	0.03 ± 0.002	0.02 ± 0.001
bone & joint	0.27 ± 0.061	0.11 ± 0.006	0.06 ± 0.003
brain	0.03 ± 0.005	0.01 ± 0.001	0.01 ± 0.000

Each value is the percentage of injected dose per gram weight ($n = 3$)/time interval. Each datum represents the mean of three measurements with standard deviation.

capability of N4, N4-AMT could be labeled with positron emitting radionuclides such as Gallium-68 or with short-ranged beta emitters for internal radiotherapeutic purposes hereafter.

Authors' Contribution

Fan-Lin Kong and Mohammad S. Ali contributed equally to this work.

Acknowledgments

References

[1] A. Buerkle and W. A. Weber, "Imaging of tumor glucose utilization with positron emission tomography," *Cancer and Metastasis Reviews*, vol. 27, no. 4, pp. 545–554, 2008.

[2] G. Yamaura, T. Yoshioka, H. Fukuda et al., "O-[18F]fluoromethyl-L-tyrosine is a potential tracer for monitoring tumour response to chemotherapy using PET: an initial comparative in vivo study with deoxyglucose and thymidine," *European Journal of Nuclear Medicine and Molecular Imaging*, vol. 33, no. 10, pp. 1134–1139, 2006.

[3] E. M. del Amo, A. Urtti, and M. Yliperttula, "Pharmacokinetic role of L-type amino acid transporters LAT1 and LAT2," *European Journal of Pharmaceutical Sciences*, vol. 35, no. 3, pp. 161–174, 2008.

[4] H. Yagita, T. Masuko, and Y. Hashimoto, "Inhibition of tumor cell growth in vitro by murine monoclonal antibodies that recognize a proliferation-associated cell surface antigen system in rats and humans," *Cancer Research*, vol. 46, no. 3, pp. 1478–1484, 1986.

[5] T. Sakata, G. Ferdous, T. Tsuruta et al., "L-type amino-acid transporter 1 as a novel biomarker for high-grade malignancy in prostate cancer," *Pathology International*, vol. 59, no. 1, pp. 7–18, 2009.

[6] G. Mariani, L. Bruselli, and A. Duatti, "Is PET always an advantage versus planar and SPECT imaging?" *European Journal of Nuclear Medicine and Molecular Imaging*, vol. 35, no. 8, pp. 1560–1565, 2008.

[7] N. R. Schechter, D. J. Yang, A. Azhdarinia, and M. Chanda, "Technologies for translational imaging using generators in oncology," *Recent Patents on Anti-Cancer Drug Discovery*, vol. 2, no. 3, pp. 251–258, 2007.

[8] S. Liu, "The role of coordination chemistry in the development of target-specific radiopharmaceuticals," *Chemical Society Reviews*, vol. 33, no. 7, pp. 445–461, 2004.

[9] S. Liu, "Bifunctional coupling agents for radiolabeling of biomolecules and target-specific delivery of metallic radionuclides," *Advanced Drug Delivery Reviews*, vol. 60, no. 12, pp. 1347–1370, 2008.

[10] K. Ohtsuki, K. Akashi, Y. Aoka et al., "Technetium-99m HYNIC-annexin V: a potential radiopharmaceutical for the in-vivo detection of apoptosis," *European Journal of Nuclear Medicine*, vol. 26, no. 10, pp. 1251–1258, 1999.

[11] C. G. Van Nerom, G. M. Bormans, M. J. De Roo, and A. M. Verbruggen, "First experience in healthy volunteers with technetium-99m L,L-ethylenedicysteine, a new renal imaging agent," *European Journal of Nuclear Medicine*, vol. 20, no. 9, pp. 738–746, 1993.

[12] C. H. Kao, S. P. ChangLai, P. U. Chieng, and T. C. Yen, "Technetium-99m methoxyisobutylisonitrile chest imaging of small cell lung carcinoma: relation to patient prognosis and chemotherapy response—a preliminary report," *Cancer*, vol. 83, no. 1, pp. 64–68, 1998.

[13] H. C. Wu, C. H. Chang, M. M. Lai, C. C. Lin, C. C. Lee, and A. Kao, "Using Tc-99m DMSA renal cortex scan to detect renal damage in women with type 2 diabetes," *Journal of Diabetes and Its Complications*, vol. 17, no. 5, pp. 297–300, 2003.

[14] A. Barth, A. R. Haldemann, J. C. Reubi et al., "Noninvasive differentiation of meningiomas from other brain tumours using combined Indium-octreotide/technetium-DTPA brain

scintigraphy," *Acta Neurochirurgica*, vol. 138, no. 10, pp. 1179–1185, 1996.

[15] K. E. Moore, P. F. Wright, and J. K. Bert, "Toxicologic studies with alpha-methyltyrosine, an inhibitor of tyrosine hydroxylase," *Journal of Pharmacology and Experimental Therapeutics*, vol. 155, no. 3, pp. 506–515, 1967.

Research Article

Technetium-99m-Labeled Autologous Serum Albumin: A Personal-Exclusive Source of Serum Component

Yuh-Feng Wang,[1, 2] Yi-Chun Chen,[1, 3] Dian-Kun Li,[1, 4] and Mei-Hua Chuang[5]

[1] *College of Medicine, Tzu Chi University, Hualien 97004, Taiwan*
[2] *Department of Nuclear Medicine, Buddhist Dalin Tzu Chi General Hospital, Chiayi 62247, Taiwan*
[3] *Division of Nephrology, Department of Internal Medicine, Buddhist Dalin Tzu Chi General Hospital, Chiayi 62247, Taiwan*
[4] *Department of Hematology and Oncology, Buddhist Dalin Tzu Chi General Hospital, Chiayi 62247, Taiwan*
[5] *Department of Pharmacy, Buddhist Dalin Tzu Chi General Hospital, Chiayi 62247, Taiwan*

Correspondence should be addressed to Yuh-Feng Wang, yuhfeng@gmail.com

Technetium-99m human serum albumin (^{99m}Tc-HSA) is an important radiopharmaceutical required in nuclear medicine studies. However, the risk of transfusion-transmitted infection remains a major safety concern. Autopreparation of serum component acquired from patient provides a "personal-exclusive" source for radiolabeling. This paper is to evaluate the practicality of on-site elusion and subsequent radiolabeling efficacy for serum albumin. Results showed that the autologous elute contained more albumin fraction than serum without extraction procedure. Good radiochemical purity and stability were demonstrated after radiolabeling. Biodistribution study showed that labeled albumin accumulated immediately in the lung, liver, and kidney. It was cleared steadily and excreted in the urine. The biologic half-life was defined, and all samples passed the pyrogenicity and sterility tests. In conclusion, autoalbumin could be extracted and radiolabeled properly in a nuclear medicine setting. Moreover, the risk of transfusion-transmitted infection associated with nonautologous, multisource ^{99m}Tc-HSA agents can be reduced.

1. Introduction

Technetium-99m-labeled human serum albumin (^{99m}Tc-HSA) is an important radiopharmaceutical commonly used in nuclear medical services. It is routinely used in lymphoscintigraphic studies, sentinel lymph node mapping, blood pool imaging, and protein-losing gastroenteropathy [1–7]. However, preparing and maintaining stocks of ^{99m}Tc-HSA remain a challenge due to a shortage in the supply of commercially available kits and a lack of awareness regarding unknown transfusion-induced infectious diseases.

HSA is the major protein component of human plasma and is crucial for maintaining plasma volume and the osmotic pressure of circulating blood [8]. Plasma-derived HSA (pHSA) is used clinically to correct circulating plasma volume and improve colloid osmotic pressure. Nevertheless, the pHSA supply is limited as it is manufactured from a fractionation of pooled, donated human plasma. This

nonautologous, multisource approach introduces significant risks of allergic reactions and contamination by blood-derived pathogens, such as human immunodeficiency virus (HIV), viral hepatitis, and Creutzfeldt-Jakob disease prions [9, 10]. Since ^{99m}Tc-HSA is widely applied to nuclear medicine techniques, constant and stable sources of albumin are necessary to sustain these diagnostic procedures.

Serum products created from a single-source or limited domestic supplies are safer than those obtained from pooled commercial sources, according to the World Health Organization (WHO) [11–13]. In our previous study, a protocol was formulated using a domestic serum product to prepare ^{99m}Tc-HSA on site in a nuclear medicine laboratory [14]. This preparation proved safer than the commercially supplied pooled serum products, biologically stable, and clinically effective.

However, the risks of introducing an unknown infectious agent could not be completely eliminated. Therefore,

a need for a protocol to create a single-source autologous serum albumin (autoalbumin) still exists. Autologous blood donation is the safest means by which clinical transfusion products can be prepared for an individual [15, 16]. In this article, we describe the development of a ^{99m}Tc-HSA preparation technique using autologous serum elution, the ^{99m}Tc-autoalbumin. In addition to labeling efficiency and stability studies, we performed *in vivo* biodistribution and biological half-life studies and tested sterility and pyrogenicity.

2. Materials and Methods

2.1. Extraction of Albumin from Serum. Fresh serum was collected following centrifugation (3,500 rpm for 5 minutes) of single-source blood samples from healthy volunteers. Affinity chromatographic columns, which is cross-linked agarose gel with covalently coupled Cibacron Blue [17] (Aurum Affi-Gel Blue column; Bio-Rad catalog no. 732-6708, CA, USA), were prepared by washing with low-salt 20 mM Tris buffer solution (pH 8.3) and desiccated in a microcentrifuge (7,000 rpm for 5 seconds). Serum samples were prepared by dilution with Tris buffer solution at 1 : 3. Serum sample (800 μL) was then added to the column, and the column was gently vortexed for 5 to 10 minutes. The column was allowed to drain and washed twice with Tris buffer solution. All flow-through was discarded, and the serum protein remained bound to the column's resin beads. Two elution buffer solutions were used to remove the protein fraction from the bead.

Preparation 1 (Pre-1). Laemmli sample buffer (Bio-Rad catalog no. 161-0737).

   Major content: 62.5 mM Tris-HCl (pH: 6.8), 25% glycerol, 2% SDS, and 0.01% Bromophenol blue.

Preparation 1 (Pre-1). Preparation 2 (Pre-2): ReadyPrep sequential extraction reagent 3 (Bio-Rad catalog no. 163-2104).

   Major content: 5 M urea, 2 M thiourea, 2% CHAPS, 2% SB 3–10, 40 mM Tris, and 0.2% Bio-Lyte 3/10 ampholyte.

   Five hundred microliters of elution buffer were added, and the column was spun for 5 seconds at 7,000 rpm in a microcentrifuge. The residual elution was collected and labeled as "serum protein."

   Albumin fraction and amount of the serum protein samples were obtained by cellulose acetate strip electrophoresis. Briefly, Tris-barbital-sodium barbital buffer solution (Electra HR Buffer, Helena laboratories catalog no. 5805, TX, US) was added to the electrophoresis tank (SPIFE 3000, Helena Laboratories). Serum sample was applied to the plate (Titan III Cellulose Acetate, Helena laboratories catalog no. 3023) and electrophoresed at 180V for 25 minutes. After the electrophoresis was done, the plates were removed from the electrophoresis chamber and stained (Ponceau S Stain, Helena Laboratories catalog no. 5526) for 5 minutes. A scanning densitometer (QuickScan 2000, Helena Laboratories) was employed for the estimation of the results of electrophoresis.

A serum sample without any extraction procedure (Pre-3) was also examined as an internal control. The preparation group with the highest albumin fraction was chosen, and the radiolabeling procedures described below were performed.

2.2. Preparation of the ^{99m}Tc-Labeled Autoalbumin. After proper serum extraction of the albumin, radiolabeling was initiated. Sodium pertechnetate (^{99m}Tc-pertechnetate) was eluted from an ^{99}Mo/^{99m}Tc generator (Ultra-Techne Kow; Daiichi Radioisotope Laboratories, LTD., Tokyo, Japan), following manufacturer's instructions. Stannous solution (Amerscan Stannous Agent, Amersham plc, Buckinghamshire, UK) was prepared fresh by careful addition of 10 mL 0.9% sodium chloride to the kit's vial. The final concentration of the stannous fluoride in the stannous solution was 0.4 mg/mL.

   Labeling was carried out by mixing autoalbumin with the stannous solution and ^{99m}Tc-pertechnetate. Two different preparation protocols of ^{99m}Tc-autoalbumin were prepared, with (Protocol A) and without (Protocol B) stannous solution. First, 0.5 mL autoalbumin was measured and aliquoted into a sterile tube (BD Vacutainer; Becton, Dickinson and Company, NJ, US), then the stannous solution (0.5 mL) was added to the Protocol A test tubes using volumetric pipettes. After ^{99m}Tc-pertechnetate elution was completed; total activity was measured by a dose calibrator (CRC-15R; Capintec, Inc., NJ, US). 1.11 GBq of ^{99m}Tc-pertechnetate was collected and added with 0.9% sodium chloride to bring the final volume to 0.5 mL, and then it was placed in a sterile tube. The autoalbumin and stannous mixtures were then transferred aseptically to the tubes containing ^{99m}Tc-pertechnetate using a syringe to carefully deliver the solution down the side wall of the tubes. Mixing was performed by gentle manual shaking to avoid bubble formation.

2.3. Radiochemical Purity and Stability. Radiochemical purity and stability were determined by instant thin-layer chromatography (ITLC). Initially, ITLC silica gel plate was cut into $0.8 \times 10 \text{ cm}^2$ strips. Using a Hamilton syringe, one drop of the specimen was placed at 1.5 cm above the bottom of the strip. The strip was developed by acetone, and the radioactivity distribution over the strip was determined with a radio-TLC imaging scanner (AR-2000; Bioscan, Inc., Washington, DC, US). Radiochemical purity was calculated as the fraction of radioactivity that remained at the origin and was designated as %RCP. After preparation, the stability of the mixture was acquired from sequential repeats ($n = 6$) of the %RCP procedure at 10 min, 30 min, 1 hour, 2 hours, 4 hours, 6 hours, and 24 hours, respectively.

2.4. Biodistribution. A gamma camera (DST-XLi, General Electric Medical Systems, Buc, France) was used to view rats (Wistar strain, male, weighing from 200 to 250 gm) that had been injected, via the tail vein, with 74 MBq of ^{99m}Tc-autoalbumin. The rats were anesthetized with an intraperitoneal injection of pentobarbital (0.006 mg/100 gm). The gamma camera was fitted with a low-energy, high-resolution

TABLE 1: Serum protein components separated by different elution buffers.

	Pre-1	Pre-2	Pre-3	Reference [18]
Total protein (gm/dL)	2.00 ± 0.16	3.12 ± 0.36	7.26 ± 0.19	6.0–8.4
Electrophoresis (%)				
Albumin	77.50 ± 2.24	4.36 ± 1.15	55.14 ± 4.82	52–68
Globulin α1	2.86 ± 0.57	2.08 ± 0.62	2.34 ± 0.21	4.2–7.2
Globulin α2	6.12 ± 1.88	87.02 ± 2.52	8.36 ± 1.06	6.8–12
Globulin β	7.04 ± 1.41	3.40 ± 1.03	13.36 ± 1.52	9.3–15
Globulin γ	6.48 ± 3.23	3.14 ± 1.13	20.80 ± 3.53	13–23

collimator, and the images were processed by a gamma-camera working station (POWERstation SPX, IBM RS6000, Vision 5.2.0, General Electric Medical Systems). Each rat was studied by taking 750 frames of 0.4 seconds, followed by 1 frame of 60 seconds (total study time, ~6 minutes).

In addition to the imaging studies, an examination of biodistribution changes over time was performed. Rats were injected via tail vein. The animals ($n = 5$, each group) were sacrificed by direct decapitation at 5, 10, 30, 60, 120, and 240 min after administration of ^{99m}Tc-autoalbumin, followed by dissection. Organs and tissues were separated, and the radioactivity was determined using a gamma counter (COBRAII, Packard, Netherlands). Organ activity was expressed as a mean of percentage of injected dose per grams (%ID/gm) of tissue.

2.5. Blood Clearance. Blood clearance studies were performed to understand the *in vivo* behavior of the injected ^{99m}Tc-autoalbumin. Rats ($n = 5$) without previous administration of any radiopharmaceutical were acquired. The radiolabeled preparations were diluted with 0.9% sodium chloride to a final concentration of 74 MBq/mL, and 0.2 mL of this preparation was injected into the proximal portion of the tail vein. At fixed time intervals (5, 10, 15, 30, 60, and 120 min), 0.2 mL blood samples were withdrawn from the distal end of the tail vein. All of the samples were counted in a gamma well counter and were compared with a value obtained for a standard radiopharmaceutical. The blood clearance rates were calculated by means of the logarithmic equation as follows:

$$\%\text{Radioactivity, blood} = q \times [\ln(\text{Time})] + b. \quad (1)$$

Time: minutes after injection, q: slope, b: intercept.

2.6. Pyrogenicity and Sterility Testing. Pyrogenicity was determined using a bacterial endotoxin test called the *limulus amebocyte lysate (LAL) test*. The sensitivity of the LAL reagent is 0.25 endotoxin units (EU)/mL. According to the requirement, as specified in *USP32/NF27* [19], the limit with regard to endotoxin content of the ^{99m}Tc-autoalbumin preparation is 175/V USP EU/mL of the injection, where V is the maximum recommended dose in milliliters.

The sterility of the ^{99m}Tc-autoalbumin preparation was tested, as stated in *USP32/NF27* [20]. One milliliter of our preparation was added to a test tube containing 15 mL of SCD and TGC medium. The tubes were observed for turbidity, and results were recorded every day for 14 days. A negative result was indicated by a clear culture medium (no turbidity noted) over the 14 days of observation.

2.7. Ethics. This study was approved by the Institutional Review Board of the Buddhist Dalin Tzu Chi General Hospital. All the animal experiments were performed in accordance with the Animal Protection Act of the Council of Agriculture, and were approved by the Institutional Animal Care and Use Committee of Dalin Tzu Chi General Hospital.

3. Results

3.1. Autoalbumin Fraction of the Elution. Five serum samples were prepared according to the protocol described above and were arranged into three groups: preparation 1 (Laemmli sample buffer; Pre-1), preparation 2 (ReadyPrep sequential extraction reagent 3; Pre-2), and preparation 3 (serum without any extraction; Pre-3). The Pre-3 served as an internal control for the electrophoresis analysis, and our data showed evenly distributed protein elements (Table 1) upon comparison to the reference range [18], with the exception of a slightly lower fraction than the globulin α1. Both Pre-1 and Pre-2 exhibited diminished total protein concentrations (2.00 gm/dL and 3.12 gm/dL, resp.) as compared to Pre-3 (7.62 gm/dL), which was caused by inevitable loss from the extraction procedure. Pre-1 yielded a higher extraction ratio of the albumin fraction from the serum protein (77.5%) as compared with Pre-2 (4.36%) and Pre-3 (55.14%) while the Pre-2 showed a high fraction in the globulin α2 (87.02%) then Pre-1 (6.12%) and Pre-3 (8.36%) (Table 1). This result indicated that Pre-1, the extraction serum with Laemmli sample buffer, effectively isolated a higher proportion of autoalbumin. All of the radiolabeling studies were performed with high-purity autoalbumin from Pre-1.

3.2. Radiochemical Purity and Stability. Protocol A contained 0.5 mL autoalbumin, 0.5 mL stannous solution, and 1.11 GBq of ^{99m}Tc-pertechnetate. Protocol B contained 0.5 mL autoalbumin with 1.11 GBq of ^{99m}Tc-pertechnetate. Figure 1 demonstrates that the radiochemical purity obtained with Protocol A was 95.82% at 10 min and maintained the 94.42% out to 6 hours after preparation. Twenty-four hours after radiolabeling, the average RCP still reached 72.77% ($n = 6$). Protocol B, however, resulted in substantially poorer labeling efficiency and was deemed unsuitable for clinical application.

(a)

	10 min	30 min	60 min	2 hr	4 hr	6 hr	24 hr
Protocol A	95.82 ± 1.7	95.65 ± 0.67	97.6 ± 2.01	96.78 ± 1.23	96.1 ± 1.54	94.42 ± 2.01	72.77 ± 9.1
Protocol B	4.3 ± 3.74	6.76 ± 8.59	7.8 ± 4.84	9.08 ± 8.05	7.29 ± 5.16	9.49 ± 6.95	7.26 ± 4.34

(b)
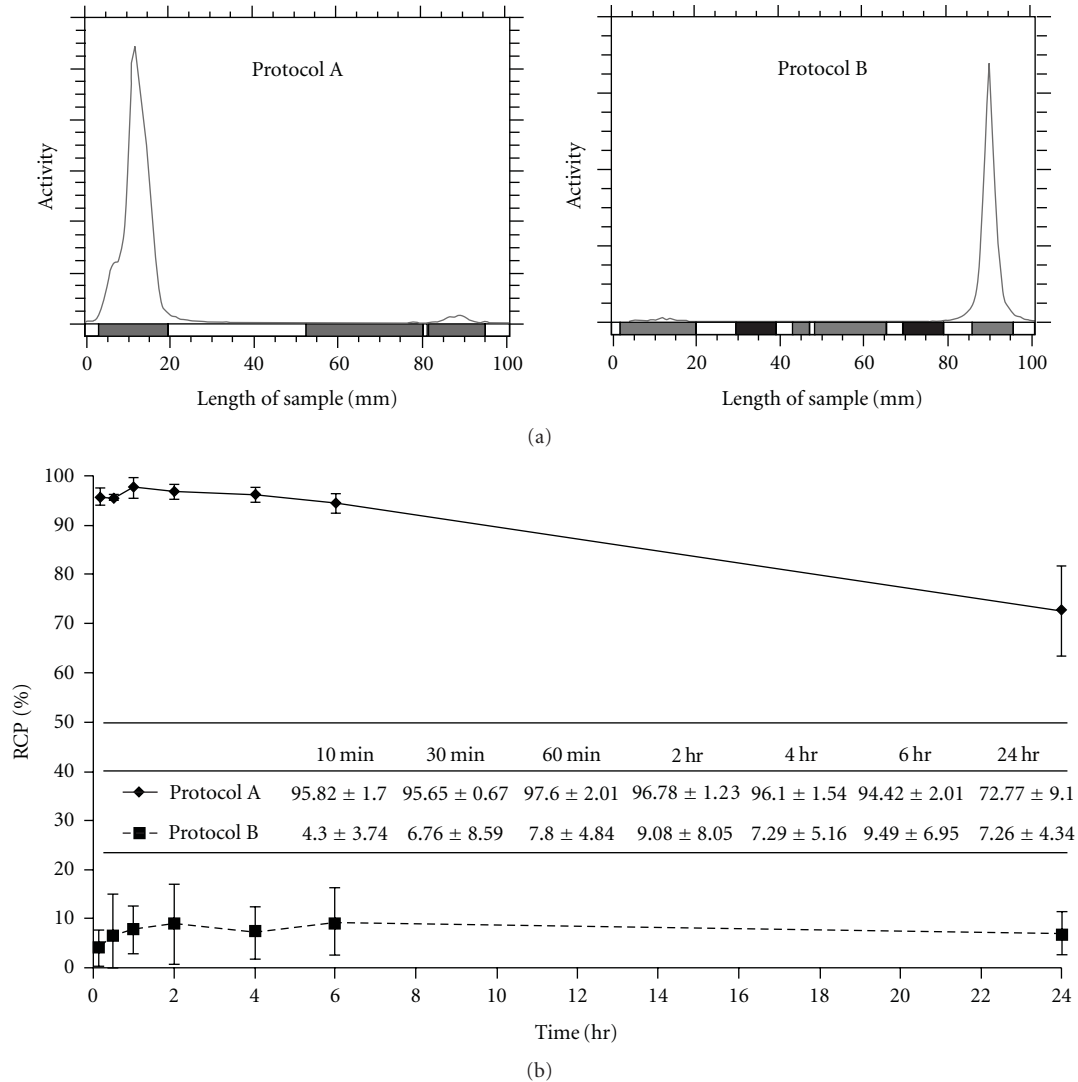
Figure 1: (a) Examples of the radiochemical purity studies from Protocol A and Protocol B. Both showed the RCP result of 30 min after radiolabeling. Radiochromatograms were acquired with a radio-TLC scanner. (b) Radiochemical purity and stability tests of the preparation protocols, determined by ITLC and presented as %RCP with mean ± SD ($n = 6$).

Table 2: *In vivo* biodistribution of the ^{99m}Tc-autoalbumin, expressed as percentage of administered dose per gram of organ (%ID/gm) (mean values ± s.e.m.).

Time (min)	Brain	Lung	Liver	Stomach	Spleen	Kidney	Muscle	Bone
5	0.14 ± 0.09	0.93 ± 0.60	1.46 ± 0.63	0.43 ± 0.23	0.48 ± 0.20	2.91 ± 0.72	0.19 ± 0.10	0.08 ± 0.02
10	0.23 ± 0.13	1.03 ± 0.64	1.27 ± 0.25	0.57 ± 0.12	0.73 ± 0.21	2.44 ± 1.10	0.64 ± 0.13	0.23 ± 0.10
30	0.02 ± 0.01	0.09 ± 0.02	0.94 ± 0.52	0.22 ± 0.08	0.30 ± 0.12	3.37 ± 0.95	0.06 ± 0.01	0.05 ± 0.01
60	0.01 ± 0.01	0.04 ± 0.01	0.76 ± 0.11	0.07 ± 0.01	0.13 ± 0.07	3.29 ± 0.86	0.12 ± 0.03	0.07 ± 0.01
120	0.02 ± 0.02	0.09 ± 0.03	0.70 ± 0.24	0.15 ± 0.08	0.30 ± 0.09	4.48 ± 0.39	0.03 ± 0.01	0.07 ± 0.02
240	0.01 ± 0.01	0.05 ± 0.02	0.52 ± 0.13	0.11 ± 0.03	0.52 ± 0.17	4.12 ± 0.69	0.04 ± 0.03	0.05 ± 0.02

3.3. Biodistribution. When the ^{99m}Tc-autoalbumin, prepared as Protocol A, was injected intravenously into a rat, the main vessels, heart, lung, liver, and kidneys were immediately visualized (Figures 2(a) and 2(b)). Results from the animal biodistribution studies were expressed as percentages of injected doses per gram and presented in Table 2. Five

minutes after initiation of the study, a percentage of the injected dose of radiolabeled autoalbumin was detected in the lung (0.93%), liver (1.46%), and kidneys (2.91%). The distributions to the lung (1.04%) and liver (1.27%) were highest at 10 minutes after intravenous injection of the radiotracer. These levels were reduced in lung and liver, but
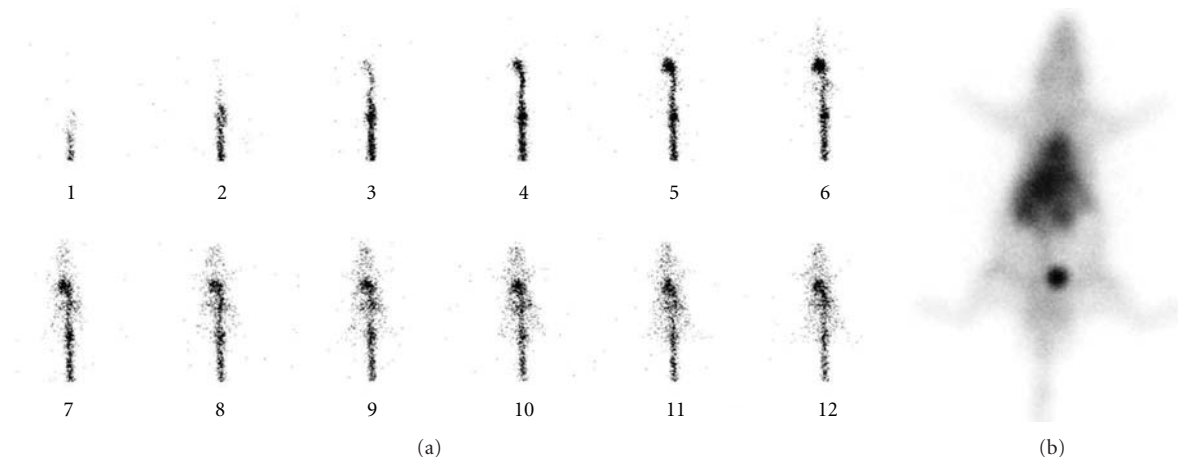
FIGURE 2: Image studies for the biodistribution of the ^{99m}Tc-autoalbumin. (a) Dynamic images, rats were studied by taking 750 frames of 0.4 seconds interval; (b) static image taken at 5 min after injection with an acquisition time of 60 seconds.
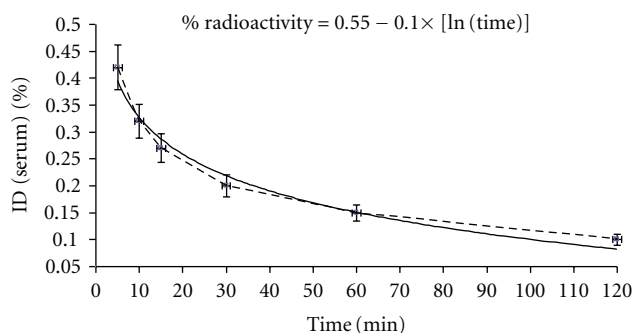
FIGURE 3: Blood clearance of the ^{99m}Tc-autoalbumin in study animals ($n = 5$).

in the kidneys gradually increased to 4.48% over the first 2 hours. The radiodistribution of the stomach and other internal organs, such as spleen, showed no apparent difference (stomach: 0.57% to 0.11%; spleen: 0.73% to 0.13%).

3.4. Blood Clearance. The serum elimination of this radiolabeled autoalbumin has been shown in Figure 3. A decline in percentage of injected dose in blood was observed over time. The formula used to calculate the blood clearance is "%Radioactivity = $0.55 - 0.1 \times [\ln(\text{Time})]$" ($r^2 > 0.95$), and the biological half-life calculated was 32.29 minutes.

3.5. Pyrogenicity and Sterility Testing. After 6 hours, remaining ^{99m}Tc-autoalbumin was used to perform pyrogen and sterility tests ($n = 5$). In the pyrogenicity tests, those samples diluted 50-fold and 83-fold (the maximum valid dilution value) yielded negative results. In addition, after being incubated for 14 days, our culture medium remained clear in appearance. All samples were found to be sterile and pyrogen-free.

4. Discussion

The term *autologous transfusion* describes any procedure by which donated blood (or serum component) is transfused (or reinfused) into the donor/patient [21]. The primary purpose of autologous transfusion is to prevent exposure to blood-borne infectious agents. This has become increasingly critical as awareness of the risks of allergenic blood products has grown in the decades following the AIDS epidemic that plagued the late 1980s and early 1990s.

The first step of this study was designed to establish an autoalbumin extraction procedure from single-source, autologous serum. Specifically, the serum sample was placed in a resin bead column to capture the protein component. Upon release from the column, total protein and separated component fractions were examined by electrophoresis. An internal control sample provided the reference range of serum protein distribution, with the exception of a relatively lower fraction of the globulin α1. Elution by Laemmli sample buffer yielded a high albumin elution fraction (77.5%) while elution by ReadyPrep sequential extraction reagent 3 yielded a higher fraction in the globulin α2. Serum samples subject to resin bead column isolation and elution by Laemmli sample buffer were determined to be suitable for use with the subsequent radiolabeling procedure.

Radiolabeling was performed by carefully mixing ^{99m}Tc-pertechnetate and autoalbumin. Stannous is essential for good radiolabeling efficiency. Our data showed that the radiochemical purity and stability were sufficient, because 6 hours after radiolabeling, the %RCP still reached more than 94%. When the radiolabeled autoalbumin was injected intravenously into a rat, the lung, liver, and kidneys were promptly visualized. The distribution to the lung and liver was highest within the initial 10 minutes and then vanished gradually. In the kidney, the accumulation of radioactivity became progressively prominent, suggesting the major excretory pathway of radiolabeled autoalbumin may be the genitourinary tract. The radioactivity to the gastric mucosa showed no

significant difference as other internal organs, for example, spleen, could be an *in vivo* demonstration of stable labeling of Technetium-99m and autoalbumin in study animals.

A previous literature report of the biodistribution in rat with ^{99m}Tc-HSA demonstrates a rapid accumulation of tracer to the liver immediately after injection while the time-activity cure showed slightly decreased radio-uptake with time [22]. Excretion of tracer through the kidneys could be also identified right after injection of tracer. Another study described the biodistribution of the recombinant human serum albumin (rHSA) also showed major initial distribution to the liver [23]. However, progressive decrement of liver uptake and increment of renal activity were also observed. In this study, time series sacrifices and dissection of organs/tissues were performed. Our results were consistent with these reports for the biodistribution study.

Autologous blood and blood components are widely believed to be the safest blood products available for clinical application; however, certain complications are still possible and should be kept under a strict watch. Contamination by bacteria or other pyrogens during the preparation steps remain a risk. Our autoalbumin preparation procedure was determined to be free from pyrogenicity and passed sterility tests; however, operator errors or negligence may still occur. Prevention of contamination is of ultimate importance in clinical practice of nuclear medicine. Another operator error that may occur is mislabeling of serum tubes. This mistake yields the identical risks associated with nonautologous transfusion and can lead to serum product administration to an incompatible patient.

Autologous preparations of blood component techniques are generally intended to replace as much of the allogenic origin as possible by reinfusion of autologous blood products. Our study demonstrates that the separation of autoalbumin takes no longer than 2 hours and radiolabeling may be carried out immediately after separation. This implies that the collection and reprocessing of radiolabeled autoalbumin and the subsequent nuclear medical procedure could be performed as a daily practice. Even though ^{99m}Tc-albumin labeling has demonstrated some clinical advantages, it is still a significantly hazardous procedure. Therefore, it may not be worth the risk if a kit formulation is available to be used.

The most recent development of nonserum sources of human albumin has been the rHSA [23–26]. Both rHSA and pHSA have been shown to be identical in structure and physiochemical and immunochemical properties [27, 28]. In the future, rHSA promises to be an ideal source for a "clean" HSA.

5. Conclusions

Radiolabeled human serum albumin is an important nuclear medicine radiopharmaceutical. However, the safety of pooled serum products remains a concern. Our study demonstrates that autoalbumin can be efficiently extracted within a nuclear medicine laboratory and immediately radiolabeled. This radiolabeled autoalbumin exhibited sufficient radiochemical purity and stability. The most important advantage

to this technique is that the risk of infection could be significantly eliminated by this preparation of autoalbumin.

References

[1] C. Vanhove, N. Walgraeve, F. De Geeter, and P. R. Franken, "Gated myocardial perfusion tomography versus gated blood pool tomography for the calculation of left ventricular volumes and ejection fraction," *European Journal of Nuclear Medicine and Molecular Imaging*, vol. 29, no. 6, pp. 735–741, 2002.

[2] S. Ferraro, P. Perrone-Filardi, A. Desiderio et al., "Left ventricular systolic and diastolic function in severe obesity: A radionuclide study," *Cardiology*, vol. 87, no. 4, pp. 347–353, 1996.

[3] N. T. Chiu, B. F. Lee, S. J. Hwang, J. M. Chang, G. C. Liu, and H. S. Yu, "Protein-losing enteropathy: diagnosis with (99m)Tc-labeled human serum albumin scintigraphy," *Radiology*, vol. 219, no. 1, pp. 86–90, 2001.

[4] I. Bedrosian, A. M. Scheff, R. Mick et al., "99mTc-human serum albumin: an effective radiotracer for identifying sentinel lymph nodes in melanoma," *Journal of Nuclear Medicine*, vol. 40, no. 7, pp. 1143–1148, 1999.

[5] Y. C. Chen, S. J. Hwang, J. S. Chiu, M. H. Chuang, M. I. Chung, and Y. F. Wang, "Chronic edema from protein-losing enteropathy: scintigraphic diagnosis," *Kidney International*, vol. 75, no. 10, p. 1124, 2009.

[6] R. Kim, A. Osaki, J. Kojima, and T. Toge, "Significance of lymphoscintigraphic mapping with Tc-99m human serum albumin and tin colloid in sentinel lymph node biopsy in breast cancer," *International journal of oncology*, vol. 19, no. 5, pp. 991–996, 2001.

[7] M. Momose, S. Kawakami, T. Koizumi et al., "Lymphoscintigraphy using technetium-99m HSA-DTPA with SPECT/CT in chylothorax after childbirth," *Radiation Medicine*, vol. 26, no. 8, pp. 508–511, 2008.

[8] B. R. Don and G. Kaysen, "Serum albumin: relationship to inflammation and nutrition," *Seminars in Dialysis*, vol. 17, no. 6, pp. 432–437, 2004.

[9] L. T. Goodnough, "Risks of blood transfusion," *Critical Care Medicine*, vol. 31, no. 12, pp. S678–S686, 2003.

[10] C. Madjdpour, V. Heindl, and D. R. Spahn, "Risks, benefits, alternatives and indications of allogenic blood transfusions," *Minerva Anestesiologica*, vol. 72, no. 5, pp. 283–298, 2006.

[11] W. R. Mayr, "The reality of self-sufficiency," *Transfusion Clinique et Biologique*, vol. 12, no. 5, pp. 362–364, 2005.

[12] The President's Emergency Plan for AIDS Relief, "Report on blood safety and HIV/AIDS," June 2006, http://www.pepfar.gov/progress/76858.htm.

[13] Centers for Disease Control and Prevention (CDC), "Progress toward strengthening blood transfusion services—14 countries, 2003-2007," *Morbidity and Mortality Weekly Report*, vol. 57, no. 47, pp. 1273–1277, 2008.

[14] Y. F. Wang, M. H. Chuang, J. S. Chiu, T. M. Cham, and M. I. Chung, "On-site preparation of technetium-99m labeled human serum albumin for clinical application," *Tohoku Journal of Experimental Medicine*, vol. 211, no. 4, pp. 379–385, 2007.

[15] L. T. Goodnough, M. E. Brecher, M. H. Kanter, and J. P. Aubuchon, "Transfusion medicine: II. Blood conservation," *New England Journal of Medicine*, vol. 340, no. 7, pp. 525–533, 1999.

[16] R. Karger and V. Kretschmer, "Modern concepts of autologous haemotherapy," *Transfusion and Apheresis Science*, vol. 32, no. 2, pp. 185–196, 2005.

[17] E. Gianazza and P. Arnaud, "Chromatography of plasma proteins on immobilized Cibacron Blue F3-GA. Mechanism of the molecular interaction," *Biochemical Journal*, vol. 203, no. 3, pp. 637–641, 1982.

[18] "Case records of the Massachusetts General Hospital. Weekly clinicopathological exercises. Normal reference values," *The New England Journal of Medicine*, vol. 314, no. 1, pp. 39–19, 1986.

[19] U.S. Pharmacopeia, "Bacterial endotoxin test," in *USP32/NF27: United States Pharmacopeia and National Formulary*, pp. 93–96, The United States Pharmacopeial Convention Inc., 2009.

[20] U.S. Pharmacopeia, "Sterility test," in *USP32/NF27: United States Pharmacopeia and National Formulary*, pp. 80–86, The United States Pharmacopeial Convention Inc., 2009.

[21] P. T. Toy, R. G. Strauss, and L. C. Stehling, "Predeposited autologous blood for elective surgery. A national multicenter study," *New England Journal of Medicine*, vol. 316, no. 9, pp. 517–520, 1987.

[22] K. Kristensen, "Biodistribution in rats of 99mTc-labelled human serum albumin," *Nuclear Medicine Communications*, vol. 7, no. 8, pp. 617–624, 1986.

[23] A. C. Perkins and M. Frier, "Experimental biodistribution studies of 99mTc-recombinant human serum albumin (rHSA): a new generation of radiopharmaceutical," *European Journal of Nuclear Medicine*, vol. 21, no. 11, pp. 1231–1233, 1994.

[24] S. Matsushita, Y. Isima, V. T. Chuang et al., "Functional analysis of recombinant human serum albumin domains for pharmaceutical applications," *Pharmaceutical Research*, vol. 21, no. 10, pp. 1924–1932, 2004.

[25] K. Kobayashi, "Summary of recombinant human serum albumin development," *Biologicals*, vol. 34, no. 1, pp. 55–59, 2006.

[26] K. Langer, M. G. Anhorn, I. Steinhauser et al., "Human serum albumin (HSA) nanoparticles: reproducibility of preparation process and kinetics of enzymatic degradation," *International Journal of Pharmaceutics*, vol. 347, no. 1-2, pp. 109–117, 2008.

[27] A. Kasahara, K. Kita, E. Tomita, J. Toyota, Y. Imai, and H. Kumada, "Repeated administration of recombinant human serum albumin caused no serious allergic reactions in patients with liver cirrhosis: a multicenter clinical study," *Journal of Gastroenterology*, vol. 43, no. 6, pp. 464–472, 2008.

[28] W. Ohtani, Y. Nawa, K. Takeshima, H. Kamuro, K. Kobayashi, and T. Ohmura, "Physicochemical and immunochemical properties of recombinant human serum albumin from Pichia pastoris," *Analytical Biochemistry*, vol. 256, no. 1, pp. 56–62, 1998.

Research Article

Molecular Imaging, Pharmacokinetics, and Dosimetry of ^{111}In-AMBA in Human Prostate Tumor-Bearing Mice

Chung-Li Ho,[1] I-Hsiang Liu,[1] Yu-Hsien Wu,[1] Liang-Cheng Chen,[1] Chun-Lin Chen,[1] Wan-Chi Lee,[1] Cheng-Hui Chuang,[1] Te-Wei Lee,[1] Wuu-Jyh Lin,[1, 2] Lie-Hang Shen,[1] and Chih-Hsien Chang[1, 2]

[1] *Isotope Application Division, Institute of Nuclear Energy Research, Taoyuan 32546, Taiwan*
[2] *Department of Biomedical Imaging and Radiological Sciences, National Yang-Ming University, Taipei 11221, Taiwan*

Correspondence should be addressed to Chih-Hsien Chang, chchang@iner.gov.tw

Molecular imaging with promise of personalized medicine can provide patient-specific information noninvasively, thus enabling treatment to be tailored to the specific biological attributes of both the disease and the patient. This study was to investigate the characterization of DO3A-CH$_2$CO-G-4-aminobenzoyl-Q-W-A-V-G-H-L-M-NH$_2$ (AMBA) *in vitro*, MicroSPECT/CT imaging, and biological activities of ^{111}In-AMBA in PC-3 prostate tumor-bearing SCID mice. The uptake of ^{111}In-AMBA reached highest with $3.87 \pm 0.65\%$ ID/g at 8 h. MicroSPECT/CT imaging studies suggested that the uptake of ^{111}In-AMBA was clearly visualized between 8 and 48 h postinjection. The distribution half-life ($t_{1/2\alpha}$) and the elimination half-life ($t_{1/2\beta}$) of ^{111}In-AMBA in mice were 1.53 h and 30.7 h, respectively. The $C_{\max}$ and AUC of ^{111}In-AMBA were 7.57% ID/g and 66.39 h*% ID/g, respectively. The effective dose appeared to be 0.11 mSv/MBq^{-1}. We demonstrated a good uptake of ^{111}In-AMBA in the GRPR-overexpressed PC-3 tumor-bearing SCID mice. ^{111}In-AMBA is a safe, potential molecular image-guided diagnostic agent for human GRPR-positive tumors, ranging from simple and straightforward biodistribution studies to improve the efficacy of combined modality anticancer therapy.

1. Introduction

Prostate cancer is estimated to rank first in number of cancer cases and second in number of deaths due to cancer among men in the Western world [1]. Gastrin-releasing peptides (GRPs), including Bombesin-like peptides (BLPs), are involved in the regulation of a large number of biological processes in the gut and central nervous system (CNS) [2]. They mediate their action on cells by binding to members of a superfamily of G protein-coupled receptors [3]. There are four known subtypes of BN-related peptide receptors, namely, gastrin-releasing peptide receptor (GRPR, BB2, BRS-2), neuromedin B receptor (NMBR, BB1, BRS-1), orphan receptor (BRS-3), and amphibian receptor (BB4-R) [4]. Except the BB4-R, all the receptors were widely distributed, especially in the gastrointestinal (GI) tract and central nervous system (CNS). The receptors have a large range of effects in both normal physiology and pathophysiological conditions [5]. GRPRs are normally

expressed in nonneuroendocrine tissues of the pancreas, breast, and neuroendocrine cells of the brain, GI tract, lung, and prostate, but are not normally expressed by epithelial cells in the colon, lung, or prostate [6, 7].

Molecular imaging enables the visualization of the cellular function and the followup of the molecular process in living organisms without perturbing them [8]. The radionuclide molecular imaging technique is the most sensitive and can provide target-specific information. The radiotracer could also be used for radionuclide therapy. Thus, the development of a personalized theranostic (image and treat) agent would allow greater accuracy in selection of patients who may respond to treatment, and assessing the outcome of therapeutic response [9]. Gastrin-releasing peptide receptors (GRPRs) are overexpressed in several primary human tumors and metastases [5]. Markwalder and Reubi reported that GRPRs are expressed in invasive prostate carcinomas and in prostatic intraepithelial neoplasms at high

density, whereas normal prostate tissue and hyperplastic prostate tissue were predominantly GRPR negative [10]. These findings suggest that GRPR may be used as a molecular basis for diagnosing and staging prostate cancer, further for imaging-guided personalized medicine using radiolabeled bombesin analogues.

Previous studies have evaluated the ^{111}In-radiolabeled BN analogues which bind rapidly into GRP receptor-positive tumor cells, including PC-3, CA20948, and AR42J using gamma camera imaging after administration [11–14]. AMBA (DO3A-CH$_2$CO-G-(4-aminobenzoyl)-QWAVGHLM-NH$_2$) (Figure 1), a BBN-related peptide agonist, has a DO3A structure that can chelate tripositive lanthanide isotopes, such as ^{68}Ga, ^{90}Y, ^{111}In, and [177]Lu. Thus, it can formulate many kinds of radiolabelled probes for various purposes [15]. Indium 111 emits γ-photons of two energies (172 and 245 keV) as well as Auger and internal conversion electrons. ^{111}In-AMBA was initially used for diagnostic purposes but remains the potential for radiotherapy. Auger electron, with a maximum energy of <30 keV, is a high linear energy transfer (LET) radiation with subcellular pathlength (2–500 nm) in tissues [16]. For imaging the presence or absence of GRPR, the ^{111}In-AMBA could be used for patient selection for further radiotherapy (^{177}Lu-AMBA), chemotherapy (BLP antagonists), or therapeutic response monitoring as imaging-guided personalized medicine. Although ^{111}In-AMBA has been evaluated as an imaging agent [17–20], the pharmacokinetics and dosimetry of the agent have not been reported yet. In this study, ^{111}In-AMBA was designed as an image-guided diagnostic agent for human GRPR-positive tumors, which only retain the last eight amino acids (Q-W-A-V-G-H-L-M-NH$_2$) from native BN. The pharmacokinetics, biodistribution, dosimetry, and micro-SPECT/CT imaging of ^{111}In-AMBA were evaluated in human androgen-independent PC-3 prostate tumor-bearing SCID mice.

2. Materials and Methods

2.1. Chemicals.
Protected N^α-Fmoc-amino acid derivatives were purchased from Calbiochem-Novabiochem (Laufelfingen, Switzerland), Fmoc-amide resin and coupling reagent were purchased from Applied Biosystems Inc. (Foster City, CA, USA), and DOTA-tetra (tBu) ester was purchased from Macrocyclics (Dallas, TX, USA). Fmoc-4-abz-OH was obtained from Bachem (Chauptstrasse, Switzerland). Bombesin was purchased from Fluka (Buchs, Switzerland).

2.2. Synthesis of AMBA.
AMBA was synthesized by solid phase peptide synthesis (SPPS) using an Applied Biosystems Model 433A full automated peptide synthesizer (Applied Biosystems, Foster City, CA, USA) employing the Fmoc (9-fluorenylmethoxy-carbonyl) strategy. Carboxyl groups on Fmoc-protected amino acids were activated by (2-(^1H-benzotriazol-1-yl)-1,1,3,3-tetramethyluronium hexafluorophosphate (HBTU), forming a peptide bond with the N-terminal amino group on the growing peptide, anchored *via* the C-terminus to the resin, provided

for stepwise amino acid addition. Rink Amide resin (0.25 mmole) and Fmoc-protected amino acids (1.0 mmoL), with appropriate side-chain protections, and DOTA-tetra (tBu ester) were used for SPPS of the BBN conjugates. Side chain protecting groups in the synthesis were Trt for Gln and His, and Boc for Trp.

The protected peptide-resin was cleaved and deprotected with mixture of 50% trifluoroacetic acid (TFA): 45% chloroform, 3.75% anisole, and 1.25% 1, 2-ethanedithiol (EDT) for 4 h at room temperature (RT). The crude peptide was isolated by precipitating with cool diethyl ether. After centrifugation, the collected precipitate was dried under vacuum. The crude peptide sample was purified by reverse phase high-performance liquid chromatography (HPLC) using a column of XTerra prep, MSC18, 5 μm, 18 × 50 mm (Waters Corp., MA, USA) with an acetonitrile/water gradient consisting of solvent A (0.1% TFA in H$_2$O) and solvent B (0.1% TFA in acetonitrile), with a 14.8% yield; flow: 6 mL/min; gradient: 20%–40% B for 20 min. The molecular weight was determined with a MALDI-TOF Mass Spectrometer (Bruker Daltonics Inc, Germany). M/z determined for the peptide was AMBA, 1,502.6 [M+H].

2.3. Radiolabeling of ^{111}In-AMBA.
AMBA was radiolabeled with ^{111}In as previously described by Zhang et al. [21]. Briefly, AMBA was labeled with [111]In ([111]InCl$_3$, Institute of Nuclear Energy Research (INER), Taoyuan (Taiwan), 16430 MBq/mL in 0.05 N HCl, pH 1.5–1.9) by reaction of 6.66×10^{-4} μmole (1 μg) peptide in 95 μL 0.1 M NH$_4$OAc (pH 5.5) with 64.75 MBq [111]InCl$_3$ in 5 μL 0.04 N HCl for 10 min at 95°C. The specific activity of ^{111}In-AMBA was 9.72×10^4 MBq/μmole. The radiolabeling efficiency was analyzed using instant thin-layer chromatography (ITLC SG, Pall Corporation, New York. USA) with 0.1 M Na-citrate (pH 5.0) as solvent (indium citrate and [111]InCl$_3$: Rf = 0.9∼ 1.0, peptide-bound [111]In: Rf = 0∼0.1) [22]. Radio high-performance liquid chromatography (Radio-HPLC) analysis was performed using a Waters 2690 chromatography system with a 2996 photodiode array detector (PDA), a Bioscan radiodetector (Washington, DC, USA), and an FC 203B fraction collector by Gilson (Middleton, WI, USA). ^{111}In-AMBA was purified by an Agilent (Santa Clara, CA, USA) Zorbax bonus-RP HPLC column (4.6 × 250 mm, 5 μm) eluted with a gradient mixture from 10% B to 40% B in 40 min. Flow rate was 1 mL/min at RT, and the retention time for ^{111}In-AMBA was 22.5 min. After purification by HPLC, 100% ethanol was used instead of acetonitrile by solvent exchange with Waters Sep-Pak Light C18 cartridge (Milford, MA, USA). Normal saline was added after evaporation, and pH value was at the range 7∼7.5.

2.4. Receptor Cold Competition Assay.
Cold competition binding assay was studied using human bombesin 2 receptor expressed in HEK-293 cells as the source of GRP receptors (PerkinElmer, Boston, MA, USA). Assays were performed using FC96 plates and the Multiscreen system (Millipore, Bedford, MA). Binding of ^{125}I-Tyr^4-Bombesin (PerkinElmer,

FIGURE 1: Representative structure of AMBA.

Boston, MA, USA) to human bombesin 2 receptor (0.16 μg per well) was determined in the presence of increasing concentrations (0.001 nmole/L to 1000 nmole/L) of unlabeled AMBA in a buffer solution (20 mmol/L HEPES, pH 7.4, 3 mmol/L $MgCl_2$, 1 mmol/L EDTA, and 0.3% BSA) with a total volume of 250 μL per well. After incubation for 60 min at RT, membranes were filtered and washed with ice-cold Tris-HCl buffer (50 mmol/L). The filters containing membrane-bound radioactivity were counted using a Cobra II gamma-counter (Packard, Meriden, CT). The inhibitory concentration of 50% (IC_{50}) was calculated using a four-parameter curve-fitting routine using the KELL software for Windows version 6 (Biosoft, Ferguson, MO, USA) [13].

2.5. Cell Culture and Animal Model.

Human androgen-independent prostate cancer PC-3 cells (Bioresource Collection and Research Center, Taiwan) were cultured in Ham's F-12K medium supplemented with 10% heat-inactivated fetal bovine serum (all from GIBCO, Grand Island, NY, USA) containing 5% CO2 at 37°C. For animal inoculation, an aliquot was thawed, grown and used within 10 passages. Five-week-old male ICR SCID (severely compromised immunodeficient) outbred mice were obtained from the National Animal Center of Taiwan (Taipei, Taiwan, ROC) and maintained on a standard diet (Lab diet; PMI Feeds, St. Louis, MO, USA) at RT, with free access to tap water in the animal house of INER). Thirty-three SCID mice were subcutaneously injected with 2×10^6 PC-3 cells in the right hind flank. The animal experiments were approved by the Institutional Animal Care and Use Committee (IACUC) of the INER.

2.6. Biodistribution Studies.

At 4 weeks after PC-3 cell inoculation, the weight of the developed tumors ranged from 0.05 to 0.2 g. Twenty-five PC-3 xenograft SCID mice ($n = 5$ for each group) were injected with 0.37 MBq (0.1 μg) of the ^{111}In-AMBA in 100-μL normal saline via the tail vein. The mice were sacrificed by CO_2 asphyxiation with tissues and organs excised at 1, 4, 8, 24, and 48 h postinjection (p.i.). Subsequently, the tissues and organs were weighed, radioactivity was counted in a Packard Cobra II gamma-counter by Perkin-Elmer (Waltham, MA, USA), and the percentage of injected dose per gram (% ID/g) for each organ or tissue was calculated [23].

2.7. Pharmacokinetic Studies.

Six PC-3 xenograft SCID mice were injected with 0.37 MBq (0.1 μg) of the ^{111}In-AMBA in 100-μL normal saline via the tail vein. At 0.25, 1, 4, 16, 24, 48, 72, 96, and 168 h p.i., 20 μL of blood was collected from the heart puncture, then the blood was weighed, radioactivity was counted in the Cobra II gamma-counter, and the percentage of injected dose per gram (% ID/g) was calculated. The data were fitted to a two-compartment model and the pharmacokinetic parameters were derived by the WinNonlin 5.0 software (Pharsight Corporation, Mountain View, CA, USA).

2.8. Micro-SPECT/CT Imaging.

Two male SCID mice bearing human PC-3 tumors of approximately 0.1 g were i.v. injected with 12.2 MBq/4 μg ^{111}In-AMBA after purification by radio-HPLC. The SPECT and CT images were acquired by a micro-SPECT/CT scanner system (XSPECT; Gamma Medica-ideas Inc., Northridge, CA, USA). SPECT imaging was performed using medium-energy, parallel-hole collimators at 1, 4, 8, 24, and 48 h. The source and detector were mounted on a circular gantry allowing them to rotate 360 degrees around the subject (mouse) positioned on a stationary bed. The field of view (FOV) was 12.5 cm. The imaging acquisition was accomplished using 64 projections at 90 seconds per projection. The energy windows were set at 173 keV $\pm$ 10% and 247 keV $\pm$ 10%. SPECT imaging was followed by CT imaging (X-ray source: 50 kV, 0.4 mA; 256 projections) with the animal in exactly the same position. A three-dimensional (3D) Feldkamp cone beam algorithm was used for CT image reconstruction, and a two-dimensional (2D) filtered back projection algorithm was used for SPECT image reconstruction. All image processing softwares, including SPECT/CT coregistration, were provided by Gamma Medica-Ideas Inc (Northridge, CA, USA). After coregistration, both the fused SPECT and CT images had 256 $\times$ 256 $\times$ 256 voxels with an isotropic 0.3-mm voxel size.

2.9. Absorbed Radiation Dose Calculations.

The relative organ mass scaling method was employed to extrapolate the animal data to humans [24, 25]. The mean absorbed dose in various tissues was calculated from the radionuclide concentration in tissues/organs of interest, assuming a homogeneous distribution of the radionuclide within any source region [26]. The calculated mean value of percentage
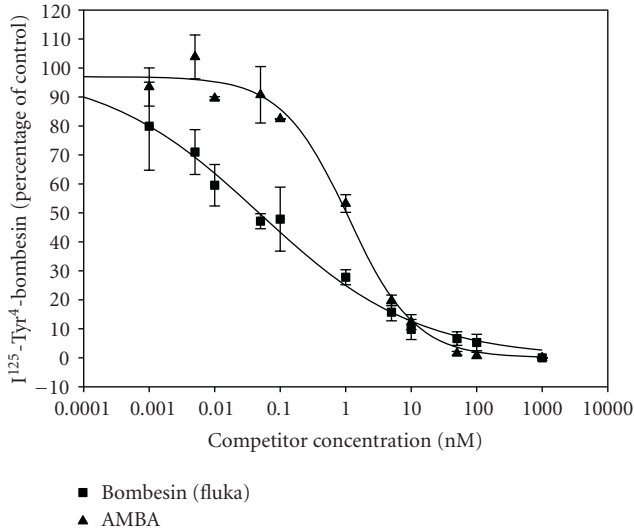
FIGURE 2: Competitive binding assay of AMBA versus ^{125}I-Tyr^4-Bombesin with human bombesin 2 receptors.

of injected activity per g (% IA/g) for the organs in mice was extrapolated to uptake in organs of a 70-kg adult using the following formula [24]:

$$\left[\left(\frac{\% IA}{g_{organ}}\right)_{animal} \times \left(Kg_{TB\ weight}\right)_{animal}\right] \times \left(\frac{g_{organ}}{Kg_{TB\ weight}}\right)_{human}$$

$$= \left(\frac{\% IA}{organ}\right)_{human}. \tag{1}$$

The extrapolated values (% IA) in the human organs at 1, 4, 8, 24, and 48 h were fitted with exponential biokinetic models and integrated to obtain the number of disintegrations in the source organs. This information was entered into the OLINDA/EXM computer program. The integrals (MBq-s) for 15 organs, including heart contents (blood), brain, muscle, bone, heart, lung, spleen, pancreas, kidneys, liver, and remainder of body were evaluated and used for dosimetry evaluation. The code also displays contributions of different source organs to the total dose of target organs. For the estimation of the tumor absorbed dose, it was assumed that once the radiopharmaceutical is inside the tumor, there is no biological elimination.

3. Results

3.1. Radiolabeling and In Vitro Receptor Binding Assay. The radiolabeling efficiency of ^{111}In-AMBA was 95.43 $\pm$ 1.37% ($n = 11$). The *in vitro* competitive binding assays were determined in the human bombesin 2 receptor using ^{125}I-Tyr^4-Bombesin as the GRP-R specific radiotracer, and unlabeled AMBA and native BN as competitors. The IC$_{50}$ of the AMBA and native BN in human bombesin 2 receptor (Figure 2) is 0.82 $\pm$ 0.41 nmol/L and 0.13 $\pm$ 0.10 nmol/L, respectively, in a single, direct, nanomolar range, demonstrating high specificity and affinity for the GRP receptor.

The Ki of AMBA and native BBN were 0.65 $\pm$ 0.32 nmol/L and 0.10 $\pm$ 0.08 nmol/L, respectively.

3.2. Biodistribution. ^{111}In-AMBA accumulated significantly in tumor, adrenal, pancreas, small intestine, and large intestine (Table 1). Fast blood clearance and fast excretion from the kidneys were observed. High levels of radioactivity were found in the kidneys before 24 h, indicating that the radioactivity was excreted rapidly in the urine within 24 h. The levels of radioactivity reached the highest with 3.87 $\pm$ 0.65 % ID/g at 8 h and then declined rapidly. The highest tumor/muscle ratio (Tu/Mu) of ^{111}In-AMBA was 11.79 at 8 h after injection and decreased progressively to 4.82 and 5.16 at 24 and 48 h after administration, respectively. Other GRPR-positive organs (small intestine and large intestine) also showed the specific binding of ^{111}In-AMBA (Table 1). The tumor/muscle ratios were decreased conspicuously at 4 and 24 h postadministration.

3.3. Pharmacokinetic Studies. The radioactivity declined to under detection limit after 24 h. The pharmacokinetic parameters derived by a two-compartment model [27] indicated that the distribution half-life ($t_{1/2\alpha}$) and distribution half-life ($t_{1/2\beta}$) of ^{111}In-AMBA were 1.53 $\pm$ 0.69 h and 30.73 $\pm$ 8.56 h, respectively (Table 2).

3.4. Micro-SPECT/CT Imaging. Micro-SPECT/CT imaging of ^{111}In-AMBA indicated significant uptake in the tumors at 8 and 24 h after intravenous injection (Figure 3). The longitudinal micro-SPECT/CT imaging showed high accumulation of ^{111}In-AMBA in pancreas and gastrointestinal tract at 4, 8, 24, and 48 h after intravenous injection.

3.5. Radiation Absorbed Dose Calculation. The radiation-absorbed dose projections for the administration of ^{111}In-AMBA to humans, determined from the residence times in mice, are shown in Table 3. The highest absorbed doses appear in the lower large intestine (0.12 mSv/MBq^{-1}), upper large intestine (0.13 mSv/MBq^{-1}), kidneys (0.12 mSv/MBq^{-1}), osteogenic cells (0.22 mSv/MBq^{-1}), and pancreas (0.25 mSv/MBq^{-1}). The effective dose appears to be approximately m0.11 mSv/MBq^{-1}. The red marrow absorbed dose is estimated to be 0.09 mSv/MBq^{-1}. For a 2-g tumor, the unit density sphere model was used and the estimated absorbed dose was 8.09 mGy·MBq^{-1}.

4. Discussion

Growth factor receptors are involved in all steps of tumor progression, enhancing angiogenesis, local invasion, and distant metastases. The overexpression of growth factor receptors on the cell surface of malignant cells might be associated with a more aggressive behavior and a poor prognosis. For these reasons, tumor-related growth factor receptors can be taken as potential targets for therapeutic intervention. Over the last two decades, GRP and other BLPs may act as a growth factor in many types of cancer. GRPR antagonists have been developed as anticancer candidate
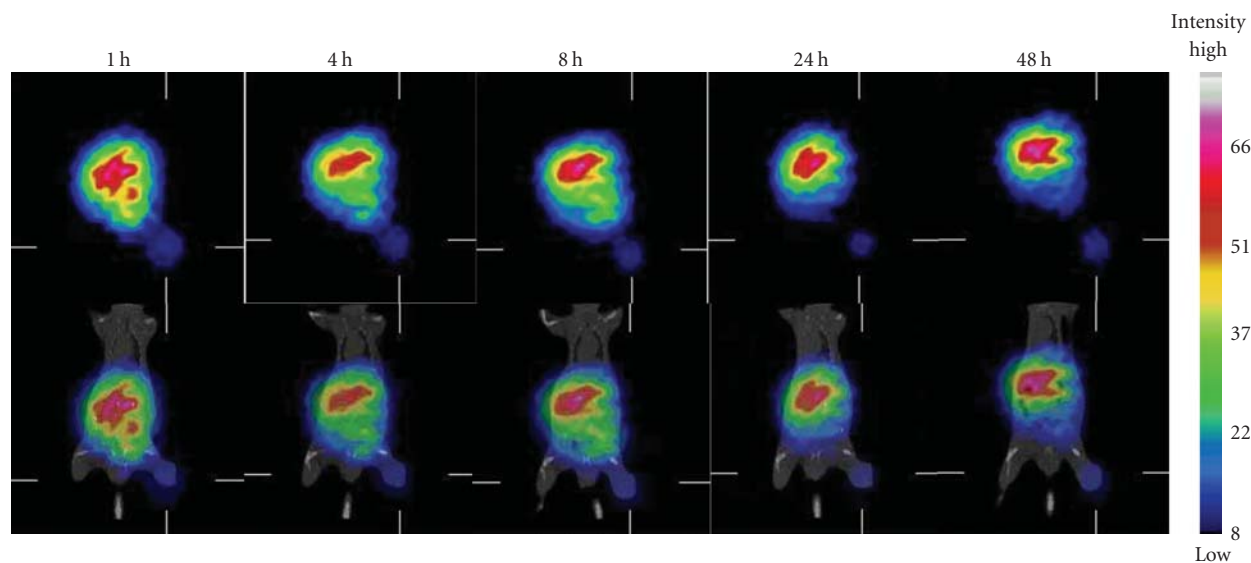
Figure 3: MicroSPECT/CT images of ^{111}In-AMBA targeting PC-3 tumors xenograft SCID mice. 12.2 MBq/4 μg ^{111}In-AMBA was administered to each mouse by intravenous injection. The images were acquired at 1, 4, 8, 24, and 48 h after injection. The energy window was set at 173 keV $\pm$ 10% and 247 keV $\pm$ 10%; the image size was set at 80 $\times$ 80 pixels. The color map shows the SPECT pixel values from 0 to the maximum expressed with an arbitrary value of 100.

Table 1: Biodistribution of ^{111}In-AMBA after intravenous injection in PC-3 prostate tumor-bearing SCID mice.

Organ	1 h	4 h	8 h	24 h	48 h
Blood	0.95 ± 0.09	0.50 ± 0.06	0.42 ± 0.02	0.19 ± 0.03	0.09 ± 0.02
Brain	0.06 ± 0.01	0.05 ± 0.01	0.05 ± 0.00	0.02 ± 0.00	0.03 ± 0.00
Skin	0.99 ± 0.22	0.60 ± 0.16	0.55 ± 0.02	0.36 ± 0.02	0.28 ± 0.02
Muscle	0.57 ± 0.19	0.33 ± 0.14	0.33 ± 0.02	0.21 ± 0.04	0.14 ± 0.02
Bone	1.02 ± 0.18	0.92 ± 0.21	1.57 ± 0.18	0.90 ± 0.13	0.60 ± 0.07
Heart	0.62 ± 0.09	0.48 ± 0.04	0.56 ± 0.08	0.41 ± 0.05	0.32 ± 0.04
Lung	1.78 ± 0.23	1.88 ± 0.46	1.70 ± 0.65	0.60 ± 0.17	0.26 ± 0.03
Adrenals	5.79 ± 1.21	7.08 ± 1.22	17.8 ± 4.65	7.41 ± 1.99	5.20 ± 1.11
Spleen	2.80 ± 1.49	6.90 ± 1.87	8.90 ± 2.34	4.41 ± 0.58	2.19 ± 0.51
Pancreas	6.14 ± 0.99	12.9 ± 2.44	54.9 ± 2.51	15.9 ± 1.94	9.80 ± 2.21
Kidney	3.56 ± 0.15	4.23 ± 0.28	3.92 ± 0.91	4.10 ± 0.72	2.74 ± 0.30
Liver	7.26 ± 0.53	8.22 ± 1.05	7.04 ± 0.24	8.64 ± 1.31	6.59 ± 1.83
Bladder	7.63 ± 2.94	1.75 ± 0.75	1.07 ± 0.12	0.64 ± 0.06	0.46 ± 0.10
Stomach	0.81 ± 0.09	0.80 ± 0.07	3.97 ± 1.15	0.97 ± 0.29	0.47 ± 0.05
SI	1.67 ± 0.22	1.56 ± 0.17	4.42 ± 0.61	1.48 ± 0.27	0.74 ± 0.10
LI	1.77 ± 0.25	3.42 ± 1.10	7.04 ± 1.48	2.39 ± 0.38	0.99 ± 0.16
Tumor (PC-3)	2.24 ± 0.66	1.86 ± 0.71	3.87 ± 0.65	1.02 ± 0.09	0.75 ± 0.08
Tumor/muscle	3.89	5.69	11.79	4.82	5.16

Values are expressed as % ID/g, mean ± SEM (n = 4-5 at each time point). SI: small intestine; LI: large intestine.

compounds, exhibiting impressive antitumoral activity both *in vitro* and *in vivo* in various murine and human tumors [28, 29]. Clinical trials with GRPR antagonists in cancer patients are in its initial phase as anticipated by animal toxicology studies and preliminary evaluation in humans [29]. Presently, efforts at the identification of the most suitable candidates for clinical trials and at improving drug formulation for human use are considered priorities. It may also be anticipated that GRPRs may be exploited as

potential carriers for cytotoxins, immunotoxins, or radioactive compounds. Thus, the visualization of these receptors through molecular image-guided diagnostic agents may become an interesting tool for tumor detection and staging in personalized medicine.

The present study showed the highest accumulation of ^{111}In-AMBA in pancreas in mice (Table 1). However, interspecies differences in structure and pharmacology of human and animal GRP receptors have been reported [30].

Table 2: Pharmacokinetic parameters of plasma in PC-3 tumor-bearing mice after intravenous injection of $10\,\mu$Ci/mouse ^{111}In-AMBA (mean $\pm$ SEM, $n = 5$).

Parameter	Unit	Value
A	% ID/g	6.15 ± 0.69
B	% ID/g	1.43 ± 0.61
α	1/h	1.19 ± 0.85
β	1/h	0.03 ± 0.01
$AUC_{0-168\,h}$	$h \times$ (% ID/g)	66.4 ± 17.3
$t_{1/2\alpha}$	h	1.53 ± 0.69
$t_{1/2\beta}$	h	30.7 ± 8.56
C_{max}	% ID/g	7.37 ± 0.64

A, B, α, β: macro rate constants; $t_{1/2\alpha}$, $t_{1/2\beta}$: distribution and elimination half-lives; $AUC_{0-168\,h}$: area under concentration of ^{111}In-AMBA versus time curve; C_{max}: maximum concentration in plasma.

Table 3: Radiation dose estimates for ^{111}In-AMBA in humans.

Organ	Estimated dose (mSv/MBq^{-1})*
Adrenals	$1.5E-01$
Brain	$3.1E-02$
Breasts	$7.7E-02$
Gallbladder Wall	$1.5E-01$
LLI Wall	$1.2E-01$
Small Intestine	$1.3E-01$
Stomach Wall	$1.1E-01$
ULI Wall	$1.3E-01$
Heart Wall	$7.2E-02$
Kidneys	$1.2E-01$
Liver	$2.0E-01$
Lungs	$7.4E-02$
Muscle	$7.0E-02$
Ovaries	$1.2E-01$
Pancreas	$2.5E-01$
Red Marrow	$8.8E-02$
Osteogenic Cells	$2.2E-01$
Skin	$5.8E-02$
Spleen	$1.2E-01$
Testes	$5.9E-02$
Thymus	$9.0E-02$
Thyroid	$9.2E-02$
Urinary Bladder Wall	$1.1E-01$
Uterus	$1.3E-01$
Total Body	$9.2E-02$
Effective Dose	$1.1E-01$

*Radiation-absorbed dose projections in humans were determined from residence times for ^{111}In-AMBA in SCID mice and were calculated by use of OLINDA/EXM version 1.0 computer program.

Because the pancreas is the primary normal tissue in these animals that expresses a high density of bloodstream-accessible GRPRs, the accumulation of ^{111}In in the pancreas is a direct reflection of the efficacy of radiolabeled BN analogs for *in vivo* targeting of cell-surface-expressed GRPRs [31]. Retention of ^{111}In-AMBA in the pancreas may be due to the

characteristic of a radioagonist with effective internalization and cell retention. Waser et al. reported that in contrast to the strongly labeled GRPR-positive mouse pancreas with ^{177}Lu-AMBA, the human pancreas did not bind ^{177}Lu-AMBA unless chronic pancreatitis was diagnosed [32].

The majority of research efforts into the design of bombesin-based radiopharmaceuticals have been carried out using GRPR agonists. The main reason for using agonists is that they undergo receptor-mediated endocytosis enabling residualization of the attached radiometal within the targeted cell [33]. Micro-SPECT/CT imaging is a noninvasive imaging modality that can longitudinally monitor the behavior of GRPR expression in the same animal across different time-points before and during therapy. In the present study, tumor targeting and localization of ^{111}In-AMBA was clearly imaged with micro-SPECT/CT after 1 to 48 h of administration, suggesting that micro-SPECT/CT imaging with ^{111}In-AMBA is a good tool for studying the tumor targeting, distribution, and real-time therapeutic response *in vivo*.

The effective dose projected for the administration of ^{111}In-AMBA to humans (0.11 mSv/MBq^{-1}) (Table 3) is comparable to that for ^{111}In-pentetreotide (0.12 mSv/MBq^{-1}) [34], the only ^{111}In-labeled peptide receptor-targeted radio-therapeutic agent to be used clinically [35, 36]. The intestines, osteogenic cells, kidneys, and pancreas appear to receive absorbed doses around 0.2 mSv/MBq^{-1} of ^{111}In-AMBA. At a maximum planned administration of 111 MBq for diagnostic imaging, the total radiation-absorbed dose to these organs kidneys would be about 12 mSv. The use of animal data to estimate human doses is a necessary first step, but such studies give only an estimate of radiation doses to be expected in human subjects. More accurate human dosimetry must be established with imaging studies involving human volunteers or patients. The dosimetry data presented here will be valuable in the dose planning of these studies, and for application of ^{111}In-AMBA to Investigational New Drug (IND) research.

Clinically, primary prostate cancer and the metastases may be heterogeneous, demonstrating a spectrum of phenotypes from androgen-sensitive to androgen-insensitive. ^{177}Lu-AMBA, a conjugated bombesin compound for imaging and systemic radiotherapy, is now in phase I clinical trials [15]. ^{177}Lu-AMBA has been evaluated in early stages of prostate cancer represented by the androgen-dependent, prostate-specific antigen-secreting hormone-sensitive prostate cancer cell line LNCaP [6], derived from a lymph node metastasis, and also in PC-3 cell line, derived from bone metastasis, is androgen-independent and is thought to represent late-stage hormone-refractory prostate cancer (HRPC) [37]. ^{177}Lu-AMBA will be clinically efficacious as a single-agent radiotherapeutic for heterogeneous metastatic prostate cancer and be a valuable adjunct to traditional chemotherapy. Thus, the visualization of GRPR receptors through ^{111}In-AMBA as an image-guided agent may contribute to the use of radiotherapeutic, ^{177}Lu-AMBA, and other traditional chemotherapy in personalized medicine.

Targeted therapeutic and imaging agents are becoming more prevalent and are used to treat increasingly smaller

population of patients. This has led to dramatic increases in the costs for clinical trials. Biomarkers have great potential to reduce the numbers of patients needed to test novel targeted agents by predicting or identifying nonresponse early on and thus enriching the clinical trial population with patients more likely to respond. GRPRs are expressed on prostate tumor cells, making it a potential biomarker for cancer. The imaging of ^{111}In-AMBA indicated the stage of prostate cancer for determining the therapeutic approach to prostate cancer and for monitoring the therapeutic efficacy. The expression of GRPR will vary from patient to patient due to the stages and individual difference. If such patients could be prescreened with ^{111}In-AMBA to identify those with higher tumor expression of GRPR, then it would be possible to select cases for receiving BLPs-specific treatment, while cases with low tumor expression of GRPR can consider other treatment options. Consequently, the proposed approaches enable optimized and individualized treatment protocols and can enhance the development of image-guide personalized medicine.

By visualizing how well drug targeting systems deliver pharmacologically active agents to the pathological site, ^{111}In-AMBA furthermore facilitates "personalized medicine" and patient individualization, as well as the efficacy of combination regimens. Regarding personalized medicine, it can be reasoned that only in patients showing high levels of target site uptake with high expression of GRPR should treatment be continued; otherwise, alternative therapeutic approaches should be considered.

5. Conclusion

^{111}In-AMBA showed a characteristic of agonist, a good bioactivity *in vitro* and uptake in human GRPR-expressing tumors *in vivo*. The molecular image-guided diagnostic agent can be used for various different purposes, ranging from simple and straightforward biodistribution studies to extensive and elaborate experimental setups aiming to enable "personalized medicine" and to improve the efficacy of combined modality anticancer therapy.

Acknowledgments

References

[1] A. Jemal, R. Siegel, E. Ward, Y. Hao, J. Xu, and M. J. Thun, "Cancer statistics, 2009," *CA Cancer Journal for Clinicians*, vol. 59, no. 4, pp. 225–249, 2009.

[2] V. Erspamer, G. F. Erpamer, and M. Inselvini, "Some pharmacological actions of alytesin and bombesin," *Journal of Pharmacy and Pharmacology*, vol. 22, no. 11, pp. 875–876, 1970.

[3] G. S. Kroog, R. T. Jensen, and J. F. Battey, "Mammalian bombesin receptors," *Medicinal Research Reviews*, vol. 15, no. 5, pp. 389–417, 1995.

[4] H. Ohki-Hamazaki, M. Iwabuchi, and F. Maekawa, "Development and function of bombesin-like peptides and their receptors," *International Journal of Developmental Biology*, vol. 49, no. 2-3, pp. 293–300, 2005.

[5] R. T. Jensen, J. F. Battey, E. R. Spindel, and R. V. Benya, "International union of pharmacology. LXVIII. Mammalian bombesin receptors: nomenclature, distribution, pharmacology, signaling, and functions in normal and disease states," *Pharmacological Reviews*, vol. 60, no. 1, pp. 1–42, 2008.

[6] M. E. Maddalena, J. Fox, J. Chen et al., "Lu-AMBA biodistribution, radiotherapeutic efficacy, imaging, and autoradiography in prostate cancer models with low GRP-R expression," *Journal of Nuclear Medicine*, vol. 50, no. 12, pp. 2017–2024, 2009.

[7] A. Nagy and A. V. Schally, "Targeting cytotoxic conjugates of somatostatin, luteinizing hormone-releasing hormone and bombesin to cancers expressing their receptors: a "smarter" chemotherapy," *Current Pharmaceutical Design*, vol. 11, no. 9, pp. 1167–1180, 2005.

[8] J. K. Willmann, N. van Bruggen, L. M. Dinkelborg, and S. S. Gambhir, "Molecular imaging in drug development," *Nature Reviews Drug Discovery*, vol. 7, no. 7, pp. 591–607, 2008.

[9] T. Lammers, F. Kiessling, W. E. Hennink, and G. Storm, "Nanotheranostics and image-guided drug delivery: current concepts and future directions," *Molecular Pharmaceutics*, vol. 7, no. 6, pp. 1899–1912, 2010.

[10] R. Markwalder and J. C. Reubi, "Gastrin-releasing peptide receptors in the human prostate: relation to neoplastic transformation," *Cancer Research*, vol. 59, no. 5, pp. 1152–1159, 1999.

[11] C.-L. Ho, L.-C. Chen, W.-C. Lee et al., "Receptor-binding, biodistribution, dosimetry, and micro-SPECT/CT imaging of [111]In-[DTPA[1], Lys[3], Tyr[4]]-bombesin analog in human prostate tumor-bearing mice," *Cancer Biotherapy and Radiopharmaceuticals*, vol. 24, no. 4, pp. 435–443, 2009.

[12] W. A. P. Breeman, M. De Jong, B. F. Bernard et al., "Preclinical evaluation of [^{111}In-DTPA-Pro[1], Tyr[4]]bombesin, a new radioligand for bombesin-receptor scintigraphy," *International Journal of Cancer*, vol. 83, no. 5, pp. 657–663, 1999.

[13] W. A. P. Breeman, M. De Jong, J. L. Erion et al., "Preclinical comparison of In-labeled DTPA- or DOTA-bombesin analogs for receptor-targeted scintigraphy and radionuclide therapy," *Journal of Nuclear Medicine*, vol. 43, no. 12, pp. 1650–1656, 2002.

[14] M. De Visser, H. F. Bernard, J. L. Erion et al., "Novel ^{111}In-labelled bombesin analogues for molecular imaging of prostate tumours," *European Journal of Nuclear Medicine and Molecular Imaging*, vol. 34, no. 8, pp. 1228–1238, 2007.

[15] M. F. Tweedle, "Peptide-targeted diagnostics and radiotherapeutics," *Accounts of Chemical Research*, vol. 42, no. 7, pp. 958–968, 2009.

[16] J. G. Kereiakes and D. V. Rao, "Auger electron dosimetry: report of AAPM Nuclear Medicine Committee Task Group No. 6," *Medical Physics*, vol. 19, no. 6, pp. 1359–1360, 1992.

[17] I.-H. Liu, C.-H. Chang, C.-L. Ho et al., "Multimodality imaging and preclinical evaluation of ^{177}Lu-AMBA for human prostate tumours in a murine model," *Anticancer Research*, vol. 30, no. 10, pp. 4039–4048, 2010.

[18] J. C. Garrison, T. L. Rold, G. L. Sieckman et al., "Evaluation of the pharmacokinetic effects of various linking group using the ^{111}In-DOTA-X-BBN(7-14)NH structural paradigm in a prostate cancer model," *Bioconjugate Chemistry*, vol. 19, no. 9, pp. 1803–1812, 2008.

[19] R. P. J. Schroeder, C. Müller, S. Reneman et al., "A standardised study to compare prostate cancer targeting efficacy of five radiolabelled bombesin analogues," *European Journal of Nuclear Medicine and Molecular Imaging*, vol. 37, no. 7, pp. 1386–1396, 2010.

[20] R. Mansi, X. Wang, F. Forrer et al., "Evaluation of a 1,4,7,10-tetraazacyclododecane-1,4,7,10-tetraacetic acid-conjugated bombesin-based radioantagonist for the labeling with single-photon emission computed tomography, positron emission tomography, and therapeutic radionuclides," *Clinical Cancer Research*, vol. 15, no. 16, pp. 5240–5249, 2009.

[21] H. Zhang, J. Chen, C. Waldherr et al., "Synthesis and evaluation of bombesin derivatives on the basis of pan-bombesin peptides labeled with Indium-111, Lutetium-177, and Yttrium-90 for targeting bombesin receptor-expressing tumors," *Cancer Research*, vol. 64, no. 18, pp. 6707–6715, 2004.

[22] W. H. Bakker, R. Albert, C. Bruns et al., "[^{111}In-DTPA-D-Phe^1]-octreotide, a potential radiopharmaceutical for imaging of somatostatin receptor-positive tumors: synthesis, radiolabeling and in vitro validation," *Life Sciences*, vol. 49, no. 22, pp. 1583–1591, 1991.

[23] C. J. Smith, H. Gali, G. L. Sieckman et al., "Radiochemical investigations of ^{177}Lu-DOTA-8-Aoc-BBN[7-14]NH: an in vitro/in vivo assessment of the targeting ability of this new radiopharmaceutical for PC-3 human prostate cancer cells," *Nuclear Medicine and Biology*, vol. 30, no. 2, pp. 101–109, 2003.

[24] M. G. Stabin and J. A. Siegel, "Physical models and dose factors for use in internal dose assessment," *Health Physics*, vol. 85, no. 3, pp. 294–310, 2003.

[25] E. M. Molina-Trinidad, C. A. D. Murphy, G. Ferro-Flores, E. Murphy-Stack, and H. Jung-Cook, "Radiopharmacokinetic and dosimetric parameters of ^{188}Re-lanreotide in athymic mice with induced human cancer tumors," *International Journal of Pharmaceutics*, vol. 310, no. 1-2, pp. 125–130, 2006.

[26] International Commission on Radiological Units and Measurements, "Absorbed-Dose Specification in Nuclear Medicine, ICRU Report 67," *Journal of the ICRU*, vol. 2, no. 1, 2002.

[27] C. H. Chang, TA. K. Chou, C. Y. Yang, T. J. Chang, YU. H. Wu, and TE. W. Lee, "Biodistribution and pharmacokinetics of transgenic pig-produced recombinant human factor IX (rhFIX) in rats," *In Vivo*, vol. 22, no. 6, pp. 693–698, 2008.

[28] S. Sotomayor, L. Muñoz-Moreno, M. J. Carmena et al., "Regulation of HER expression and transactivation in human prostate cancer cells by a targeted cytotoxic bombesin analog (AN-215) and a bombesin antagonist (RC-3095)," *International Journal of Cancer*, vol. 127, no. 8, pp. 1813–1822, 2010.

[29] D. B. Cornelio, R. Roesler, and G. Schwartsmann, "Gastrin-releasing peptide receptor as a molecular target in experimental anticancer therapy," *Annals of Oncology*, vol. 18, no. 9, pp. 1457–1466, 2007.

[30] T. Maina, B. A. Nock, H. Zhang et al., "Species differences of bombesin analog interactions with GRP-R define the choice of animal models in the development of GRP-R-targeting drugs," *Journal of Nuclear Medicine*, vol. 46, no. 5, pp. 823–830, 2005.

[31] J. L. Scemama, A. Zahidi, and D. Fourmy, "Interaction of [^{125}I]-Tyr-bombesin with specific receptors on normal human pancreatic membranes," *Regulatory Peptides*, vol. 13, no. 2, pp. 125–132, 1986.

[32] B. Waser, V. Eltschinger, K. Linder, A. Nunn, and J. C. Reubi, "Selective in vitro targeting of GRP and NMB receptors in human tumours with the new bombesin tracer Lu-AMBA," *European Journal of Nuclear Medicine and Molecular Imaging*, vol. 34, no. 1, pp. 95–100, 2007.

[33] C. J. Smith, W. A. Volkert, and T. J. Hoffman, "Radiolabeled peptide conjugates for targeting of the bombesin receptor superfamily subtypes," *Nuclear Medicine and Biology*, vol. 32, no. 7, pp. 733–740, 2005.

[34] S. Louis, "Octreoscan kit for the preparation of indium-111 pentetreotide [product monograph]," 1995.

[35] M. Ferrari, M. Cremonesi, M. Bartolomei et al., "Dosimetric model for locoregional treatments of brain tumors with Y-conjugates: clinical application with Y-DOTATOC," *Journal of Nuclear Medicine*, vol. 47, no. 1, pp. 105–112, 2006.

[36] E. P. Krenning, P. P. M. Koolj, W. H. Bakker et al., "Radiotherapy with a radiolabeled somatostatin analogue, [^{111}In-DTPA-D-Phe^1]-Octreotide. A case history," *Annals of the New York Academy of Sciences*, vol. 733, pp. 496–506, 1994.

[37] L. E. Lantry, E. Cappelletti, M. E. Maddalena et al., "^{177}Lu-AMBA: synthesis and characterization of a selective ^{177}Lu-labeled GRP-R agonist for systemic radiotherapy of prostate cancer," *Journal of Nuclear Medicine*, vol. 47, no. 7, pp. 1144–1152, 2006.

Research Article

Diagnostic Value of I-131 NP-59 SPECT/CT Scintigraphy in Patients with Subclinical or Atypical Features of Primary Aldosteronism

Yi-Chun Chen,[1] Yu-Chieh Su,[2] Chang-Kuo Wei,[3] Jainn-Shiun Chiu,[4] Chih-En Tseng,[5] Shao-Jer Chen,[6] and Yuh-Feng Wang[7]

[1] *Division of Nephrology, Department of Internal Medicine, Buddhist Dalin Tzu Chi General Hospital,*
  Chiayi, and School of Medicine, Tzu Chi University, Hualien 97004, Taiwan
[2] *Division of Hematology-Oncology, Department of Internal Medicine, Buddhist Dalin Tzu Chi General Hospital,*
  Chiayi, and School of Medicine, Tzu Chi University, Hualien 97004, Taiwan
[3] *Department of General Surgery, Buddhist Dalin Tzu Chi General Hospital, Chiayi 622, Taiwan*
[4] *Department of Nuclear Medicine, Chang Bing Show Chwan Memorial Hospital, Changhua County 505, Taiwan*
[5] *Department of Pathology, Buddhist Dalin Tzu Chi General Hospital, Chiayi 622, Taiwan*
[6] *Department of Medical Imaging, Buddhist Dalin Tzu Chi General Hospital, Chiayi 622, Taiwan*
[7] *Department of Nuclear Medicine, Buddhist Dalin Tzu Chi General Hospital, and School of Medicine,*
  Tzu Chi University, Hualien 97004, Taiwan

Correspondence should be addressed to Yuh-Feng Wang, alineycc@gmail.com

Received 30 December 2010; Accepted 15 February 2011

Academic Editor: David J. Yang

Accumulating evidence has shown the adverse effect of long-term hyperaldosteronism on cardiovascular morbidity that is independent of blood pressure. However, the diagnosis of primary aldosteronism (PA) remains a challenge for patients who present with subtle or atypical features or have chronic kidney disease (CKD). SPECT/CT has proven valuable in the diagnosis of a number of conditions. The aim of this study was to determine the usefulness of I-131 NP-59 SPECT/CT in patients with atypical presentations of PA and in those with CKD. The records of 15 patients with PA were retrospectively analyzed. NP-59 SPECT/CT was able to identify adrenal lesion(s) in CKD patients with suspected PA. Patients using NP-59 SPECT/CT imaging, compared with those not performing this procedure, significantly featured nearly normal serum potassium levels, normal aldosterone-renin ratio, and smaller adrenal size on CT and pathological examination and tended to feature stage 1 hypertension and non-suppressed plasma renin activity. These findings show that noninvasive NP-59 SPECT/CT is a useful tool for diagnosis in patients with subclinical or atypical features of PA and those with CKD.

1. Introduction

Primary aldosteronism (PA) is the most common cause of surgically curable secondary hypertension and affects more than 10% of the general hypertensive population [1]. Stage 2 hypertension according to the Seventh Joint National Committee (JNC 7) [2] with or without symptomatic hypokalemia leads to a higher probability of PA detection, and the diagnostic approach is straightforward in three steps: case-finding screening testing of elevated plasma aldosterone concentration (PAC), sussppressed plasma renin activity

(PRA), and a high aldosterone to renin ratio (ARR), followed by aldosterone suppression confirmatory testing and subtype studies of computed tomography (CT) imaging, adrenal vein sampling, or I-6-beta-iodomethylnorcholesterol (I-131 NP-59) scintigraphy. However, normotensive PA patients, featured as elevated PAC, have been reported [3], and the ARR is not reliable in patients with chronic kidney disease (CKD) [4]. Therefore, diagnosing PA can be tricky when clinical and biochemical features vary widely and the criteria for PA cannot be met, especially in patients with CKD or who present with subclinical symptoms featured as

stage 1 hypertension or are found to have atypical laboratory testing.

It has been reported that an increased serum aldosterone level in normotensive individuals leads to the development of sustained hypertension in the future [5]. Moreover, patients with PA are at greater risk than those with the same degree of blood pressure (BP) but without PA for cardiovascular events and stroke because long-term hyperaldosteronism leads to vessel and heart damage that is independent of BP [6]. Therefore, normalization of circulating aldosterone is the paramount therapeutic goal for PA [7], and timely identification of subclinical or atypical features of PA is of clinical value.

The common modalities used for subtype identification of PA also have limitations. Adrenal CT scan is considered the initial diagnostic modality for the identification of adrenal nodules; however, its diagnostic sensitivity is estimated to be 50% [8]. Adrenal CT imaging cannot correctly detect adrenal microadenoma smaller than 1 cm in diameter and bilateral adrenal hyperplasia, both of which may present normal-appearing adrenals. Adrenal vein sampling is the diagnosis of choice to differentiate unilateral from bilateral disease in patients with PA; however, this technique is invasive and difficult to access the right adrenal vein [9] and inevitably carries some risk of adrenal hemorrhage [10], despite being performed by an experienced radiologist. Moreover, it appears to be rarely applied to patients with CKD and an increased bleeding tendency. Dexamethasone-suppression NP-59 scintigraphy has a high affinity for adrenocortical tissue, but traditional planar imaging has low sensitivity and specificity for detection of early adrenal activity, especially adenoma smaller than 1 cm in diameter [11]. Therefore, diagnosis can be challenging in patients who have CKD or/and present with subclinical symptoms or/and are found to have atypical laboratory testing or/and negative imaging studies.

Single photon emission computed tomography (SPECT)/CT imaging is a significant technical innovation that simultaneously provides anatomic and functional information to allow for better localization of tracer activity and to enhance diagnostic accuracy and sensitivity [12]. SPECT/CT has proven valuable in oncology and neurology [13] and has the advantage of identifying small lesions demonstrated in several case reports of nephrology [14, 15]. Recently, I-131 NP-59 SPECT/CT has been recommended as a diagnostic method of choice for patients with clinically confirmed PA, but inclusive CT or adrenal vein sampling results, because of its high sensitivity (up to 81.8%) and diagnostic accuracy [16]. To the best of our knowledge, there has been no clinical study of the use of NP-59 SPECT/CT in patients with subclinical or atypical PA or CKD patients with suspected PA. Thus, this aim of this study was to determine the usefulness of I-131 NP-59 SPECT/CT in patients with atypical presentations of PA and in those with CKD.

2. Materials and Methods

2.1. Patients.
The records of 14 patients with PA (5 males, 10 females) with a median age of 55.9 years (range,

27–72 years) who underwent adrenalectomy at our institution from April 2007 to April 2010 were retrospectively reviewed. Patients were followed until October 2010. One patient who did not undergo adrenalectomy because of clinically confirmed bilateral adrenal hyperplasia was also included in the analysis. Therefore, the study included 15 patients, 14 with pathologically confirmed PA, and one with clinically confirmed PA. Of the 15 patients, 6 who received NP-59 SPECT/CT imaging served as the SPECT/CT group, and the other 9 who did not receive NP-59 SPECT/CT imaging served as the control group. The complete data of these 15 patients are presented in Tables 1 and 2 and summarized in Figure 1 . The median period of followup was 216 days (range: 183–527 days). The study was approved by our Institutional Review Board.

2.2. Data Collection.
We collected clinical data including age, gender, systolic and diastolic BP at admission, chief complaints, laboratory results (serum potassium [K], plasma aldosterone concentration [PAC], plasma renin activity [PRA], aldosterone-renin-ratio [ARR], and transtubular potassium gradient [TTKG]) or 24-hour urinary potassium excretion, and confirmatory tests results (including saline loading test or/and captopril test) if done, followup outcomes, and imaging and pathological data. PAC and PRA were measured by commercial RIA kits (ALDOCTK, #P2714, Diasorin Inc., MN, USA, and GAMMACOAT PLASMA RENIN ACTIVITY, #CA-1533, Diasorin Inc., MN, USA, resp.). Normal ranges for PAC and PRA are 3.7–24 ng/dL and 0.15–2.33 ng/mL/h, respectively.

2.3. Definitions.
The definition of hypertension stage was based on the JNC 7 classifications [2], that is, stage 1 hypertension was defined as a BP of 140/90 mm Hg or greater, and stage 2 hypertension was defined as a BP of 160/100 mm Hg or greater. A positive captopril test was defined as PAC suppression >30% after oral administration of 25 mg of captopril, taken 2 hours before sampling [17]. A positive saline loading test was defined as PAC > 10 ng/dL after intravenous infusion of 2 L of 0.9% saline over 4 h [17]. An ARR > 30 was considered to be positive [10]. All drugs that can affect the ARR were discontinued for 2 weeks before performing confirmatory tests. Symptomatic hypokalemia was defined as serum K < 3.0 mEq/L. A TTKG > 4 was considered positive for kaliuria. Improvement was defined as a well-controlled BP with no or a decreased dose of antihypertensive medications, and normalization or decrease of PAC, PRA, and serum K. CKD was defined as an estimated glomerular filtration rate (eGFR) < 60 mL/min/1.73 m^2, based on the National Kidney Foundation Kidney Disease Outcome Quality Initiative guidelines [18]. Stage 3 CKD was defined as an eGFR of 30 to 59 mL/min/1.73 m^2. Stage 4 was defined as an eGFR of 15 to 29 mL/min/1.73 m^2. Stage 5 was defined as an eGFR of less than 15 mL/min/1.73 m^2.

2.4. Patient Preparation and NP-59 Planar, SPECT, and SPECT/CT Imaging.
A dexamethasone suppression regimen (1 mg orally 4 times daily) was initiated 7 days before

TABLE 1: Demographic and clinical data of study subjects.

Patient	Age (y)	Gender	BP (mm Hg) at admission SBP	BP (mm Hg) at admission DBP	HTN* stage	Chief complaint	Serum K (mEq/L)	PAC# (ng/dL)	PRA# (ng/mL/h)	ARR	TTKG	Test	Result
												Laboratory tests	Confirmatory tests
						Control group (n = 9)							
1	50	F	230	130	2	HTN	2.2	60.08	0.13	462	—	Captopril	Positive
2	34	F	186	105	2	Weakness	1.6	45.80	0.13	352	4.5	Saline loading	Positive
3	58	F	220	120	2	HTN	2.69	29.28	0.13	225	—	Captopril	Positive
4	32	F	182	121	2	HTN	2.87	40.00	1.71	23	—	—	—
5	71	F	146	94	1	Weakness	2.61	32.10	0.05	642	6.2	—	—
6	59	M	152	71	1	HTN	3.49	25.55	0.45	57	—	Saline loading	Positive
7	60	F	160	90	2	Weakness	1.74	110.70	0.18	615	11.9	—	—
8	72	M	180	117	2	Weakness	1.96	31.80	0.06	122	—	—	—
9	56	F	154	83	1	Weakness	2.76	21.70	0.53	41	6.1	—	—
						SPECT/CT group (n = 6)							
10	55	F	140	90	1	Accidentally palpable Irregular pulse	3.24	31.9	2.52	13	8.8	Saline loading Captopril	Negative
11	48	F	145	80	1	HTN	4.01	26.8	0.06	447	—	Saline loading Captopril	Negative
12[†]	57	M	170	100	2	HTN	2.79	37.2	0.32	116	72.1 mEq/d[!]	Saline loading	Negative
13	56	M	144	90	1	—	4.14	25.3	1.31	12	—	—	—
14	39	M	206	115	2	HTN	2.2	27.5	1.68	16	8.2	—	—
15[†]	27	F	150	88	1	HTN	4.32	29.3	1.62	18	—	Captopril	Negative

Abbreviations: SBP: systolic blood pressure; DBP: diastolic blood pressure; HTN: hypertension; S/S: symptom/sign; K: potassium; PAC: plasma aldosterone concentration; PRA: plasma renin activity; ARR: aldosterone-renin ratio; TTKG: transtubular potassium gradient; F: female; M: male.

#Normal range of PAC, PRA, and serum K is 3.7–24 ng/dL, 0.15–2.33 ng/mL/h, and 3.5 to 5.0 mEq/L, respectively.

* HTN stage according to JNC 7 report.

†Patients 12 and 15 had stages 3 and 4 chronic kidney disease with serum creatinine level of 2.2 mg/dL (eGFR 32.9 mL/min/1.73 m^2) and 2.5 mg/dL (eGFR 24.6 mL/min/1.73 m^2), respectively.

!24-hour urine excretion of potassium.

Screening testing and confirmatory testing		Pathology-p (n = 14)*							
		Category 1# (n = 8)			Category 2# (n = 2)	Category 3# (n = 2)		Category 4# (n = 3)	
		Control (n = 6)		SPECT/CT (n = 2)	Control (n = 2)	Control (n = 1)	SPECT/CT (n = 1)	SPECT/CT (n = 3)	
		CT-p		CT-p	CT-p	CT-p	CT-n	CT-p	CT-n
		BP-imp	BP-not	BP-imp	BP-imp	BP-imp		BP-imp	
PAC↑, PRA↓, ARR↑ (typical features)	test-p	Patient 2 (kaliuria)	Patient 1, 3					Patient 11	
	test-n								
	test-nd	Patient 8			Patient 5 (kaliuria)				
PAC↑, PRA—, ARR↑	test-p					Patient 6			
	test-n			Patient 12 (stage 3 CKD) (kaliuria)					
	test-nd	Patient 7 (kaliuria)							
PAC↑, PRA—, ARR—	test-n						Patient 10 (kaliuria)	Patient 15 (stage 4 CKD) (Figure 2)	
	test-nd	Patient 4		Patient 14 (kaliuria)				Patient 13	
PAC—, PRA—, ARR↑					Patient 9 (kaliuria)				

Abbreviations: p, positive; n, negative; nd, not done; BP-imp, BP improve; BP-not, BP not improve; ↑,elevate; ↓, suppressed; — , within normal range; test, confirmatorytest; other abbreviations are the same as Tables 1 and 2.

Arrow from left to right denotes symptoms presented from severe to mild form; arrow from up to down denotes screening testing from typical to atypical features.

*Exclude patient 15 because of bilateral adrenal hyperplasia.

#Four categories were ordered by the severity of symptoms: category 1, stage 2 hypertension and hypokalemia; category 2, stage 1 hypertension and hypokalemia; category 3, stage 1 hypertension and low-normal potassium level; category 4, stage 1 hypertension and normal potassium level.

Figure 1: Qualitative analysis of Tables 1 and 2.

tracer injection and this was continued throughout the imaging procedure and for 5 days postinjection [12]. Patients were also given 5 drops daily of Lugol's solution 3 days before the start of imaging to block thyroid uptake of free I-131, and This was continued until the end of the imaging period. All drugs that can interfere with NP-59 uptake were discontinued for 4 weeks before imaging [12]. NP-59 scanning was performed on days 1 through 5 to obtain planar images after intravenous injection of 1.5 mCi (56 MBq) NP-59. SPECT/CT scanning was performed on days 2 through 5 with a dural-head gamma camera (DST-XLi; GE Medical Systems, Buc, France) to obtain SPECT and merged SPECT/CT images.

2.5. Imaging Interpretation. CT images with fine cuts (3 mm) were obtained and interpreted by a well-experienced radiologist. The NP-59 planar, SPECT, and SPECT/CT images were interpreted by 2 nuclear medicine specialists. Aldosteronism on the affected side(s) was considered if there was early visualization of the tracer on imaging before the fifth postinjection day and intense uptake greater than that in the liver [12].

2.6. Adrenalectomy and Pathological Interpretation. Of the 15 patients, 14 underwent laparoscopic adrenalectomy by an experienced surgeon. The histopathological examinations of the surgical specimens were performed by an experienced pathologist.

2.7. Statistical Analysis. All data are expressed as median (range). The differences between the SPECT/CT group and the control group were compared by Fisher's exact test for categorical variables, or by Mann-Whitney U test for continuous variables. A two-sided P value less than .05 was considered statistically significant. All data were analyzed using SPSS version 13.0 (SPSS Inc., Chicago, IL).

3. Results

Pathological examination showed that 12 of 15 patients had unilateral adenomas, 1 had a micronodule, and 1 had unilateral focal nodular hyperplasia (Table 2). 1 had clinically confirmed bilateral adrenal hyperplasia (Figure 2).

3.1. Differences of Clinical Pictures between the Control and SPECT/CT Groups (Table 1). In the control group (n = 9), 6 subjects had stage 2 hypertension along with symptomatic hypokalemia; 2 had stage 1 hypertension along with symptomatic hypokalemia; one had stage 1 hypertension

(a)

96 hours
Post-abdomen

(b)

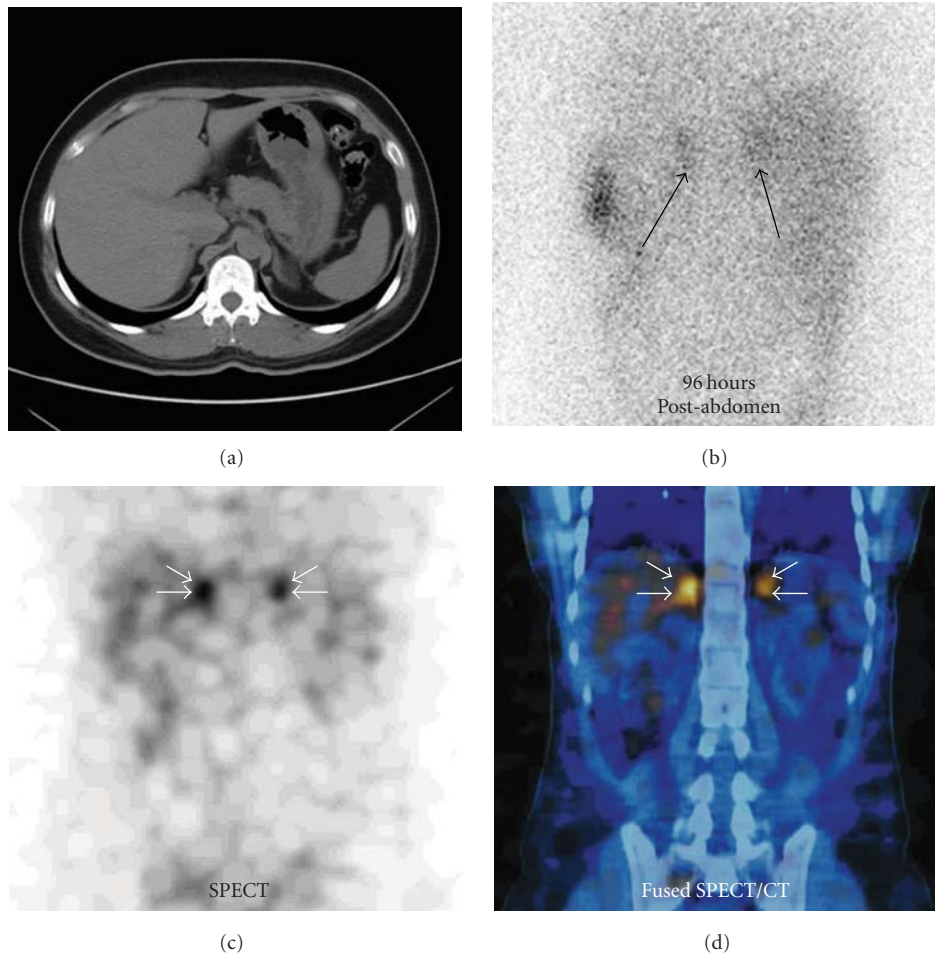SPECT

(c)

Fused SPECT/CT

(d)

FIGURE 2: A 27-year-old woman (patient 15) who had stage 4 CKD presented with stage 1 hypertension alone due to bilateral adrenal hyperplasia, whose PAC was elevated, but whose serum potassium level was normal, whose PRA was nonsuppressive, whose ARR was negative, whose confirmatory testing was negative, whose bilateral adrenal lesions had normal appearing on CT (a) and faint uptakes on planar imaging (b) but true positive on SPECT (c) and coronal SPECT/CT (d) imaging. After treatment with 25 mg of spironolactone, her BP and PAC were normalized.

without symptomatic hypokalemia. In the SPECT/CT group ($n = 6$), 4 subjects had stage 1 hypertension without symptomatic hypokalemia; 2 had stage 2 hypertension along with symptomatic hypokalemia.

3.2. Differences of Screening Testing and Confirmatory Testing between the Control and SPECT/CT Groups (Table 1). In the control group ($n = 9$), 8 subjects had elevated PAC and one had normal PAC; 5 had suppressed PRA and 4 had nonsuppressed PRA; 8 had positive ARR and one had negative ARR; 4 had positive confirmatory testing and 5 had absent results. In the SPECT/CT group ($n = 6$), 6 subjects had elevated PAC; one had suppressed PRA and 5 had nonsuppressed PRA; 2 had positive ARR and 4 had negative ARR; 4 had negative confirmatory testing and 2 had absent results.

3.3. Differences of Imaging Modalities between the Control and SPECT/CT Groups (Table 2). CT produced 9 (100%)

true positive results in the control group. CT produced 2 (33%) false negative and 4 (67%) true positive results in the SPECT/CT group. NP-59 planar imaging produced 2 (33%) true positive and 4 (67%) false negative results. NP-59 SPECT and SPECT/CT produced 6 (100%) true positive results, indicating 100% sensitivity.

3.4. Integrated Analysis of All Features between the 2 Groups (Figure 1). We divided all 15 patients into 4 categories based on the severity of hypertension and hypokalemia: category 1 (stage 2 hypertension and hypokalemia; $n = 8$; 6 in the control group and 2 in the SPECT/CT group); category 2 (stage 1 hypertension and hypokalemia; $n = 2$; all in the control group); category 3 (stage 1 hypertension and low-normal potassium level; $n = 2$; 1 in the control group and 1 in the SPECT/CT group); category 4 (stage 1 hypertension and normal potassium level; $n = 3$; all in the SPECT/CT group). The screening testing from typical to atypical features was ordered from the top to bottom. PA

TABLE 2: Imaging and pathological data of study subjects.

Patient	Age (y)	Gender	CT result		NP-59 result			Pathological result		Followup improvement
			Appearance (side)	Size (mm)	Planar	SPECT	SPECT/CT	Finding	Size (mm)	
Control group (n = 9)										
1	50	F	Nodule (L)	20	—	—	—	Adenoma	21	PAC, PRA, K
2	34	F	Nodule (L)	18	—	—	—	Adenoma	16	PAC, PRA, K, BP
3	58	F	Nodule (R)	17	—	—	—	Adenoma	17	PAC, PRA, K
4	32	F	Nodule (L)	20	—	—	—	Adenoma	20	PAC, K, BP
5	71	F	Nodule (L)	17	—	—	—	Adenoma	25	PAC, PRA, K, BP
6	59	M	Nodule (L)	11	—	—	—	Adenoma	10	PAC, BP
7	60	F	Nodule (R)	21	—	—	—	Adenoma	20	PAC, K
8	72	M	Nodule (R)	22	—	—	—	Adenoma	20	PAC, PRA, K, BP
9	56	F	Nodule (L)	17	—	—	—	Adenoma	17	PAC, K, BP
SPECT/CT group (n = 6)										
10	55	F	Normal	—	N	R	R	Micronodule	0.8	PAC, K, BP
11	48	F	Nodule (L)	17	L	L	L	Adenoma	17	PAC, PRA, K, BP
12[†]	57	M	Enlarge (L)	9 (in thickness)	N	L	L	Focal nodular hyperplasia	6	PAC, PRA, K, BP
13	56	M	Nodule (L)	12	N	L	L	Adenoma	10	PAC, BP
14	39	M	Nodule (R)	14	N	R	R	Adenoma	12	PAC, K, BP
15[†]	27	F	Normal	—	Faint	Bil	Bil	—[#]	—[#]	PAC, BP

Abbreviations: CT: computed tomography; L: left; R: right; Bil: bilateral; other abbreviations are the same as Table 1.
[†]Patients 12 and 15 had stages 3 and 4 chronic kidney disease with serum creatinine level of 2.2 and 2.5 mg/dL, respectively.
[#]Patient 15 did not undergo adrenalectomy because of bilateral adrenal hyperplasia.

was easily diagnosed from the typical clinical presentations of stage 1 or 2 hypertension along with hypokalemia and typical screening testing followed by positive CT results (patients 1–3, 5, and 8). Despite the presence of atypical screening testing, PA also could be diagnosed from typical clinical presentations together with positive CT results (patients 4, 7, and 9). However, we found that the SPECT/CT group had a higher percentage of mild clinical presentations, such as stage 1 hypertension and low-normal or normal serum potassium level (patients 10, 11, 13, and 15), atypical laboratory features of PA (patients 10, 12–15), and negative CT results (patients 10 and 15). All patients were found to have an improvement of BP after adrenalectomy and/or medical treatment, except for patients 1, 3, and 7 in the control group. This table implies that the timing of using NP-59 SPECT/CT tends to categories 3 and 4, as well as atypical screening and confirmatory testing.

3.5. Relationship of NP-59 SPECT/CT Lateralization Results to Clinical Outcome and to Pathological Features (Table 2 and Figure 1). NP-59 SPECT/CT correctly identified 3 adenomas (median size, 12 mm; range 10–17 mm), 1 micronodule (0.8 mm in size), 1 focal nodular hyperplasia (with the largest micronodule 6 mm in size), and 1 bilateral adrenal

hyperplasia (Figure 2) in 6 patients. Of these 3 adenomas, 2 were not detected on planar images. 2 (33%) of the SPECT/CT group had stages 3 and 4 CKD, both of which had atypical laboratory testing. All 6 patients had a clinical improvement of BP and normalization of PAC, 4 of whom had stage 1 hypertension and cured BP.

3.6. Comparison of Parameters between the Control and SPECT/CT Groups (Table 3). The median level of serum potassium was significantly higher in the SPECT/CT group than in the control group (3.6 versus 2.6 mEq/L, resp., $P = .029$), and the median level of ARR was significantly lower in the SPECT/CT group than in the control group (18.7 versus 352.3, resp., $P = .025$). The median size of the affected adrenal gland on CT scan and pathological examination was significantly less in the SPECT/CT group than in the control group (10.5 versus 18 mm, resp., $P = .007$; 10 versus 20 mm, resp., $P = .015$). Compared with the control group, the SPECT/CT group featured lower systolic BP (147 mm Hg) and nonsuppressed PRA (1.47 ng/mL/h) although the difference was not statistically significant. Furthermore, both groups had elevated PAC (32.1 versus 28.4 ng/dL in the control and SPECT/CT group, resp.) although the difference was not statistically significant.

TABLE 3: Comparison of variables between the control and SPECT/CT groups.

Variable	Control group ($n = 9$)	SPECT/CT group ($n = 6$)	P‡
Age (y)†	58 (32–72)	51 (27–57)	.157
Male gender (n [%])	2 (22%)	3 (50%)	.329
Systolic BP (mm Hg)†	180 (146–230)	147 (144–206)	.077
Diastolic BP (mm Hg)†	105 (71–130)	90 (80–115)	.237
Serum potassium (mEq/L)†	2.6 (1.6–3.49)	3.6 (2.2–4.32)	.029
PAC (ng/dL)†	32.1 (21.7–110.7)	28.4 (25.3–37.2)	.239
PRA (ng/mL/h)†	0.06 (0.05–0.53)	1.47 (0.06–2.52)	.058
Aldosterone-renin ratio (ARR)†	352.3 (23–642)	18.7 (13–447)	.025
CT size (mm)†	18 (11–22)	10.5# (9–17#)	.007
Pathological size (mm)†	20 (10–25)	10* (0.8–17*)	.015

Abbreviations are the same as Tables 1 and 2.
†Data are expressed as median (range).
#$n = 4$; patients 10 and 15 were excluded in this variable because of normal appearance of adrenal glands on the CT scan.
*$n = 5$; patient 15 was excluded in this variable because of bilateral adrenal hyperplasia.
‡$P < .05$ as significant.

4. Discussion

This is the first study to report the use of NP-59 SPECT/CT in patients with normal renal function and those with CKD who are clinically suspected to have PA but have subtle clinical symptoms, atypical results on screening tests, negative confirmatory tests, or negative CT findings. This study adds novel data to existing knowledge of PA by qualitatively analyzing the associations between clinical symptoms and screening tests (Figure 1), as well as quantitatively comparing clinical and pathological parameters between control and SPECT/CT groups (Table 3). First, our findings show that the screening testing and confirmatory testing may be unreliable in subclinical PA characterized by stage 1 hypertension without symptomatic hypokalemia, and in the setting of CKD, and second, They show that NP-59 SPECT/CT imaging adds value in the diagnosis of probable PA when elevated PAC and stage 1 or 2 hypertension coexists, but the other criteria were not present.

The first part of this study qualitatively analyzed the application of NP-59 SPECT/CT in patients suspected of having PA, but clinically not confirmed, as shown in Figure 1. Only 5 patients (patients 1–3, 5, and 8) presented with typical clinical pictures, which lead to a rapid diagnosis. Most of the patients presented with atypical signs and symptoms: subclinical (stage 1 hypertension in the absence of symptomatic hypokalemia) PA ($n = 5$), nonsuppressed PRA ($n = 9$), negative ARR ($n = 5$), negative confirmatory tests ($n = 4$), and negative CT results ($n = 2$). This finding is consistent with the viewpoint of Mosso et al. [19] that PA should be considered a continuous pathological disorder, in which most of the patients present with normokalemia and a mild form, and only a minority of patients present with a classical clinical picture of PA. Furthermore, it has been reported that the saline loading testing has low accuracy in patients with normokalemic PA [9]. The lower right area of Figure 1 corresponds to difficulty in arriving at a diagnosis of PA because of subtle symptoms, atypical screening testing, inclusive confirmatory testing, or negative

CT findings and is where NP-59 SPECT/CT is useful because it allows accurate localization of tumors because of its high sensitivity and diagnostic accuracy [16]. Therefore, the diagnosis of subclinical PA cannot rely on screening testing and confirmatory testing.

In addition, it is worth noting that 2 patients with CKD (patients 12 and 15) were diagnosed with PA by means of NP-59 SPECT/CT in this study. The diagnosis of PA in patients with CKD is difficult and easily missed, and only 2 cases have been reported in the English literature [20, 21]. This is because CKD masks the typical hallmarks of PA (hypertension, hypokalemia, and low PRA), shares some features with PA (such as hypertension and elevated PAC) [22], and disturbs the renin-angiotension-aldosterone system leading to a further decrease of the response of renin/aldosterone to stimuli or suppressive manoeuvres [23]. Furthermore, PRA varies from low to high level [22], the ARR is not reliable, and there are no clear-cut levels of PAC, PRA, and ARR for the diagnosis of PA in patients with CKD [4]. Adrenal vein sampling is more risky in patients with CKD than in those with normal renal function. In this setting, NP-59 SPECT/CT allows safe lateralization and prompt decision-making.

The second part of our study analyzed the differences in clinical and pathological parameters between the 2 groups, as shown in Table 3. We found that patients using NP-59 SPECT/CT imaging tended to feature stage 1 hypertension (median BP, 147 mm Hg) and nonsuppressed PRA (median level, 1.47 ng/mL/h) and significantly had negative ARR, nearly normal serum potassium level, and smaller adrenal size on CT imaging and pathological examination. Taking together, patients with probable PA who required NP-59 SPECT/CT imaging featured subclinical or atypical presentations. We also found that PAC was elevated, but not statistically significant, in both groups, and that the control group had higher PAC and systolic BP (median level, 32.4 ng/dL; median BP, 180 mm Hg, resp.) than the SPECT/CT group (median level, 28.4 ng/dL; median BP, 147 mm Hg, resp.). These findings implied that this clinical

clue of stage 1 hypertension along with elevated PAC may be useful when initially assessing the potential for subclinical PA and that elevated PAC precedes evident hypertension in patients with subclinical PA. It has been reported that the existence of normotensive PA was featured as elevated PAC [3]. Since PA is a continuous pathological disorder [19] and prolonged hyperaldosteronism causes subsequent hypertension [5] and excessive cardiovascular damage [6], non-invasive NP-59 SPECT/CT can provide value for early diagnosis and intervention of subclinical PA and may be a reliable method to distinguish between patients with low-renin essential hypertension and subclinical PA.

The Framingham offspring study has shown that an excess of circulating aldosterone in normotensive individuals results in the development of sustained hypertension [5] and cardiovascular morbidity and mortality that is beyond the effect of hypertension alone [6]. The cost effectiveness of a workup for subclinical PA remains to be determined. However, a timely identification of subclinical PA is rewarding for a number of reasons because a long-term cure implies saving the costs of lifetime antihypertensive medications, testing for monitoring the target organ damage, and treatment of complications [24]. Furthermore, long-term cure rate of hypertension correlates with the duration and severity of hypertension and ranges from 30 to 60% [7]. In the present study, 4 patients in the SPECT/CT group presented with stage 1 hypertension and had cured hypertension, and 2 patients with stage 2 hypertension merely improved BP. Therefore, vascular remodelling and duration of hypertension emphasize the importance of an early diagnosis of subclinical or atypical features of PA for a more favorable outcome.

The present study has some limitations. First, this was a retrospective study, and confirmatory testing and NP-59 SPECT/CT were not performed in all patients. Second, the specificity and diagnostic accuracy of NP-59 SPECT/CT cannot be established because of the small number of cases. Third, all patients did not undergo adrenal vein sampling.

5. Conclusion

In summary, our findings demonstrated that NP-59 SPECT/CT could be a reliable and non-invasive tool for an early diagnosis of PA in patients with subclinical or atypical features of PA and in CKD patients with suspected PA. NP-59 SPECT/CT imaging may transform the diagnostic process and lead to early identification and prompt management of these patients to achieve the cure of hypertension.

6. Conflict of Interests

The authors have no conflict of interests.

Acknowledgments

References

[1] S. Douma, K. Petidis, M. Doumas et al., "Prevalence of primary hyperaldosteronism in resistant hypertension: a retrospective observational study," *The Lancet*, vol. 371, no. 9628, pp. 1921–1926, 2008.

[2] A. V. Chobanian, G. L. Bakris, H. R. Black et al., "Seventh report of the Joint National Committee on Prevention, Detection, Evaluation, and Treatment of High Blood Pressure," *Hypertension*, vol. 42, no. 6, pp. 1206–1252, 2003.

[3] M. C. Vantyghem, N. Ronci, F. Provost et al., "Aldosterone-producing adenoma without hypertension: a report of two cases," *European Journal of Endocrinology*, vol. 141, no. 3, pp. 279–285, 1999.

[4] P. F. Plouin and X. Jeunemaitre, "Would wider screening for primary aldosteronism give any health benefits?" *European Journal of Endocrinology*, vol. 151, no. 3, pp. 305–308, 2004.

[5] R. S. Vasan, J. C. Evans, M. G. Larson et al., "Serum aldosterone and the incidence of hypertension in nonhypertensive persons," *New England Journal of Medicine*, vol. 351, no. 1, pp. 33–41, 2004.

[6] C. Mattsson and W. F. Young, "Primary aldosteronism: diagnostic and treatment strategies," *Nature Clinical Practice Nephrology*, vol. 2, no. 4, pp. 198–208, 2006.

[7] W. F. Young, "Minireview: primary aldosteronism—changing concepts in diagnosis and treatment," *Endocrinology*, vol. 144, no. 6, pp. 2208–2213, 2003.

[8] P. Mulatero, R. G. Dluhy, G. Giacchetti, M. Boscaro, F. Veglio, and P. M. Stewart, "Diagnosis of primary aldosteronism: from screening to subtype differentiation," *Trends in Endocrinology and Metabolism*, vol. 16, no. 3, pp. 114–119, 2005.

[9] G. Giacchetti, P. Mulatero, F. Mantero, F. Veglio, M. Boscaro, and F. Fallo, "Primary aldosteronism, a major form of low renin hypertension: from screening to diagnosis," *Trends in Endocrinology and Metabolism*, vol. 19, no. 3, pp. 104–108, 2008.

[10] A. Ganguly, "Primary aldosteronism," *New England Journal of Medicine*, vol. 339, no. 25, pp. 1828–1834, 1998.

[11] M. D. Gross, B. Shapiro, and J. E. Freitas, "Limited significance of asymmetric adrenal visualization on dexamethasone-suppression scintigraphy," *Journal of Nuclear Medicine*, vol. 26, no. 1, pp. 43–48, 1985.

[12] A. M. Avram, L. M. Fig, and M. D. Gross, "Adrenal gland scintigraphy," *Seminars in Nuclear Medicine*, vol. 36, no. 3, pp. 212–227, 2006.

[13] G. Mariani, L. Bruselli, T. Kuwert et al., "A review on the clinical uses of SPECT/CT," *European Journal of Nuclear Medicine and Molecular Imaging*, vol. 37, no. 1, pp. 1959–1985, 2010.

[14] Y. C. Chen, C. K. Wei, P. F. Chen, J. E. Tzeng, T. L. Chuang, and Y. F. Wang, "Seeking the invisible: I-131 NP-59 SPECT/CT for primary hyperaldosteronism," *Kidney International*, vol. 75, no. 6, p. 663, 2009.

[15] Y.-C. Chen, Y.-C. Su, J.-S. Chiu, C.-K. Wei, and Y.-F. Wang, "Peritoneo-scrotal shunting diagnosed by Tc-99m DTPA SPECT/CT imaging," *Kidney International*, vol. 78, no. 5, p. 523, 2010.

[16] R. F. Yen, V. C. Wu, K. L. Liu et al., "I-6β-iodomethyl-19-norcholesterol SPECT/CT for primary aldosteronism patients with inconclusive adrenal venous sampling and CT results," *Journal of Nuclear Medicine*, vol. 50, no. 10, pp. 1631–1637, 2009.

[17] J. W. Funder, R. M. Carey, C. Fardella et al., "Case detection, diagnosis, and treatment of patients with primary aldosteronism: an endocrine society clinical practice guideline," *Journal of Clinical Endocrinology and Metabolism*, vol. 93, no. 9, pp. 3266–3281, 2008.

[18] S. G. Massry, J. W. Coburn, G. M. Chertow et al., "K/DOQI clinical practice guidelines for bone metabolism and disease in chronic kidney disease," *American Journal of Kidney Diseases*, vol. 42, no. 4, supplement 3, p. S1S201, 2003.

[19] L. Mosso, C. Carvajal, A. González et al., "Primary aldosteronism and hypertensive disease," *Hypertension*, vol. 42, no. 2, pp. 161–165, 2003.

[20] K. Oka, K. Hayashi, T. Nakazato, T. Suzawa, K. Fujiwara, and T. Saruta, "Malignant hypertension in a patient with primary aldosteronism with elevated active renin concentration," *Internal Medicine*, vol. 36, no. 10, pp. 700–704, 1997.

[21] H. Ito, A. Sasaoka, T. Takao et al., "Aldosterone-producing adrenocortical adenoma complicated by chronic renal failure," *American Journal of Nephrology*, vol. 18, no. 6, pp. 541–546, 1998.

[22] H. Koshiyama, T. Fujisawa, N. Kuwamura et al., "A case of normoreninemic aldosterone-producing adenoma associated with chronic renal failure: case report and literature review," *Endocrine*, vol. 21, no. 3, pp. 221–226, 2003.

[23] C. W. Yang, Y. S. Kim, K. H. Yang et al., "Primary aldosteronism detected after renal transplantation," *American Journal of Nephrology*, vol. 14, no. 3, pp. 220–222, 1994.

[24] G. P. Rossi, A. C. Pessina, and A. M. Heagerty, "Primary aldosteronism: an update on screening, diagnosis and treatment," *Journal of Hypertension*, vol. 26, no. 4, pp. 613–621, 2008.

Research Article

Direct Determination of ECD in ECD Kit: A Solid Sample Quantitation Method for Active Pharmaceutical Ingredient in Drug Product

Ming-Yu Chao,[1] Kung-Tien Liu,[1] Yi-Chih Hsia,[1] Mei-Hsiu Liao,[2] and Lie-Hang Shen[3]

[1] *Chemical Analysis Division, Institute of Nuclear Energy Research, Taoyuan 32546, Taiwan*
[2] *Isotope Application Division, Institute of Nuclear Energy Research, Taoyuan 32546, Taiwan*
[3] *Institute of Nuclear Energy Research (INER), Taoyuan 32546, Taiwan*

Correspondence should be addressed to Kung-Tien Liu, ktliu@ecic.com.tw

Technetium-99m ethyl cysteinate dimer (Tc-99m-ECD) is an essential imaging agent used in evaluating the regional cerebral blood flow in patients with cerebrovascular diseases. Determination of active pharmaceutical ingredient, that is, L-Cysteine, N, N'-1,2-ethanediylbis-, diethyl ester, dihydrochloride (ECD) in ECD Kit is a relevant requirement for the pharmaceutical quality control in processes of mass fabrication. We here presented a direct solid sample determination method of ECD in ECD Kit without sample dissolution to avoid the rapid degradation of ECD. An elemental analyzer equipped with a nondispersive infrared detector and a calibration curve of coal standard was used for the quantitation of sulfur in ECD Kit. No significant matrix effect was found. The peak area of coal standard against the amount of sulfur was linear over the range of 0.03–0.10 mg, with a correlation coefficient (r) of 0.9993. Method validation parameters were achieved to demonstrate the potential of this method.

1. Introduction

To date, technetium-99m ethyl cysteinate dimer (Tc-99m-ECD or bicisate) is one of the most essential single-photon emission-computed tomography (SPECT) imaging agents in hospitals. According to the practice guidelines of the American College of Radiology (ACR) and the European Association of Nuclear Medicine Neuroimaging Committee (ENC), clinical indications of Tc-99m-ECD include evaluating the regional cerebral blood flow (rCBF) in patients with (i) cerebrovascular diseases, (ii) transient ischemic attack, (iii) various forms of dementia, (iv) symptomatic traumatic brain injury, (v) encephalitis, (vi) vascular spasm following subarachnoid hemorrhage, (vii) inflammation, (viii) epileptic foci, and (ix) lacunar infarctions [1, 2].

The indications of Tc-99m-ECD in SPECT brain perfusion imaging of neuropsychiatric disorders and chronic fatigue syndrome have not been fully characterized [1, 2]. However, investigations of the conversion in patients of mild cognitive impairment (MCI) to Alzheimer's disease (AD)

[3], the functional compensation mechanism in incipient AD [4], the mechanism for suppression of parkinsonian tremor by thalamic stimulation [5], the mechanism by which thyroid hormone availability affects cerebral activity [6], brain glucose metabolism in hypothyroidism [7], reduction in the bifrontal regions and diffusion-weighted imaging of Creutzfeldt-Jakob disease [8, 9], quantitation and differentiation in patients with Tourette's syndrome [10–12], and abnormal rCBF in patients with Sjögren's syndrome [13] were reported.

For clinical implements, Tc-99m-ECD is obtained by radiolabeling of active pharmaceutical ingredient (API), that is, L-Cysteine, N, N'-1,2-ethanediylbis-, diethyl ester, dihydrochloride (ECD) with Tc-99m. Radiochemical purity (RCP) of Tc-99m-ECD is used for the quality control (QC) purpose [14–16]. Although the characteristics of Tc-99m-ECD, such as *in vivo* kinetics and biodistribution studies in healthy human [15, 17], pharmacological studies in primates [14, 18], uptake, clearance, and brain retention [19–22], biotransformation, metabolites, and stability [14, 21, 23], have

Table 1: Optimized parameters of elemental analyzer for quantitation of ECD in ECD Kit.

Parameters	
Operation mode	CHNS
Combustion temperature (°C)	1150
Reduction temperature (°C)	900
Flush gas/time (sec)	He/10
O_2 dosing time (sec)	120
Column standby temperature (°C)	
CO_2	Ambient temperature
H_2O	Ambient temperature
SO_2	140
Column desorption temperature (°C)	
CO_2	240
H_2O	150
SO_2	220
Carrier gas/Flow rate (mL/min)[1]	He/230
Flow rate of O_2 (mL/min)	15
Flow rate of O_2 during combustion (mL/min)	30–35

[1] Same as the mass flow control (MFC) TCD flowing gas and flow rate.

been well-investigated, the chemical properties (such as purity and content) of ECD in ECD Kit (Vial A), that is, API in drug product, which might significantly disqualify the efficacy of Tc-99m-ECD have not been much discussed. Moreover, no analytical method for the determination of content and uniformity of ECD in ECD Kit has been published.

Analysis of the content and uniformity of ECD in ECD Kit is a relevant requirement for the pharmaceutical QC in processes of mass fabrication. In the stability study of Mikiciuk-Olasik and Bilichowski, they demonstrated that ECD decomposed as soon as it was dissolved in phosphate buffer solutions [24]. Our earlier observations also agreed with findings of Verduyckt et al. [25], showing that the composition of ECD Kit is the major obstacle to determine stability of ECD in (non)aqueous solutions.

ECD is the only component which contains sulfur in ECD Kit. Methods for the determination of sulfur, including Eschka method [26], gas chromatography-mass spectrometry (GC-MS) [26], inductively coupled plasma atomic emission spectrometry (ICP-AES) [27], instrumental neutron activation analysis (INAA) [27], X-ray fluorescence [27, 28], and elemental analyzer coupled with a thermal conductivity detector (EA-TCD) [29] or an isotope ratio mass spectrometer (EA-IRMS) [30], have been developed. We here presented a direct solid sample determination method of ECD in ECD Kit without sample dissolution to avoid the rapid degradation of ECD in aqueous solution using elemental analyzer (EA) coupled with a nondispersive infrared detector (NDIR). Method validation parameters were achieved to demonstrate the potential of this method.

2. Experimental

2.1. Materials and Reagents.
ECD (purity: 97.53%) was obtained from ABX (Radeberg, Germany). Coal standard (ELTRA coal standard no. 92510-50; C: 76.6%, S: 3.07%) was purchased from ELTRA (Neuss, Germany). All chemicals and reagents were of analytical grade and used as received without further purification.

2.2. Elemental Analyzer.
An elemental analyzer (EA) (vario EL cube, Elementar Analysensysteme GmbH, Hanau, Germany), equipped with a microbalance (Mettler-Toledo XP6, Mettler-Toledo GmbH, Giessen, Germany), a nondispersive infrared detector (NDIR), and a thermal conductivity detector (TCD) was employed for the measurement of sulfur. The microbalance was connected to control a personal computer (PC) of the EA for automatic transmission of the sample weight to the PC. The measurement of sulfur was switched to NDIR photometer in operation mode of "CHNS". Since the NDIR detector is sensitive to water vapor, the measured gas was dried with a U-tube filled with Sicapent (phosphorus pentoxide drying agent) before entering the NDIR.

For EA analysis, the samples were sealed in a tin container and were dropped automatically into a combustion tube filled with catalytic material (WO_3 granulate) and maintained at a temperature of 1150°C. As the sample entered the combustion tube, a fixed amount of oxygen was injected into the helium carrier. Time for oxygen dosing was set at 120 seconds. The exothermic oxidation of tin made the samples combust completely. After passing through a reduction tube (silver wool, corundum balls, and copper) at a temperature of 900°C, elements of nitrogen, carbon, sulfur, and hydrogen in the samples were converted into gases of nitrogen, carbon dioxide, sulfur dioxide, and water, respectively. The mixture of gases was separated by gas chromatographic column, and the TCD or NDIR signals of CO_2, H_2O, and SO_2 were recorded. Data were acquired and processed with software from Elementar (vario EL version of 1.3.1., Hanau, Germany). The optimized EA parameters are presented in Table 1. Figure 1 shows the typical EA analytical chromatogram of ECD in ECD Kit.

2.3. Method Development/Validation

2.3.1. Preparation of Standards, QC, and Blank Samples.
The preparation of ECD Kit (Vial A) was done according to the procedure of Walovitch et al. [14], which was freeze-dried under an N_2 headspace and contained 0.90 mg ECD, 72 μg $SnCl_2 \cdot 2H_2O$, 360 μg $Na_2EDTA \cdot 2H_2O$, and 24 mg mannitol.

Compositions of ECD calibration standards (Std_{ECD}), blanks (Bk_{Kit}), and QC samples (QC_{ECD}: QC-L, QC-M, QC-H) for method validation were prepared by Isotope Application Division, Institute of Nuclear Energy Research (INER, Taoyuan, Taiwan) and summarized in Table 2. ECD Kit and Kit blank samples were grounded by using an agate mortar for 40 seconds before determination.

Coal calibration standards (Std_{coal}) were freshly prepared daily by weighing 1.00 to 3.50 mg of coal standard. Coal QC samples (QC_{coal}) were prepared in the same way as the coal
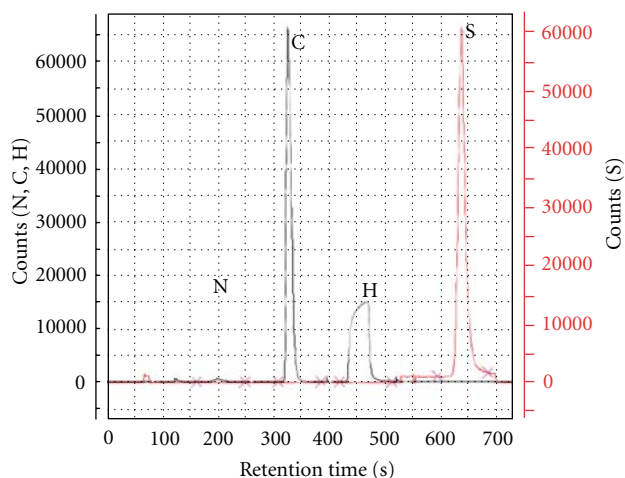
Figure 1: Typical elemental analyzer chromatogram of ECD in ECD Kit.

calibration standards by weighing 2.00 ± 0.20 mg of coal standard.

2.3.2. Method Validation. The method was modified and validated according to the International Conference on Harmonization (ICH) guidelines for the validation parameters of analytical method, including specificity, linearity, precision, accuracy, stability, robustness, and system suitability.

Three tin blanks (tin container without sample) and three 7.60 mg Kit blanks (Table 2) were analyzed. Peak areas appeared on the retention time of sulfur were determined to evaluate the specificity (selectivity) of the method in resolution between sulfur and other elements. The calibration curves of five coal standards (1.08 to 3.39 mg) were plotted against the peak areas. The linearity was evaluated by the linear least squares regression method with three coal QC samples determined at concentration of 2.10 mg. The precision of the method was assessed by the same batch of ECD Kit at five concentrations (1.08 to 3.39 mg) and three QC samples determined at concentration of 2.10 mg. Intraday precision (repeatability) and inter-day precision (reproducibility) were evaluated by one analyst within one day and on two different days, respectively. The accuracy was determined by the recovery test. ECD quality control (QC) samples of low (QC-L), medium (QC-M), and high (QC-H) concentration at 0.23, 0.27, and 0.31 mg/vial (nominal weight of ECD per vial of ECD Kit, Table 2) and one coal QC sample at concentration of 2.15 mg were analyzed by the proposed method. Experimental values (Sulfur(mg)$_{\text{exp}}$ or Sulfur(%)$_{\text{exp}}$) were obtained by interpolation to the linear least squares regression equation of a fresh prepared calibration curve (1.08 to 3.45 mg) and compared to the theoretical values (Sulfur(mg)$_{\text{nominal}}$ or Sulfur(%)$_{\text{nominal}}$):

$$\text{Recovery yield (\%)} = \frac{\text{Sulfur(mg)}_{\text{exp}}}{\text{Sulfur(mg)}_{\text{nominal}}} \times 100\%, \quad (1)$$

or

$$\text{Recovery yield (\%)} = \frac{\text{Sulfur(\%)}_{\text{exp}}}{\text{Sulfur(\%)}_{\text{nominal}}} \times 100\%. \quad (2)$$

The bench-top stabilities were examined by analyzing 2.05 ± 0.05 mg of coal standards and 7.52 ± 0.03 mg of ECD Kit samples for three consecutive days. The samples were kept in an autosampler at ambient temperature for EA analysis over this period. Experimental data were obtained by comparing the linear least squares regression equations of calibration curves. The robustness of an analytical method is a basic measurement of its capacity to remain unaffected by small variations in method parameters. In this case, method robustness was evaluated through the effects of dosing time of oxygen, temperatures of combustion tube and reduction tube. The system suitability was assessed by the triplicate analyses of tin blanks and Kit blanks with acceptance criterion of 5,000 counts.

3. Results

3.1. Method Development. Various sulfur forms are presented in coal, that is, pyrite, ferrous sulfate, gypsum, organic sulfur, and elemental sulfur [26, 28, 31]. For direct solid sample analysis of sulfur, effects of matrix, chemical form, and homogeneity of the analyte in sample are relevant to the reliability of analytical results [32–34].

The matrix effect on the determination of sulfur was examined as shown in Table S1 in Supplementary Material available online at doi:10.1155/2011/196238. The average peak area of Kit blanks was ten times higher than that of tin blanks. The linear least squares regression equations of coal standard without and with the existence of Kit blanks were $Y = 1.565 \times 10^{-6}X + 3.174 \times 10^{-3}$ and $Y = 1.547 \times 10^{-6}X + 8.932 \times 10^{-3}$, respectively. No significant differences of linear equations, linearities, and linear ranges were detected. Determination of different concentration ECD standards (0.78 to 1.07 mg, Table 2) in Kit blank using coal for calibration curve were shown in supplemental Table S2. Again, no significant difference of inter-day study coal standard curves was found. Some results of the recovery yields of Std$_{\text{ECD}}$ no. 2 and Std$_{\text{ECD}}$ no. 4 were outside the acceptance criterion ($\pm 5.00\%$).

3.2. Method Validation. In supplemental Table S1, it is shown that the peak areas on the retention time of sulfur were 248 ± 11 and 2438 ± 642 for tin blanks and Kit blanks, respectively. Data are expressed as average $\pm$ SD. Although the peak areas of Kit blanks were higher than those of tin blanks, the areas were approximately half of the acceptance criterion of system suitability (5000 counts).

Standard curves were constructed by plotting peak areas (counts) against the amounts of coal standard and were linear over the range of 1.08 to 3.39 mg (X in weight of sulfur = 0.033–0.104 mg). The linear least squares regression equation of the standard curve in this range was $Y = 1.615 \times 10^{-6}X + 4.747 \times 10^{-3}$, with a correlation coefficient (r) of 0.9993.

TABLE 2: Preparation and composition of ECD calibration standards, blank, and quality control samples.

Sample	W_{ECD}[1] (mg/vial)	W_{Kit}[2] (mg/vial)	W_S[3] (mg/vial)	$\%W_S$[4] (%, w/w)
Kit blank (Bk_{Kit})	0.00	25.61	0.00	0.00
ECD Calibration standards				
Std_{ECD} no. 1	0.78	26.27	0.123	0.47
Std_{ECD} no. 2	0.89	26.00	0.140	0.54
Std_{ECD} no. 3	0.97	26.10	0.152	0.58
Std_{ECD} no. 4	1.07	26.04	0.168	0.65
ECD QC samples (QC_{ECD})				
QC-L	0.23	7.27	0.036	0.48
QC-M	0.27	7.23	0.042	0.57
QC-H	0.31	7.19	0.049	0.65

[1] Nominal weight of ECD in ECD Kit.
[2] Total weight of ECD Kit.
[3] Nominal weight of sulfur in ECD Kit.
[4] Percentage of sulfur (%, w/w) in ECD Kit.

TABLE 3: Precision and accuracy in the analysis of QC samples and ECD in ECD Kit.

Day	Standard curve[1]			Sulfur weight (%)[2]	Recovery yield (%)	
	Dynamic range of sulfur (mg)	Linear least squares regression equation	Correlation coefficient (r)	QC_{coal}	QC_{coal}	QC_{ECD}[3]
1	0.033–0.104	$Y = 1.615 \times 10^{-6}X + 4.747 \times 10^{-3}$	0.9993	3.13 ± 0.07 (2.25%)	102.08 ± 2.29	—
1	0.031–0.105	$Y = 1.623 \times 10^{-6}X + 1.741 \times 10^{-3}$	0.9989	3.10 ± 0.02 (0.60%)	100.89 ± 0.60	—
2	0.034–0.107	$Y = 1.634 \times 10^{-6}X + 1.034 \times 10^{-3}$	0.9994	3.08 ± 0.04 (1.21%)	100.15 ± 1.21	—
3	0.033–0.106	$Y = 1.576 \times 10^{-6}X + 4.202 \times 10^{-3}$	0.9996	3.18	103.79	102.78 (QC-L) 100.00 (QC-M) 102.08 (QC-H)

[1] Standard curves of coal.
[2] Content percentage of sulfur in coal standard: 3.07% (w/w); data are expressed as average $\pm$ SD (%R.S.D.), $n = 3$.
[3] Purity of ECD: 97.53%; compositions of ECD QC samples (QC-L, QC-M, and QC-H) were shown in Table 2.

Table 3 provides the results of repeatability, reproducibility, and accuracy of the proposed method. The Intraday precisions of sulfur weight (%) in coal QC samples were 0.60% to 2.25%. The inter-day precisions of sulfur weight (%) and slope of the calibration curve in coal QC samples were 1.69% and 1.56%, respectively. Average recovery yield of ECD in ECD QC samples was 101.62% $\pm$ 1.45% (R.S.D. = 1.42%).

The samples for bench-top stability study were kept in the EA autosampler under ambient environment for a three-consecutive-day experiment (Table 4). Average recovery yields for the determination of sulfur in coal QC samples and ECD in ECD QC samples were 100.88% $\pm$ 1.46% (R.S.D. = 1.45%) and 98.93% $\pm$ 3.24% (R.S.D. = 3.28%), respectively. The recovery yield of QC_{coal} was approximately 100%. However, recovery yields of QC_{ECD} increased gradually from 96.02% $\pm$ 2.33% (day 1) to 102.31% $\pm$ 1.63% (day 3).

The method robustness was evaluated through the effects of dosing time of oxygen, temperatures of combustion tube and reduction tube as shown in Table 5. Optimal dosing time of oxygen, temperatures of combustion tube and reduction tube were 120 sec, 1150°C and 900°C, respectively. No

statistically significant difference of linear equations and correlation coefficients were found.

The acceptance criterion of system suitability was assessed by triplicate analyses of the tin blanks and Kit blanks for peak area and was set at 5000 counts.

3.3. Real Sample Analysis. Analytical data of three batch real samples are summarized in Table S3. One in five QC_{coal} samples was outside the acceptance criterion ($\pm$5.00%). The determined (experimental) value of ECD by the proposed method gradually increased from 0.934 $\pm$ 0.021 mg (batch 1) to 0.984 $\pm$ 0.007 mg (batch 3).

4. Discussion

No significant matrix effect of Kit blank on the peak area, linearity of calibration curve, and selectivity of sulfur was found (Table S1). The findings suggest that coal standard (without being spiked into Kit blank) is more convenient and stable (Table S2) than ECD standard to construct the calibration curve.

Table 4: Stability study of QC samples analysis.

Day	Standard curve			Recovery yield (%)[1]	
	Dynamic range of sulfur (mg)	Linear least squares regression equation	Correlation coefficient (r)	QC_{coal}[2]	QC_{ECD}[3]
1	0.032–0.105	$Y = 1.627 \times 10^{-6}X + 4.149 \times 10^{-3}$	0.9994	101.10 ± 0.94	96.02 ± 2.33
2	0.033–0.103	$Y = 1.629 \times 10^{-6}X + 2.390 \times 10^{-3}$	0.9994	99.82 ± 0.90	98.48 ± 1.96
3	0.031–0.105	$Y = 1.609 \times 10^{-6}X + 2.608 \times 10^{-3}$	0.9997	101.72 ± 2.00	102.31 ± 1.63

[1] Data are expressed as average $\pm$ SD, $n = 3$.
[2] QC_{coal}: 2.05 ± 0.05 mg of coal QC samples (S = 3.07%, w/w) were analyzed.
[3] QC_{ECD}: 7.52 ± 0.03 mg of ECD QC samples (ECD = 3.61%; S = 0.58%, w/w) were analyzed.

Table 5: Robustness study in the analysis of ECD.

Parameter		Standard curve of coal[1]		QC_{coal}[2]	
		Linear least squares regression equation	Correlation coefficient (r)	Sulfur weight (%)	Recovery yield (%)[3]
Dosing time (sec)	90	$Y = 1.544 \times 10^{-6}X + 3.394 \times 10^{-3}$	0.9992	3.14 ± 0.06	102.36 ± 2.58
	120	$Y = 1.615 \times 10^{-6}X + 4.747 \times 10^{-3}$	0.9993	3.13 ± 0.07	101.91 ± 2.30
	150	$Y = 1.604 \times 10^{-6}X + 7.508 \times 10^{-4}$	0.9999	3.05 ± 0.10	99.17 ± 2.84
Temperature of combustion tube (°C)	1120	$Y = 1.605 \times 10^{-6}X + 8.215 \times 10^{-4}$	0.9997	3.13 ± 0.06	102.01 ± 1.85
	1150	$Y = 1.615 \times 10^{-6}X + 4.747 \times 10^{-3}$	0.9993	3.13 ± 0.07	101.91 ± 2.30
	1180	$Y = 1.586 \times 10^{-6}X + 1.126 \times 10^{-3}$	0.9985	3.03 ± 0.03	98.68 ± 1.14
Temperature of reduction tube (°C)	850	$Y = 1.621 \times 10^{-6}X + 9.226 \times 10^{-5}$	0.9997	3.12 ± 0.06	102.01 ± 1.75
	900	$Y = 1.615 \times 10^{-6}X + 4.747 \times 10^{-3}$	0.9993	3.13 ± 0.07	101.91 ± 2.30
	950	$Y = 1.649 \times 10^{-6}X - 1.288 \times 10^{-3}$	0.9996	3.00 ± 0.02	97.97 ± 0.87

[1] Standard curves were constructed by the coal concentration range of 1.01 to 3.49 mg.
[2] Data are expressed as average $\pm$ SD, $n = 3$.
[3] Recovery yield (%) = Sulfur(mg)$_{exp}$/Sulfur(mg)$_{nominal}$ $\times$ 100%.

In this investigation, background peak area of sulfur is attributed to the sample moisture and usage of EA tubes such as Sicapent tube, combustion tube, and reduction tube. Although the background peak area of sulfur is variable, the proposed method has sufficient selectivity (resolution) to the sulfur determination.

The system suitability can be simply assessed by background peak areas of tin blanks and Kit blanks. Background of coal standard and ECD Kit can be deducted by tin and Kit blanks, respectively. Although samples of multiple batches can be assayed within one single day, background peak area of each batch should be determined separately. Each analytical batch should consist of tin blanks, Kit blanks, coal QC samples, calibration coal standards, and unknown samples.

Coal standards are grounded and dried under 110~120°C for at least 2 hours before determination and prepared for the standards curve freshly.

The number of QC samples (in multiples of three) depends on the total number of samples in a batch. Table S3 demonstrates that triplicate QC samples analyses are necessary to ensure quality of the assay for a batch within 10–20 samples. Acceptance criterion is suggested to set at least 67% (2 out of 3) of QC samples, which should be within ±5% of their respective nominal value, and 33% of the QC samples may be outside ±5% of nominal value.

Nominal content of ECD in each ECD Kit vial is 0.900 ± 0.135 mg/vial, which is equal to the weight of sulfur in the range of 0.033–0.104 mg/vial. Therefore, one-third to half of content of ECD Kit was suggested to sample for EA analysis.

The observation of three-day stability study of ECD Kit in Table 4 (recovery yields of QC_{ECD} increased gradually) is difficult to explain, but it might be related to the degradation of ECD in ECD Kit due to the moisture. For example, an intermolecular sulfur-sulfur bonding compound was found in our preliminary forced degradation study.

In Table 5, the results of method robustness evaluation further support the optimal conditions of Table 1. Additionally, the results of method validation in Tables 3, 4, and 5 indicate the potential of this method in pharmaceutical QC.

However, this method is limited to QC analysis of "fresh prepared" ECD Kit, where purity of ECD should be determined prior to mass fabrication processes. Based on the test specification in practice guidelines of the American College of Radiology (ACR) and the European Association of Nuclear Medicine Neuroimaging Committee (ENC), the radiochemical purity (RCP) determinations of Tc-99m-ECD should be performed on each vial prior to injection and can also be used to verify the quality of ECD Kit [1, 2].

5. Conclusion

Since the composition of ECD Kit may cause degradation of ECD as soon as it is dissolved in (non)aqueous solutions, the best way to adopt for the quantitation is highly restricted to

a method of direct solid samples analysis. This investigation provides a method for the intended purpose, for example, routine QC of chemical manufacturing. ECD is one of the diamino dithiol (DADT) derivatives to form stable complexes with radiorhenium or radiotechnetium. Therefore, this method can be also a useful tool to investigate the QC quantitation and properties of thiol-contained derivatives. Finally, this research not only enhances our understanding of ECD Kit about its stability but also raises some questions that require further investigation, especially the degradation pathways, degradation compounds of ECD in ECD Kit and a more stable ECD Kit, formulation design.

Acknowledgments

References

[1] The American College of Radiology, *ACR Practice Guideline for the Performance of Single-Photon Emission Computed Tomography (SPECT) Brain Perfusion Imaging*, The American College of Radiology, 2002.

[2] Ö. L. Kapucu, F. Nobili, A. Varrone et al., "EANM procedure guideline for brain perfusion SPECT using 99mTc-labelled radiopharmaceuticals, version 2," *European Journal of Nuclear Medicine and Molecular Imaging*, vol. 36, no. 12, pp. 2093–2102, 2009.

[3] B. Borroni, D. Anchisi, B. Paghera et al., "Combined Tc-ECD SPECT and neuropsychological studies in MCI for the assessment of conversion to AD," *Neurobiology of Aging*, vol. 27, no. 1, pp. 24–31, 2006.

[4] A. Caroli, C. Geroldi, F. Nobili et al., "Functional compensation in incipient Alzheimer's disease," *Neurobiology of Aging*, vol. 31, no. 3, pp. 387–397, 2010.

[5] J. P. Wielepp, J. M. Burgunder, T. Pohle, E. P. Ritter, J. A. Kinser, and J. K. Krauss, "Deactivation of thalamocortical activity is responsible for suppression of parkinsonian tremor by thalamic stimulation: a Tc-ECD SPECT study," *Clinical Neurology and Neurosurgery*, vol. 103, no. 4, pp. 228–231, 2001.

[6] F. V. Schraml, L. L. Beason-Held, D. W. Fletcher, and B. P. Brown, "Cerebral accumulation of Tc-99m ethyl cysteinate dimer (ECD) in severe, transient hypothyroidism," *Journal of Cerebral Blood Flow and Metabolism*, vol. 26, no. 3, pp. 321–329, 2006.

[7] M. Bauer, D. H. S. Silverman, F. Schlagenhauf et al., "Brain glucose metabolism in hypothyroidism: a positron emission tomography study before and after thyroid hormone replacement therapy," *Journal of Clinical Endocrinology and Metabolism*, vol. 94, no. 8, pp. 2922–2929, 2009.

[8] I. Sunada, T. Ishida, S. Sakamoto, and N. Tsuyuguchi, "A discrepancy between Tc-99m HMPAO SPECT and Tc-99m ECD SPECT in Creutzfeldt-Jacob disease," *Journal of Clinical Neuroscience*, vol. 11, no. 6, pp. 648–650, 2004.

[9] R. Ukisu, T. Kushihashi, E. Tanaka et al., "Diffusion-weighted MR imaging of early-stage Creutzfeldt-Jakob disease: typical and atypical manifestations," *Radiographics*, vol. 26, pp. S191–S204, 2006.

[10] R. S. Diler, M. Reyhanli, F. Toros, M. Kibar, and A. Avci, "Tc-99m-ECD SPECT brain imaging in children with Tourette's Syndrome," *Yonsei Medical Journal*, vol. 43, no. 4, pp. 403–410, 2002.

[11] W. Y. Chen, C. Y. Lin, I. C. Chou, F. J. Tsai, and S. S. Sun, "The role of 99mTc-ECD brain SPECT in differentiating Tourrettes syndrome from chronic tic disorder," *Annals of Nuclear Medicine and Sciences*, vol. 16, pp. 59–63, 2003.

[12] S. S. Sun, I. C. Chou, Y. H. Lai, and C. H. Kao, "99mTc-ECD SPECT image in children with Gilles de la Tourette's syndrome: a preliminary report," *Annals of Nuclear Medicine and Sciences*, vol. 14, pp. 149–153, 2001.

[13] C. P. Chang, Y. C. Shiau, J. J. Wang, S. T. Ho, and A. Kao, "Abnormal regional cerebral blood flow on Tc ECD brain SPECT in patients with primary Sjögren's syndrome and normal findings on brain magnetic resonance imaging," *Annals of the Rheumatic Diseases*, vol. 61, no. 9, pp. 774–778, 2002.

[14] R. C. Walovitch, T. C. Hill, S. T. Garrity et al., "Characterization of technetium-99m-L,L-ECD for brain perfusion imaging, Part 1: pharmacology of technetium-99m ECD in nonhuman primates," *Journal of Nuclear Medicine*, vol. 30, no. 11, pp. 1892–1901, 1989.

[15] J. Leveille, G. Demonceau, M. De Roo et al., "Characterization of technetium-99m-L,L-ECD for brain perfusion imaging, Part 2: biodistribution and brain imaging in humans," *Journal of Nuclear Medicine*, vol. 30, no. 11, pp. 1902–1910, 1989.

[16] Bristol-Myers Squibb Medical Imaging, *Neurolite® Kit for the Preparation of Technetium Tc99m Bicisate for Injection*, Bristol-Myers Squibb Medical Imaging, North Billerica, Mass, USA, 2003.

[17] S. Vallabhajosula, R. E. Zimmerman, M. Picard et al., "Technetium-99m ECD: a new brain imaging agent: in vivo kinetics and biodistribution studies in normal human subjects," *Journal of Nuclear Medicine*, vol. 30, no. 5, pp. 599–604, 1989.

[18] I. C. Dormehl, D. W. Oliver, K. J. Langen, N. Hugo, and S. A. Croft, "Technetium-99m-HMPAO, technetium-99m-ECD and iodine-123-IMP cerebral blood flow measurements with pharmacological interventions in primates," *Journal of Nuclear Medicine*, vol. 38, no. 12, pp. 1897–1901, 1997.

[19] I. Y. Hyun, J. S. Lee, J. H. Rha, I. K. Lee, C. K. Ha, and D. S. Lee, "Different uptake of Tc-ECD and Tc-HMPAO in the same brains: analysis by statistical parametric mapping," *European Journal of Nuclear Medicine*, vol. 28, no. 2, pp. 191–197, 2001.

[20] M. R. Jacquier-Sarlin, B. S. Polla, and D. O. Slosman, "Cellular basis of ECD brain retention," *Journal of Nuclear Medicine*, vol. 37, no. 10, pp. 1694–1697, 1996.

[21] H. P. Vanbilloen, B. J. Cleynhens, and A. M. Verbruggen, "Importance of the two ester functions for the brain retention of Tc-labelled ethylene dicysteine diethyl ester (Tc-ECD)," *Nuclear Medicine and Biology*, vol. 25, no. 6, pp. 569–575, 1998.

[22] L. G. Flores, S. Jinnouchi, S. Nagamachi et al., "Retention of Tc-99m ECD in delayed SPECT of the brain," *Annals of Nuclear Medicine*, vol. 13, no. 1, pp. 1–4, 1999.

[23] C. Tsopelas and D. Smyth, "Characterization and quality control analysis of ^{99m}Tc-bicisate," *Journal of Nuclear Medicine Technology*, vol. 33, no. 2, pp. 89–93, 2005.

[24] E. Mikiciuk-Olasik and I. Bilichowski, "Determination of L,L-ethylene dicysteine di-ethylester stability by RP HPLC," *Chemia Analityczna*, vol. 45, no. 6, pp. 809–813, 2000.

[25] T. Verduyckt, D. Kieffer, D. Huyghe et al., "Identity confirmation of Tc-MAG3, Tc-Sestamibi and Tc-ECD using radio-LC-MS," *Journal of Pharmaceutical and Biomedical Analysis*, vol. 32, no. 4-5, pp. 669–678, 2003.

[26] G. Gryglewicz and S. Gryglewicz, "Determination of elemental sulfur in coal by gas chromatography—mass spectrometry," *Analytical and Bioanalytical Chemistry*, vol. 370, no. 1, pp. 60–63, 2001.

[27] M. Nečemer, P. Kump, M. Rajčevič, R. Jačimović, B. Budič, and M. Ponikvar, "Determination of sulfur and chlorine in fodder by X-ray fluorescence spectral analysis and comparison with other analytical methods," *Spectrochimica Acta—Part B*, vol. 58, no. 7, pp. 1367–1373, 2003.

[28] M. Z. Duz, A. Saydut, S. Erdogan, and C. Hamamci, "Removal of sulfur and ash from coal using molten caustic leaching, a case study from Hazro fields,Turkey," *Energy Exploration and Exploitation*, vol. 27, no. 6, pp. 391–400, 2009.

[29] H. D. Fiedler, R. Rubio, G. Rauret, and I. Casals, "Acid volatile sulfide determination in sediments using elemental analyzer with thermal conductivity detector," *Talanta*, vol. 48, no. 2, pp. 403–407, 1999.

[30] H. P. Sieper, H. J. Kupka, T. Williams et al., "A measuring system for the fast simultaneous isotope ratio and elemental analysis of carbon, hydrogen, nitrogen and sulfur in food commodities and other biological material," *Rapid Communications in Mass Spectrometry*, vol. 20, no. 17, pp. 2521–2527, 2006.

[31] N. F. Shimp, J. K. Kuhn, and R. J. Helfinstine, "Determination of forms of sulfur in coal," *Energy Sources*, vol. 3, no. 2, pp. 93–109, 1977.

[32] J. H. Bullock Jr., J. D. Cathcart, and W. J. Betterton, "Analytical methods utilized by the United States geological survey for the analysis of coal and coal combustion by-products," U.S. Department of the Interior, U.S. Geological Survey, 2002.

[33] M. A. Belarra, M. Resano, F. Vanhaecke, and L. Moens, "Direct solid sampling with electrothermal vaporization/atomization: what for and how?" *TrAC: Trends in Analytical Chemistry*, vol. 21, no. 12, pp. 828–839, 2002.

[34] D. Günther and B. Hattendorf, "Solid sample analysis using laser ablation inductively coupled plasma mass spectrometry," *TrAC: Trends in Analytical Chemistry*, vol. 24, no. 3, pp. 255–265, 2005.

Research Article

In Vitro Study on Apoptosis Induced by Strontium-89 in Human Breast Carcinoma Cell Line

Cheng Wang,[1, 2] Jing Wang,[1] Han Jiang,[1] Min Zhu,[2] Baoguo Chen,[2] and Weiguang Bao[2]

[1] *Department of Nuclear Medicine, Second Affiliated Hospital of Zhejiang University School of Medicine,*
  Hangzhou, Zhejiang 310009, China
[2] *Department of Nuclear Medicine, Taizhou Hospital, Taizhou, Zhejiang 317000, China*

Correspondence should be addressed to Jing Wang, wangjingisme@gmail.com

Received 30 December 2010; Revised 24 March 2011; Accepted 25 March 2011

Academic Editor: Zhen Cheng

Many radiopharmaceuticals used for medical diagnosis and therapy are beta emitters; however, the mechanism of the cell death caused by beta-irradiation is not well understood. The objective of this study was to investigate the apoptosis of human breast carcinoma MCF-7 cell lines induced by Strontium-89 (^{89}Sr) and its regulation and control mechanism. High-metastatic Breast Carcinoma MCF-7 cells were cultured in vitro using ^{89}Sr with different radioactive concentration. The inhibition rate of cell proliferation was measured by MTT color matching method. The cell cycle retardation, apoptosis conditions, mitochondrion transmembrane potential difference and Fas expression were tested and analyzed. The genes P53 and bcl-2 expressions was also analyzed using immunity histochemical analysis. After being induced by ^{89}Sr with various of radioactive concentration, it was found that the inhibition of cell proliferation of MCF-7 cells was obviously, the retardation of cell cycle occurred mainly in G2-M. It was also found that the obvious apoptosis occurred after being induced by ^{89}Sr, the highest apoptosis rate reached 46.28%. The expressions of Fas acceptor and P53 gene increased, while bcl-2 gene expression decreasesd. These findings demonstrate that in the ranges of a certain radioactive concentration, the inhibition rate of MCF-7 cell proliferation and retardation of cell cycle had positive correlation with the concentration of ^{89}Sr. And the mitochondrion transmembrane potential decrease would induce the apoptosis of MCF-7 cell notably, which were controlled by P53 and bcl-2 genes, involved with the Fas acceptor.

1. Introduction

Cancer is a major public health problem in the United States and other countries. Currently, one in four deaths in the United States is due to cancer [1]. Among the major therapy approaches, ionizing radiation is used as a widespread therapeutic modality for cancer treatment. Currently, one of the challenges in radiobiology and oncology is to understand how the cells respond to oxidative stress resulting from exposure to radiation, whether they will die by an apoptotic process or will survive and proliferate. From the point of view of neontology, DNA and cell membrane are the targets of ionization radiation therapy, which gives rise to a series of biochemical and physiological changes of cells, and then induce the inhibition of cell proliferation and retardation of cell cycle, even apoptosis and necrosis. The therapeutic change has relation to the sensitivity, time phase of cell cycle, absorbed radiation dose, and the type of ray [2–4].

It is well known that cell exposure to radiation results in direct and indirect DNA damage, and the extent of damage will depend on the type of radiation and the dose applied, as well as other factors. The higher the ionization density, that is, the higher the radiation linear energy transfer (LET), the greater the complexity of the lesions, and, therefore, repair of the induced lesions is more difficult. When activated by gamma irradiation, p53 induce apoptosis pathways by its positive transcriptional activity on proapoptotic molecules [5]. DNA damage and p53 activation may be initial events in gamma-irradiation-induced apoptosis [5]. In addition, mitochondria-directed apoptotic stimuli induce a variety of mitochondrial changes, including production of oxygen radicals and the opening of membrane pores. This leads to the release of apoptogenic factors such as cytochrome c, apoptosis-inducing factor (AIF). The status of cell proliferation and cell cycle are also thought to be important factors to radiation-induced apoptosis [6]. Radiation-induced cell

cycle arrest at the G1 and G2 restriction points allows cells to repair DNA damage before cells proceed with DNA synthesis and cell division. It is known that irradiated non-small-cell lung cancer (NSCLC) cell lines with wild-type p53 pass beyond the G1 and G2 blocks with delayed and markedly lower probability than cell lines with inactive p53. As a result, the fraction of late post-G2 apoptosis, induced in NSCLC cell lines with intact p53, was lower than in cell lines with functionally inactive p53 [7].

Studying the effects of β radiation at the cellular level is of particular interest for direct application in nuclear medicine. Many radiopharmaceuticals used for diagnosis and therapy are β emitters (e.g., ^{153}Sm-EDTMP, Na^{131}I, ^{186}Re-HEDP, and ^{89}SrCl), which showed promising therapeutic results. However, the mechanism by which cell death is caused by β irradiation is not well understood. ^{89}Sr therapy has the best effect on breast carcinoma and prostate carcinoma; breast carcinoma MCF-7 is a high metastatic cell type, so we choose MCF-7 as the model. In this study, we investigated the mechanism for apoptosis in response to ^{89}Sr, one of the significant and effective β radiation emitting therapeutic radioisotopes, in breast carcinoma MCF-7 cells.

2. Materials and Methods

2.1. Cell Culture. Human breast carcinoma MCF-7 cells were grown in RPMI 1640, containing 10% fetal calf serum. Cells were incubated in a 37°C incubator with 95% air, 5% CO$_2$, and 100% humidity. Fresh medium was supplemented every 2 days. Passaging was carried out every 3-4 days and consisted of a gentle mechanical dissociation using a polished Pasteur pipette. The cells in the logarithmic growth phase are adopted in all the experiments.

2.2. Inhibition of Cell Proliferation by ^{89}Sr. The equilibrium dose constant for ^{89}Sr is $9.32 \times 10^{-14}\,\mathrm{Gy\,kg\,Bq^{-1}\,s^{-1}}$ ($1.24\,\mathrm{g\,rad\,\mu Ci^{-1}\,h^{-1}}$). The mean emitted energy of the β-particle from ^{89}Sr is 0.583 MeV ($E_{\max} = 1.492\,\mathrm{MeV}$). ^{89}Sr solution was purchased from Shanghai Anshen Kexing Corporation as a kind of leuco transparent liquid, pH value = 8.0, radiochemical purity >98%, radioactive specific activity = $3.7 \times 10^7\,\mathrm{Bq/mL}$. MCF-7 cell solution was adjusted as 1×10^5/mL. Every orifice inoculated 100 μL MCF-7 cell solution on the 96-orifice cell culture plate, applied with ^{89}Sr solution in different concentrations of 37 Bq/mL, 74 Bq/mL, 148 Bq/mL, 296 Bq/mL, 592 Bq/mL, 1184 Bq/mL, 2368 Bq/mL, and 4736 Bq/mL. Every group has 3 duplicate orifices as control orifice of normal cells. MCF-7 cells were incubated with ^{89}Sr at 37°C with 95% air, 5% CO$_2$, and 100% humidity for 24 h. At the time of 4 hours before the culturing finished, 10 μL MTT (5 mg/mL) was added to every orifice, continued to incubate 4 hours, and then carried through level centrifugal cleaning culturing plate. 150 μL DMSO was added to each orifice and fully blended, and then absorbance was determined using a spectrophotometer at 570 nm absorbance.

2.3. Determination of Cell Cycle Phase. Cells at different stages of the cell cycle can be distinguished by their DNA content. Experimentally, cellular DNA content can be determined by incubation with a fluorescent dye (propidium iodide) that binds to DNA, followed by analysis in fluorescence-activated cell sorter (FACS). In this study, collected MCF-7 cells were added 70% ethanol, kept steady for 24 hours at −20°C, and washed twice by PBS, adjusted cells solution to be 1×10^6/mL. Then 100 μL of cell suspension was added to test tube with 200 μL PI, reacted at 4°C, no light, for 30 minutes, then tested by using a flow cytometer (FACScan, Becton Dickinson) and analyzed the results. The Cycletest Plus DNA Reagent Kit (BD Corporation) was used in detecting the distribution of cells within the different phases of cell cycle.

2.4. Measurement of Cell Apoptosis. 1×10^5/mL MCF-7 cells were moved to 6 orifices, then ^{89}Sr solution in different concentrations of 37 Bq/mL, 74 Bq/mL, 148 Bq/mL, 296 Bq/mL, 592 Bq/mL, 1184 Bq/mL, 2368 Bq/mL, 4736 Bq/mL, 185 kBq/mL, 370 kBq/mL, 740 kBq/mL, 1480 kBq/mL, 2960 kBq/mL, 3330 kBq/mL, 6660 kBq/mL, and 13320 kBq/mL, respectively, and incubated at 37°C, 5% CO$_2$ for 24 hours. After twice centrifugal washing of the cells with precooling PBS, the cells were resuspended in 100 μL of PBS and then were added 5 μL AnnexinV^{FITC} (Bender MedSystems Corporation) solution and fully blended. Then the cells were tested using flow cytometer soon after 15-minute reaction at 4°C without light and adding 10 μL PI. This measurement was repeated for the 3330 kBq/mL group at time points of 36 h, 48 h, and 72 h.

2.5. Measurement of Mitochondrial Membrane Potential. Mitochondrial membrane potential, $\Delta\Psi m$, is an important parameter of mitochondrial function used as an indicator of cell health. To evaluate $\Delta\Psi m$, MCF-7 cells were incubated with ^{89}Sr with the above concentration for 24 hours, then treated with Rh123C and followed by analysis on a flow cytometer (FACScan, Becton Dickinson).

2.6. Fas Detection. The cell surface Fas (CD95/APO-1) is a 45 kD type I membrane protein, and Fas ligand (FasL) is a 37 to 40 kD type II membrane protein that belongs to the tumor necrosis factor (TNF) receptor and ligand families [8]. Activation of Fas by crosslinking with agonistic antibodies or by binding with FasL resulted in apoptotic cell death in susceptible cells [9]. The three MCF-7 cell groups were incubated separately with 3330 kBq/mL, 6660 kBq/mL, and 13320 kBq/mL for 24 hours, then collected cells and suspended in PBS and adjusted cells concentration as 1×10^6/mL. The 100 μL of cells suspension was incubated in two tubes, one with 20 μL mouse IgG fluorescein isothiocyanate (FITC) used as homotype reference, and another tube with 20 μL Fas FITC was incubated at 4°C without light for 15 minutes. The cells were analyzed for surface Fas expression by flow cytometer.

2.7. DNA Gel Electrophoresis. DNA damage and cell apoptosis were detected by DNA gel electrophoresis. DNA of MCF-7 cells were extracted after being induced by ^{89}Sr at different

concentrations as shown previously for 24 hours. After air drying, cells were conserved in the TE buffer solution. DNA sample was taken out and electrophoresed in 1.2% agarose gel with 100 V for 30 to 60 minutes and detected by pigment EB staining. The DNA samples were investigated by ultraviolet spectrometry and then imaged.

2.8. Immunohistochemical Analysis. The cell coverslips were incubated with 100 uL rabbit anti-Bcl-2 and rabbit anti-P53 over night at 4°C. After rinsing with tris-buffered saline (TBS) for five times, 5 min each rinse, the coverslips were incubated in rabbit antimouse secondary antibodies for 30 min at 37°C. The coverslips were subsequently rinsed with TBS for five times, 5 min each rinse and then added 100 uL DAB solution to each coverslip and incubated coverslips for 1 minute at room temperature.

2.9. Estimation of the Cell Integral Absorbed Dose by ^{89}Sr. The estimation of the cell integral absorbed dose by ^{89}Sr was calculated based on the following formula [4]: $D = AE/m$, where D is absorbed dose, A the radioactive activity of ^{89}Sr internal radiation (unit: kBq), E the average energy of ^{89}Sr ray, and m the mass of the irradiated cell.

2.10. Statistical Analysis. All data are calculated as percentage. X^2 verification is adopted between groups.

3. Results

3.1. MCF-7 Cell Integral Absorbed Dose by ^{89}Sr Internal Radiation. After being induced by ^{89}Sr with various radioactive concentrations (37 Bq/mL, 74 Bq/mL, 148 Bq/mL, 296 Bq/mL, 592 Bq/mL, 1184 Bq/mL, 2368 Bq/mL, 4736 Bq/mL, 185 kBq/mL, 370 kBq/mL, 740 kBq/mL, 1480 kBq/mL, 2960 kBq/mL, 3330 kBq/mL, 6660 kBq/mL, and 13320 kBq/mL), the accumulative absorbed doses are measured as 0.025 mGy, 0.05 mGy, 0.1 mGy, 0.2 mGy, 0.4 mGy, 0.8 mGy, 1.6 mGy, 3.2 mGy, 0.125 Gy, 0.25 Gy, 0.5 Gy, 1 Gy, 2 Gy, 2.25 Gy, 4.5 Gy, and 9 Gy, respectively. If induced by ^{89}Sr with the radioactive concentration of 3330 kBq/mL for 36 hours, 48 hours, and 72 hours, the accumulative absorbed doses are 3.38 Gy, 4.5 Gy, and 6.76 Gy, respectively.

3.2. MCF-7 Cellular Morphological Change and Cell Proliferation Inhibition. After being induced by ^{89}Sr with various radioactive concentrations (74 Bq/mL, 148 Bq/mL, 296 Bq/mL, 592 Bq/mL, 1184 Bq/mL, 2368 Bq/mL, and 4736 Bq/mL) and cultured for 24 hours, the numbers of MCF-7 cells obviously decreased and cellular morphological change occurred obviously, the outline shrank, and the function of adhering to the cell wall layer was found to be obviously weakened compared with the control group (Figure 1).

No obvious inhibition was found at 37 Bq/mL. With the increase of the concentration (exceeding 74 Bq/mL), the proliferation inhibition rate obviously rose, showed a positive correlation with the concentration (Figure 2, $P < .05$).

3.3. MCF-7 Cell Cycle Retardation. After being induced by ^{89}Sr with various radioactive concentrations (185 kBq/mL,
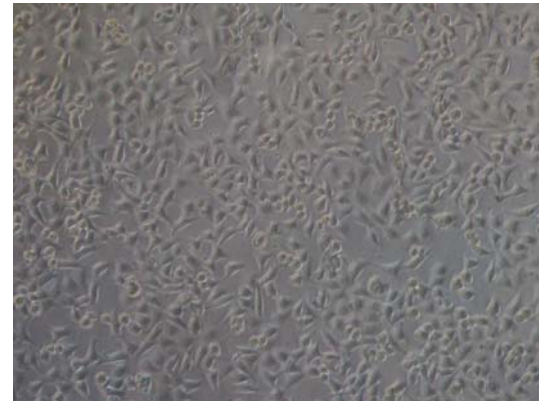
(a)
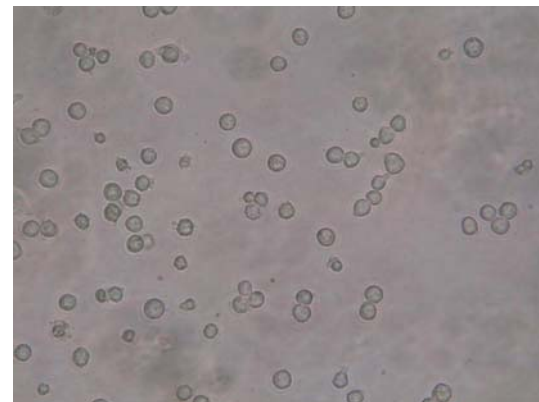
(b)

FIGURE 1: Digital photo before (a) and after (b) being induced by ^{89}Sr (3330 kBq/mL) (microscopically).
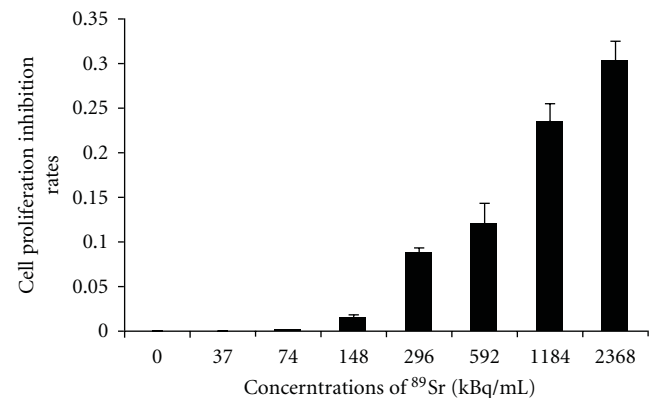

FIGURE 2: MCF-7 cell proliferation inhibition rate due to being induced by ^{89}Sr of various concentrations.

370 kBq/mL, 740 kBq/mL, 1480 kBq/mL, 2960 kBq/mL, 3330 kBq/mL, 6660 kBq/mL, and 13320 kBq/mL) and cultured for 24 hours, the retardation appeared obvious. The retardation became significant when the concentration increased. The retardation was mainly found in the cycle G2-M at the concentration less than 6660 kBq/mL, reached the
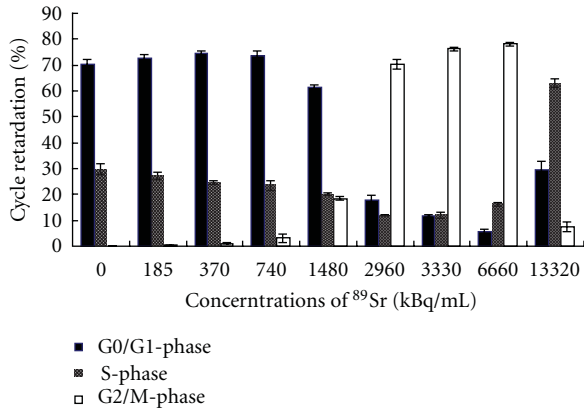
FIGURE 3: MCF-7 cell cycle retardation due to being induced by ^{89}Sr of various radioactive concentrations.
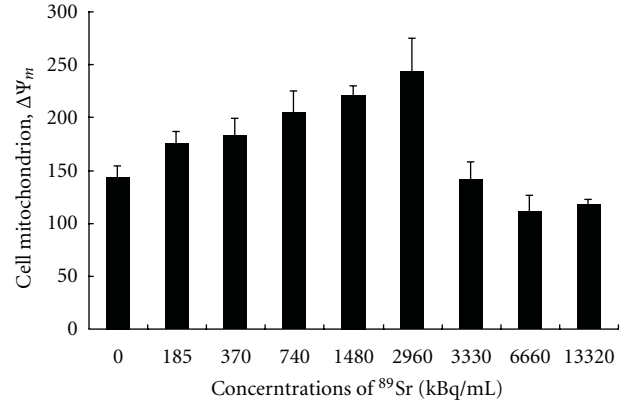

FIGURE 6: The mitochondrion $\Delta\Psi m$ of MCF-7 cell apoptosis due to being induced by ^{89}Sr of various radioactive concentrations.
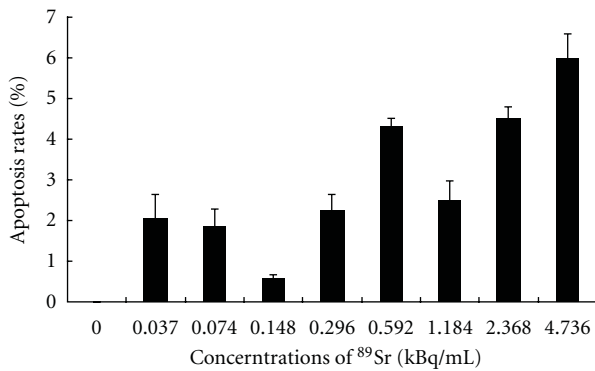

FIGURE 4: Percentage of MCF-7 cell apoptosis due to being induced by ^{89}Sr of various radioactive concentrations.
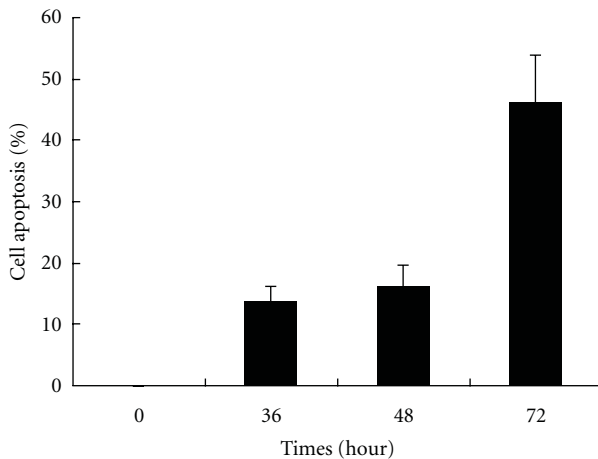

FIGURE 7: The Fas expression of MCF-7 cell due to being induced by ^{89}Sr of various concentrations.

FIGURE 5: Cell apoptosis of 4 groups of the experimental group 3330 kBq/mL.

3.4. MCF-7 Cell Apoptosis. Again after being induced by ^{89}Sr with the same radioactive concentrations and cultured for 24 hours, all the rates of cell apoptosis were lower than 10% (Figure 4). There were no obvious differences in all the groups ($P > .05$). The DNA electrophoresis analysis in each group found no typical "ladder diagram" band distribution.

According to our previous study, the experimental group 3330 kBq/mL was divided into 4 groups: 36 h, 48 h, 72 h, and 96 h. With the time passing, the numbers of cell apoptosis increased obviously, reached the peak at 46.28% at 72 h, and had a dosage-dependency relationship. However, most of cells died after 96 hours (Figure 5).

3.5. The Variation of MCF-7 Cell Mitochondrion $\Delta\Psi m$. After being induced by ^{89}Sr of radioactive concentrations and cultured for 24 hours, the cell mitochondrion $\Delta\Psi m$ did not decrease obviously but increased slightly when the concentration was lower than 3330 kBq/mL. When the concentration was above 3330 kBq/mL, the cell mitochondrion $\Delta\Psi m$ decreased obviously (Figure 6).

peak at 78.09%. When the concentration was more than 13320 kBq/mL, the retardation in the cycle G2-M decreased obviously, but the retardation in the cycle S became obvious, reached the peak at 62.97% (Figure 3).
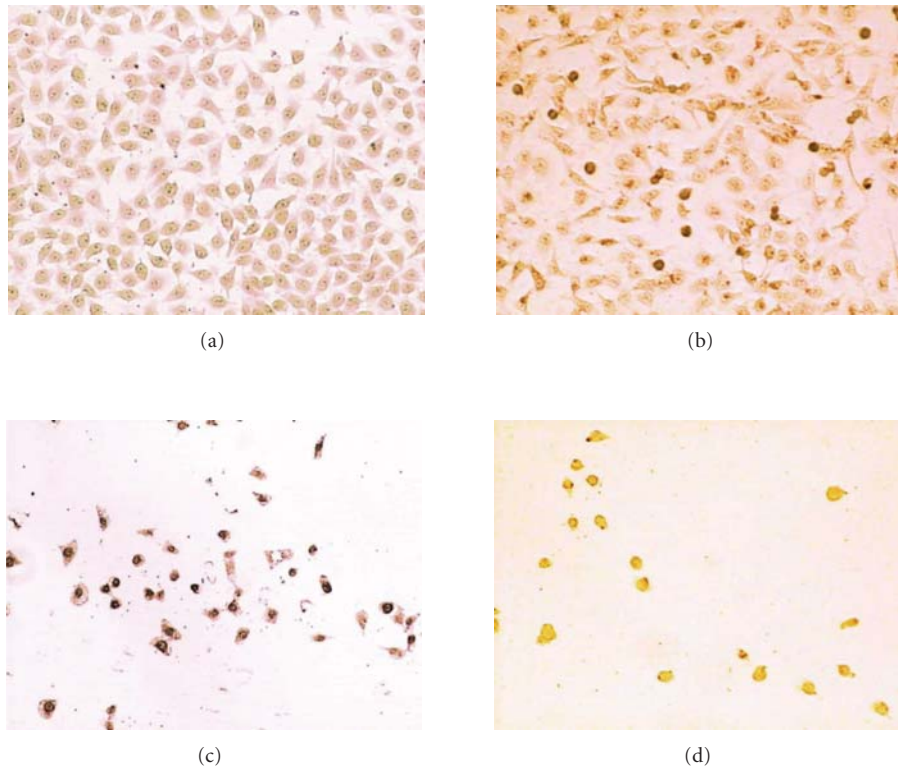
(a)

(b)

(c)

(d)

FIGURE 8: (a) P53 coloration before being induced; (b) bcl-2 coloration before being induced; (c) P53 coloration after being induced; (d) bcl-2 coloration after being induced.

3.6. The Fas Expression of MCF-7 Cell. Based on the pretest, induced MCF-7 cells in all the 3 experimental groups (3330 kBq/mL, 6660 kBq/mL, and 13320 kBq/mL) for 24 hours, their Fas receptor expressions were obviously higher than their respective control groups (Figure 7).

3.7. Immunohistochemical Analysis. For the control group, the positive rate of P53 expression was 95%, but the coloration generally weakened, weakly positive. While the positive rate of bcl-2 expression was 91%, the coloration deepened.

For the experimental group 3330 kBq/mL, after being induced for different periods, the positive rate of P53 expression was 97%, but the coloration was obviously darker than the control group. While the positive rate of bcl-2 expression was 88%, the coloration generally weakened, especially in the group 72 h (Figure 8).

4. Discussion

^{89}Sr is a short-lived artificial radioisotope with a half-life of 50.5 days, which has very high energy (8 mm penetration). ^{89}Sr is used for the medical treatment of high metastatic bone tumor. Due to its simple treatment method and good curative effect, it has been found in widespread application [5, 6], but the unsatisfactory curative effect on some patients occurred due to their tumor cell resistance to the radiation. ^{89}Sr treatment mechanism primarily is to inhibit the growth of the tumor cells or to kill them by radiation damage. The previous studies on the radiation damage were mainly focused on the external radiation, especially X-ray or γ-ray, and few reports focus on the internal radiation of β-ray remitted by radionuclide. Because the internal radiation has the characteristics, selectivity of action spot and durability of acting time, it is very important to study the mechanism and contributing factors of the radiation damage by internal radiant of radionuclide.

The research findings showed that MCF-7 cells were induced by ^{89}Sr and irradiated by β-ray for 24 hours, the inhibition of cell proliferation was obvious, and had a positive correlation with the concentration of ^{89}Sr. When the concentration reached 1480 kBq/mL and the cell absorbed dose reached 1 Gy, the cell cycle retardation appeared obviously; this is mainly manifested in G2-M the cells in the cycle retardation time phase and other time phases had a proportional relation with the accumulative absorbed dose. In 1968, it is reported that the cell cycle G1 retardation was induced by X-ray. There were also many studies which reported that the tumor cell cycle retardation was induced by γ-ray radiation, and most of people thought that the tumor cell cycle G2-M retardation was induced by γ-ray radiation [7, 8]. Such case was also found when MCF-7 tumor cells were induced by ^{89}Sr and irradiated by β-ray. In the experimental group 13320 kBq/mL, the accumulative absorbed dose reached 9 Gy, mass mortality of cell was found, and the cycle S retardation of the residual cells was obvious.

The patterns of MCF-7 cell death induced by ^{89}Sr were apoptosis and necrosis, and they coexisted. When the radioactive concentration was lower than 2960 kBq/mL and the cell accumulative absorbed dose was less than 2 Gy, although the inhibition of cell proliferation and cycle retardation were obvious, the cell apoptosis was not obvious and was independent of the time of irradiation. When the radioactive concentration reached 3330 kBq/mL, after being cultured for 72 hours, the cell accumulative absorbed dose reached 6.76 Gy, and the percentage of cell apoptosis increased obviously, reached the peak at 46.28%, and had correlation with irradiation time. When the radioactive concentration reached 13320 kBq/mL, the cell accumulative absorbed dose exceeded 9 Gy, the percentage of cell necrosis increased obviously, and even total necrosis, and there were little apoptosis. That is because the cell apoptosis is an active process that needs gene expression and protein synthesis, when the radiation dose exceeds 9 Gy which is sufficient for destroying genetic transcription or directly destroying the integrality of membrane, it makes the cell unable to support the ion gradient inside and outside of cell, thus will make the loop of cell apoptosis unable to be initiated. When the accumulative absorbed dose falls in a certain range, both apoptosis and necrosis exist, and the ratio of necrosis to apoptosis is related to irradiation time and dose effect. The apoptosis rate as the function of the dose of ^{89}Sr was not significant, that is because the apoptosis rate is related to irradiation time, dose, and some other factors. For the accumulative absorbed dose 4.5 Gy, apoptosis was few when the cell was induced by the radioactive concentration at 6660 kBq/mL for 24 hours, while apoptosis increased obviously when the cell was induced by the radioactive concentration at 3330 kBq/mL for 48 hours. It is explained that if the cell absorbed the same dose in a short or long period, the pattern of cell death is different. It is because DNA damage caused by high dose once in a short period was more serious than that caused by low dose for many times; the cell was unable to heal caused by high dose once. The above manifestation, basically, is the same as the changes of cells irradiated externally. But some research findings showed that, if the same dose was adopted, the proportion of cell apoptosis induced by γ-ray is higher than that induced by β-ray; similarly, the loop was initiated earlier [4].

The radiation-induced inhibition of proliferation did not appear to be related to apoptosis, but rather to delayed progression through the cell cycle [6].

In the process of MCF-7 cell apoptosis induced by ^{89}Sr, there are many genes involved in regulation and expression. Among them, gene P53 and bcl-2 play an active role. The gene P53, as a transcription, combines and involves in genetic regulation, plays an important role in the cell apoptosis induced by the radiation or other factors [9–11]. The gene bcl-2 can inhibit the cell apoptosis induced by many factors, including ionizing radiation, over oxidation of plasma membrane, and lack of blood serum and growth factor [12–14]. In the experimental group with obvious apoptosis in this research, the coloration of cell karyon deepened obviously, p53 expression was reinforced, and the coloration of cell cytoplasm weakened obviously, bcl-2 expression was depressed. It shows that the cell apoptosis induced by β-ray radiation was initiated by the high expression of p53 and is depressed by bcl-2 expression.

In the process of MCF-7 cell apoptosis induced by ^{89}Sr, Fas and plastosome are also involved in regulation and expression. It is proved that Fas plays an important role in the process of cell apoptosis induced by radiation damage and other DNA damage [15–17]. In the experimental group with obvious apoptosis in this research, Fas expression is higher than that of the control group. It shows that Fas expression is also involved in the signal transmission of apoptosis in the process of cell apoptosis induced by β-ray radiation. There are probably two ways of Fas expression mediates the signal transmission of the next level: through the actions of cystic death domain (DD) and cystic connector proteins, Fas initiates the caspase-8 and leads to the cell apoptosis; Fas plays a role in inducing the cell apoptosis through the ceramide, as second messenger [18]. Similarly, in the experimental group with obvious apoptosis, the plastosome $\Delta\Psi m$ decreased obviously, comparing with any other group, which shows that the plastosome is also involved in the cell apoptosis induced by β-ray radiation. The probable mechanism is that the plastosome initiates the caspases through releasing Cyt c, plays an important controlling role [19]. In some other cancer cells, apoptosis induced by ^{89}Sr is regulated by decreasing the bcl-2 expression protein, thus decreasing bcl-2/bax [20].

In short, after being irradiated by β-rays, the inhibition of MCF-7 cell proliferation and its rate in various periods are changing with the amount of radiation dose. If the accumulative absorbed dose falls in a certain range, β-ray can induce the cell apoptosis and also the cell necrosis, and there is a dose-effect curve. Many genes are involved in regulation and expression in the process of cell apoptosis, and the signal transmission and regulation are very intricate. It is very important to the tumor radiotherapy in the further research.

References

[1] A. Jemal, R. Siegel, E. Ward, T. Murray, J. Xu, and M. J. Thun, "Cancer statistics, 2007," *Ca-A Cancer Journal for Clinicians*, vol. 57, no. 1, pp. 43–66, 2007.

[2] M. Bralic, M. Muhvic-Urek, V. Stemberga et al., "Cell death and cell proliferation in mouse submandibular gland during early post-irradiation phase," *Acta Medica Okayama*, vol. 59, no. 4, pp. 153–159, 2005.

[3] C. Fournier and G. Taucher-Scholz, "Radiation induced cell cycle arrest: an overview of specific effects following high-LET exposure," *Radiotherapy and Oncology*, vol. 73, no. 2, pp. S119–S122, 2004.

[4] C. Friesen, A. Lubatschofski, J. Kotzerke, I. Buchmann, S. N. Reske, and K. M. Debatin, "Beta-irradiation used for systemic radioimmunotherapy induces apoptosis and activates apoptosis pathways in leukaemia cells," *European Journal of Nuclear Medicine and Molecular Imaging*, vol. 30, no. 9, pp. 1251–1261, 2003.

[5] J. Milner, "DNA damage, p53 and anticancer therapies," *Nature Medicine*, vol. 1, no. 9, pp. 879–880, 1995.

[6] N. A. Scott, I. R. Crocker, Q. Yin, D. Sorescu, J. N. Wilcox, and K. K. Griendling, "Inhibition of vascular cell growth

by X-ray irradiation: comparison with gamma radiation and mechanism of action," *International Journal of Radiation Oncology Biology Physics*, vol. 50, no. 2, pp. 485–493, 2001.

[7] A. Sak, R. Wurm, B. Elo et al., "Increased radiation-induced apoptosis and altered cell cycle progression of human lung cancer cell lines by antisense oligodeoxynucleotides targeting p53 and p21$^{WAF1/CIP1}$," *Cancer Gene Therapy*, vol. 10, no. 12, pp. 926–934, 2003.

[8] T. Suda, T. Takahashi, P. Golstein, and S. Nagata, "Molecular cloning and expression of the Fas ligand, a novel member of the tumor necrosis factor family," *Cell*, vol. 75, no. 6, pp. 1169–1178, 1993.

[9] K. Y. Jen and V. G. Cheung, "Identification of novel p53 target genes in ionizing radiation response," *Cancer Research*, vol. 65, no. 17, pp. 7666–7673, 2005.

[10] B. Fischer, S. Benzina, P. Jeannequin et al., "Fast neutrons-induced apoptosis is Fas-independent in lymphoblastoid cells," *Biochemical and Biophysical Research Communications*, vol. 334, no. 2, pp. 533–542, 2005.

[11] K. Viktorsson, L. De Petris, and R. Lewensohn, "The role of p53 in treatment responses of lung cancer," *Biochemical and Biophysical Research Communications*, vol. 331, no. 3, pp. 868–880, 2005.

[12] T. Hara, M. Omura-Minamisawa, C. Chao, Y. Nakagami, M. Ito, and T. Inoue, "Bcl-2 inhibitors potentiate the cytotoxic effects of radiation in Bcl-2 overexpressing radioresistant tumor cells," *International Journal of Radiation Oncology Biology Physics*, vol. 61, no. 2, pp. 517–528, 2005.

[13] J. Wendt, C. von Haefen, P. Hemmati, C. Belka, B. Dörken, and P. T. Daniel, "TRAIL sensitizes for ionizing irradiation-induced apoptosis through an entirely Bax-dependent mitochondrial cell death pathway," *Oncogene*, vol. 24, no. 25, pp. 4052–4064, 2005.

[14] I. M. Ghobrial, T. E. Witzig, and A. A. Adjei, "Targeting apoptosis pathways in cancer therapy," *Ca-A Cancer Journal for Clinicians*, vol. 55, no. 3, pp. 178–194, 2005.

[15] T. Hamasu, O. Inanami, T. Asanuma, and M. Kuwabara, "Enhanced induction of apoptosis by combined treatment of human carcinoma cells with X rays and death receptor agonists," *Journal of Radiation Research*, vol. 46, no. 1, pp. 103–110, 2005.

[16] M. E. Szperka, E. E. Connor, M. J. Paape, J. L. Williams, and D. D. Bannerman, "Characterization of bovine FAS-associated death domain gene," *Animal Genetics*, vol. 36, no. 1, pp. 63–66, 2005.

[17] A. Semont, E. B. Nowak, C. Silva Lages et al., "Involvement of p53 and Fas/CD95 in murine neural progenitor cell response to ionizing irradiation," *Oncogene*, vol. 23, no. 52, pp. 8497–8508, 2004.

[18] S. J. Chmura, E. Nodzenski, M. A. Beckett, D. W. Kufe, J. Quintans, and R. R. Weichselbaum, "Loss of ceramide production confers resistance to radiation-induced apoptosis," *Cancer Research*, vol. 57, no. 7, pp. 1270–1275, 1997.

[19] K. Cain, S. B. Bratton, C. Langlais et al., "Apaf-1 oligomerizes into biologically active ~700-kDa and inactive ~1.4-MDa apoptosome complexes," *The Journal of Biological Chemistry*, vol. 275, no. 9, pp. 6067–6070, 2000.

[20] J. Zhang, C. Hong, and S. Zhu, "The characteristics and mechanism of apoptosis in K562 cells induced by radionuclides strontium-89," *Journal of Radiation Research and Radiation Progressing*, vol. 21, no. 1, pp. 416–418, 2003.

Research Article

Investigation of a Potential Scintigraphic Tracer for Imaging Apoptosis: Radioiodinated Annexin V-Kunitz Protease Inhibitor Fusion Protein

Mei-Hsiu Liao,[1, 2] Tong-Rong Jan,[3] Chao-Chih Chiang,[2] Kuo-Chen Yen,[2] Tse-Zung Liao,[2] Ming-Wei Chen,[2] Chin-Wen Chi,[1, 4] Tze-Chein Wun,[5] Tzu-Chen Yen,[6] and Shiaw-Pyng Wey[6, 7]

[1] *Institute of Pharmacology, School of Medicine, National Yang-Ming University, Taipei 112, Taiwan*

[2] *Division of Isotope Application, Institute of Nuclear Energy Research, Taoyuan 325, Taiwan*

[3] *Department of Veterinary Medicine, National Taiwan University, Taipei 106, Taiwan*

[4] *Department of Medical Research and Education, Taipei Veterans General Hospital, Taipei 112, Taiwan*

[5] *EVAS Therapeutics LLC, 613 Huntley Heights Drive, Ballwin, MO 63021, USA*

[6] *Department of Nuclear Medicine and Molecular Imaging Center, Chang Gung Memorial Hospital and Chang Gung University College of Medicine, 259 Wen-Hwa First Road, Kwei-Shan, Taoyuan 333, Taiwan*

[7] *Department of Medical Imaging and Radiological Sciences, Chang Gung University, Taoyuan 333, Taiwan*

Correspondence should be addressed to Tze-Chein Wun, tcwun@hotmail.com and Shiaw-Pyng Wey, spwey@mail.cgu.edu.tw

Radiolabeled annexin V (ANV) has been widely used for imaging cell apoptosis. Recently, a novel ANV-Kunitz-type protease inhibitor fusion protein, ANV-6L15, was found to be a promising probe for improved apoptosis detection based on its higher affinity to phosphatidylserine (PS) compared to native ANV. The present paper investigates the feasibility of apoptosis detection using radioiodinated ANV-6L15. Native ANV and ANV-6L15 were labeled with iodine-123 and iodine-125 using Iodogen method. The binding between the radioiodinated proteins and erythrocyte ghosts or chemical-induced apoptotic cells was examined. ANV-6L15 can be radioiodinated with high yield (40%−60%) and excellent radiochemical purity (>95%). ^{123}I-ANV-6L15 exhibited a higher binding ratio to erythrocyte ghosts and apoptotic cells compared to ^{123}I-ANV. The biodistribution of ^{123}I-ANV-6L15 in mice was also characterized. ^{123}I-ANV-6L15 was rapidly cleared from the blood. High uptake in the liver and the kidneys may limit the evaluation of apoptosis in abdominal regions. Our data suggest that radiolabled ANV-6L15 may be a better scintigraphic tracer than native ANV for apoptosis detection.

1. Introduction

Apoptosis (programmed cell death) plays an important role in the maintenance of physiological homeostasis as well as in the pathogenesis of a number of disorders including cerebral and myocardial ischemia, autoimmune diseases, and neurodegeneration [1–3]. Apoptosis also plays a crucial role in tumor response to radiation, chemotherapy, and photodynamic therapy (PDT) [4]. The extent and time frame of cancer cell apoptosis induced by anticancer treatments provide crucial clinical information on both the disease status and the therapeutic efficacy.

The plasma membrane phospholipids of mammalian cells are normally asymmetrically distributed, in which the phosphatidylserine (PS) and phosphatidylethanolamine (PE) are segregated to the internal leaflet whereas the phosphatidylcholine (PC) and sphingomyelin (SM) reside on the outer leaflet [5, 6]. Once apoptosis has been initiated, the caspase-mediated signaling cascade of cells is activated. One of the earliest events occurred in apoptotic cells is the externalization of PS to the outer leaflet of the plasma membrane.

Annexin V (ANV), an endogenous human protein with a molecular weight of 35.8 kDa, binds to membrane-bound

PS in a Ca^{2+}-dependent manner with a high affinity ($K_d = 0.5$–7 nM). Since externalization of PS occurs in the early stage of apoptosis, fluorescein- and radionuclide-labeled ANV have been used for detection of apoptosis *in vitro* and under development for *in vivo* imaging as well [3, 7]. However, the physiological concentration of Ca^{2+} is lower than that required for optimal binding of native ANV to PS [8], rendering a suboptimal binding condition for apoptosis detection *in vivo*. In addition, excessive uptake by the liver and the kidney further limits the application of native ANV for *in vivo* apoptosis imaging [9]. In light of these drawbacks of native ANV concerning the *in vivo* detection of apoptosis, the development of derivatives of ANV with an improved binding profile to PS and pharmacokinetic properties has been under intensive investigation recently.

ANV possesses anticoagulant and antithrombotic activity by forming 2-dimensional arrays on anionic membrane surfaces, and thus making the anionic phospholipids unavailable for assembly of coagulation enzyme complexes [10]. In attempts to developing potent thrombogenesis inhibitors, a series of recombinant anticoagulant fusion proteins, consisting of an ANV moiety and a Kunitz protease inhibitor (KPI) domain that binds to various coagulation factors with high affinity and specificity, were reported recently [11]. One of these constructs, ANV-6L15, was found to possess a higher binding affinity to PS compared to native ANV at physiological Ca^{2+} concentrations; the apparent dissociation constant for ANV-6L15 binding to erythrocyte ghosts was approximately 4-fold lower than that of ANV at 1.2–2.5 mM Ca^{2+} [12]. The previous study reveals that ANV-6L15 may provide improved detection of PS exposed on the membrane surfaces of pathological cells *in vitro* and *in vivo*. The present study investigates the use of radioiodinated ANV-6L15 as an imaging agent for apoptosis detection.

2. Materials and Methods

2.1. Materials and Reagents. ^{123}I-NH$_4$I was produced by a compact cyclotron (Ebco TR30/15, Vancouver, Canada) at the Institute of Nuclear Energy Research (INER, Longtan, Taoyuan, Taiwan). ^{125}I-NaI was supplied by IZO-TOP Institute of Isotopes (Budapest, Hungary). Iodogen (1,3,4,6-tetrachloro-3,6-diphenylglycoluril) precoated iodination tubes were purchased from Pierce Biotechnology (Rockford, IL, USA). ANV-6L15 was produced by expression in *Escherichia coli* as described previously [9]. ANV and FITC-ANV apoptosis detection kit were obtained from Becton Dickinson (Franklin Lakes, NJ, USA). Nanosep 10 K Centrifugal Devices were purchased from Pall Life Science (Ann Arbor, MI, USA). Stabilized 5C Cell Control was a generous gift from Beckman Coulter (Fullerton, CA, USA). Camptothecin (CPT) was purchased from Sigma (Cambridge, MA, USA). Acute lymphoblastic cell line of human Jurkat T-cell was obtained from Bioresource Collection and Research Center (Hsinchu, Taiwan). Cell culture materials were obtained from Gibco BRL (Grand Island, NY, USA). All other chemicals were purchased from Merck (Darmstadt, Germany).

2.2. Radioiodination of ANV and ANV-6L15. The Iodogen method [13, 14] was adopted for radiolabeling of ANV and ANV-6L15 with ^{123}I or ^{125}I. Briefly, ten μg of ANV and ANV-6L15 were dissolved in 15 μL of 0.1 M KH$_2$PO$_4$ (pH 8) solution and reacted with radioiodide (370 MBq ^{123}I-NH$_4$I or 185 MBq ^{125}I-NaI) in a tube precoated with 50 μg of Iodogen. After gentle agitation of the tube at room temperature for 10 min, the reaction mixture and the rinse of the tube (with 400 μL 0.01 M KH$_2$PO$_4$ solution, pH 7.4) were loaded on a Nanosep 10 K Centrifugal Device prewashed with 400 μL 0.01 M KH$_2$PO$_4$ solution (pH 7.4). After centrifugation of the Nanosep tube at 15,000×g for 5 min and washing twice with 400 μL 0.01 M KH$_2$PO$_4$ (pH 7.4) solution, the radioiodinated protein on the membrane of Nanosep tube was harvested.

2.3. Radiochemical Analysis by High-Pressure Liquid Chromatography. The radiochemical purities of radioiodinated ANV and ANV-6L15 were determined on an analytical HPLC system (Waters 600E, Milford, MA, USA) equipped with a size-exclusion column (Waters Ultrahydrogel 250 column, 7.8 × 300 mm, 6 μm) and a Waters Ultrahydrogel guard column (6.0 mm × 40 mm, 6 μm). After loading 10 μL of diluted radiolabeled protein, the column was eluted with 0.01 M KH$_2$PO$_4$ solution (pH 7.4) at a flow rate of 0.8 mL/min. The radioactivity of the eluate was monitored online by a flow detector (FC-1000, Bioscan, Washington, DC, USA).

2.4. Erythrocyte Ghost Binding Assay. Stabilized erythrocyte ghosts were prepared by hypotonic treatment of 5C Cell Control (Beckman Coulter) to expose more PS sites. The cell control erythrocytes were incubated alternatively with water and 10 mM HEPES buffer (containing 137 mM NaCl, 4 mM KCl, 0.5 mM MgCl$_2$, 0.5 mM NaH$_2$PO$_4$, 0.1% D-glucose, and 0.1% BSA; pH 7.4) twice at 37°C for 45 min. Following centrifugation at 16,000×g for 5 min, the pellet of stabilized erythrocytes was resuspended in 10 mM HEPES buffer. For the binding studies, erythrocyte ghosts (1.1×10^9 cells/mL) were incubated with ^{125}I-ANV and ^{125}I-ANV-6L15, respectively, in binding buffers (10 mM HEPES buffer, pH 7.4, with 1.2–10 mM calcium chloride solution) at room temperature for 30 min. Bound and free radioiodinated proteins were then separated by centrifugation at 16,000×g for 10 min. The radioactivities in the pellet and the supernatants were measured using an automatic gamma counter (Wizard 1470, PerkinElmer Wallac, Turku, Finland), and the percentage of radioactivity bound to erythrocyte ghosts was calculated. Binding of ^{125}I-NaI to erythrocyte ghosts served as a negative control.

2.5. Apoptotic Cell Binding Assay. Apoptotic Jurkat T-cells were prepared by treatment with an anticancer drug camptothecin (CPT; 8 μM) for 24 hours [15, 16]. In brief, cell culture flasks with RPMI 1640 medium (5 mL containing 10^7 cells) mixed with CPT-DMSO solution (5 μL; 8 mM) and DMSO (5 μL) served as CPT-treated and vehicle-treated groups, respectively. Apoptosis of Jurkat T-cells was
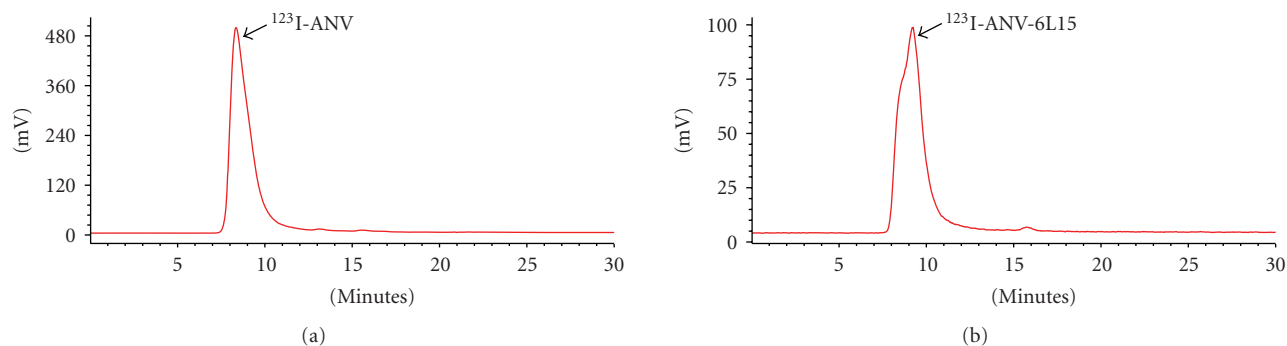
(a)

(b)

FIGURE 1: Representative HPLC radiochromatograms of (a) ^{123}I-ANV and (b) ^{123}I-ANV-6L15. HPLC analysis was performed on a Waters Ultrahydrogel 250 column, $(7.8 \times 300$ mm, $6\,\mu$m) guarded with a Waters Ultrahydrogel guard column (6.0 mm $\times$ 40 mm, $6\,\mu$m), with mobile phase of isocratic 0.01 M KH_2PO_4 solution (pH 7.4) at a flow rate of 0.8 mL/min.

confirmed by flow cytometry using FITC-ANV and propidium iodide (PI) staining. Apoptotic cells were identified as ANV^+PI^- and live cells as ANV^-PI^- on a FACScan analyzer (Becton, Dickinson and Company, CA, USA). For binding assay, untreated (neither CPT-DMSO nor DMSO mixed), vehicle-treated and CPT-treated Jurkat T-cells were incubated with approximately 66.6 MBq ^{123}I-ANV, ^{123}I-ANV-6L15, or ^{123}I-NH$_4$I, respectively, in 0.5 mL binding buffer (10 mM HEPES, 137 mM NaCl, 4 mM KCl, 0.5 mM $MgCl_2$, 0.5 mM NaH_2PO_4, 0.1% glucose, 0.1% BSA, 1.2 mM $CaCl_2$, pH 7.4) at room temperature for 15 min. The cells were pelleted, washed once with the binding buffer, and resuspended in the same buffer. The radioactivity bound to the cells was measured using an automatic gamma counter (Wallac 1470 Wizard).

2.6. Biodistribution and Imaging of Radioiodinated ANV-6L15.

All animal experiments were approved by the Institutional Animal Care and Use Committee (IACUC) of INER. All animals were kept in a temperature-controlled room (at $22.5 \pm 2°$C) with illumination cycle of 12 hours per day and were maintained on a standard diet (Lab diet; PMI Feeds, St. Louis, MO, USA) with free access to tap water.

For biodistribution study, 18 eight-week-old male BALB/c mice (obtained from the National Animal Center, Taipei, Taiwan) were injected intravenously via the lateral tail vein with 444 ± 37 kBq ^{123}I-ANV-6L15 and sacrificed at 2, 10, 30, 60, 120, and 180 min after injection (three mice for each time point) under isoflurane anesthesia. Blockade of specific uptake of free iodide was achieved by intraperitoneal injection of KI (3.9 mg per mouse) 30 min before radiotracer injection. At the selected time, main organs and tissues were obtained, weighed, and counted for radioactivity on a Wallac 1470 gamma counter. The distribution data were expressed as percentage of the injected dose per organ (%ID/organ) and per gram of tissue (%ID/g).

For *in vivo* imaging study, one BALB/c mouse was injected via tail vein with 18.5 MBq of ^{123}I-ANV-6L15 in physiological saline (100 μL). Under isoflurane anesthesia, whole body scans were acquired on an X-SPECT (Gamma Medica, Northridge, CA, USA) equipped with an HRES

TABLE 1: Labeling yields and radiochemical purities of radioiodinated ANV and radioiodinated ANV-6L15.

	Labeling yield (%)	Radiochemical purity (%)	
^{123}I-ANV	51.4 ± 8.4	96.0 ± 3.9	$(n = 7)$
^{123}I-ANV-6L15	44.2 ± 4.9	98.0 ± 2.6	$(n = 6)$
^{125}I-ANV	74.0 ± 6.6	97.6 ± 1.0	$(n = 4)$
^{125}I-ANV-6L15	74.5 ± 7.3	96.1 ± 1.4	$(n = 4)$

Data expressed as mean $\pm$ SD.

(high resolution electronic system) collimator 60–210 min after injection.

2.7. Statistical Analysis.
Data were expressed as mean $\pm$ standard deviation (SD). The binding of ^{123}I-ANV and ^{123}I-ANV-6L15 in CPT-treated Jurkat T-cells were compared using Student's t-test, with $P < .05$ indicating statistical significance.

3. Results and Discussion

3.1. Radiochemical Profile of Radioiodinated Proteins.
ANV-6L15 as well as native ANV were successfully labeled with radioiodine using Iodogen method. The representative size-exclusion chromatograms of radioiodinated ANV and ANV-6L15 were shown in Figure 1. The retention times of radioiodinated ANV, ANV-6L15, and radioiodide were 8.33 ± 0.07 min, 9.20 ± 0.15 min, and 15.5 ± 0.25 min, respectively. Since the molecular weight of ANV-6L15 (contains 378 amino acids) is larger than that of ANV (contains 319 amino acids), the slightly longer retention time of radioiodinated ANV-6L15 compared to that of ^{123}I-ANV possibly reflected the difference in molecular conformation and/or interaction with the chromatographic medium rather than the difference in molecular size. The labeling yields of ^{123}I-ANV, ^{123}I-ANV-6L15, ^{125}I-ANV, and ^{125}I-ANV-6L15 were 51.4 ± 8.4%, 44.2 ± 4.9%, 74.0 ± 6.6%, and 74.5 ± 7.3%, respectively. The radiochemical purities of ^{123}I-ANV, ^{123}I-ANV-6L15, ^{125}I-ANV, and ^{125}I-ANV-6L15 were 96.0 ± 3.9%, 98.0 ± 2.6%, 97.6 ± 1.0%, and 96.1 ± 1.4%, respectively (Table 1).
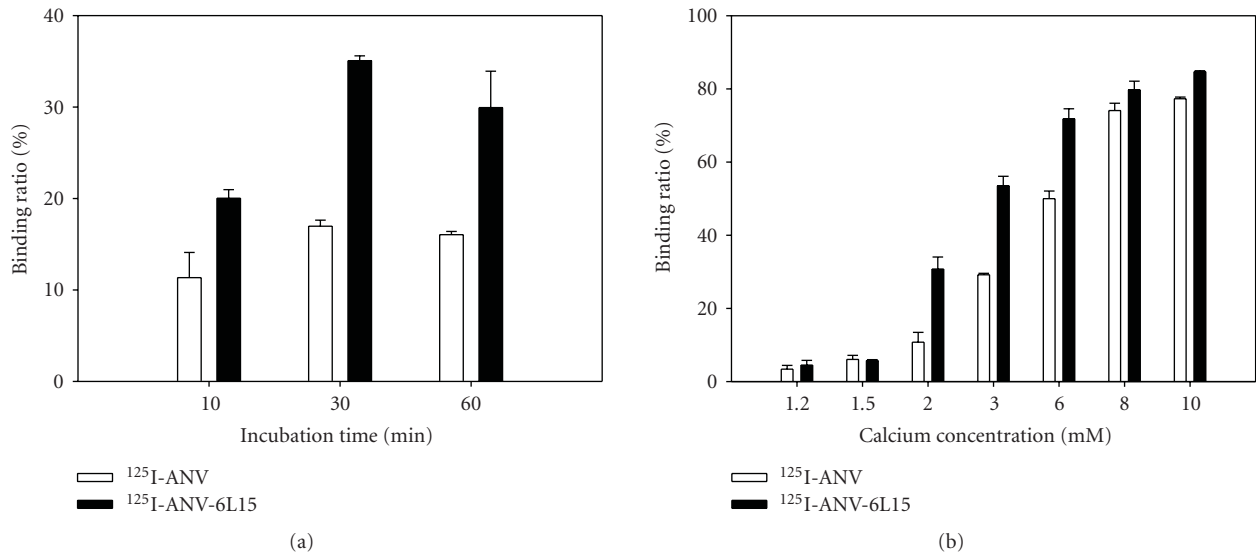
(a)

(b)

FIGURE 2: Binding of ^{125}I-ANV and ^{125}I-ANV-6L15 to erythrocyte ghosts. (a) Time course of binding of ^{125}I-ANV or ^{125}I-ANV-6L15 to ghost erythrocytes in the presence of 2.5 mM Ca^{2+} at room temperature. (b) Binding of ^{125}I-ANV or ^{125}I-ANV-6L15 to ghost erythrocytes under various concentrations of Ca^{2+}. Data are expressed as mean ± SD of three independent experiments.

The radioiodinated proteins were stable at room temperature for up to 10 hours (data not shown).

The most commonly used techniques for radioiodination of proteins are Iodogen, Iodobead and chloramine-T methods. Previously reported labeling yields of radioiodinated ANV using Iodogen and Iodobead were 70% and 40%, respectively [13, 14, 17]. The labeling yields of radioiodinated ANV and ANV-6L15 in this study were comparable with the data reported in the literature.

Due to limited availability of ^{123}I, we used ^{123}I mainly for animal studies (biodistribution and SPECT imaging) and related Jurkat T-cell binding assay. To prevent frequent shortage of ^{123}I during the course of study, we used relatively longer half-lived and commercially available ^{125}I for in vitro study on erythrocyte ghost cell. We assume similar binding characteristics between radiolabels of ^{123}I and ^{125}I.

3.2. Erythrocyte Ghost Binding Assay.

To determine whether ANV-6L15 maintained its biological activity after radioiodination, erythrocyte ghost binding assay was performed. The results showed that the binding of ^{125}I-ANV or ^{125}I-ANV-6L15 to erythrocyte ghosts was time- and Ca^{2+}-dependent (Figures 2(a) and 2(b)). Maximal binding of either ^{125}I-ANV or ^{125}I-ANV-6L15 to erythrocyte ghosts occurred after 30 min incubation in the presence of 2.5 mM Ca^{2+}; the binding ratio was 16.97 ± 0.66% and 35.07 ± 0.53% for ^{125}I-ANV and ^{125}I-ANV-6L15, respectively (Figure 2(a)). The binding of either radioiodinated protein to erythrocyte ghosts steeply increased as Ca^{2+} concentration increased from 1.2 mM to 10 mM, and the binding ratio reached 77.3 ± 0.45% and 84.7 ± 0.26% for ^{125}I-ANV and ^{125}I-ANV-6L15, respectively, at 10 mM Ca^{2+} (Figure 2(b)). ^{125}I-ANV-6L15 exhibited higher binding ratios than ^{125}I-ANV (Figures 2(a) and 2(b)). Thus, radioiodinated ANV-6L15 appeared

to possess a higher affinity to membrane PS-binding sites compared to radioiodinated ANV.

Lahorte et al. [13] reported that the optimal incubation time for maximal platelet binding was 20 min or longer in the presence of 5 mM Ca^{2+} and reached a plateau at 20 mM Ca^{2+} when incubated for 30 min. Our data showed that the maximal binding of either ^{125}I-ANV or ^{125}I-ANV-6L15 to erythrocyte ghosts appeared at 30 min in the presence of 2.5 mM Ca^{2+} and reached a plateau at 8 mM Ca^{2+} when incubated for 30 min.

The mechanism for the increased binding affinity of ANV-6L15 for erythrocyte membranes compared with ANV is currently unknown. The coexpression of phosphatidylethanolamine (PE) on the erythrocyte membranes was proposed to contribute importantly to the increased affinity of ANV-6L15 compared with ANV [12].

3.3. Apoptotic Cell Binding Assays.

Figure 3 showed a typical flow cytometric dot plot for the untreated and apoptotic CPT-treated Jurkat T-cells. An increased proportion of apoptotic (ANV$^+$PI$^-$) and necrotic (ANV$^+$PI$^+$) cells was observed in CPT-treated cells. The binding of ^{123}I-ANV-6L15 to CPT-treated cells (23.3 ± 2.1 cpm/10^4 cells) was significantly higher than those of untreated- (8.2 ± 0.4 cpm/10^4 cells) and vehicle- (DMSO-) treated Jurkat T-cells ($P < .03$; Figure 4). In contrast, the binding of ^{123}I-ANV (approximately 4 cpm/10^4 cells) or ^{123}I-iodide (<1 cpm/10^4 cells) was far below those of ^{123}I-ANV-6L15 among different groups, and no increase of ^{123}I-ANV binding to apoptotic Jurkat T-cells was observed (Figure 4). The lack of increased ^{123}I-ANV binding to apoptotic Jurkat T-cells was possibly due to relatively low binding affinity of ^{123}I-ANV for PS-exposed membranes at the physiological concentration Ca^{2+} (1.2 mM).
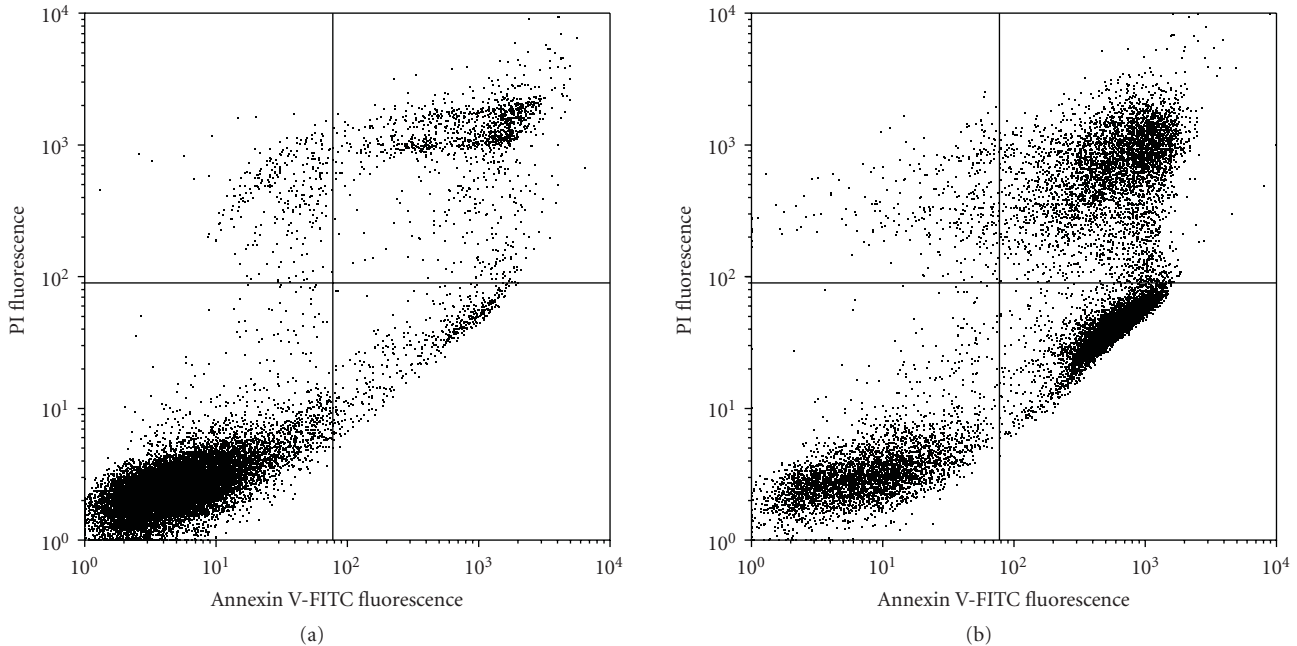
(a)

(b)

FIGURE 3: Representative flow cytometric histograms of apoptotic Jurkat T-cells stained with annexin V-FITC and propidium iodide (PI). Jurkat T-cells (2×10^6/mL) were left untreated or treated with camptothecin (CPT, $8\,\mu$M) at $37°$C for 24 h, followed by staining with ANV-FITC and PI. Apoptotic cells were identified as ANV^+PI^- and live cells as ANV^-PI^- on an FACScan analyser.
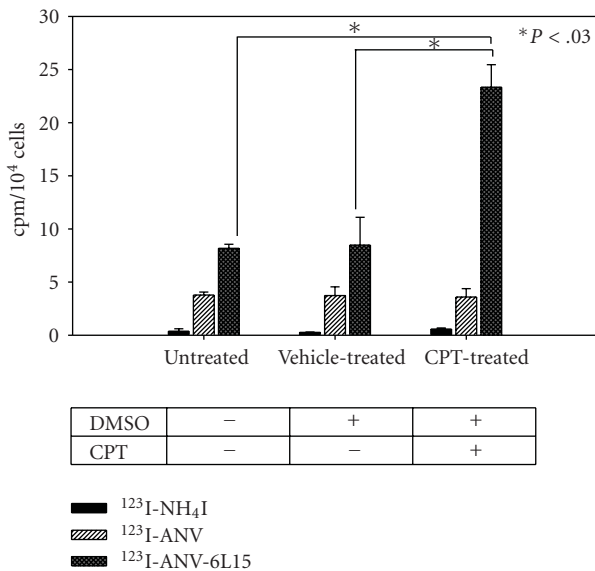

FIGURE 4: Binding of ^{123}I-ANV and ^{123}I-ANV-6L15 to apoptotic Jurkat T-cells. Jurkat T-cells were either left untreated or treated with camptothecin (CPT, $8\,\mu$M) and/or vehicle ($5\,\mu$L DMSO).

3.4. Biodistribution and Imaging of Radioiodinated ANV-6L15 in Mice. The biodistribution of ^{123}I-ANV-6L15 in BALB/c mice are depicted in Table 2. After bolus injection via tail vein (approximately 25 ng protein/mouse),

^{123}I-ANV-6L15 showed an initial rapid clearance from the blood ($40.01 \pm 6.25\%$ and $12.29 \pm 1.22\%$ ID/organ at 2 min and 60 min after injection, resp.). The liver had the highest radioactivity ($11.40 \pm 1.34\%$ ID/organ) at 2 min after injection. The organ with the second highest radioactivity was the kidneys ($8.61 \pm 0.35\%$ ID/organ at 10 min after injection). ^{123}I-ANV-6L15 fusion protein did not cross the blood-brain barrier as indicated by the low brain uptake ($<0.5\%$ ID/g in average). Low uptake in the thyroid reflected low level of radioiodide dissociation from the radiolabeled protein in vivo. The slight increase of thyroid uptake at 120 and 180 min could be due to in vivo ^{123}I dissociation from the radiolabeled protein.

As reported previously [3, 14], ^{123}I-ANV was rapidly cleared from the blood following a biexponential decay and predominant uptake in the kidneys, liver, and gastrointestinal tract. The result of this study revealed that ^{123}I-ANV-6L15 also excreted via kidneys.

In vivo imaging of ^{123}I-ANV-6L15 distribution in a BALB/c mouse after bolus injection via tail vein (approximately $1\,\mu$g protein/mouse) showed high uptake of the tracer in the liver and the kidneys (Figure 5). The uptake of ^{123}I-ANV-6L15 in these organs may limit the evaluation of apoptosis in abdominal regions. Further studies of biodistribution and SPECT imaging will be performed at later time points. We will conduct dosimetry calculation for ^{123}I-ANV-6L15 and compare with ^{123}I-ANV. The novel tracer will be evaluated in animal models with stress-induced apoptosis in the future.

TABLE 2: Biodistribution of ^{123}I-ANV-6L15 fusion protein in healthy BALB/c mice ($n = 3$).

Organ	%ID/organ						%ID/g of tissue					
	2 min	10 min	30 min	60 min	120 min	180 min	2 min	10 min	30 min	60 min	120 min	180 min
Brain	0.29 ± 0.07	0.22 ± 0.07	0.15 ± 0.02	0.13 ± 0.03	0.11 ± 0.03	0.13 ± 0.06	0.74 ± 0.16	0.54 ± 0.26	0.38 ± 0.05	0.32 ± 0.06	0.28 ± 0.03	0.33 ± 0.18
Thyroid	0.39 ± 0.05	0.25 ± 0.06	0.37 ± 0.03	0.34 ± 0.06	0.59 ± 0.09	0.49 ± 0.03	2.47 ± 0.20	1.93 ± 0.61	2.14 ± 0.03	2.15 ± 0.15	3.37 ± 1.17	3.01 ± 0.12
Heart	1.02 ± 0.45	0.58 ± 0.01	0.45 ± 0.14	0.32 ± 0.09	0.33 ± 0.09	0.21 ± 0.04	7.50 ± 2.48	4.36 ± 0.21	3.44 ± 0.56	2.41 ± 0.67	2.45 ± 0.51	1.70 ± 0.42
Lung	2.12 ± 0.32	1.54 ± 0.05	1.00 ± 0.30	0.85 ± 0.28	0.89 ± 0.24	0.54 ± 0.18	14.8 ± 1.19	11.1 ± 2.09	8.65 ± 1.53	5.51 ± 1.31	6.08 ± 0.32	4.49 ± 0.20
Liver	11.40 ± 1.34	11.16 ± 0.73	6.53 ± 0.52	3.33 ± 1.23	3.30 ± 0.26	2.66 ± 0.51	9.20 ± 1.04	8.56 ± 2.49	5.10 ± 0.54	3.01 ± 0.32	2.78 ± 0.46	2.09 ± 0.32
Spleen	0.66 ± 0.19	1.06 ± 0.12	0.88 ± 0.07	0.58 ± 0.09	0.51 ± 0.08	0.35 ± 0.06	7.53 ± 1.66	9.65 ± 1.06	9.61 ± 1.6	5.99 ± 0.33	5.15 ± 0.86	3.75 ± 0.53
Stomach	0.16 ± 0.08	0.25 ± 0.39	0.39 ± 0.09	0.49 ± 0.01	0.70 ± 0.52	0.79 ± 0.38	1.29 ± 0.46	1.42 ± 0.09	3.13 ± 0.24	3.08 ± 0.21	4.56 ± 3.35	5.11 ± 2.21
Intestine	0.05 ± 0.03	0.07 ± 0.00	0.09 ± 0.03	0.11 ± 0.02	0.12 ± 0.03	0.09 ± 0.05	1.08 ± 0.13	1.36 ± 0.18	2.06 ± 0.23	2.20 ± 0.56	1.95 ± 0.56	1.74 ± 0.85
Kidneys	5.23 ± 0.74	8.61 ± 0.35	5.72 ± 1.12	2.95 ± 0.46	2.33 ± 0.02	1.88 ± 0.32	13.57 ± 2.76	21.11 ± 3.31	14.97 ± 3.48	8.22 ± 1.99	5.75 ± 0.61	4.63 ± 0.74
Bladder	0.06 ± 0.03	0.05 ± 0.01	0.15 ± 0.10	0.14 ± 0.08	0.07 ± 0.02	0.13 ± 0.09	1.42 ± 1.16	2.13 ± 0.76	4.76 ± 2.62	5.40 ± 2.70	2.37 ± 0.49	6.24 ± 6.14
Urine	0.01 ± 0.01	0.14 ± 0.2	1.02 ± 1.12	2.36 ± 1.57	0.13 ± 0.22	1.64 ± 2.72	12.13 ± 15.9	11.41 ± 16.13	32.75 ± 2.19	80.92 ± 51.1	18.58 ± 22.31	50.03 ± 7.25
Testis	0.11 ± 0.02	0.10 ± 0.01	0.16 ± 0.02	0.16 ± 0.02	0.25 ± 0.02	0.25 ± 0.05	0.71 ± 0.16	0.62 ± 0.08	1.05 ± 0.08	1.04 ± 0.09	1.72 ± 0.33	1.50 ± 0.33
Blood*	40.01 ± 6.25	25.07 ± 0.35	16.30 ± 1.8	12.29 ± 0.22	11.96 ± 0.13	9.19 ± 0.82	26.21 ± 3.17	15.91 ± 2.35	10.46 ± 0.67	7.91 ± 1.01	7.55 ± 1.05	5.79 ± 0.51
Muscle#	6.68 ± 0.74	5.91 ± 0.29	7.31 ± 1.79	7.88 ± 2.62	8.84 ± 1.12	6.52 ± 2.78	0.77 ± 0.08	0.66 ± 0.09	0.82 ± 0.16	0.90 ± 0.32	0.97 ± 0.11	0.72 ± 0.31
Bone+	3.68 ± 0.80	3.09 ± 0.38	2.61 ± 0.65	2.33 ± 0.88	3.55 ± 0.34	2.73 ± 0.15	2.60 ± 0.54	2.12 ± 0.46	1.80 ± 0.35	1.62 ± 0.63	2.42 ± 0.34	1.85 ± 0.12

*Estimated total blood volume: 7.0% of total body weight.
#Estimated total muscle: 40.0% of total body weight.
+Estimated total bone: 6.5% of total body weight.
%ID: percentage of injected dose.
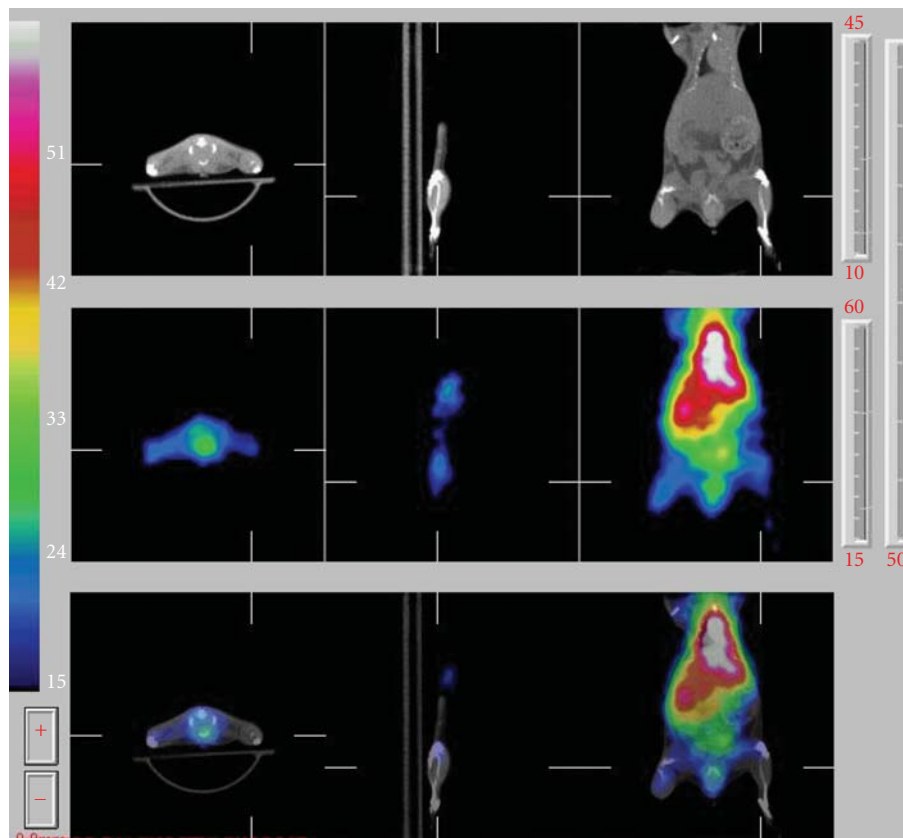Data expressed as mean ± SD.

FIGURE 5: *In vivo* SPECT images of ^{123}I-ANV-6L15 fusion protein in an eight-week-old male BALB/c mouse. ^{123}I-ANV-6L15 (18.5 MBq in 100 μL physiological saline) was injected via tail vein of the mouse under isoflurane anesthesia. Whole body scan was acquired at 60–210 min after injection.

4. Conclusions

ANV-6L15 was successfully labeled with radioiodine using Iodogen method. Radioiodinated ANV-6L15 showed significantly higher binding to PS-exposed erythrocyte ghosts and camptothecin-induced apoptotic Jurkat T-cells at physiological concentration of Ca^{2+} compared to that of radioiodinated ANV *in vitro*. Biodistribution study showed that ^{123}I-ANV-6L15 was rapidly cleared from the blood. Further imaging studies in animal models of apoptosis are warranted. Owing to higher binding affinity to PS, radioiodinated ANV-6L15 could be more sensitive than radioiodinated ANV to detect the apoptosis-associated treatment and human disorders, such as radiation/chemotherapy efficacy, myocardial ischemia or infarct, infectious diseases, and neurodegenerative diseases. Taken together, these results suggest that the radioiodinated ANV-6L15 may be a better scintigraphic tracer for apoptosis detection compared with ANV.

Acknowledgments

References

[1] F. G. Blankenberg, P. D. Katsikis, J. F. Tait et al., "Imaging of apoptosis (programmed cell death) with ^{99m}Tc annexin V," *Journal of Nuclear Medicine*, vol. 40, no. 1, pp. 184–191, 1999.

[2] J. F. Taiy, "Imaging of apoptosis," *Journal of Nuclear Medicine*, vol. 49, pp. 1573–1576, 2008.

[3] C. M. M. Lahorte, J. L. Vanderheyden, N. Steinmetz, C. V. De Wiele, R. A. Dierckx, and G. Slegers, "Apoptosis-detecting radioligands: current state of the art and future perspectives," *European Journal of Nuclear Medicine and Molecular Imaging*, vol. 31, no. 6, pp. 887–919, 2004.

[4] M. Subbarayan, U. O. Häfeli, D. K. Feyes, J. Unnithan, S. N. Emancipator, and H. Mukhtar, "A simplified method for preparation of ^{99m}Tc-annexin V and its biologic evaluation for in vivo imaging of apoptosis after photodynamic therapy," *Journal of Nuclear Medicine*, vol. 44, no. 4, pp. 650–656, 2003.

[5] R. F. A. Zwaal and A. J. Schroit, "Pathophysiologic implications of membrane phospholipid asymmetry in blood cells," *Blood*, vol. 89, no. 4, pp. 1121–1132, 1997.

[6] E. Kazuo, T. S. Noriko, K. Hajime, I. Keizo, and U. Masato, "Exposure of phosphatidylethanolamine on the surface of apoptotic cells," *Experimental Cell Research*, vol. 232, no. 2, pp. 430–434, 1997.

[7] B. L. Wood, D. F. Gibson, and J. F. Tait, "Increased erythrocyte phosphatidylserine exposure in sickle cell disease: flow-cytometric measurement and clinical associations," *Blood*, vol. 88, no. 5, pp. 1873–1880, 1996.

[8] J. F. Tait, C. Smith, Z. Levashova, B. Patel, F. G. Blankenberg, and J. L. Vanderheyden, "Improved detection of cell death in vivo with annexin V radiolabeled by site-specific methods," *Journal of Nuclear Medicine*, vol. 47, no. 9, pp. 1546–1583, 2006.

[9] G. Niu and X. Chen, "Apoptosis imaging: beyond annexin V," *Journal of Nuclear Medicine*, vol. 51, pp. 1659–1662, 2010.

[10] W. L. Van Heerde, P. G. De Groot, and C. P. M. Reutelingsperger, "The complexity of the phospholipid binding protein annexin V," *Thrombosis and Haemostasis*, vol. 73, no. 2, pp. 172–179, 1995.

[11] H. H. Chen, C. P. Vicente, LI. He, D. M. Tollefsen, and T. C. Wun, "Fusion proteins comprising annexin V and Kunitz protease inhibitors are highly potent thrombogenic site-directed anticoagulants," *Blood*, vol. 105, no. 10, pp. 3902–3909, 2005.

[12] T.-C. Yen, S.-P. Wey, C.-H. Liao et al., "Measurement of the binding parameters of annexin derivative-erythrocyte membrane interactions," *Analytical Biochemistry*, vol. 406, no. 1, pp. 70–79, 2010.

[13] C. Lahorte, G. Slegers, J. Philippé, C. Van de Wiele, and R. A. Dierckx, "Synthesis and in vitro evaluation of ^{123}I-labelled human recombinant annexin V," *Biomolecular Engineering*, vol. 17, no. 2, pp. 51–53, 2001.

[14] C. M. Lahorte, C. van de Wiele, K. Bacher et al., "Biodistribution and dosimetry study of ^{123}I-rh-annexin V in mice and humans," *Nuclear Medicine Communications*, vol. 24, no. 8, pp. 871–880, 2003.

[15] B. Dekker, H. Keen, S. Lyons et al., "MBP-annexin V radiolabeled directly with iodine-124 can be used to image apoptosis in vivo using PET," *Nuclear Medicine and Biology*, vol. 32, no. 3, pp. 241–252, 2005.

[16] H. G. Keen, B. A. Dekker, L. Disley et al., "Imaging apoptosis in vivo using ^{124}I-annexin V and PET," *Nuclear Medicine and Biology*, vol. 32, no. 4, pp. 395–402, 2005.

[17] J. Russell, J. A. O'Donoghue, R. Finn et al., "Iodination of annexin V for imaging apoptosis," *Journal of Nuclear Medicine*, vol. 43, no. 5, pp. 671–677, 2002.

Research Article

Comparison of Cell Proliferation, Protein, and Glucose Metabolism in Musculoskeletal Tumors in a PET Study

Mei Tian,[1,2,3] **Hong Zhang,**[1,2,4,5,6] **and Keigo Endo**[2]

[1] *Department of Nuclear Medicine, Second Affiliated Hospital of Zhejiang University School of Medicine, Hangzhou, Zhejiang 310009, China*

[2] *Department of Nuclear Medicine and Diagnostic Radiology, Gunma University School of Medicine, Maebashi, Gunma 371-8511, Japan*

[3] *The University of Texas MD Anderson Cancer Center, Houston, TX 77030, USA*

[4] *Zhejiang University Medical PET Center, Hangzhou, Zhejiang 310058, China*

[5] *The Institute of Nuclear Medicine and Molecular Imaging of Zhejiang University, Hangzhou, Zhejiang 310009, China*

[6] *Key Laboratory of Medical Molecular Imaging of Zhejiang Province, Hangzhou, Zhejiang 310009, China*

Correspondence should be addressed to Hong Zhang, hzhang21@gmail.com

^{11}C-choline and ^{18}F-FAMT are known to correlate with tumor cell proliferation and amino acid metabolism. We investigated the ability of ^{11}C-Choline and ^{18}F-FAMT PET in diagnosis of musculoskeletal tumors in thirty-six patients in comparison of ^{18}F-FDG PET. ^{11}C-Choline and ^{18}F-FDG PET were positive in all the malignant tumors ($n = 13$), whereas ^{18}F-FAMT was positive in 11 tumors. The mean SUVs for malignant tumors were significantly higher than those for benign lesions in all three tracers imaging. A moderate correlation was found between ^{11}C-Choline and ^{18}F-FDG ($r = 0.540$, $P < .05$), or ^{18}F-FAMT and FDG ($r = 0.596$, $P < .05$). The diagnostic sensitivity and specificity for malignancy were 91.7% and 71.4%, respectively, using ^{11}C-choline with a SUV cut-off of 2.69. The sensitivity and specificity of ^{18}F-FAMT for malignancy were 66.7% and 85.7%, respectively, using a SUV cut-off of 1.26. For ^{18}F-FDG, using a SUV cut-off of 2.77, the sensitivity and specificity were 83.3% and 71.4%, respectively. According to ROC analysis, the ROC curves for ^{11}C-Choline, ^{18}F-FAMT, and ^{18}F-FDG were 0.855, 0.734, and 0.847, respectively. ^{11}C-Choline PET is superior in the visualization of musculoskeletal tumors with high contrast imaging, whereas the combination of ^{18}F-FAMT and ^{18}F-FDG PET provides valuable information for the preoperative planning in patients with musculoskeletal tumors.

1. Introduction

Musculoskeletal tumors generally present clinically as large masses that are often heterogeneous and have different biological behaviors. The diagnosis and treatment of such lesions is often complex [1]. Generally, the anatomical imaging methods, such as conventional radiology, CT, and MRI, are very important for the assessment of tumor location, form, size, infiltration, and extent. However, the radiographic appearance of many tumors is indeterminate, especially CT and MRI have limited ability to allow distinction of malignant from benign lesions and final diagnosis may only be achieved using biopsy and histopathologic evaluation. Furthermore, in case of large-size tumors, the

highest-grade part of the lesion may be missed on a biopsy of only a small region [2]. This results in errors in the diagnosis and grading of the tumor and thus suboptimal management of the disease. An imaging technique that enables reliable distinction of malignant from benign musculoskeletal lesions would thus be of considerable clinical value.

During the last decade, positron emission tomography (PET) has become an essential tool in the management of a growing number of cancer patients [3–5]. 2-[^{18}F]fluoro-2-deoxy-D-glucose (^{18}F-FDG) is by far the most common radiopharmaceutical for PET in clinical use and has shown a high sensitivity for diagnosing and staging a wide variety of malignant diseases. However, there are several limitations for the use of ^{18}F-FDG in discriminating benign lesions from soft

tissue sarcomas [6]. Glucose metabolism is not significantly increased in some bone tumor types [7]. The most significant drawback of ^{18}F-FDG for oncologic purpose results from the absence of specificity for musculoskeletal tumor [8]. Infection, inflammation, granulomatous diseases, and many other physiologic or pathologic conditions can also show high ^{18}F-FDG uptake. To overcome these limitations, new PET imaging agents and its applications are required.

So far, only few PET imaging agents have been developed and used for the detection of musculoskeletal tumors. One potential imaging agent is radiolabeled amino acid, which can be used as the marker of cell proliferation and microvessel density of the tumors [3, 9]. Various studies have demonstrated that increased uptake of amino acid compound is predominantly due to a higher L-amino acid transporter (LAT) activity. Transport of the amino acid into the cell can be followed by rapid metabolization and trapping inside the cell, for example, as in the case for L-3-[^{18}F]-6 α-methyltyrosine (^{18}F-FAMT). Although the exact trapping mechanism is not known, this selective uptake pattern results in a very high tumor-to-background (T/B) ratio enabling clear delineation of the tumor [10–12].

Another attractive imaging agent is [methyl-^{11}C] choline (^{11}C-choline), which has been increasingly used for the evaluation of various cancers [4]. Choline is quaternary amine that is ubiquitously distributed in cells, mostly in the form of phospholipids. In vivo and in vitro studies have shown that the increased ^{11}C-choline uptake in the tumor cells is proportional to the rate of tumor duplication [13–15]. ^{11}C-choline PET imaging shows that liver and kidney are the major sites for choline oxidation or excretion; negligible activity is present in the bone and soft tissues, which indicates its noteworthy advantage for the detection of musculoskeletal tumors.

Since the differences in uptake mechanism are present, it will be interesting to find out the correlations and differences in the patterns of PET imaging of ^{18}F-FDG, ^{18}F-FAMT and ^{11}C-choline, especially during the same time period within the same setting. However, until now, there has as yet only limited experience of use of ^{18}F-FAMT and ^{11}C-choline PET in patients with musculoskeletal tumors [4, 16]. The aim of this study was to compare the characteristics of ^{18}F-FDG, ^{18}F-FAMT, and ^{11}C-choline PET for the detection of musculoskeletal tumors in the same patient population.

2. Materials and Methods

2.1. Patients. Thirty-six consecutive patients (14 female and 22 male; age range: 11 to 84 years) with or suspected of having malignancies in the musculoskeletal system were enrolled in this prospective study. All the patients underwent ^{18}F-FDG PET, ^{18}F-FAMT, ^{11}C-choline, and computed tomography (CT) or magnetic resonance imaging (MRI) in a random order within a maximum interval of 2 weeks. No therapeutic medication has been changed during this period, and none of the patients had diabetes mellitus. The blood glucose level during the PET study was ranged from 64 to 95 mg/dL (3.5–5.3 mmol/L). Patients had surgical operation or biopsy after the completion of the above imaging examinations based on

the information of tumor PET imaging and CT and MRI images, and the resected tumor specimens were submitted for the pathological diagnosis. The imaging protocols of ^{18}F-FDG PET, ^{18}F-FAMT, and ^{11}C-choline were approved by the Institutional Review Board of the Institute of Gunma University. Informed consents of this study were obtained from all patients.

2.2. PET Imaging. PET imaging agents of ^{18}F-FDG, ^{18}F-FAMT, and ^{11}C-choline were prepared using a cyclotron and automated synthetic apparatuses that were reported by Hamacher et al. [17], Tomiyoshi et al. [10], and Hara and Yuasa [13], respectively. PET scans were performed with a SET-2400 W (Shimadzu Corporation, Kyoto, JAPAN), which had a large 20 cm axial field of view and 59.5 cm transaxial field of view, giving 63 two-dimensional imaging planes. The transaxial spatial resolution was 4.2 mm full width at half maximum (FWHM) at the center of the field of view, and the axial resolution was 5.0 mm FWHM. Each patient had an overnight fasting before ^{18}F-FDG, ^{18}F-FAMT, and ^{11}C-choline PET. ^{18}F-FDG and ^{18}F-FAMT PET were started 40 min after the administration of approximately 320 MBq ^{18}F-FDG and 260 MBq ^{18}F-FAMT, and static image data was acquired for 8 min per bed position, respectively. ^{11}C-choline PET was performed 5 min after the intravenous injection of approximately 370 MBq ^{11}C-choline, and static image data was acquired for 5 min per bed position. PET data was acquired by simultaneous transmission-emission method [18]. Images were reconstructed by the order subsets expectation maximization (OSEM) algorithm into a 128 × 128 matrix with pixel dimensions of 4.0 mm in plane and 3.125 mm axially. The image with 9.4 mm thickness was generated for interpretation and semiquantitative analysis.

2.3. Image Analysis. PET images were separately interpreted by two nuclear medicine physicians until consensus was reached. Clinical information and conventional images such as radiographys, CT scans, and MRI images were available at the time of image interpretation. The ^{18}F-FDG, ^{18}F-FAMT, and ^{11}C-choline uptakes were evaluated by both qualitative and semiquantitative methods. The qualitative analysis was performed by the visual evaluation of tumor tracer uptake. Tumor lesions were identified as areas of focally increased uptake, exceeding that of surrounding tissues or organs. The degree of tracer uptake was visually classified as negative ($-$) and positive ($+$ or $++$) results. The semiquantitative analysis was performed using the standardized uptake value (SUV). The regions of interest (ROI) in 1 cm diameter were drawn on the lesions including the highest activity. SUV was then determined as the average of the radioactivity in the tumors divided by the injected radioactivity normalized to the body weight. The mean value per pixel in the ROI for assessing SUV was employed for semiquantitative analysis. All PET findings were finally compared with CT and/or MRI images, and the results of pathological diagnosis.

2.4. Statistical Analysis. Data were expressed as mean ± SD or total number (%). A linear regression analysis was

TABLE 1: Patient characteristics and results of PET studies.

Patient no.	Age	Sex	Histological diagnosis	Grade	Location	Lesion size (mm)	Choline Visual	SUV	FAMT Visual	SUV	FDG Visual	SUV
Benign												
1	44	F	Xanthofibroma	—	Tibia	$40 \times 40 \times 40$	++	4.90	++	1.10	++	3.30
2	51	F	Enchondroma	—	Scapular	$27 \times 30 \times 60$	+	0.75	+	0.72	+	0.70
3	50	M	No definite residual tumor cells	—	Knee	$50 \times 50 \times 50$	++	0.98	++	1.24	++	1.74
4	58	M	Schwannoma	—	Thigh	$35 \times 35 \times 35$	++	1.80	+	0.71	++	1.70
5	59	F	Bursitis with synovitis	—	Knee	$20 \times 20 \times 20$	++	1.13	—	—	+	0.60
6	15	F	Eosinophilic granuloma	—	Eosinophilic	$30 \times 30 \times 55$	++	2.20	++	0.90	++	2.69
7	57	M	Fibroma	—	Scapula	$30 \times 30 \times 50$	+	0.62	++	1.70	++	1.53
8	62	F	Schwannoma	—	Carpal	$5 \times 9 \times 10$	++	1.50	++	0.91	++	1.80
9	60	M	Neurofibroma	—	Femur	$50 \times 60 \times 150$	++	5.10	++	1.40	++	3.49
10	53	M	Giant cell tumor	—	Knee	$35 \times 35 \times 35$	++	4.20	+	0.65	++	4.36
11	53	M	Degeneration of skeletal muscle	—	Lower leg	$27 \times 30 \times 60$	++	0.90	+	0.74	+	0.60
12	26	F	Giant cell tumor	—	Femur	$28 \times 31 \times 42$	++	8.00	++	1.10	++	8.39
13	15	F	Desmoid tumor	—	Lower leg	$40 \times 60 \times 70$	++	3.30	+	0.76	++	2.20
14	27	F	Giant cell tumor	—	Knee	$30 \times 30 \times 40$	++	1.12	+	0.71	++	3.23
15	48	M	Desmoid tumor	—	Carpal	$30 \times 40 \times 60$	++	3.10	++	1.00	++	2.77
16	61	M	Desmoid tumor	—	Back	$40 \times 40 \times 70$	++	2.30	++	1.17	++	2.14
17	55	M	Lymphangioma	—	Knee	$30 \times 40 \times 50$	++	1.69	++	0.92	++	1.37
18	51	M	Lymphangioma	—	Axilla	$30 \times 40 \times 50$	++	1.70	++	1.26	++	2.10
19	31	M	Schwannoma	—	Lower leg	$10 \times 20 \times 30$	++	0.88	+	0.56	++	0.81
20	47	M	Desmoid tumor	—	Thigh	$65 \times 46 \times 68$	++	2.46	++	1.64	++	3.27
21	58	M	Aseptic necrosis	—	Talus	$30 \times 30 \times 30$	++	2.40	++	1.20	++	1.74
22	20	M	Pigmented villonodular synovitis	—	Poples	$30 \times 30 \times 50$	++	2.69	++	0.86	++	2.60
23	53	F	Degenerative joint disease	—	Femur	$40 \times 70 \times 110$	++	2.24	+	0.58	++	2.40
Malignant												
24	47	M	Liposarcoma	1	Thigh	$70 \times 70 \times 120$	++	0.82	—	—	+	0.61
25	43	F	Osteosarcoma	2	Tibia	$20 \times 24 \times 55$	++	9.30	++	2.00	++	6.00
26	53	F	Malignant lymphoma	3	Clavicle	$27 \times 28 \times 30$	++	4.50	++	0.91	++	4.90
27	17	M	Ewing's sarcoma	3	Femur	$54 \times 50 \times 150$	++	2.60	+	0.58	++	0.89
28	54	F	Metastatic carcinoma	3	Carpal	$50 \times 50 \times 60$	++	9.00	++	1.06	++	3.19
29	83	F	Malignant lymphoma	3	Femur	$50 \times 80 \times 196$	++	7.30	++	7.00	++	14.49
30	12	M	Osteosarcoma	3	Femur	$50 \times 50 \times 60$	++	6.40	++	2.62	++	3.15
31	14	F	Osteosarcoma	3	Femur	$60 \times 70 \times 160$	++	4.12	++	1.27	++	13.66
32	11	M	Osteosarcoma	3	Femur	$60 \times 70 \times 170$	++	3.68	++	2.12	++	4.90
33	12	M	Osteosarcoma	3	Femur	$50 \times 100 \times 140$	++	3.03	++	1.38	++	5.37

TABLE 1: Continued.

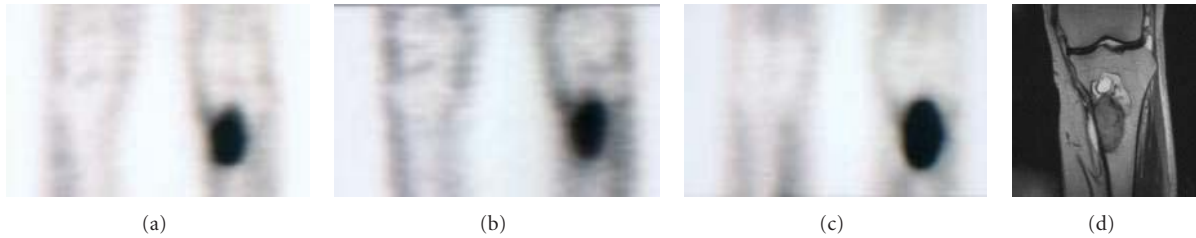| Patient no.	Age	Sex	Histological diagnosis	Grade	Location	Lesion size (mm)	Choline Visual	Choline SUV	FAMT Visual	FAMT SUV	FDG Visual	FDG SUV
34	64	M	Myeloma	3	Sacrum	$40 \times 51 \times 60$	++	3.60	++	1.80	++	2.55
35	84	M	Liposarcoma	3	Femur	$230 \times 280 \times 360$	++	3.20	—	0.30	++	6.00
36	44	M	Metastatic carcinoma	3	Femur	$11 \times 22 \times 40$	++	5.10	++	1.90	++	1.90

| (a) | (b) | (c) | (d) |

FIGURE 1: A 43-year-old female with osteosarcoma. ^{18}F-FDG (SUV = 6.0) (a), ^{18}F-FAMT (SUV = 2.0) (b), and ^{11}C-choline (SUV = 9.3) (c) demonstrated high tracer uptake in the tumor of the left tibia, which corresponded to the area that was enhanced on MRI image (d).

TABLE 2: Results of the ROC analysis of FDG, FAMT, and choline PET in musculoskeletal tumors.

Tracer	AUC	SUV cutoff	Sensitivity (%)	Specificity (%)	Accuracy (%)
FDG	0.847	2.77	83.3	71.4	69.7
FAMT	0.734	1.26	66.7	85.7	78.8
Choline	0.855	2.69	91.7	71.4	78.8

AUC: area under the ROC curve.

performed for the correlation study. A multiple comparison test and t-test were used for the statistical analysis. A receiver operating characteristic (ROC) analysis was performed to compare the diagnostic abilities of ^{18}F-FDG, ^{18}F-FAMT, and ^{11}C-choline PET. A P value <.05 was considered statistically significant.

3. Results

This study population included 36 patients with 36 musculoskeletal lesions. Patient clinical characteristics and imaging findings of ^{11}C-choline, ^{18}F-FAMT, and ^{18}F-FDG PET were summarized in Table 1. Three typical cases are illustrated in Figures 1, 2, and 3.

3.1. Visual Analysis. In all 36 patients, 13 patients had malignant tumors and 23 had benign lesions, based on pathological findings of biopsy or surgical specimens. The diameter of the lesions ranged from $5 \times 9 \times 10$ mm to $230 \times 280 \times 360$ mm as determined by CT, MRI, or dissected surgical specimen. ^{11}C-choline and ^{18}F-FDG PET was positive in all the 36 patients (100%), whereas ^{18}F-FAMT PET imaging were positive in 33 patients (84%) and negative in 3 patients (1 bursitis with synovitis and 2 liposarcoma).

3.2. Semiquantitative Analysis. The mean ($\pm$SD) SUVs for malignant tumors were significantly higher than those for benign lesions in all ^{18}F-FDG, ^{18}F-FAMT, and ^{11}C-choline PET analysis (5.2 $\pm$ 4.3, $n = 13$ versus 2.5 $\pm$ 1.7, $n = 23$, $P < .002$; 1.9 $\pm$ 1.7, $n = 13$ versus 1.0 $\pm$ 0.3, $n = 23$, $P < .02$; 4.8 $\pm$ 2.5, $n = 13$ versus 2.4 $\pm$ 1.8, $n = 23$, $P < .001$, resp.). The P value showed a trend of significant relationship as ^{11}C-choline >[18]F-FDG >[18]F-FAMT for distinguishing malignant tumors from benign lesions.

As shown in Figure 4, the mean SUV of ^{18}F-FDG and ^{11}C-choline was significantly higher than that of ^{18}F-FAMT in either malignant tumors or benign tumors ($P < .002$, $P < .001$ and $P < .0001$, $P < .0002$, resp.), but there was no significant difference between ^{18}F-FDG and ^{11}C-choline in either malignant tumors or benign tumors (n.s.).

The linear regression analysis was performed between ^{11}C-choline and ^{18}F-FDG, as well as ^{18}F-FAMT and ^{18}F-FDG (Figure 5). Moderate correlations were noted between ^{11}C-choline and ^{18}F-FDG in all lesions ($r = 0.540$, $n = 36$) and ^{18}F-FAMT and ^{18}F-FDG ($r = 0.596$, $n = 36$).

3.3. ROC Analysis. The results of ROC analysis using histopathological diagnosis as the gold standard were shown in Figure 6. The area under the curve (AUC) of ^{18}F-FDG PET, ^{18}F-FAMT, and ^{11}C-choline PET was 0.847, 0.734, and 0.855, respectively. Table 2 summarized the sensitivity, specificity, and accuracy of ^{18}F-FDG, ^{18}F-FAMT, and ^{11}C-choline PET. For example, in ^{18}F-FDG PET, the sensitivity, specificity, and accuracy were 83.3%, 71.4%, and 69.7%, respectively, when 2.77 of SUV was used as a cutoff. This would be 66.7%, 85.7%, and 78.8%, respectively, for ^{18}F-FAMT as using a cutoff of SUV 1.26. ^{11}C-choline PET was 91.9%, 71.4%, and 78.8%, respectively, when 2.69 of SUV was used as a cutoff. The trend observed in the ROC analysis was that ^{18}F-FDG PET and ^{11}C-choline PET had almost the same detect
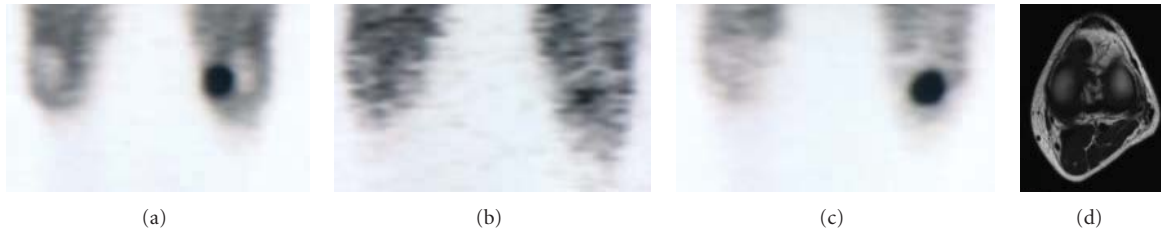
FIGURE 2: A 53-year-old male with giant cell tumor in the left knee. ^{18}F-FDG (SUV = 4.36) (a) and ^{11}C-choline (SUV = 4.20) (c) demonstrated high tracer uptake in the tumor of the left knee, whereas ^{18}F-FAMT (SUV = 0.65) (b) showed mild uptake, which corresponded to the area that was shown on MRI image (d).
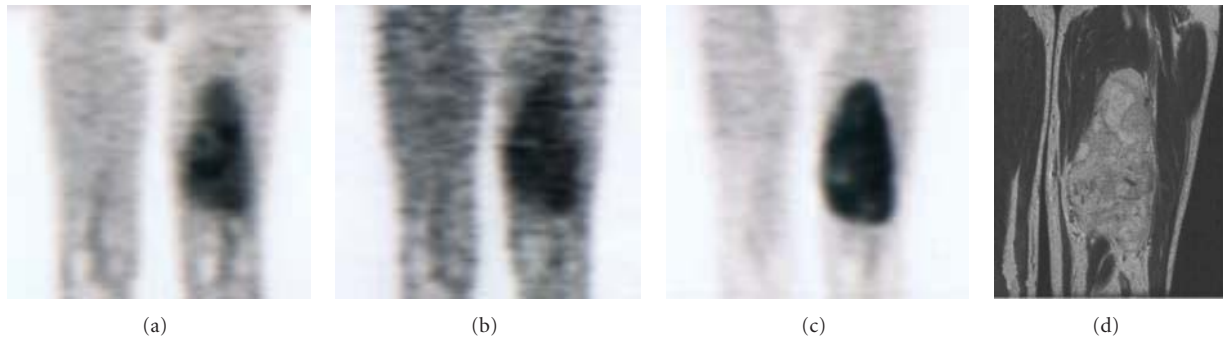

FIGURE 3: A 60-year-old male with neurofibroma in the left femur. ^{18}F-FDG (SUV = 3.49) (a), ^{18}F-FAMT (SUV = 1.40) (b), and ^{11}C-choline (SUV = 5.10) (c) showed clear tracer uptake in the tumor of the left femur, which corresponded to the area that was enhanced on MRI image (d).
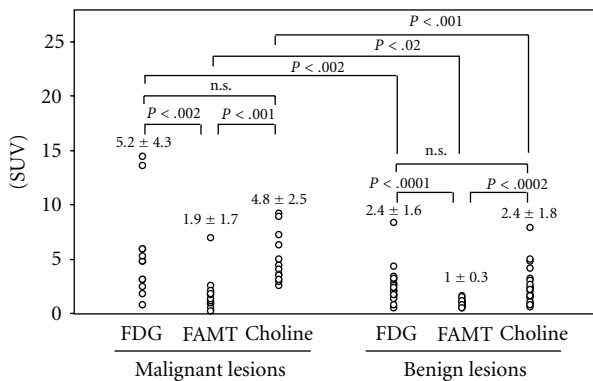

FIGURE 4: Standardized uptake value (SUV) of ^{18}F-FDG, ^{18}F-FAMT, and ^{11}C-choline in malignant and benign lesions. ^{18}F-FDG, ^{18}F-FAMT, and ^{11}C-choline revealed significant higher SUV in malignant lesions than in benign lesions ($P < .002$, $P < .02$, and $P < .001$, resp.). Differences of tumor SUVs between ^{18}F-FDG and ^{11}C-choline were not significant in both malignant and benign lesions, whereas both ^{18}F-FDG and ^{11}C-choline SUVs were significantly higher than that of ^{18}F-FAMT.

ability in this patient population and showed better detection performance than that of ^{18}F-FAMT PET.

4. Discussion

The results of the present study indicate that ^{11}C-choline and ^{18}F-FDG PET perform better than ^{18}F-FAMT in the detection of musculoskeletal tumors on the whole data analysis. However, in some benign lesions, such as bursitis or synovitis, ^{18}F-FAMT PET performed better than ^{11}C-choline and ^{18}F-FDG PET in visualizing focal lesions. On the other hand, ^{11}C-choline and ^{18}F-FAMT PET showed higher contrast compared with ^{18}F-FDG PET. Our findings were interpreted based on the pathological findings and analyzed to compare simultaneously the 3 PET imaging modalities.

Unsurprisingly, ^{18}F-FDG PET detected all the malignant tumors successfully; however, some benign lesions, such as benign giant cell tumor, desmoids tumor, and synovitis, also showed focal intensive uptakes. Although ^{18}F-FDG PET has been widely used for the evaluation of various tumors, recent reports suggested that ^{18}F-FDG PET could not be used as a screening method for differential diagnosis between benign and malignant musculoskeletal lesions. A high accumulation of ^{18}F-FDG can be observed in histiocytic, fibroblastic, and some neurogenic lesions, regardless of whether they are benign or malignant. More specific uses of ^{18}F-FDG PET, such as grading, staging, and monitoring of musculoskeletal sarcomas, should be considered for each tumor of a different histologic subtype [19].

The original application of ^{11}C-choline was for detection of brain tumor and prostate cancer [20, 21]. ^{11}C-choline PET can give clearer images of brain tumors, whereas ^{18}F-FDG PET does not always delineate the border of the tumor. The high uptake of ^{18}F-FDG in the normal brain tissue frequently obscures the tumor uptake. Our present results showed that all the malignant tumors showed significant intensive accumulation in ^{11}C-choline PET imaging. This was superior
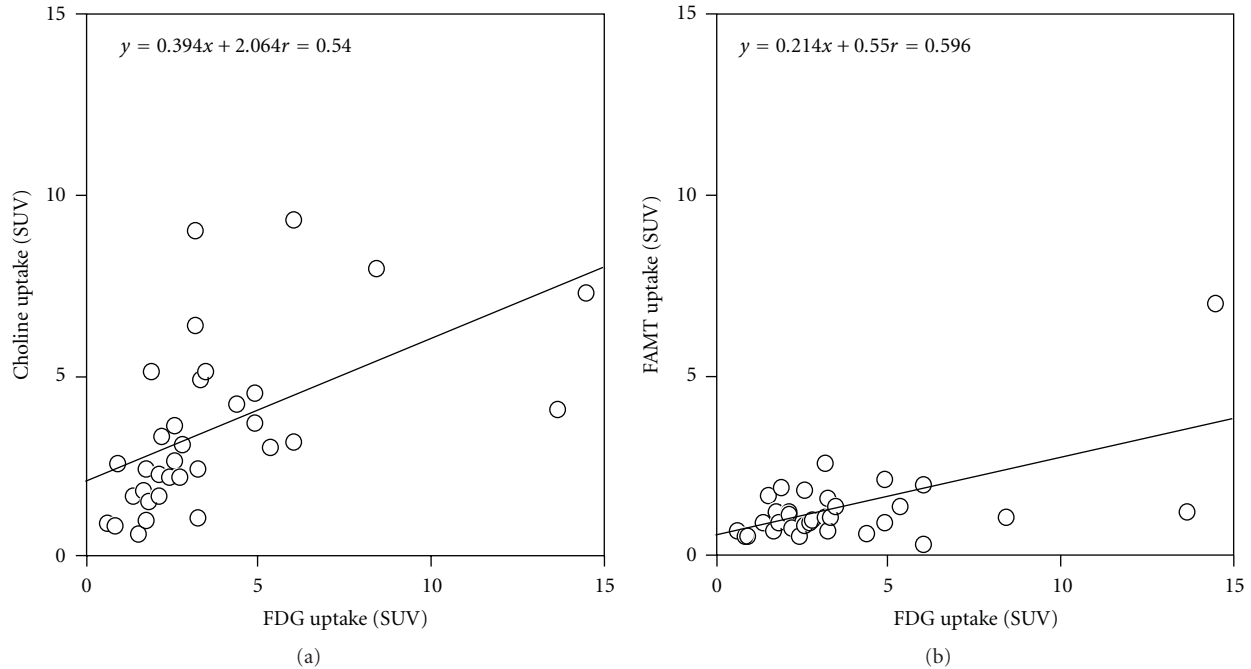
$y = 0.394x + 2.064r = 0.54$

$y = 0.214x + 0.55r = 0.596$

(a)   (b)

FIGURE 5: Relationship among ^{18}F-FDG, ^{18}F-FAMT, and ^{11}C-choline uptakes in musculoskeletal tumors. Moderate correlation was observed between ^{11}C-choline uptake and ^{18}F-FDG uptake, and ^{18}F-FAMT and ^{18}F-FDG in all lesions.
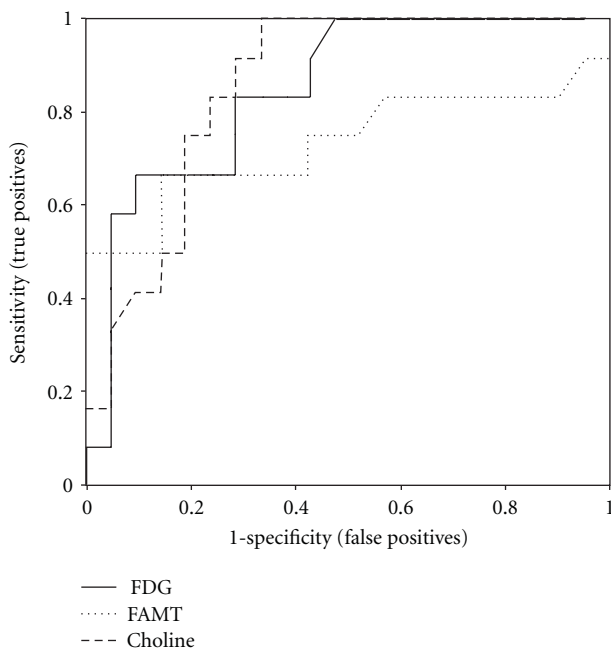

FIGURE 6: Comparison among ^{18}F-FDG, ^{18}F-FAMT, and ^{11}C-choline PET in differential diagnosis between malignant tumors and benign lesions by ROC analysis in musculoskeletal tumors.

to ^{18}F-FDG PET and ^{18}F-FAMT in differentiation between malignant and benign lesions. Thus, ^{11}C-choline PET might be useful as a screening method for malignant bone and soft tissue tumors. The application of ^{11}C-choline PET in evaluation of bone and soft tissue tumors is not yet well known.

Similarly, ^{18}F-FAMT was also developed for the detection of brain tumors [22]. Watanabe et al. previously reported that ^{18}F-FAMT may be superior to ^{18}F-FDG in the differentiation between benign and malignant tumors, while ^{18}F-FDG may be the better choice for noninvasive malignancy grading [16]. In the present patient population, the ^{18}F-FAMT uptake was significantly higher in malignant tumors than in benign lesions, which partly supported the previous study.

To the best of our knowledge, this is the first study to compare the clinical utility of ^{18}F-FDG, ^{18}F-FAMT, and ^{11}C-choline PET in detection of musculoskeletal tumors in a same patient population. We found that ^{11}C-choline PET could detect and differentiate malignant musculoskeletal tumors with high sensitivity, as well as ^{18}F-FDG PET, compared with ^{18}F-FAMT PET. Based on visual evaluation, PET imaging clearly demonstrated intensive radioactive accumulation in 100% of the musculoskeletal tumors by using ^{18}F-FDG and ^{11}C-choline, but only 84% if using ^{18}F-FAMT. The uptakes of all the 3 imaging agents, ^{18}F-FDG, ^{18}F-FAMT, and ^{11}C-choline, were significantly higher in malignant musculoskeletal tumors than those in benign lesions. ^{11}C-choline and ^{18}F-FDG showed equal ability in detection of musculoskeletal tumors, followed by ^{18}F-FAMT.

A considerable overlap of SUVs was observed in the present study, due to a relatively large number of benign cases with various histological types included. It is noted that high ^{11}C-choline uptake (SUV > 2.4) was found in 2 of 3 giant cell tumors, 3 of 4 desmoid tumors, 1 xanthofibroma, 1 neurofibroma, and 1 pigmented villonodular synovitis. Such false-positive cases were similar in ^{18}F-FDG PET. High FDG uptake (SUV > 2.4) was noted in all 3 giant cell tumors, 2 of 4 desmoid tumors, 1 xanthofibroma, 1 neurofibroma,

1 eosinophilic granuloma, and 1 pigmented villonodular synovitis. Most of the false-positive cases in this study could be classified as histiocytic or giant cell-containing lesions [23, 24]. Histiocytes and giant cells in a tissue are in monocyte-macrophage lineage. Macrophages play a central role in the host response to injury and infection, and their energy is predominantly supplied by means of intracellular glucose metabolism [25, 26]. High uptake of ^{18}F-FDG in inflammatory lesions found in this study was consistent with previous studies [27–29]. Although it is still controversial whether histiocytes and giant cells in primary bone tumors are reactive or neoplastic, these cells might partially contribute to the high uptake of ^{18}F-FDG in the benign bone and soft tissue lesions [30]. It may be reasonable to consider that high uptake of ^{11}C-choline in reactive or neoplastic cells of histiocytes and giant cells is due to the high ^{11}C-choline utilization by these cell membranes. Further investigation is necessary to verify this point. The overlap of SUVs was also observed in ^{18}F-FAMT PET. High ^{18}F-FAMT uptake (SUV > 1.0) was found in 1 of 3 giant cell tumors, 2 of 4 desmoid tumors, 1 xanthofibroma, 1 fibroma, 1 neurofibroma, 1 lymphangioma, and 1 aseptic necrosis. This may also be explained from the above reasons.

The differentiation of malignant from benign lesions is crucial to preoperative planning for treatment of musculoskeletal tumors. This study in the current patient population showed that the sensitivity of ^{11}C-choline PET was higher than that of ^{18}F-FDG PET in musculoskeletal tumors. This is consistent with our previous study [31], which could be explained as follows. A high uptake of ^{18}F-FDG in tumors is accomplished only if the tumor metabolism is biased toward excessive glycolysis by activation of the glucose transporter and hexokinase [32]. This may occur, although there seemed to be rare exceptions, if the tumor size is large and the tumor environment is hypoxic because of insufficient blood (oxygen) supply. In contrast, the uptake of ^{11}C-choline in tumors is the result of cell membrane synthesis. When ^{11}C-choline is incorporated in tumors, it is rapidly phosphorylated (yielding ^{11}C-phosphorylcholine) and chemically trapped inside the cell membranes. ^{11}C-phosphorylcholine may be the major chemical derived from ^{11}C-choline at the time of PET scanning. Thereafter, it is further metabolized and converted to ^{11}C-phosphatidylcholine and then integrated in tumor cell membrane [33]. This is the only metabolic pathway known for choline in tumors, although there are other metabolic pathway in other normal organs. Thus, it could be assumed that the ^{11}C-choline uptake in tumors is proportional to the tumor cell proliferation rate [15]. When the cut-off value was set at 1.26, the sensitivity of ^{18}F-FAMT PET for correctly diagnosing malignancy was 66.7% with a specificity of 85.7%, resulting in an accuracy of 78.8%. The sensitivity of ^{18}F-FAMT PET was lower than that of ^{18}F-FDG and ^{11}C-choline, whereas it is noteworthy that the specificity was clearly higher than that of ^{18}F-FDG and ^{11}C-choline.

In this study, we did not evaluate the ability of the agents in grading of malignancy, due to the small histopathological types and tumor grades. Almost all the tumors were in Grade 3. It should be noted that almost all (12/13) the malignant musculoskeletal tumors were correctly diagnosed by ^{11}C-choline PET using a cutoff of 2.6 of SUV. It is recommended that ^{11}C-choline PET might be used as a screening method for malignant musculoskeletal tumors. Watanabe et al. reported [16], in a 75 musculoskeletal tumors patients study, that ^{18}F-FAMT appeared to be inferior to ^{18}F-FDG with regard to malignancy grading, and the latter tracer consequently may be more useful for noninvasive grading in the surgical staging of musculoskeletal sarcoma. Use of ^{18}F-FAMT PET in combination with ^{18}F-FDG PET might be a useful approach for preoperative planning in patients with musculoskeletal tumors. Due to the differences in the accumulation mechanisms of the 3 imaging agents and the difference in patient selection, larger patient populations might be considered to determine which agent is more useful for evaluating the histological grade of musculoskeletal tumors.

5. Conclusion

Our findings indicate that ^{11}C-choline, ^{18}F-FDG, and ^{18}F-FAMT are useful agents for the evaluation of musculoskeletal tumors. In particular, ^{11}C-choline may be superior to the ^{18}F-FDG and ^{18}F-FAMT in detection of musculoskeletal tumors and, thus, may be important for preoperative planning. The use of ^{18}F-FAMT PET in combination with ^{18}F-FDG or ^{11}C-choline PET might be a useful approach for preoperative planning in patients with musculoskeletal tumors. The high uptake of ^{18}F-FDG and ^{11}C-choline in some benign musculoskeletal tumors and tumor-like lesions, especially histiocytic and giant cell-containing lesions, should be aware of in clinical practice.

Acknowledgments

References

[1] H. Jadvar, S. Gamie, L. Ramanna, and P. S. Conti, "Musculoskeletal system," *Seminars in Nuclear Medicine*, vol. 34, no. 4, pp. 254–261, 2004.

[2] K. L. Verstraete, H. J. VanderWoude, P. C. Hogendoorn, Y. DeDeene, M. Kunnen, and J. L. Bloem, "Dynamic contrast-enhanced MR imaging of musculoskeletal tumors: basic principles and clinical applications," *Journal of Magnetic Resonance Imaging*, vol. 5, pp. 311–321, 1996.

[3] H. Zhang, K. Yoshikawa, K. Tamura et al., "[11]C-methionine positron emission tomography and survival in patients with bone and soft tissue sarcomas treated by carbon ion radiotherapy," *Clinical Cancer Research*, vol. 10, no. 5, pp. 1764–1772, 2004.

[4] M. Tian, H. Zhang, N. Oriuchi, T. Higuchi, and K. Endo, "Comparison of ^{11}C-choline PET and FDG PET for the differential diagnosis of malignant tumors," *European Journal*

of Nuclear Medicine and Molecular Imaging, vol. 31, no. 8, pp. 1064–1072, 2004.

[5] M. Tian, H. Zhang, Y. Nakasone, K. Mogi, and K. Endo, "Expression of Glut-1 and Glut-3 in untreated oral squamous cell carcinoma compared with FDG accumulation in a PET study," *European Journal of Nuclear Medicine and Molecular Imaging*, vol. 31, no. 1, pp. 5–12, 2004.

[6] O. E. Nieweg, J. Pruim, R. J. van Ginkel et al., "Fluorine-18-fluorodeoxyglucose PET imaging of soft-tissue sarcoma," *Journal of Nuclear Medicine*, vol. 37, no. 2, pp. 257–261, 1996.

[7] A. C. Kole, O. E. Nieweg, H. J. Hoekstra, J. R. Van Horn, H. S. Koops, and W. Vaalburg, "Fluorine-18-fluorodeoxyglucose assessment of glucose metabolism in bone tumors," *Journal of Nuclear Medicine*, vol. 39, no. 5, pp. 810–815, 1998.

[8] H. Watanabe, T. Shinozaki, T. Yanagawa et al., "Glucose metabolic analysis of musculoskeletal tumours using fluorine-18-FDG PET as an aid to preoperative planning," *Journal of Bone and Joint Surgery*, vol. 82, no. 5, pp. 760–767, 2000.

[9] P. L. Jager, W. Vaalburg, J. Pruim, E. G. E. De Vries, K. J. Langen, and D. A. Piers, "Radiolabeled amino acids: basic aspects and clinical applications in oncology," *Journal of Nuclear Medicine*, vol. 42, no. 3, pp. 432–445, 2001.

[10] K. Tomiyoshi, K. Amed, S. Muhammad et al., "Synthesis of isomers of 18F-labelled amino acid radiopharmaceutical: position 2- and 3-L-18F-α-methyltyrosine using a separation and purification system," *Nuclear Medicine Communications*, vol. 18, no. 2, pp. 169–175, 1997.

[11] T. Inoue, K. Tomiyoshi, T. Higuichi et al., "Biodistribution studies on L-3-[Fluorine-18]Fluoro-α-methyl tyrosine: a potential tumor-detecting agent," *Journal of Nuclear Medicine*, vol. 39, no. 4, pp. 663–667, 1998.

[12] R. Kumar, H. Dhanpathi, S. Basu, D. Rubello, S. Fanti, and A. Alavi, "Oncologic PET tracers beyond [(18)F]FDG and the novel quantitative approaches in PET imaging," *Quarterly Journal of Nuclear Medicine and Molecular Imaging*, vol. 52, no. 1, pp. 50–65, 2008.

[13] T. Hara and M. Yuasa, "Automated synthesis of [^{11}C]choline, a positron-emitting tracer for tumor imaging," *Applied Radiation and Isotopes*, vol. 50, no. 3, pp. 531–533, 1999.

[14] O. Kobori, Y. Kirihara, N. Kosaka, and T. Hara, "Position emission tomography of esophageal carcinoma using (11)C-choline and (18)F-fluorodeoxyglucose: a novel method of preoperative lymph node staging," *Cancer*, vol. 86, no. 9, pp. 1638–1648, 1999.

[15] T. Hara, K. Inagaki, N. Kosaka, and T. Morita, "Sensitive detection of mediastinal lymph node metastasis of lung cancer with ^{11}C-choline PET," *Journal of Nuclear Medicine*, vol. 41, no. 9, pp. 1507–1513, 2000.

[16] H. Watanabe, T. Inoue, T. Shinozaki et al., "PET imaging of musculoskeletel tumours with fluorine-18 α-methyltyrosine: comparison with fluorine-18 fluorodeoxyglucose PET," *European Journal of Nuclear Medicine*, vol. 27, no. 10, pp. 1509–1517, 2000.

[17] K. Hamacher, H. H. Coenen, and G. Stocklin, "Efficient stereospecific synthesis of no-carrier-added 2-[18F]-fluoro-2-deoxy-D-glucose using aminopolyether supported nucleophilic substitution," *Journal of Nuclear Medicine*, vol. 27, no. 2, pp. 235–238, 1986.

[18] H. Zhang, T. Inoue, S. Alyafei, M. Tian, N. Oriuchi, and K. Endo, "Tumour detectability in 2-dimensional and 3-dimensional positron emission tomography using the SET-2400W: a phantom study," *Nuclear Medicine Communications*, vol. 22, no. 3, pp. 305–314, 2001.

[19] J. Aoki, K. Endo, H. Watanabe et al., "FDG-PET for evaluating musculoskeletal tumors: a review," *Journal of Orthopaedic Science*, vol. 8, no. 3, pp. 435–441, 2003.

[20] N. Shinoura, M. Nishijima, T. Hara et al., "Brain tumors: detection with C-11 choline PET," *Radiology*, vol. 202, no. 2, pp. 497–503, 1997.

[21] T. Hara, N. Kosaka, and H. Kishi, "PET imaging of prostate cancer using carbon-11-choline," *Journal of Nuclear Medicine*, vol. 39, no. 6, pp. 990–995, 1998.

[22] T. Inoue, T. Shibasaki, N. Oriuchi et al., "F-18 α-methyl tyrosine PET studies in patients with brain tumors," *Journal of Nuclear Medicine*, vol. 40, no. 3, pp. 399–405, 1999.

[23] J. Johnston, "Giant cell tumor of bone. The role of the giant cell in orthopedic pathology," *Orthopedic Clinics of North America*, vol. 8, no. 4, pp. 751–770, 1977.

[24] L. Ling, M. J. Klein, H. A. Sissons, G. C. Steiner, and R. J. Winchester, "Expression of Ia and monocyte-macrophage lineage antigens in giant cell tumor of bone and related lesions," *Archives of Pathology and Laboratory Medicine*, vol. 112, no. 1, pp. 65–69, 1988.

[25] K. Mészáros, G. J. Bagby, and J. J. Spitzer, "Contribution of different organs to increased glucose consumption after endotoxin administration," *The Journal of Biological Chemistry*, vol. 262, no. 23, pp. 10965–10970, 1987.

[26] R. L. Gamelli, H. Liu, L. K. He, and C. A. Hofmann, "Augmentations of glucose uptake and glucose transporter-1 in macrophages following thermal injury and sepsis in mice," *Journal of Leukocyte Biology*, vol. 59, no. 5, pp. 639–647, 1996.

[27] A. Guhlmann, D. Brecht-Krauss, G. Suger et al., "Chronic osteomyelitis: detection with FDG PET and correlation with histopathologic findings," *Radiology*, vol. 206, no. 3, pp. 749–754, 1998.

[28] W. E. Palmer, D. I. Rosenthal, O. I. Schoenberg et al., "Quantification of inflammation in the wrist with gadolinium-enhanced MR imaging and pet with 2-[F-18]-fluoro-2-deoxy-D-glucose," *Radiology*, vol. 196, no. 3, pp. 647–655, 1995.

[29] L. H. Brudin, S. O. Valind, C. G. Rhodes et al., "Fluorine-18 deoxyglucose uptake in sarcoidosis measured with positron emission tomography," *European Journal of Nuclear Medicine*, vol. 21, no. 4, pp. 297–305, 1994.

[30] J. Aoki, H. Watanabe, T. Shinozaki et al., "FDG PET of primary benign and malignant bone tumors: standardized uptake value in 52 lesions," *Radiology*, vol. 219, no. 3, pp. 774–777, 2001.

[31] H. Zhang, M. Tian, N. Oriuchi et al., "^{11}C-choline PET for the detection of bone and soft tissue tumours in comparison with FDG PET," *Nuclear Medicine Communications*, vol. 24, no. 3, pp. 273–279, 2003.

[32] A. C. Clavo, R. S. Brown, and R. L. Wahl, "Fluorodeoxyglucose uptake in human cancer cell lines is increased by hypoxia," *Journal of Nuclear Medicine*, vol. 36, no. 9, pp. 1625–1632, 1995.

[33] R. Katz-Brull and H. Degani, "Kinetics of choline transport and phosphorylation in human breast cancer cells; NMR application of the zero trans method," *Anticancer Research*, vol. 16, no. 3, pp. 1375–1380, 1996.

Research Article

Ursolic Acid Inhibits Proliferation and Induces Apoptosis of Cancer Cells In Vitro and In Vivo

Xuemei Wang,[1] Fan Zhang,[2] Ling Yang,[2] Ying Mei,[2] Hai Long,[2] Xiaowen Zhang,[3] Jialing Zhang,[2] Qimuge-Suyila,[2] and Xiulan Su[2]

[1] *PET-CT Center, The Affiliated Hospital of Inner Mongolia Medical College, TongDao North Street, Hohhot 010050, China*
[2] *Clinical Medical Research Center of the Affiliated Hospital, Inner Mongolia Medical College, TongDao North Street, Hohhot 010050, China*
[3] *Department of Medical Education, The Affiliated People's Hospital of Inner Mongolia Medical College, Zhaoruda Street, Hohhot 010010, China*

Correspondence should be addressed to Xiulan Su, xlsu@hotmail.com

The aims of the study are to explore the effect of ursolic acid (UA) on the growth of gastric cancer cell line BGC-803 and hepatocellular cancer cell H22 xenograft and to understand the mechanism. UA inhibits growth of BGC-803 cells in vitro in dose-dependent and time-dependent manner. Treated with UA in vivo, tumor cells can be arrested to G0/G1 stage. The apoptotic rate was significantly increased in tumor cells treated with UA both in vitro and in vivo. DNA fragmentation was found in BGC-803 cells exposed to UA. UA activated caspase-3, -8, and -9 and down regulated expression of Bcl-2 in BGC-803 cells. The expression of caspase-3 and -8 was elevated in tumor cells from xenograft treated with UA. ^{18}F-FLT PET-CT imaging confirmed tumor model and UA effectiveness. Our results indicated that UA inhibits growth of tumor cells both in vitro and in vivo by decreasing proliferation of cells and inducing apoptosis.

1. Introduction

Gastric cancer is the second cause of cancer-related death worldwide, and it has now become the first cancer-related death in China. Hepatocellular carcinoma is a primary ma-lignancy of the liver and is the third leading cause of cancer-related death worldwide. There are about 110,000 people died of gastric cancer and hepatocellular carcinoma in China every year, which accounts for 45% (for both cancer combined) mortality worldwide. In addition to surgery, radiotherapy, and chemotherapy, it is essential to find a more effective way to treat gastric cancer and hepatocellular carcinoma.

More and more clinical practice shows that the Chinese medicinal herbs have antitumor activity, which sheds a light on new therapeutic strategy for cancer treatment [1–3]. Ursolic acid (UA) is a pentacyclic triterpene compound and exists in medicinal herbs such as *Oldenlandia diffusa* and *Radix actinidiae*. UA has been shown to have the effects of anti-inflammatory, antioxidant, and antitumor [4–6]. Studies have found that UA can inhibit the activities of DNA polymerase and DNA topoisomerase and decrease the rate of cell proliferation [7]. Moreover, UA can induce apoptosis of tumor cell by increasing the level of intracellular calcium ion [8], suppressing the expression of FoxM1 [9], and upregulating of death receptors [10]. In this study, we evaluated the effect of UA treatment on the gastric cancer cell and the hepatocellular carcinoma xenograft.

2. Materials and Methods

2.1. Material. UA was purchased from Shanxi Huike Plant Development Corporation (UR: 2003 0610 purity ≥98%). 3-(4,5-dimethylthiazol-2-yl)-2,5-diphenyltetrazolium bromide (MTT) and DMSO were purchased from SIGMA Company. Annexin-V-FITC apoptosis kit was purchased from BD Biosciences. RPMI 1640 and calf serum was purchased from GIBCO, Invitorgen. All the antibodies used in

western blot (rabbit antihuman β-actin, mouse antihuman procaspase-3, mouse antihuman procaspase-8, mouse antihuman procaspase-9, mouse antihuman Bcl-2, and mouse antihuman Bax antibodies) were purchased from SANTA CRUZ Biotechnology. Far infrared-marked goat antirabbit or mouse secondary antibodies were purchased from ROCKLAND Immunochemicals. Odyssey far infrared scanner was purchased from LI-COR Biosciences (USA).

2.2. Cell Lines and Culture Conditions. BGC-803 cell and hepatocellular carcinoma cell line H22 (ATCC, USA) were generous gifts from Dr. Yang Ke at the Cancer Research Center, Peking University. Gastric cancer cell line BGC-803 was maintained in RPMI-1640 with 10% calf serum. Cells were grown at $37°C$ in a CO_2 incubator. The cells in the exponential growth phase were collected for cell proliferation, cell cycle, and apoptosis assay.

2.3. Mouse Model. Ten male and ten female kunming mice were bought from The Research Center for Laboratory Animal Science in Beijing, and H22 cells of exponential growth phase were injected subcutaneously into right front axilla of kuming mice. The mice were divided into two groups with equal numbers of male and female mice. One group was given 0.2 mL/mouse physiological saline by oral administration as negative control; another group was given 2.53 mg/mouse UA everyday for 10 days. Mice were sacrificed at the end of the treatment. Tumors tissues were either fixed in 75 ethanol filtered after treated by 500 mesh to get the single cell suspension for flow cytometry analysis or fixed in 4% paraformaldehyde for pathological analysis. Samples prepared from tumor tissues were also flash frozen in liquid nitrogen for Western blot analysis. All animal experiments were approved by Animal Care and Use Committee, Inner Mongolia Medical College.

2.4. Cell Proliferation Assay. Cell proliferation was assessed by MTT staining. $250 \mu L$ of BGC-803 cells (1.2×10^4/mL) were added to each well in the 96-well plate. UA was added to the final concentration of $10–60 \mu M$. DMSO and culture medium were added as control. Each group was performed in 8 wells. MTT was added 12 h, 24 h, 36 h, and 48 h, respectively, after incubation, and the absorbance values were examined. The inhibiting proliferation rates were calculated using the following equation:

Inhibiting proliferation rate (%)

$$= \frac{(\text{A values of control group} - \text{A values of treated group})}{\text{A values of control group}}$$

$$\times 100\%.$$

$$(1)$$

2.5. ^{18}F-FLT PET-CT Imaging. Proliferation of tumor cells in mouse xenograft model was examined with positron-emission tomography-computed tomography (PET-CT) using ^{18}F fluoro-L-thymidine (FLT). ^{18}F-FLT was given to the mouse by tail intravenous injection. Mice were anesthetized by ether and then were imaged by PET-CT.

2.6. Cell Cycle and Apoptosis Assay. BGC-803 cells were treated with UA either at concentration of median inhibition concentration (IC_{50}) (24 h) for 24 h, or at concentration of IC_{50} (36 h) for 36 h, and then cells were fixed in 75% ethanol. Tumor cells obtained from xenograft were also fixed in 75% ethanol after filtered by 500 mesh. The single-cell suspension obtained above was used for apoptosis analysis using flow cytometry and for cell cycle analysis using ModFit analysis. DNA was extracted from BGC-803 cells according to protocol provided by manufacturer and then isolated in the 1.5% agarose gel by electrophoresis (65 V, 1.75 h). Photographs were taken using a gel-imaging system to detect DNA Ladder.

2.7. Western Blot Analysis. Expression of procaspase-3, -8, and -9, Bcl-2, and Bax in BGC-803 treated with UA for 36 h at IC_{50} and expression of caspase-3 and -8 in tumor cells obtained from xenograft was determined by western blot. Cells were treated with RIPA buffer (1% deoxycholate, 0.1% SDS). Concentration of protein was determined by BCA assay. Proteins were transferred to PVDF membrane after separation by SDS-PAGE and incubated with proper primary and secondary antibodies. The signal was detected by far infrared scanner. Result was analyzed by Quantity One. The relative amount of protein expressed was determined by using β-actin as an internal control.

2.8. Statistical Analysis. Statistical analysis was performed using the program SPSS13.0. In each experimental group, one-factor analysis of variance and MANOVA of repeated measuring were used. The t-test was used for comparison between groups. A value of $P < .05$ was considered to be statistically significant. IC_{50} values at different time points were calculated by Probit Analysis.

3. Results

3.1. Inhibition of Proliferation in BGC-803 Cells. Proliferation of BGC-803 cells was examined to assess whether UA had inhibitory effect on BGC-803. Cells were treated with different concentrations of UA (10, 20, 30, 40, 50, 60 μmol/L) for 12, 24, 36, 48 h, respectively. Compared with control, UA (20–60 μmol/L) inhibited BGC-803 cell proliferation in dose- and time-dependent manners. However, 10 μmol/L of UA did not show inhibitory effect (Figure 1(a)). The IC_{50} of UA at different time points (12 h, 24 h, 36 h and 48 h) were $61.29 \mu M$, $43.78 \mu M$, $35.94 \mu M$, and $24.95 \mu M$, respectively (Table 1).

3.2. Induction of Apoptosis in BGC-803 Cells. Morphological changes of BGC-803 cells after UA treatment. Cells not treated with UA showed single-layer adherence growth with rich cytoplasm, round or oval nuclei. Cells exposed to UA rounded up, lacked cell-cell contact with low density of cell (Figure 1(b)). Furthermore, H&E staining revealed

TABLE 1: IC$_{50}$ of UA at different time points in human gastric cancer cell BGC-803.

	IC$_{50}$ (uM)	X^2	P	Probit
12 h	61.29	0.005	1.0	7.60-13.5x
24 h	43.78	0.027	1.0	5.49-9.01x
36 h	35.94	0.07	0.99	3.08-4.79x
48 h	24.95	0.018	1.0	5.74-8.08x

that cells treated with UA showed typical morphology for apoptosis: nuclear fragmentation, chromatin condensation, and loss of membrane asymmetry (Figure 1(c)). In addition, fragments of degraded DNA were observed in agarose gel electrophoresis for BGC-803 cells treated with 43.78 and 35.94 μM UA. This was an indication that apoptosis occurred in the cells. For the control cells without treatment, no fragment of DNA was observed (Figure 1(d)). We further evaluated the apoptotic rate by Annexin-V staining. BGC-803 cells treated with UA had more apoptotic cells than cells treated with DMSO or without treatment ($F = 72.579$, $P < .01$, Figures 1(e) and 1(f)), while there was no significant difference in apoptosis between cells treated with DMSO or without treatment indicating that apoptosis was specifically induced by UA treatment.

We investigated the mechanism how UA induced apoptosis. Expression of Pro caspase-3, -8, and -9, Bcl-2, Bax was detected by Western blot (Figure 1(g)). Relative amount of protein was calculated (Figure 1(h)). Our data showed that expression of pro caspase-3, -8, and -9 protein declined after UA treatment ($P < .05$), indicating that activated caspase-3, -8, -9 proteins were induced by UA treatment. Expression of Bcl-2 protein was downregulated by UA treatment ($P < .05$), while Bax protein expression did not show significant change with and without UA treatment. Our result suggested that UA may activate caspase cascade and downregulate Bcl-2 protein to induce apoptosis in gastric cancer cell line BGC-803.

3.3. Inhibition of Tumor Growth in Mouse Xenograft Model.
Compared to negative control, xenografts which were treated with UA were robust and had more weight (Table 2). There was 52.8% inhibition rate of tumor growth in UA treatment xenografts. Tumor tissue was examined under optical microscope after H&E staining. Tumor cells in negative control resembled nests or cords and showed vigorous mitosis. Nuclei of tumor cells were round or oval; while there was more necrosis and apoptosis in UA treatment group, density of tumor cells decreased. We examined the proliferation of tumor cells in xenografts by PET-CT. Xenografts was injected with ^{18}F-FLT, and the whole mouse was imaged by PET-CT. Focal ^{18}F-FLT uptake could be observed in tumor and abdominal cavity in xenografts of PS control (Figure 2(a) upper panel). Xenografts with UA treatment showed lower ^{18}F-FLT uptake in tumor (Figure 2(a) lower panel). The image of PET-CT showed directly that proliferation of tumor cells declined by UA treatment in vivo. To elucidate the mechanism how UA inhibited proliferation of tumor cells, we examined cell cycle of these tumor cells in xenografts.

Percentage of 38.71 ± 3.27 of the tumor cells treated with UA were in G0/G1 stage ($P < .05$, Figure 2(b)), but $48.97 \pm 3.96\%$ and $23.53 \pm 5.97\%$ cells were in S or G2/M stage for the negative control, suggesting that UA treatment decreased proliferation of tumor cells in mouse xenograft model.

3.4. Induction of Apoptosis in Mouse Xenograft Model.
In addition to cell cycle, we also examined the apoptosis of tumor cells in xenografts. Tumor cells in xenografts treated with UA had more apoptosis as shown in Figure 2(b) (sub-G1). The apoptotic tumor cells were quantified by flow cytometry after cells were incubated with FITC conjugated Annexin-V. Comparison of apoptotic rate of the PS control to the UA treatment group revealed statistically significant different (12.91 ± 1.43 for PS control versus 37.24 ± 3.85 for UA treatment, $P < .05$, Figure 2(c)), indicating that UA treatment could induce apoptosis of tumor cells in mouse xenograft model. Furthermore, we examined the expression of Caspase-3, -8 in these tumor cells. The result of western blot showed that the protein level of Caspase-3, -8 was elevated after treatment with UA (Figure 2(d)). Our data suggested that UA may induce apoptosis through upregulation of Caspase-3 and 8.

4. Discussion

UA is one anticancer active compound in Chinese anticancer herbal medicines. Previous studies showed that UA could inhibit growth of colon cancer cells, endometrial cancer cells, and melanoma cells [11–13]. It has been reported that UA inhibited growth of tumor cells through multiple functions, such as cytotoxicity [14, 15], induction of apoptosis [9, 10, 16, 17], and prevention of angiogenesis [18, 19].

Our results showed that UA decreased proliferation of tumor cells both in vitro and in vivo. UA inhibited proliferation of BGC-803 cells in dose- and time-dependent manners. Inhibition rate of tumor growth is 52.8% in H22 xenografts treated with UA. Cell cycle of tumor cells from xenagrafts treated with UA was arrested in G0/G1 stage. Our data are consistent with the results of lung cancer cell A549 treated with UA [20], Hsu showed that UA up-regulated P21 expression through a P53-dependent manner and decreased expression of cyclins and their activating partner cdks. UA may block cell cycle progression in G0/G1 stage in gastric cancer cell and tumor cells from xenografts by activating P53/P21 pathway concomitant with inactivating cyclins/cdks.

Mammalian cell apoptosis is initiated either by mitochondria-mediated or Fas receptor coupled extrinsic signals mediated pathways. Many apoptotic-related genes involved in these processes, including proapoptotic genes (Bax, Bid, and Bak), antiapoptotic genes (Bcl-Xl and Bcl-2), and cysteine proteases called caspases (caspase-3, -8, and -9). Bcl-2 family plays an important role in preventing apoptosis. The ratio of Bax to Bcl-2 can be used to assess apoptosis. The higher this ratio is, the more possibility apoptosis would happen, and vice versa. We found that the expression of Bcl-2 protein decreased, but the level of Bax protein did
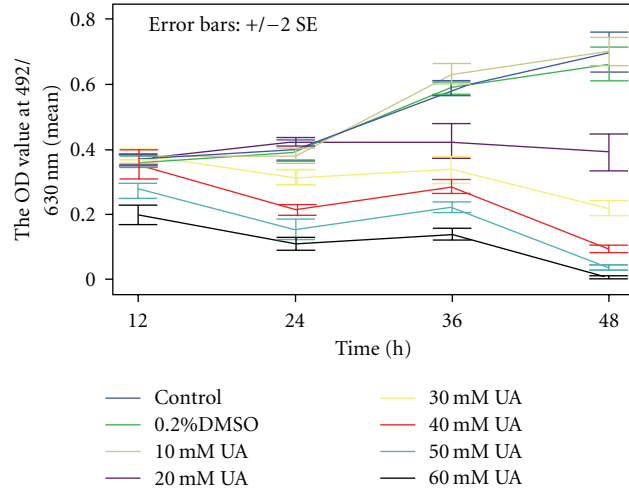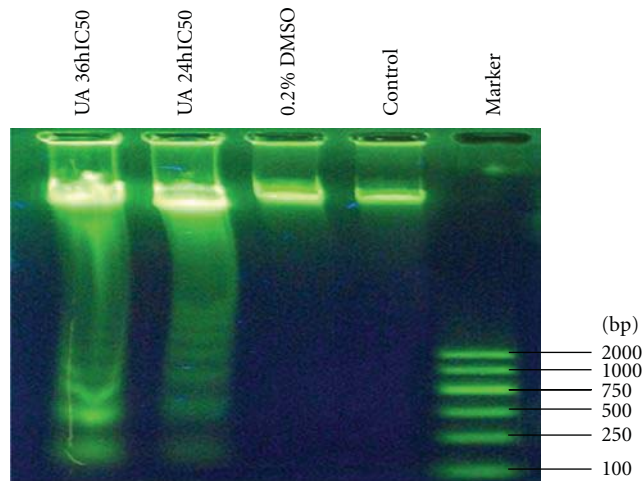
(a)
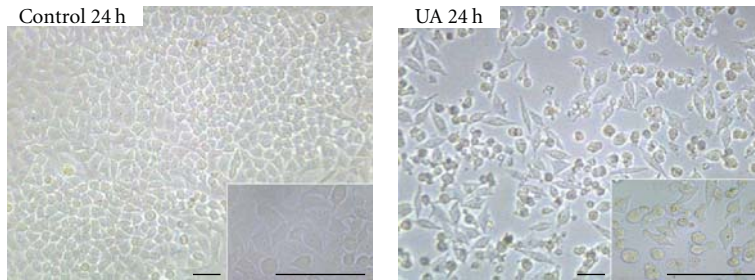
(b)
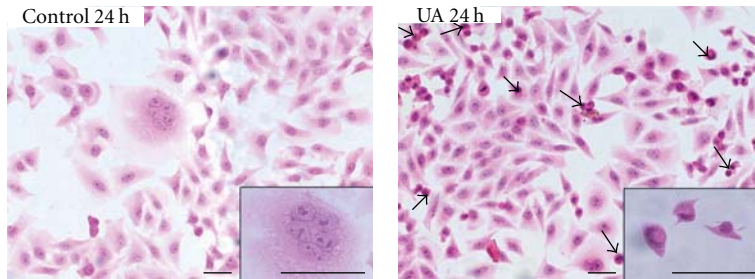
(c)

(d)

FIGURE 1: Continued.
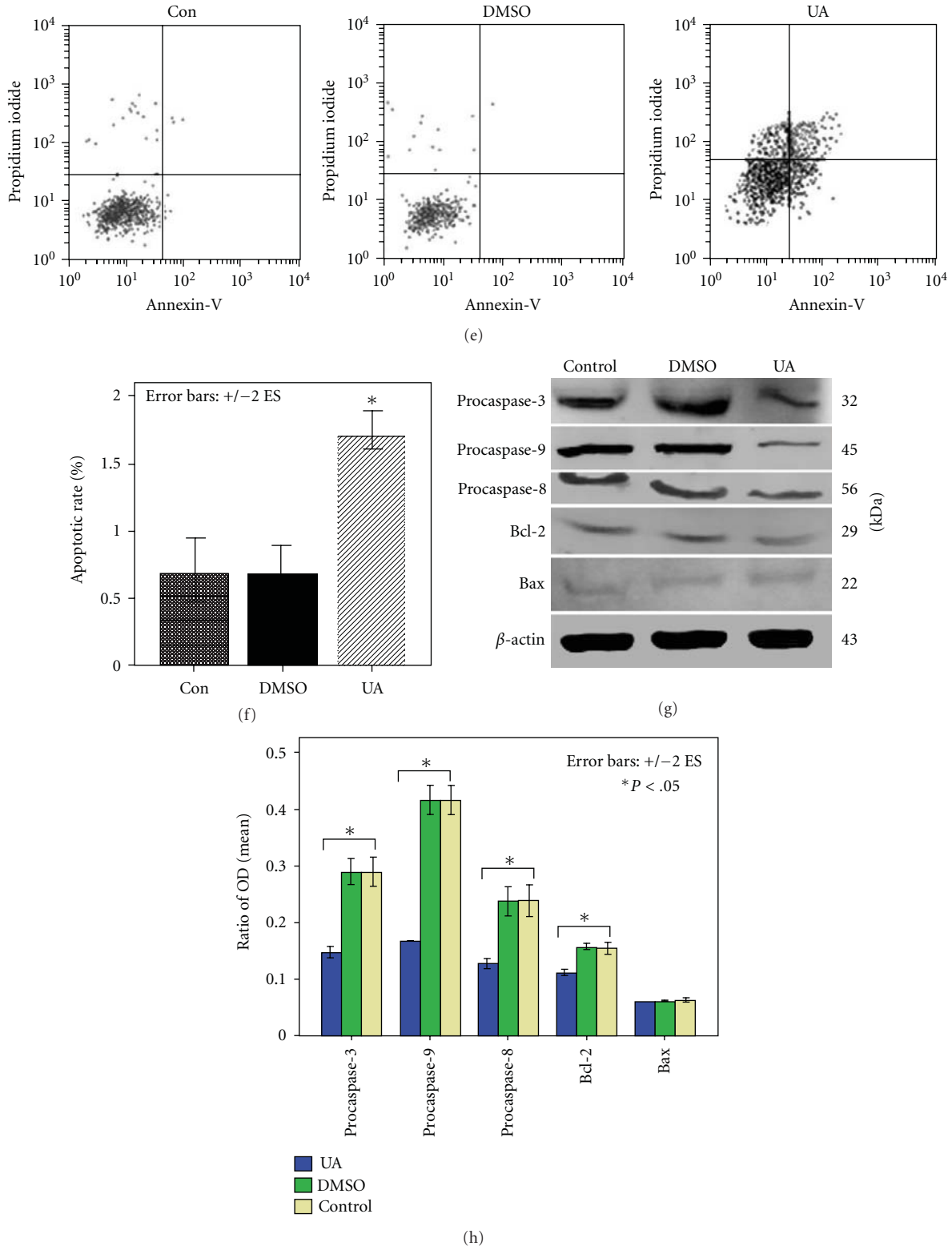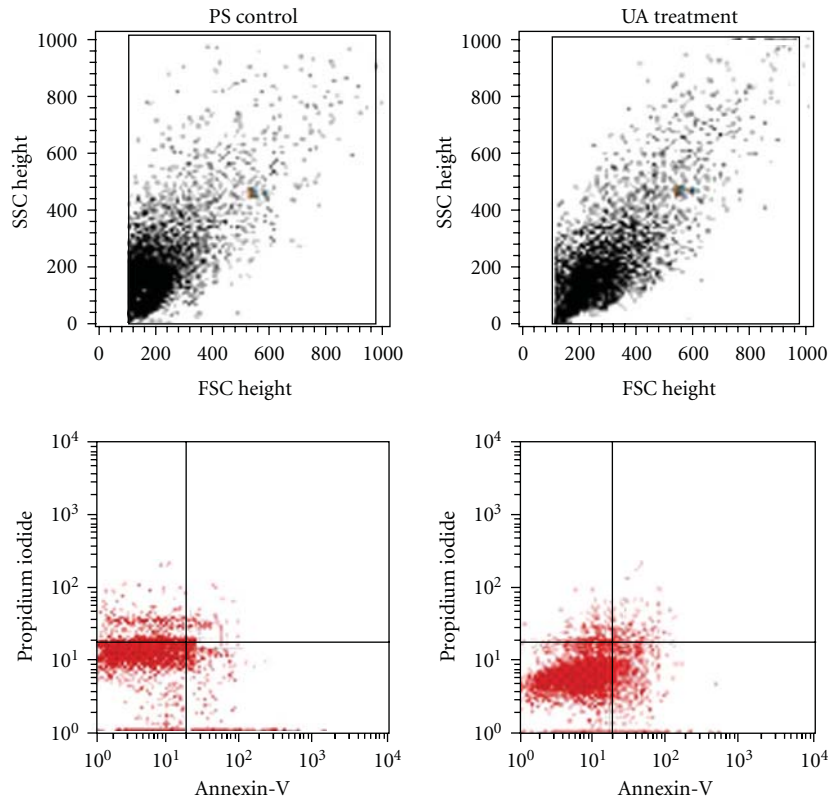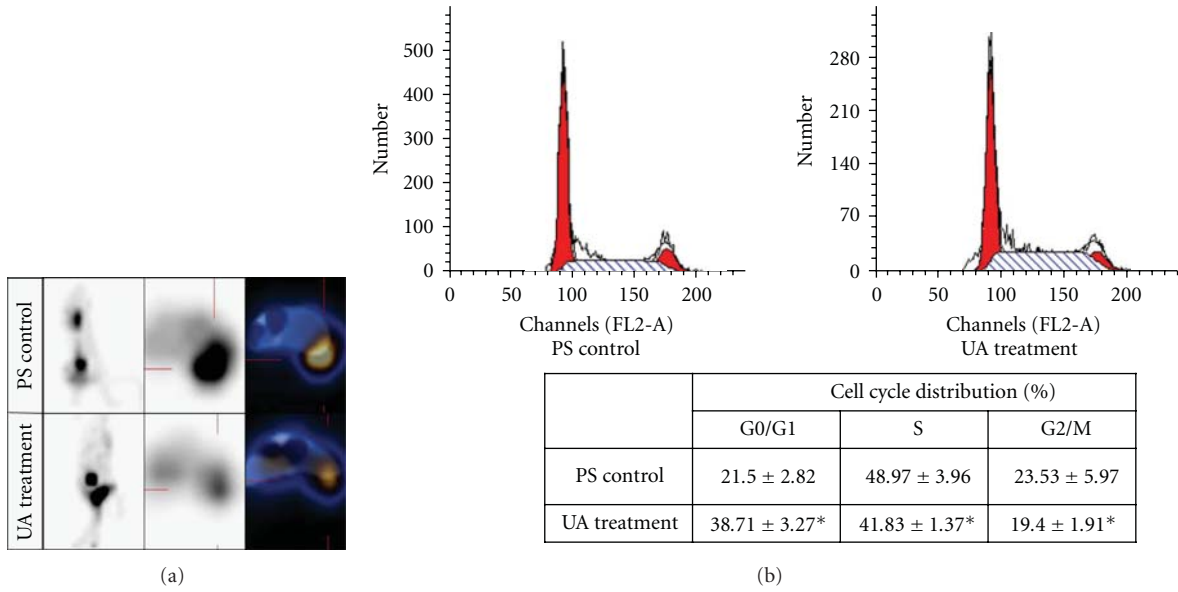
(e)

(f)

(g)

(h)

FIGURE 1: UA inhibited proliferation and induced apoptosis in gastric cancer cell BGC-803. (a) Inhibition of proliferation of BGC-803 was assessed by MMT staining. (b) Morphological changes of BGC-803 cells after UA (IC_{50} (24 h)) treatment for 24 h (Bar represents 200 μm); magnified image of cells was showed in corner (Bar represents 200 μm). (c) H&E staining of BGC-803 cells after UA (IC_{50} (24 h)) treatment for 24 h (Bar represents 200 μm), and arrows indicated apoptotic cells; magnified image of cells was showed in corner (Bar represents 200 μm). (d) DNA ladder was found in BGC-803 cells treated with UA (IC_{50} (24 h) and IC_{50} (36 h)), not in BGC-803 cells treated with 0.2% DMSO or without treatment. (e) Apoptosis of BGC-803 cells induced by UA was detected by Annexin-V staining and flow cytometry. (f) was the quantified data from experiment showed in (e). Apoptotic rate was 0.66 ± 0.15, 0.67 ± 0.08, and 1.69 ± 0.11 in control, DMSO, and UA treated cells, respectively, ($*P < .01$). (g) Western blot showed expression of apoptotic related genes in BGC-803 cell treated with DMSO, UA and without treatment; β-actin was used as internal control. (h) showed related amount of protein from (g) ($*P < .05$).

(a)

	Cell cycle distribution (%)		
	G0/G1	S	G2/M
PS control	21.5 ± 2.82	48.97 ± 3.96	23.53 ± 5.97
UA treatment	38.71 ± 3.27*	41.83 ± 1.37*	19.4 ± 1.91*

(b)

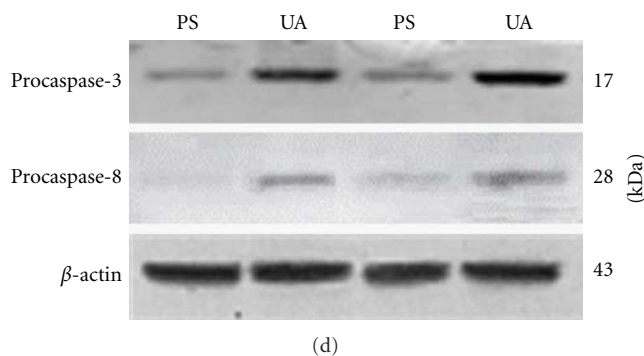|	AI (X% ± S)
PS control	12.91 ± 1.43
UA treatment	37.24 ± 3.85*

(c)

FIGURE 2: Continued.

(d)

FIGURE 2: UA inhibited proliferation and induced apoptosis in hepatocellular carcinoma cell H22 mouse xenograft. (a) Xenografts treated with PS or UA were imaged by PET-CT. (b) Cell cycle of tumor cells from xenografts treated with PS or UA was examined. Cell cycle distribution was showed in the table ($*P < .05$). (c) Apoptosis of tumor cells from xenografts induced by UA was detected by Annexin-V staining and flow cytometry. Quantified data showed in the table below ($*P < .05$). (d) Western blot showed expression of Caspase-3 and Caspase-8 in tumor cells from xenografts treated with PS or UA.

TABLE 2: Weight of xenografts treated with PS or UA.

	Day 1	Day 3	Day 5	Day 7	Day 9	Day 11
PS control (g)	22.04 ± 0.73	23.93 ± 0.83	25.41 ± 0.65	27.46 ± 1.35	29.51 ± 1.47	30.05 ± 1.51
UA treatment (g)	21.88 ± 0.57	24.85 ± 0.53	27.17 ± 0.89	29.39 ± 1.62	31.66 ± 2.43	32.68 ± 2.65

not change in BGC-803 cells treated with UA. The ratio of Bax/Bcl-2 increased, which would lead to apoptosis. Previous studies showed that Bax expression increased and Bcl-2 expression decreased in lung cancer cell line A549 treated with UA [20]. Expression of Bax protein significantly increased in human breast cancer cell line MCF-7 [21]. The results above are different from ours, suggesting that UA may function differently in different type of cancer cells to induce apoptosis. Caspase-3 is a key protease in mammalian cell apoptosis. We found that caspase-3 was activated in BGC-803 cells and H22 cell xenograft treated with UA. It is reported that cytochrome C was released and caspase-3 was activated in BGC-823 cells with UA treatment [22]. Our data showed that caspase-8 and -9 were all activated in BGC-803 cells, indicating that UA induced apoptosis through two classical apoptotic pathways. Studies have demonstrated that caspase-3, -8, and -9 are necessary for UA inducing tumor cell apoptosis [23]. Our findings of decreased level of Bcl-2 with no change of Bax and activated caspase-8 and -9 in cell line BGC-803 enrich the understanding of mechanisms how UA induces apoptosis in gastric cancer cell line BGC-803. Furthermore, we found expression of caspase-8 was elevated in tumor cells obtained from H22 xenograft, indicating that UA also can induce apoptosis in vivo.

5. Conclusions

In summary, we found that UA inhibited growth of gastric cancer cell line BGC-803 in dose-dependent and time-dependent manner in vitro. UA treatment arrested tumor cells from xenograft to G0/G1 stage in vivo. The apoptotic rate was significantly increased in tumor cells treated with UA both in vitro and in vivo ($P < .05$). DNA fragmentation

was found in BGC-803 cells exposed to UA. UA activated caspase-3, -8, -9 and downregulated expression of Bcl-2 in BGC-803 cells, but had no effect on expression of Bax. Expression of caspase-3 and -8 were elevated in tumor cells from xenograft treated with UA. UA inhibited growth of tumor cells in vitro and vivo by decreasing proliferation and inducing apoptosis. Understanding the mechanism of UA will help us fully understand how Chinese medical herbs work.

Conflict of Interests

The authors declare that they have no conflict of interests.

Acknowledgments

References

[1] Y. Xiao, Y. Fan, B. Chen, Q. Zhang, and H. Zeng, "Polysaccharides from Scurrula parasitica L. inhibit sarcoma S180 growth in mice," *Zhongguo Zhongyao Zazhi*, vol. 35, no. 3, pp. 381–384, 2010.

[2] T. Gan, Z. Wu, L. Tian, and Y. Wang, "Chinese herbal medicines for induction of remission in advanced or late gastric cancer," *Cochrane Database of Systematic Reviews*, no. 1, Article ID CD005096, 2010.

[3] Z. G. Zhong, J. L. Huang, H. Liang et al., "The effect of gallic acid extracted from leaves of Phyllanthus emblica on apoptosis of human hepatocellular carcinoma BEL-7404 cells," *Zhong Yao Cai*, vol. 32, no. 7, pp. 1097–1101, 2009.

[4] N. Banno, T. Akihisa, H. Tokuda et al., "Triterpene acids from the leaves of Perilla frutescens and their anti-inflammatory and antitumor-promoting effects," *Bioscience, Biotechnology and Biochemistry*, vol. 68, no. 1, pp. 85–90, 2004.

[5] R. E. De Angel, S. M. Smith, R. D. Glickman, S. N. Perkins, and S. D. Hursting, "Antitumor effects of ursolic acid in a mouse model of postmenopausal breast cancer," *Nutrition and Cancer*, vol. 62, no. 8, pp. 1074–1086, 2010.

[6] A. A. Ramos, C. Pereira-Wilson, and A. R. Collins, "Protective effects of ursolic acid and luteolin against oxidative DNA damage include enhancement of DNA repair in Caco-2 cells," *Mutation Research*, vol. 692, no. 1–2, pp. 6–11, 2010.

[7] Y. Mizushina, A. Iida, K. Ohta, F. Sugawara, and K. Sakaguchi, "Novel triterpenoids inhibit both DNA polymerase and DNA topoisomerase," *Biochemical Journal*, vol. 350, no. 3, pp. 757–763, 2000.

[8] F. Lauthier, L. Taillet, P. Trouillas, C. Delage, and A. Simon, "Ursolic acid triggers calcium-dependent apoptosis in human Daudi cells," *Anti-Cancer Drugs*, vol. 11, no. 9, pp. 737–745, 2000.

[9] J. S. Wang, T. N. Ren, and T. Xi, "Ursolic acid induces apoptosis by suppressing the expression of FoxM1 in MCF-7 human breast cancer cells," *Medical Oncology*, 2010. In press.

[10] S. Prasad, V. R. Yadav, R. Kannappan, and B. B. Aggarwal, "Ursolic acid, a pentacyclin triterpene, potentiates TRAIL-induced apoptosis through p53-independent up-regulation of death receptors: evidence for the role of reactive oxygen species and JNK," *The Journal of Biological Chemistry*, vol. 286, no. 7, pp. 5546–5557, 2011.

[11] Y. Achiwa, K. Hasegawa, T. Komiya, and Y. Udagawa, "Ursolic acid induces Bax-dependent apoptosis through the caspase-3 pathway in endometrial cancer SNG-II cells," *Oncology Reports*, vol. 13, no. 1, pp. 51–57, 2005.

[12] D. Andersson, J. J. Liu, A. Nilsson, and R. D. Duan, "Ursolic acid inhibits proliferation and stimulates apoptosis in HT29 cells following activation of alkaline sphingomyelinase," *Anticancer Research*, vol. 23, no. 4, pp. 3317–3322, 2003.

[13] P. O. Harmand, R. Duval, C. Delage, and A. Simon, "Ursolic acid induces apoptosis through mitochondrial intrinsic pathway and caspase-3 activation in M4Beu melanoma cells," *International Journal of Cancer*, vol. 114, no. 1, pp. 1–11, 2005.

[14] K. H. Lee, Y. M. Lin, T. S. Wu et al., "The cytotoxic principles of Prunella vulgaris, Psychotria serpens, and Hyptis capitata: ursolic acid and related derivatives," *Planta Medica*, vol. 54, no. 4, pp. 308–311, 1988.

[15] M. Ganblod, J. Barker, R. Ma, L. Jones, and M. Carew, "Cytotoxicity and bioavailability studies on a decoction of Oldenlandia diffusa and its fractions separated by HPLC," *Journal of Ethnopharmacology*, vol. 131, no. 2, pp. 396–403, 2010.

[16] J. Li, W. J. Guo, and Q. Y. Yang, "Effects of ursolic acid and oleanolic acid on human colon carcinoma cell line HCT15," *World Journal of Gastroenterology*, vol. 8, no. 3, pp. 493–495, 2002.

[17] W. Huang, J. Huang, D. Zhang, R. Zhang, and Z. Liao, "Study on anti-invasive effect and apoptosis induction of pentacyclic triterpenoid in human lung cancer cells," *Chinese Journal of Lung Cancer*, vol. 6, no. 4, pp. 254–257, 2003.

[18] M. Kanjoormana and G. Kuttan, "Antiangiogenic activity of ursolic acid," *Integrative Cancer Therapies*, vol. 9, no. 2, pp. 224–235, 2010.

[19] C. C. Lin, C. Y. Huang, M. C. Mong, C. Y. Chan, and M. C. Yin, "Antiangiogenic potential of three triterpenic acids in human liver cancer cells," *Journal of Agricultural and Food Chemistry*, vol. 59, no. 2, pp. 755–762, 2011.

[20] Y. L. Hsu, P. L. Kuo, and C. C. Lin, "Proliferative inhibition, cell-cycle dysregulation, and induction of apoptosis by ursolic acid in human non-small cell lung cancer A549 cells," *Life Sciences*, vol. 75, no. 19, pp. 2303–2316, 2004.

[21] W. Zhang, Y. Li, G. Zhang, J. Lü, and H. Ou, "Experimental study on MCF-7 cell apoptosis induced by ursolic acid," *Zhong Yao Cai*, vol. 28, no. 4, pp. 297–301, 2005.

[22] J. Zhang, T. Deng, and H. Chen, "Ursolic acid inhibits proliferation and induces apoptosis in human gastric carcinoma cell line BGC-823," *Medical Journal of Wuhan University*, vol. 26, no. 3, pp. 375–378, 2005.

[23] Y. H. Choi, J. H. Baek, M. A. Yoo, H. Y. Chung, N. D. Kim, and K. W. Kim, "Induction of apoptosis by ursolic acid through activation of caspases and down-regulation of c-IAPs in human prostate epithelial cells," *International Journal of Oncology*, vol. 17, no. 3, pp. 565–571, 2000.

Research Article

Brown Adipose Tissue Can Be Activated or Inhibited within an Hour before ^{18}F-FDG Injection: A Preliminary Study with MicroPET

Chenxi Wu, Wuying Cheng, Haiqun Xing, Yonghong Dang, Fang Li, and Zhaohui Zhu

Department of Nuclear Medicine, Peking Union Medical College Hospital,
Chinese Academy of Medical Sciences and Peking Union Medical College, Beijing 100730, China

Correspondence should be addressed to Zhaohui Zhu, zzh_1969@yahoo.com.cn

Brown adipose tissue (BAT) is emerging as a potential target for treating human obesity. It has been indicated that BAT is rich in innervations of sympathetic nerve control. Using ^{18}F-FDG microPET imaging, this study aims at evaluating how factors related to sympathetic activation/inhibition changed BAT metabolism of mice. BAT ^{18}F-FDG uptake were semiquantitatively evaluated in different groups of mice under temperature (cold or warm stimulus) or pharmacological interventions (norepinephrine, epinephrine, isoprenaline, or propranolol) and were compared with the corresponding controls. It was found that BAT activation can be stimulated by cold exposure ($P = 1.96 \times 10^{-4}$), norepinephrine ($P = .002$), or both ($P = 2.19 \times 10^{-6}$) within an hour before ^{18}F-FDG injection and can also be alleviated by warming up ($P = .001$) or propranolol lavage ($P = .027$). This preliminary study indicated that BAT function could be evaluated by ^{18}F-FDG PET imaging through short-term interventions, which paved the way for further investigation of the relationship between human obesity and BAT dysfunction.

1. Introduction

Brown adipose tissue (BAT) is a kind of fat tissue different from white adipose tissue (WAT). In mammals, BAT has its function mainly in nonshivering thermogenesis, responsible for control of body temperature and regulation of energy balance [1]. BAT is commonly found in human newborns and small mammals, and it is previously thought that there is only a vestigial amount of BAT in adulthood [2]. Recently, ^{18}F-FDG PET/CT demonstrated a relatively broad distribution of functional BAT in adult human, mainly along the way of sympathetic nerve control, such as paravertebral and periadrenal regions [3, 4]. These functional BATs have drawn our attention as a potential therapeutic target for inducing weight loss through its energy expenditure pathway [2, 5], because excision or denervation of interscapular BAT can produce abnormal increase in the amounts of WAT in those animals, meaning that they are becoming fatter [6]. Some other studies, though showing limited success, have already tried to activate BAT by stimulating SNS to control

body weight, using, for instance, β_3-adrenoceptor agonists CL-316243 or L-796568 [7, 8]. But none of them monitored BAT metabolic function during their researches.

Cold stimulus has been proved to increase ^{18}F-FDG uptake, an indicator of BAT metabolism, in either animal or human studies [9, 10]. Cold can activate sympathetic nerve system (SNS) to excrete norepinephrine, and then the BAT, which is rich in sympathetic nerve terminals, will produce more heat [11]. Genomic studies have indicated that the heat production is related to uncoupling protein 1 (UCP1), which is highly expressed in the mitochondria of BAT cells and can convert glucose and free fatty acid into heat [12]. For further evaluation of how the influence factors related to SNS changed the BAT metabolism, this study investigated several interventions to stimulate or inhibit SNS and BAT metabolism of mice, and under the application of microPET, BAT metabolic statuses were clearly seen in vivo, showing different degree of FDG uptake under different interventions which could be semiquantitatively analyzed in real time. MicroPET served as a useful tool in monitoring

BAT function under different interventions and showed the potential to guide further study of the relationship between BAT metabolism and obesity and diabetes.

2. Materials and Methods

2.1. Animals and Grouping. Five-to-ten-wk female Kunming mice (provided by Beijing Medical College Animal Breeding Center) were enrolled in this study (mean body weight = 25 g). All animals were kept in the Animal Breading Center of PUMCH with constant room temperature of 21°C. Food and water were given ad libitum. Control mice ($n = 12$) were examined under room temperature of 20-21°C. Three intervention groups were involved in this study (Table 1). In physical intervention group, mice were exposed to cold ($n = 6$, 6°C-7°C, $t = 1$ h), cold and then warm ($n = 6$, 6°C-7°C, $t = 1$ h, and then 35°C-36°C, $t = 1.5$ h), or only warm ($n = 6$ and $t = 1.5$ h). For pharmacological stimulation group, under 21°C mice received intraperitoneal injection of norepinephrine (NE, 0.4 mg/kg, $n = 5$), epinephrine (0.02 mg/kg, $n = 5$), isoprenaline (0.016 mg/Kg, $n = 6$), respectively, or both cold and NE (NE: 0.04 mg/kg, $n = 7$). For pharmacological inhibition group, cold pre-exposure mice received intragastric administration of propranolol (13.2 mg/kg, $n = 3$) or saline ($n = 3$).

2.2. Temperature Interventions. Control mice were kept in the examination room with constant temperature of 20°C-21°C without physical intervention or pharmacological stimulation. For cold intervention, we put the mice in a plastic box and kept them in a temperature-regulative refrigerator (BC-185FA, Aucma, China) with a constant temperature of 6°C-7°C (measured by a thermometer in the refrigerator) for 1 h. For warm stimuli, we placed the mice in a plastic box laid above a power-regulative heating pad (ML-1.5-4, Tianjin Tester Company, China) with the temperature of 35°C-36°C (measured by a thermometer in the box) for 1 h and kept warming the mouse for 0.5 h after FDG injection. All these animals were provided with food and water supply during the interventions.

2.3. Pharmacological Interventions. Norepinephrine (Tianjin Jinhui Amino Acids Co.), epinephrine (Beijing Yongkang Phar Co.), and isoprenaline (Shanghai Harvest Phar Co.) were diluted with saline and injected into peritoneal cavity of mouse in the volume of 100 μL (0.4 mg/kg), 100 μL (0.02 mg/kg), and 30 μL (0.016 mg/Kg), respectively, 1 h before FDG injection. Propranolol tablets (Tianjin Lisheng Phar Co.) were dissolved in saline to 1 mg/mL and administered intragastrically through a small animal lavage needle in the volume of 300 μL (13.2 mg/kg) per mouse 1 h before FDG injection. To monitor the combination effect of cold stimuli and NE, we performed the cold stimuli protocol as stated and gave NE injection with 0.04 mg/kg 1 h before FDG injection. All of these pharmacological interventions were performed under room temperature of 21°C, and after interventions, water and food were provided.

TABLE 1: Groups according to interventions and the number of mice in each group.

Interventions	Mouse number
Temperature intervention	**18**
Cold exposure	6
Cold exposure + warm stimuli	6
Warm stimuli	6
Pharmacological stimulation	**23**
Norepinephrine (NE)	5
epinephrine	5
isoprenaline	6
NE + cold exposure	7
Pharmacological inhibition	**6**
Cold + propranolol	3
Cold + saline	3
Controls	**12**

2.4. MicroPET Protocol. All mice were examined under nonfasted status. After physical or pharmacological interventions, 3.7 MBq ^{18}F-FDG was injected into peritoneal cavity for each mouse. Water and food was supplied after FDG injection. Anesthesia using Summit AS-1-000-7 animal anesthesia system (USA) was performed with 1.5% isoflurane (with O_2 combination of 2 liter per minute) 40 min later. PET data acquisition procedure was performed under Siemens Inveon system 10 min after anesthesia when mice were totally unconscious. Acquisition procedure lasted for 300 sec for each mouse. Anesthesia was continued during the scanning process with the same flow rate through a facemask designed for small animal.

2.5. Data Analysis. All microPET images were studied by two researchers (Wu and Cheng) on a high-resolution computer screen applying ASIPro VM software. Both visual and semiquantitative analyses were performed for each mouse. For visual analysis, the two researchers compared the interscapular BAT ^{18}F-FDG uptake color intensity of mouse from different intervention groups. For semiquantitative analysis, 3D round regions of interests (ROI) were placed carefully over the interscapular BAT and brain on microPET images for each mouse, respectively. ^{18}F-FDG uptake value was acquired in the form of nanocurie per cubic centimeter (nCi/cc) automatically after placing ROIs. Uptake ratio (R) of maximum interscapular BAT uptake and mean brain uptake was calculated for each mouse and compared between different interventions.

2.6. Statistical Analysis. Data were reported as means ± SD. Statistical analysis was performed using SPSS software, Version 17.0. One way ANOVA was used, and $P < .05$ was considered significant.
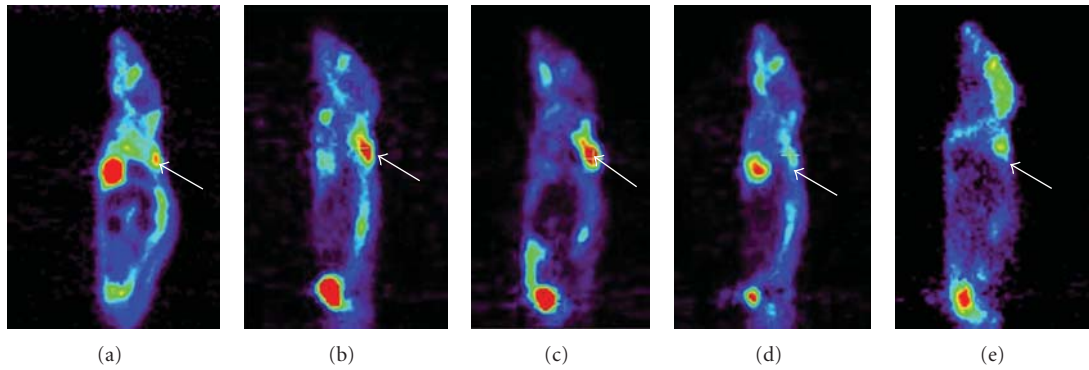
FIGURE 1: Comparison of interscapular BAT uptake in mice receiving different interventions from microPET sagittal images. For visual analysis, microPET images showed that mouse interscapular BAT ^{18}F-FDG uptake (arrow) varied under different interventions. (c) Cold plus NE interventions showed highest BAT uptake ($R = 15.64 \pm 5.58$, $P = 2.19 \times 10^{-6}$) compared to (b) cold exposure ($R = 10.22 \pm 4.13$, $P = 1.96 \times 10^{-4}$) and (a) control ($R = 4.08 \pm 1.32$), while (d) warming ($R = 2.13 \pm 0.43$, $P = .001$) and (e) propranolol ($R = 1.30 \pm 0.16$, $P = .027$) showed decreased BAT uptake in cold pre-exposure mice.
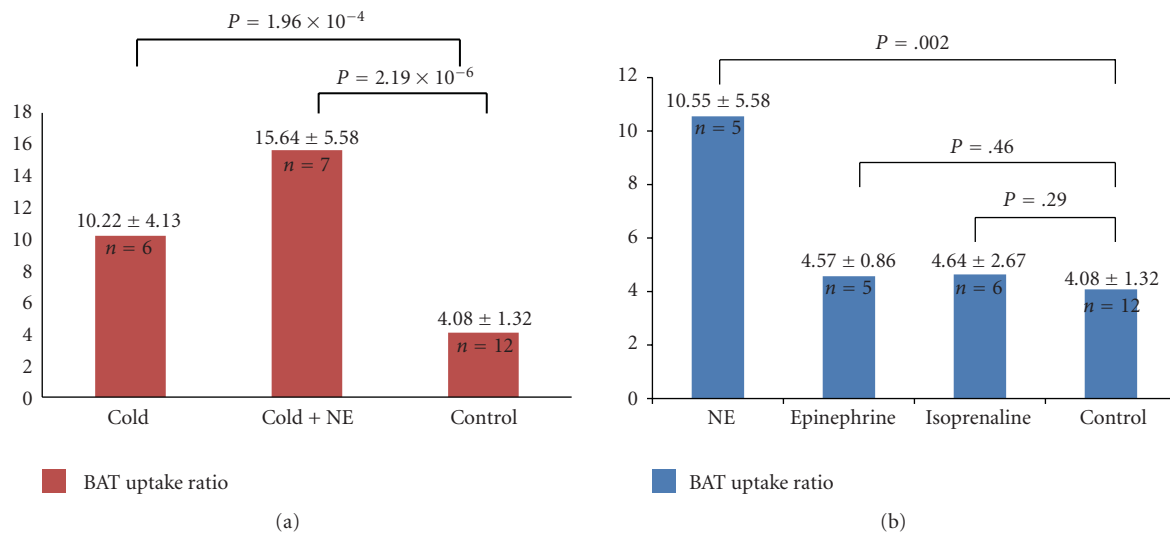

FIGURE 2: Comparison of the effects of different interventions to stimulate interscapular BAT in mice. (a) BAT FDG uptake ratio in cold, cold + NE and control group. Cold together with NE intervention showed the highest uptake in BAT. (b) BAT FDG uptake ratio in NE, epinephrine, isoprenaline, and control group. All these pharmaceutics increase BAT activity, but only NE showed significant difference ($P = .002$).

3. Results

In visual analysis, different interscapular BAT ^{18}F-FDG uptake intensity was found under different interventions as demonstrated by the microPET images (Figure 1). Cold and NE exposure caused the highest BAT uptake, followed by cold exposure and the control, while propranolol lavage and warming up showed decreased BAT uptake in cold pre-exposed mice.

In semiquantitative analysis, BAT ^{18}F-FDG uptake was significantly higher under cold exposure compared to control mice under room temperature (R: 10.22 ± 4.13 versus 4.08 ± 1.32, $P = 1.96 \times 10^{-4}$) and highest with both cold exposure and NE stimulations (R: 15.64 ± 5.58 versus 4.08 ± 1.32,

$P = 2.19 \times 10^{-6}$). A stimulation with only NE (R: 10.55 ± 5.85), epinephrine (R: 4.57 ± 0.86), or isoprenaline (R: 4.64 ± 2.67) at room temperature all increased BAT uptake compared with the controls (R: 4.08 ± 1.32), but only NE showed significant difference compared with the controls ($P = .002$) (Figure 2).

For BAT inhibition, warming could significantly reduce BAT uptake in mice with cold pre-exposure (R: 2.13 ± 0.43 versus 10.22 ± 4.13, $P = .001$) and without cold pre-exposure (R: 2.48 ± 0.88 versus 4.08 ± 1.32, $P = .017$). In addition, propranolol could significantly reduce BAT uptake in cold pre-exposed mice (R: 1.30 ± 0.16 versus 3.09 ± 0.90, $P = .027$) (Figure 3).
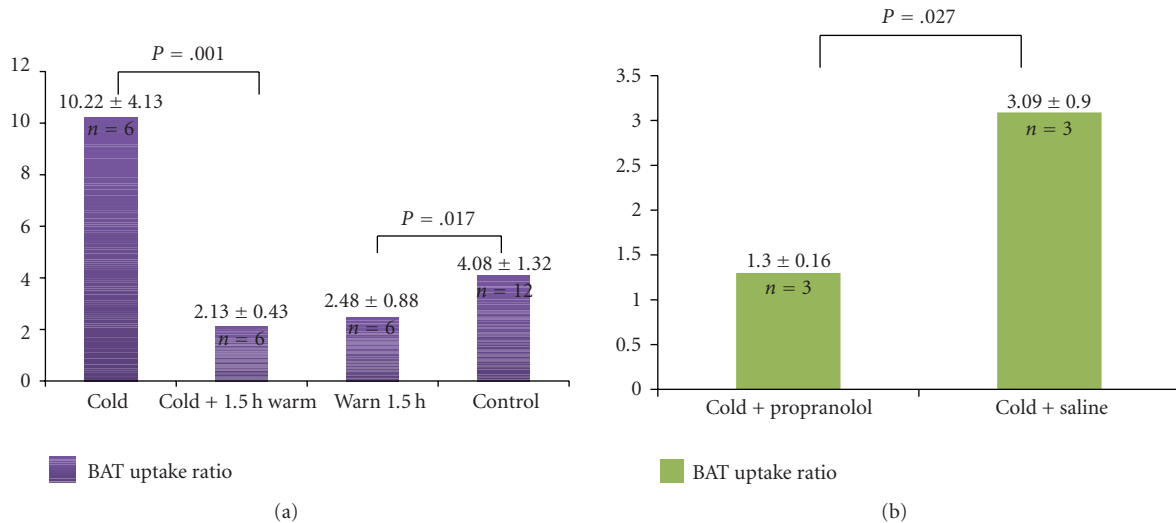
FIGURE 3: Comparison of the effects of warming and propranolol to inhibit interscapular BAT in mice. (a) BAT FDG uptake ratio under warm intervention. Warming could significantly decrease BAT metabolism in mice with or without cold pre-exposure ($P = .001$ and .017, resp.). (b) BAT FDG uptake ratio under propranolol intervention. Propranolol could significantly decrease BAT activity in cold pre-exposure mice ($P = .027$).

4. Discussion

Brown adipose tissue (BAT) has been shedding new light on weight control of human recently, but few researches focused on monitoring BAT metabolic function using molecular imaging. It is well known that BAT has more sympathetic innervations than WAT [13], which means that BAT may be activated by stimulating SNS. For future investigation of new methods to control obesity through activation of BAT function, the present study aimed mainly at establishing a technology platform using microPET to evaluate the BAT function through interventions with factors related to SNS activation or inhibition. Considering that the SNS might probably be modulated by short-term interventions, the temperature control or drug administration was generally set as 1 h before FDG injection in this study. Moreover, peritoneal injection or lavage was used to obtain a more stable effect. The results proved that these choices were feasible.

BAT can bring in false positive results in PET images of human by showing increased radioactive uptake especially in the supraclavicular area [14, 15]; many studies, therefore, try to find methods to inhibit BAT uptake in humans, for instance, by keeping the patients warm or giving orally propranolol administration [16–18]. Our study provided new data concerning these two methods in inhibiting BAT uptake that only 1.5 hour of warm intervention (1 h before and 0.5 hour after FDG injection) could quickly and markedly inhibit BAT metabolism (R: 2.48 ± 0.88 versus 4.08 ± 1.32, $P = .017$), and compared with propranolol intervention, warming seemed to be more effective in reducing BAT activity ($P = .001$). Based on this result, in clinics, to prevent BAT uptake in PET images, providing a warm environment for patients right before PET scan would be a more effective, convenient, and safer way than propranolol intake.

Cold stimulus was proved useful to increase BAT metabolism in either animal or human studies [9, 10] because it can activated sympathetic nerve terminals surrounding the BAT to excrete NE for more heat production [11]. In our study, cold exposure also significantly increased BAT activity (R: 10.22 ± 4.13 versus 4.08 ± 1.32, $P = 1.96 \times 10^{-4}$), and this effect was more obvious when combined with NE injection ($P = 2.19 \times 10^{-6}$), well confirming that BAT metabolism was correlated with catecholamine system. Moreover, cold effect could be quickly suppressed by warming (R: 2.13 ± 0.43 versus 10.22 ± 4.13, $P = .001$) or propranolol administration afterwards (R: 1.30 ± 0.16 versus 3.09 ± 0.90, $P = .027$), both of which were antagonistic to sympathetic-adrenal system, thus prohibiting BAT activity.

In our present study the β-adrenoceptor agonists (NE, epinephrine and isoprenaline) all increased interscapular BAT activity in mouse, but only NE showed a significant difference to controls ($P = .002, .459$, and $.293$, resp.). We think the dosage insufficiency of epinephrine and isoprenaline we gave mice may answer this question. With limited researches and few examples to follow, we gave a tentative dosage of epinephrine (0.02 mg/kg) and isoprenaline (0.016 mg/Kg) to mice, which is about the clinical dosage for children (about half of adult dose), much smaller than the advised dose for mouse (about 9-fold clinical dosage for adults) based on surface area per kilogram [19]. However, the dosage of NE (0.4 mg/kg) we gave mice was 11 times the dosage for human adult, so only NE was effective in activating BAT metabolism. Baba et al. [20] used epinephrine in 5 mg/kg, and microPET scan showed significant BAT uptake compared to controls; therefore, we think increasing dosage in future study may overcome this problem.

There are some limitations in this study. For instance, only female mice were enrolled in this study, and the mouse number in each intervention group was not big enough

($n = 3 \sim 7$). Furthermore, some uncontrollable factors such as environmental noise and stimuli caused by experimental handling may potentially influence the nerve system of mouse and thus the activity of BAT. In future studies, we will make improvement in these aspects.

In general, this preliminary study gives new prospective in studying the stimulation and inhibition of BAT of mouse by a quantitative analyzing tool of microPET. By applying microPET, the BAT activate status can be evaluated in vivo semiquantitatively in real-time.

5. Conclusion

Environment temperature control can significantly stimulate or alleviate BAT uptake of ^{18}F-FDG within 1 h in mice. Stimulating sympathetic nerve system by norepinephrine can significantly increase the metabolism of BAT within 1 h, while inhibiting SNS by warming or propranolol can alleviate BAT function. This preliminary study with ^{18}F-FDG microPET warrants further investigations of the mechanism of BAT and various methods of intervention according to clinical purposes. However, better optimization of different intervention conditions as well as some other methods for activating BAT should be further explored and studied in the hope of future human application.

Acknowledgments

References

[1] M. Ghorbani, T. H. Claus, and J. Himms-Hagen, "Hypertrophy of brown adipocytes in brown and white adipose tissues and reversal of diet-induced obesity in rats treated with a β-adrenoceptor agonist," *Biochemical Pharmacology*, vol. 54, no. 1, pp. 121–131, 1997.

[2] G. Frühbeck, S. Becerril, N. Sáinz, P. Garrastachu, and M. J. García-Velloso, "BAT: a new target for human obesity?" *Trends in Pharmacological Sciences*, vol. 30, no. 8, pp. 387–396, 2009.

[3] D. Hull, "The structure and function of brown adipose tissue," *British Medical Bulletin*, vol. 22, no. 1, pp. 92–96, 1966.

[4] J. Nedergaard, T. Bengtsson, and B. Cannon, "Unexpected evidence for active brown adipose tissue in adult humans," *American Journal of Physiology*, vol. 293, no. 2, pp. E444–E452, 2007.

[5] A. M. Cypess and C. R. Kahn, "Brown fat as a therapy for obesity and diabetes," *Current Opinion in Endocrinology, Diabetes and Obesity*, vol. 17, no. 2, pp. 143–149, 2010.

[6] J. B. Hansen and K. Kristiansen, "Regulatory circuits controlling white versus brown adipocyte differentiation," *Biochemical Journal*, vol. 398, no. 2, pp. 153–168, 2006.

[7] P. G. Shekelle, M. L. Hardy, S. C. Morton et al., "Efficacy and safety of ephedra and ephedrine for weight loss and athletic performance: a meta-analysis," *Journal of the American Medical Association*, vol. 289, no. 12, pp. 1537–1545, 2003.

[8] M. A. Van Baak, G. B. J. Hul, S. Toubro et al., "Acute effect of L-796568, a novel β-adrenergic receptor agonist, on energy expenditure in obese men," *Clinical Pharmacology and Therapeutics*, vol. 71, no. 4, pp. 272–279, 2002.

[9] W. D. Van Marken Lichtenbelt, J. W. Vanhommerig, N. M. Smulders et al., "Cold-activated brown adipose tissue in healthy men," *New England Journal of Medicine*, vol. 360, no. 15, pp. 1500–1508, 2009.

[10] B. J. Fueger, J. Czernin, I. Hildebrandt et al., "Impact of animal handling on the results of ^{18}F-FDG PET studies in mice," *Journal of Nuclear Medicine*, vol. 47, no. 6, pp. 999–1006, 2006.

[11] J. Himms-Hagen, "Role of thermogenesis in the regulation of energy balance in relation to obesity," *Canadian Journal of Physiology and Pharmacology*, vol. 67, no. 4, pp. 394–401, 1989.

[12] M. Watanabe, T. Yamamoto, C. Mori et al., "Cold-induced changes in gene expression in brown adipose tissue: implications for the activation of thermogenesis," *Biological and Pharmaceutical Bulletin*, vol. 31, no. 5, pp. 775–784, 2008.

[13] C. Atgié, F. D'Allaire, and L. J. Bukowiecki, "Role of β- and β-adrenoceptors in the regulation of lipolysis and thermogenesis in rat brown adipocytes," *American Journal of Physiology*, vol. 273, no. 4, pp. C1136–C1142, 1997.

[14] T. F. Hany, E. Gharehpapagh, E. M. Kamel, A. Buck, J. Himms-Hagen, and G. K. Von Schulthess, "Brown adipose tissue: a factor to consider in symmetrical tracer uptake in the neck and upper chest region," *European Journal of Nuclear Medicine*, vol. 29, no. 10, pp. 1393–1398, 2002.

[15] C. Cohade, M. Osman, H. K. Pannu, and R. L. Wahl, "Uptake in supraclavicular area fat ("USA-Fat"): description on 18F-FDG PET/CT," *Journal of Nuclear Medicine*, vol. 44, no. 2, pp. 170–176, 2003.

[16] S. Basu and A. Alavi, "Optimizing interventions for preventing uptake in the brown adipose tissue in FDG-PET," *European Journal of Nuclear Medicine and Molecular Imaging*, vol. 35, no. 8, pp. 1421–1423, 2008.

[17] G. Williams and G. M. Kolodny, "Method for decreasing uptake of ^{18}F-FDG by hypermetabolic brown adipose tissue on PET," *American Journal of Roentgenology*, vol. 190, no. 5, pp. 1406–1409, 2008.

[18] K. A. Zukotynski, F. H. Fahey, S. Laffin et al., "Constant ambient temperature of 24°C significantly reduces FDG uptake by brown adipose tissue in children scanned during the winter," *European Journal of Nuclear Medicine and Molecular Imaging*, vol. 36, no. 4, pp. 602–606, 2009.

[19] S. Xu, R. Bian, and X. Chen, *Methodology of Pharmacology Experiment (Chinese)*, People's Health Press, Beijing, China, 3rd edition, 2001.

[20] S. Baba, M. Tatsumi, T. Ishimori, D. L. Liliein, J. M. Engles, and R. L. Wahl, "Effect of nicotine and ephedrine on the accumulation of ^{18}F-FDG in brown adipose tissue," *Journal of Nuclear Medicine*, vol. 48, no. 6, pp. 981–986, 2007.

Research Article

Development of ^{68}Ga-Glycopeptide as an Imaging Probe for Tumor Angiogenesis

Ning Tsao,[1] Chau-Hui Wang,[2] Li-Jane Her,[3] Kai-Yuan Tzen,[4] Jing-Yi Chen,[2] Dong-Fang Yu,[1] and David J. Yang[1]

[1] *Division of Diagnostic Imaging, University of Texas MD Anderson Cancer Center, 1515 Holcombe Boulevard, Houston, TX 77030, USA*
[2] *Chemistry, Manufacturing and Control, SeeCure LLC, Houston, TX 77036, USA*
[3] *Innovation Center, Taiwan HOPAX Chems, MFG, Company Ltd., Kaohsiung 831, Taiwan*
[4] *Department of Nuclear Medicine, National Taiwan University Hospital, Taipei 100, Taiwan*

Correspondence should be addressed to Ning Tsao, ning.tsao@mdanderson.org

Objective. This study was aimed to study tissue distribution and tumor imaging potential of ^{68}Ga-glycopeptide (GP) in tumor-bearing rodents by PET. *Methods.* GP was synthesized by conjugating glutamate peptide and chitosan. GP was labeled with ^{68}Ga chloride for in vitro and in vivo studies. Computer outlined region of interest (counts per pixel) of the tumor and muscle (at the symmetric site) was used to determine tumor-to-muscle count density ratios. To ascertain the feasibility of ^{68}Ga-GP in tumor imaging in large animals, PET/CT imaging of ^{68}Ga-GP and ^{18}F-FDG were conducted in New Zealand white rabbits bearing VX2 tumors. Standard uptake value of tumors were determined by PET up to 45 min. To determine blood clearance and half-life of ^{68}Ga-GP, blood samples were collected from 10 seconds to 20 min. *Results.* Radiochemical purity of ^{68}Ga-GP determined by instant thin-layer chromatography was >95%. Tumor uptake values (SUV) for ^{68}Ga-GP and ^{18}F-FDG in New Zealand white rabbits bearing VX2 tumors were 3.25 versus 7.04. PET images in tumor-bearing rats and rabbits confirmed that ^{68}Ga-GP could assess tumor uptake. From blood clearance curve, the half-life of ^{68}Ga-GP was 1.84 hr. *Conclusion* Our data indicate that it is feasible to use ^{68}Ga-GP to assess tumor angiogenesis.

1. Introduction

With progress of molecular biology in recent years, imaging techniques are undergoing tremendous development and improvement. These imaging modalities play a major role in the development of novel therapies, since they generate information about target expression as well as function, pathway activity, and cell migration in the intact organism. For instance, angiogenesis, the proliferation of endothelial and smooth muscle cells to form new blood vessels, is an essential component of the metastatic pathway. These vessels provide the principal route by which tumor cells exit the primary tumor site and enter the circulation. For many tumors, the vascular density can provide a prognostic indicator of metastatic potential, with the highly vascular tumors having a higher incidence of metastasis than poorly

vascular tumors [1]. Experimental research suggests that it is possible to block angiogenesis by specific inhibitory agents, and that modulation of angiogenic activity is associated with tumor regression in animals with different types of neoplasia. The promising angiosuppressive agents for clinical testing are naturally occurring inhibitors of angiogenesis (angiostatin, endostatin, platelet factor-4, and others). Measuring angiogenesis (blood vessel density) and/or its main regulators such as vascular endothelial growth factor (VEGF) and basic fibroblast growth factor (bFGF), or the levels of apoptosis after treatment in solid tumors provides new and sensitive markers for tumor progression, metastasis, and prognosis [2, 3].

Polysaccharides such as heparin, chitosan, and chondroitin play a potent role in tumor growth, tissue repair, and angiogenesis. Chitosan, an angiogenesis biomer, interacts

with vascular endothelia cells and potentiates the fibroblast growth factor (FGF-2) activity. Chitosan is known as a wound-dressing and tissue-adhesive material showing biocompatibility, anti-infective activity, and the ability to accelerate wound healing [4–6]. During the healing process, chitosan enhances macrophage activation, cytokine (IL-8) production by macrophages and fibroblasts, anti-inflammatory action, angiogenesis stimulation, granulation, and scar formation. Though chitosan has made outstanding advantage in the field of angiogenesis, some significant limitations still remain in the treatment of cancer via intracellular delivery of cytotoxic drugs. In order to enhance therapeutic index of chitosan in cancer treatment, we conjugated glutamate peptide with chitosan.

The excitatory amino acid glutamate (Glu) is a potent neurotransmitter in the central nervous system and exerts its action via a variety of glutamate transporters [7]. It is known that cellular uptake of polyglutamate peptide (GAP) is specific to glutamate transporter [8]. Chain of 5 or more glutamic acids could reduce renal uptake in animal models [9]. Conjugation of GAP with chitosan resulting in GP would be a novel agent to target tumor vascular and cellular component. Radiolabeled GP would support this concept.

Imaging science enables the comprehensive characterization of therapeutic intervention and can be used in preclinical studies, pharmacokinetic studies, dose-finding studies, and proof-of-concept studies. Positron emission tomography (PET) and single photon emission computed tomography (SPECT) permit mapping and measuring the rate of physiological, biochemical, and molecular processes with radiolabeled compounds and appropriate tracer kinetic models. Cellular imaging by PET and SPECT provides valuable information in monitoring and guiding clinical trial using cell-based therapies in the treatment of malignant and other diseases. ^{68}Ga and ^{99m}Tc are the most attractive radiometals obtained from generators for PET and SPECT clinical applications due to their energy (511 and 140 keV), half-life (68 min and 6 h), and simple coordination chemistry. We previously have reported that glycopeptide (GP), a copolymer of chitosan and glutamate peptide, provides an opportunity to target tumor vasculature and cellular via glutamate transporters [10]. In vitro assays revealed that cell uptake of ^{99m}Tc-GP was via glutamate transporters. ^{99m}Tc-GP was able to measure tumor uptake changes after paclitaxel treatment. Biodistribution of ^{99m}Tc-GP showed increased tumor-to-tissue count density ratios as a function of time. Planar images confirmed that it is feasible to use ^{99m}Tc-GP to assess tumor angiogenesis. To evaluate whether GP could also be labeled with a different isotope for PET imaging of tumors, here, we report the tissue distribution and tumor imaging potential of ^{68}Ga-GP.

2. Materials and Methods

2.1. Synthesis of ^{68}Ga-Glycopeptide (GP).
To a stirred solution of chitosan (200 mg, MW 3,500–5,000) in water (4 mL) and 3-ethyl-3-(3-dimethylaminopropyl) carbodiimide-HCl (EDC) (128.5 mg, 0.67 mmoL) (Pierce Chemical Company, Rockford, IL) was added. Glutamate peptide sodium salt
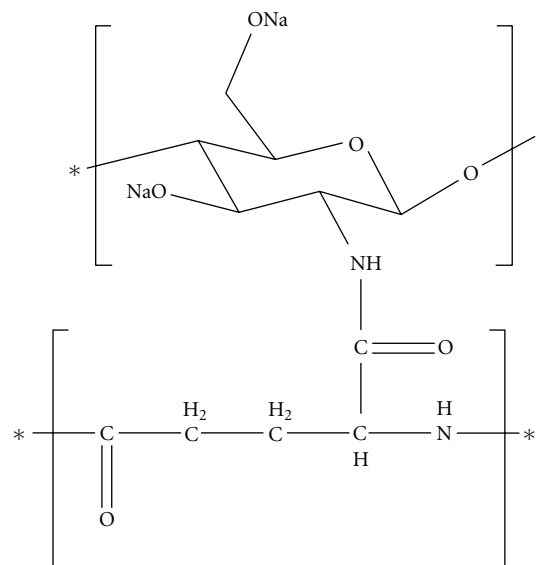

FIGURE 1: Structure of glycopeptide (GP).

TABLE 1: Biodistribution of ^{68}Ga-GP in breast tumor-bearing Rats. % of injected dose per gram of tissue weight (n = 3/time, interval, iv)*.

	30 min	60 min	120 min
Blood	2.61 ± 0.18	1.81 ± 0.05	1.37 ± 0.05
Heart	0.59 ± 0.06	0.43 ± 0.02	0.32 ± 0.02
Lung	2.34 ± 0.45	2.58 ± 0.16	1.38 ± 0.06
Thyroid	1.10 ± 0.11	1.40 ± 0.87	0.59 ± 0.06
Pancreas	0.38 ± 0.03	0.34 ± 0.04	0.28 ± 0.02
Liver	3.81 ± 0.32	4.83 ± 0.54	4.94 ± 0.38
Spleen	2.13 ± 0.07	2.65 ± 0.14	2.97 ± 0.11
Kidney	1.35 ± 0.02	1.36 ± 0.01	1.41 ± 0.11
Stomach	0.58 ± 0.04	0.65 ± 0.07	0.74 ± 0.18
Intestine	0.54 ± 0.12	0.53 ± 0.07	0.78 ± 0.22
Uterus	0.70 ± 0.02	0.65 ± 0.05	0.57 ± 0.03
Tumor	0.68 ± 0.12	0.89 ± 0.10	1.18 ± 0.09
Muscle	0.12 ± 0.02	0.12 ± 0.00	0.10 ± 0.02
Bone	0.45 ± 0.12	0.46 ± 0.09	0.59 ± 0.03
Brain	0.08 ± 0.01	0.07 ± 0.01	0.07 ± 0.01
Tumor/blood	0.26 ± 0.03	0.49 ± 0.07	0.86 ± 0.09
Tumor/muscle	6.12 ± 1.87	7.20 ± 0.83	13.26 ± 4.41

*Value shown represent the mean ± standard deviation of data from 3 animals at (Count at 460–560 keV window).

(200 mg, MW 1,308) was then added. The mixture was stirred at room temperature for 24 hr. The mixture was dialyzed for 48 hr using Spectra/POR molecular porous membrane with cutoff at 5,000 (Spectrum Medical Industries Inc., Houston, TX). After dialysis, the product was filtered and dried using a freeze dryer (Labconco, Kansas City, MO). The GP in the salt form weighed 320 mg. The chemical structure is shown in Figure 1. Gel permeation chromatogram (GPC) and capillary electrophoresis (CE) were used to analyze the purity of GP.

GPC spectrum of GP

(a)

GPC spectrum of GP
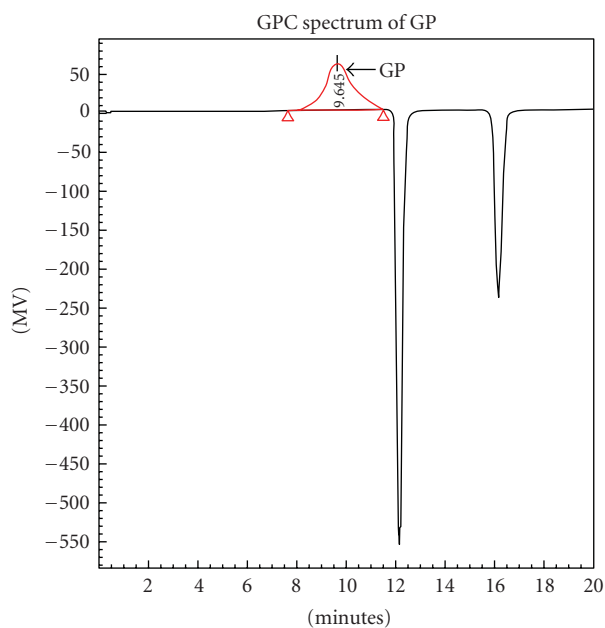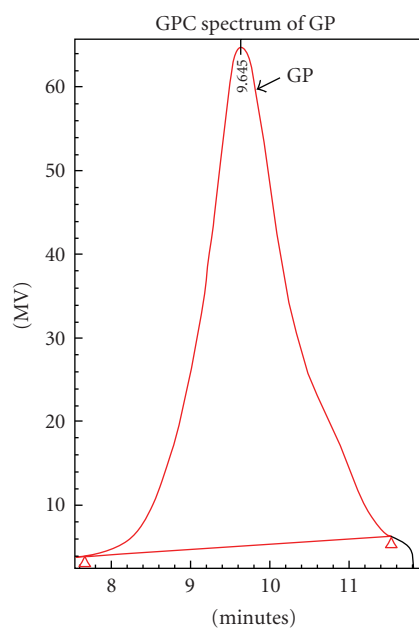
(b)

FIGURE 2: Gel permeation chromatogram (GPC) analysis of GP showed the purity of GP was greater than 95%. The spectrum showed the retention time of 9.645 min and the estimated molecular weight of 7,484.

2.2. Radiolabeling of GP with ^{68}Ga.

Radiolabeling of GP with ^{68}Ga was performed in a standard manner [11]; briefly, GP (5 mg) was dissolved in 0.2 ml of water, and ^{68}Ga chloride (5 mCi) evaporated to dryness and reconstituted in 0.1 ml of sterilized water at room temperature, followed by heating up to 55°C for 10 min. Radiochemical purity was determined by instant thin-layer chromatography (ITLC Silica-Gel coated, Gelman Sciences, Ann Arbor, MI) eluted with saline.
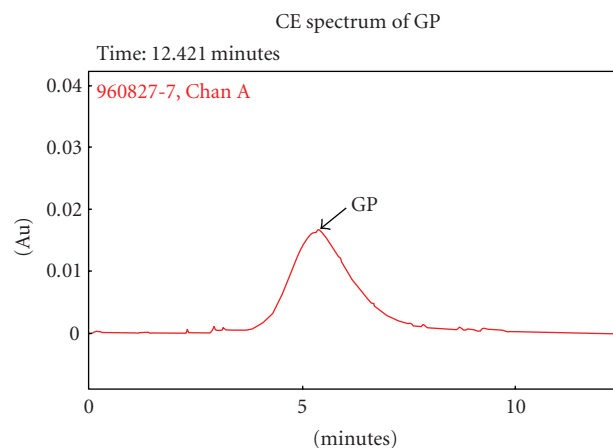
CE spectrum of GP

FIGURE 3: Capillary electrophoresis (CE) analysis of GP. The spectra showed that the purity of GP was greater than 95%.

TABLE 2: Biodistribution of FDG in breast tumor-bearing rats. % of injected dose per gram of tissue weight ($n = 3$/time, interval, i.v.)*.

	30 min	60 min	120 min
Blood	0.40 ± 0.04	0.13 ± 0.01	0.06 ± 0.00
Heart	1.57 ± 0.06	1.38 ± 0.13	1.08 ± 0.07
Lung	0.55 ± 0.06	0.42 ± 0.02	0.46 ± 0.03
Thyroid	1.07 ± 0.08	1.04 ± 0.04	1.05 ± 0.07
Pancreas	0.26 ± 0.03	0.21 ± 0.01	0.20 ± 0.02
Liver	0.40 ± 0.05	0.16 ± 0.01	0.13 ± 0.01
Spleen	0.82 ± 0.08	0.74 ± 0.03	0.86 ± 0.07
Kidney	0.71 ± 0.05	0.37 ± 0.01	0.24 ± 0.02
Stomach	0.61 ± 0.08	0.44 ± 0.03	0.39 ± 0.03
Intestine	0.69 ± 0.07	0.53 ± 0.03	0.52 ± 0.02
Uterus	0.51 ± 0.04	0.42 ± 0.03	0.41 ± 0.03
Tumor	2.13 ± 0.11	2.49 ± 0.08	2.03 ± 0.18
Muscle	0.33 ± 0.04	0.34 ± 0.03	0.74 ± 0.02
Bone	0.33 ± 0.04	0.44 ± 0.06	0.50 ± 0.03
Brain	2.00 ± 0.15	1.99 ± 0.05	1.39 ± 0.09
Tumor/blood	5.19 ± 0.38	19.78 ± 1.37	34.37 ± 1.76
Tumor/muscle	5.88 ± 0.57	7.54 ± 0.56	2.87 ± 0.24

*Value shown represent the mean ± standard deviation of data from 3 animals at (Count at 460–560 keV window).

2.3. In Vitro Stability Assays of ^{68}Ga-GP.

^{68}Ga-GP was prepared in the concentration of 5 mg/1 mCi/ml. 0.1 mL of ^{68}Ga-GP was incubated with 0.1 mL phosphate buffered saline (pH = 7.4) at 37°C for 30–120 min. In vitro stability of ^{68}Ga-GP was determined by chromatographic analysis, as described in the above section. There was no breakdown of ^{68}Ga-GP up to 2 hr.

2.4. Biodistribution Studies.

Female Fischer 344 rats (150–175 g) (Harlan Sprague-Dawley, Inc., Indianapolis, IN) were inoculated subcutaneously in the right leg with breast cancer cells (10^6 cells in 0.1 mL/rat) from the 13762 cell line (known as DMBA-induced breast cancer cell line). Biodistribution studies were performed on day 14 after inoculation.
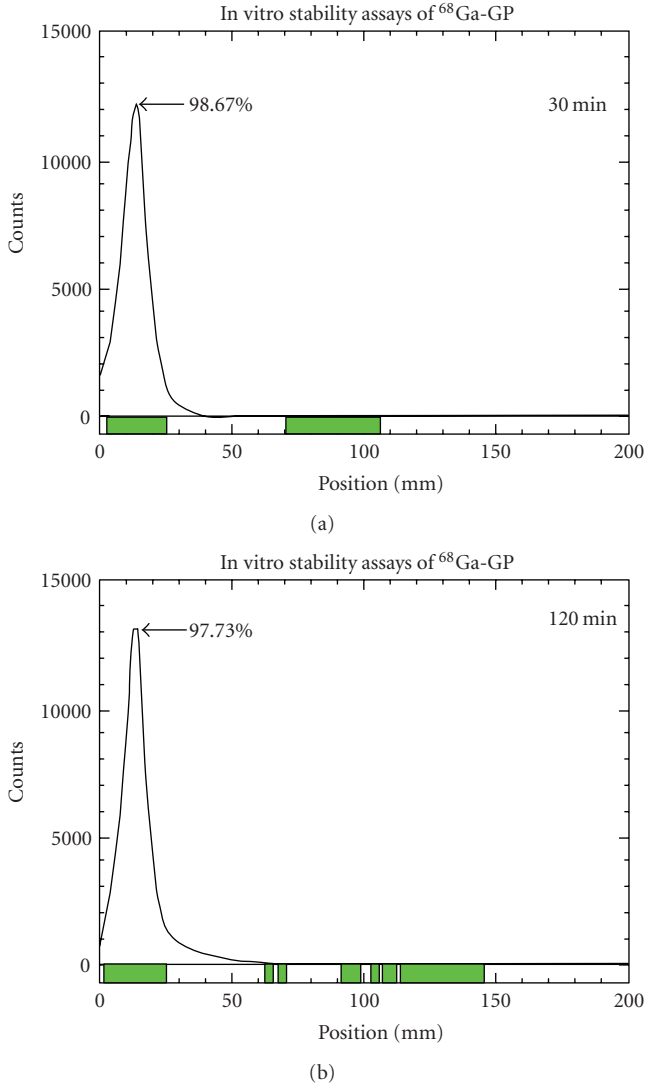
In vitro stability assays of ^{68}Ga-GP

(a)

In vitro stability assays of ^{68}Ga-GP

(b)

FIGURE 4: ^{68}Ga-GP was prepared in the concentration of 5 mg/1 mCi/1 mL. 0.1 mL of ^{68}Ga-GP was incubated with 0.1 mL phosphate buffered saline (pH = 7.4) at 30–120 min. There was no breakdown of ^{68}Ga-GP up to 120 min.

A group of Female Fischer 344 tumor-bearing rats was injected intravenously with ^{68}Ga-GP or ^{18}F-FDG (30 μCi/rat, $n = 3$ rats/time point) through the tail vein. The injected mass was 30 μg of ^{68}Ga-GP per rat. At 30, 60, and 120 min following administration of the radiotracers, the animals were sacrificed, and the tumor and selected tissues were excised, weighed, and counted for radioactivity with a gamma counter (Packard Instruments, Downers Grove, IL). The biodistribution of ^{68}Ga-GP or ^{18}F-FDG in each sample was calculated as a percentage of the injected dose per gram of the tissue's wet weight (%ID/g).

2.5. MIRD Dosimetry Estimates. Rat absorbed doses estimates for ^{68}Ga-GP were computed from their respective biodistribution data. Fitted residence time functions were plotted and multiplied by the exponential decay functions

TABLE 3: Radiation dose estimates of reference adult for ^{68}Ga-GP from rabbits.

Organs (5 rem annual/15 rem total)			
Target organ	rad/mCi	Human dose (mCi)	rad
adrenals	$2.54E-04$	20	0.005
brain	$7.37E-06$	20	0.000
breasts	$2.78E-04$	20	0.006
gall bladder wall	$1.03E-04$	20	0.002
lli wall	$8.24E-06$	20	0.000
small int	$2.34E-05$	20	0.000
stomach	$1.69E-04$	20	0.003
uli wall	$3.02E-05$	20	0.001
heart wall	$2.30E-02$	20	0.460
kidneys	$7.92E-05$	20	0.002
liver	$2.13E-04$	20	0.004
lungs	$4.62E-04$	20	0.009
muscle	$9.27E-05$	20	0.002
pancreas	$2.54E-04$	20	0.005
bone surfaces	$8.54E-05$	20	0.002
skin	$4.65E-05$	20	0.001
testes	$2.09E-06$	20	0.000
thymus	$8.81E-04$	20	0.018
thyroid	$5.34E-05$	20	0.001
urine bladder wall	$5.92E-06$	20	0.000
uterus	$1.11E-05$	20	0.000
eff dose	$1.48E-04$	20	0.003
Blood-forming organs (3 rem annual/5 rem total)			
ovaries	$1.16E-05$	20	0.000
red marrow	$1.29E-04$	20	0.003
spleen	$1.18E-04$	20	0.002
eff dose eq	$1.60E-03$	20	0.032
total body	$1.92E-04$	20	0.004

(i.e., half-life) for ^{68}Ga-GP. These functions were then integrated analytically to determine the area under the curve (AUC) to yield the residence time of each organ. It was assumed that the injected activity distribution was uniformly distributed throughout the body immediately following injection. It was further assumed that no excretion occurred after the last time point and that the activity distribution remained unchanged after this time point; that is, no biological excretion was assumed after the last time point. Mass correction factors were used to account for the different ratios of organ to total body weights in the rat and in humans and allowed for the scaling of the rat residence times to human residence times. For the organs where total organ weight was unavailable, the organ weights derived from the Cristy-Eckerman mathematic phantoms for the adult male were used to estimate total tissue activity. Residence times were then used to calculate target organ absorbed radiation doses with S-value tables for a standard 70 kg male model using the MIRDose Olinda software package (Oakridge, TN). Each organ dose was computed from the sum of self-dose plus the dose it received from each source organ in
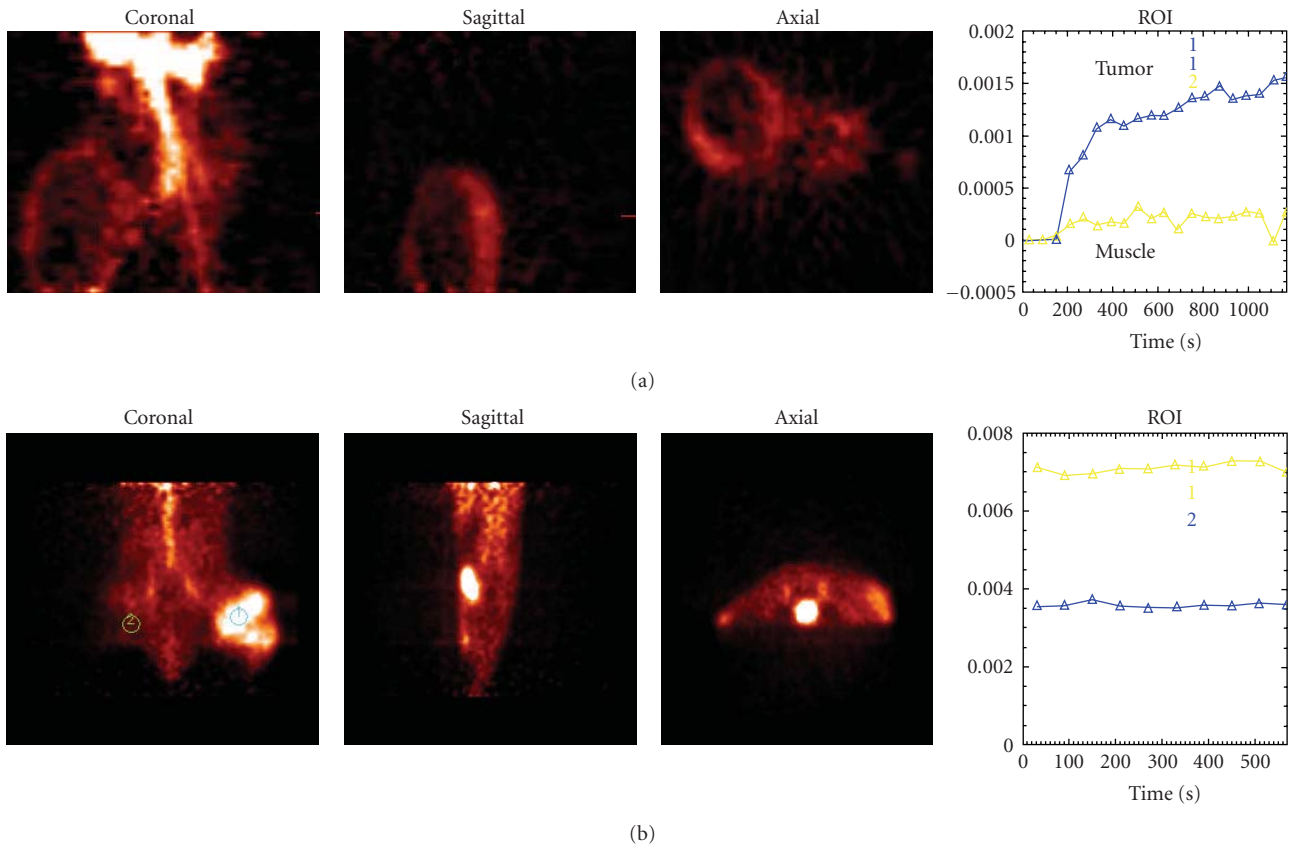
(a)

(b)

FIGURE 5: Dynamic mPET Imaging of ^{68}Ga-GP (a) and ^{18}F-FDG (b) in breast tumor bearing rats (0.003 mg, 600 uCi/rat, iv) at 0–20 min showed tumor could be visualized by both compounds.
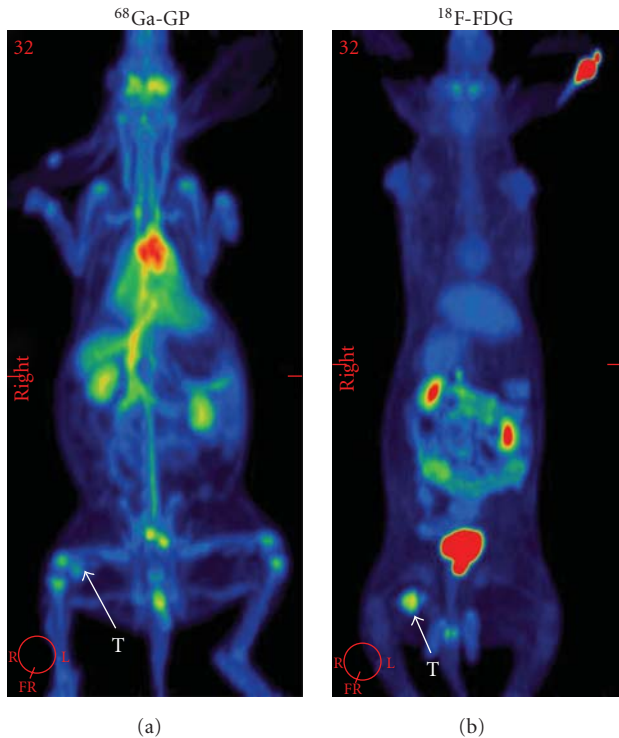

(a) (b)

FIGURE 6: PET whole body at 45 min in New Zealand white rabbits bearing VX2 tumors.

the body or from the remainder of the body. The estimated human radiation absorption dose was determined.

2.6. PET Imaging Studies. For microPET imaging, the images were acquired on a microPET R4 scanner, a dedicated 3D small-animal PET (Concorde Microsystems, Knoxville TN). A group of female Fischer 344 tumor-bearing rats was injected intravenously with ^{68}Ga-GP or ^{18}F-FDG ($n = 3$ rats/compound) through the tail veins. Each animal will be anesthetized and secured onto the microPET. Cradle notches, laser lights, and animal felt pen markings will be used to ensure reproducible animal positioning before and after administration of ^{68}Ga-GP and ^{18}F-FDG. Each animal will then be injected with 1.62 μCi/g body weight of ^{68}Ga-GP and ^{18}F-FDG and imaged for 2 hr in a dynamic mode. A minimum of ~20 million events will be acquired in 120 minutes covering the tumor bearing area. The acquired list mode data will then be histogramed into frames of varying durations using Fourier rebinning. The corresponding images will be reconstructed into $128*128*63(0.72*0.72*1.3$ mm) matrix using ordered subset expectation maximization techniques. All corrections for attenuation, scatter, dead-time, and randomizations were applied to generate quantifiable images. Computer-outlined region of interest (counts per pixel) of the tumor and muscle (at the symmetric site) was used to determine tumor-to-muscle count density ratios.
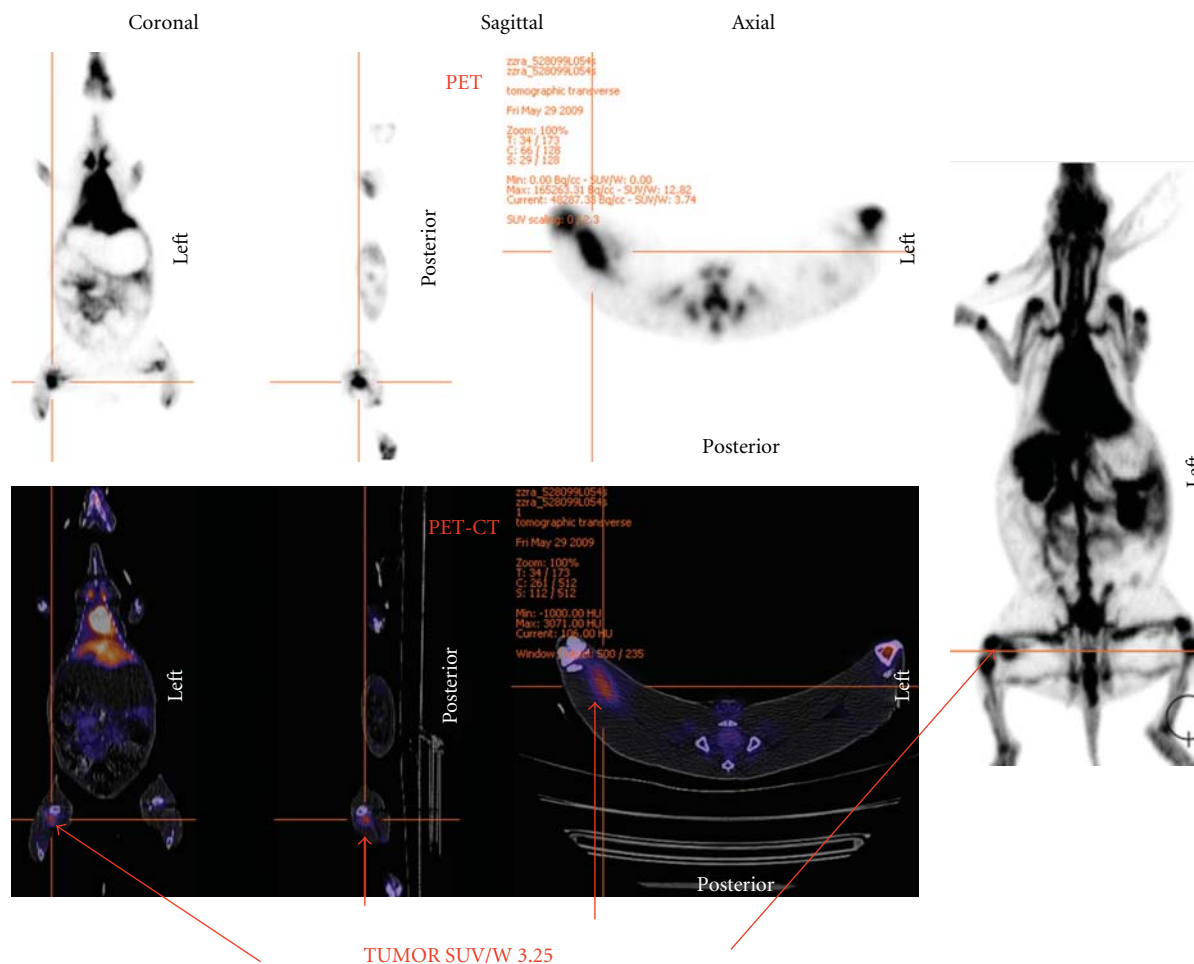
FIGURE 7: 45 minutes dynamic image with PET-CT of ^{68}Ga-GP in a New Zealand white rabbit bearing VX2 tumor showed SUV of the tumor was 3.25.

For PET/CT imaging in large animals, New Zealand white rabbits were inoculated with VX-2 tumor mass (rabbit-driven squamous tumors). The rabbits were administered intravenously (iv) 2 mCi of ^{68}Ga-GP and ^{18}F-FDG (control). The images were acquired on a dedicated Advance 3D PET/CT (GE Medical system) at 0.5–2 hr after i.v. injection of the radiotracers. Standard uptake value of tumors was determined by dynamic PET up to 45 min.

2.7. Kinetic Study of Blood Clearance of ^{68}Ga-GP in New Zealand White Rabbit. New Zealand white rabbits were administered intravenously (iv) 2 mCi of ^{68}Ga-GP. To determine blood clearance and half-life of ^{68}Ga-GP, 0.1 ml blood samples were collected from 10 seconds to 20 min (14 time points) after injection. Blood samples were weighted, and the radioactivities were counted by gamma counter (Packard Instruments, Downers Grove, IL). The radioactivity of each sample was calculated as a percentage of the injected dose per gram of the blood's net weight (%ID/g).

3. Results

3.1. Chemistry. Elemental analysis of GP ($C_{11}H_{14}N_2Na_2O_6$, C, H, N) showed C: 41.54, H: 10 : 62, and N: 7.19. (calculated C: 41.77, H: 8.86, and N: 4.43). The estimated purity of GP was greater than 95% (based upon carbon content). Gel permeation chromatogram (GPC) and capillary electrophoresis (CE) spectra showed that the purity of GP was greater than 95% (Figures 2 and 3). From radio-TLC (Bioscan, Washington, DC) analysis, the radiochemical purity was more than 95% (Rf = 0.1). In vitro stability assays indicated that the radiation yield is 98.67% at 30 min and 97.73% at 2 hr after labeling. There was no breakdown ^{68}Ga-GP up to 2 hr (Figure 4).

3.2. Biodistribution Studies. There was an increased uptake in tumors (percent of injected dose per gram of tissue), tumor-to-blood and tumor-to-muscle count density ratios by ^{68}Ga-GP at 0.5–2 hr, whereas the optimum tumor uptake and tumor-to-muscle count density ratios for ^{18}F-FDG were at 1 hr after administrations (Tables 1 and 2). In biodistribution
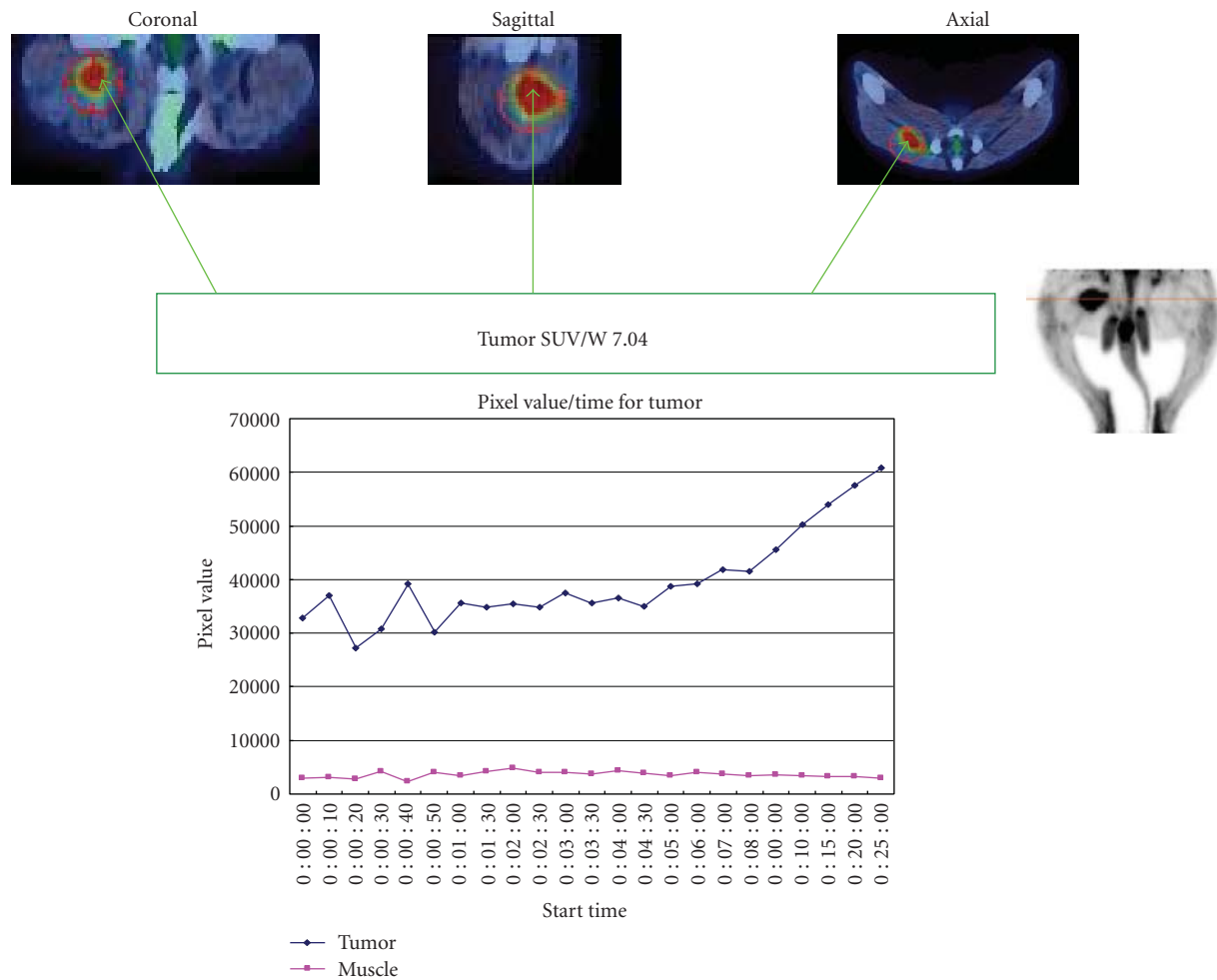
FIGURE 8: 45 minutes dynamic image with PET-CT of ^{18}FDG in New Zealand white rabbit bearing VX2 tumor showed SUV of the tumor was 7.04.

studies at 30, 60, and 120 min, tumor uptake values, tumor/blood, and tumor/muscle ratios for ^{68}Ga-GP were 0.68 ± 0.12 to 1.18 ± 0.09, 0.26 ± 0.03 to 0.86 ± 0.09, and 6.12 ± 1.87 to 13.26 ± 4.41 and for ^{18}F-FDG were 2.03 ± 0.18 to 2.49 ± 0.08, 5.19 ± 0.38 to 34.37 ± 1.76, and 2.87 ± 0.24 to 7.54 ± 0.56, respectively (Tables 1 and 2).

3.3. MIRD Dosimetry Estimates. The rabbit imaging data was used to calculate residence times for each organ through analytical integration. The residence times were scaled from rabbit to human (70 kg reference adult model) using organ correction factors to generate human residence time estimates. The kidneys and spleen are the primary and secondary contributors for ^{68}Ga-GP, respectively. The MIRD output was multiplied by a proposed human dose of 20 mCi for ^{68}Ga-GP to yield total absorbed dose shown in Table 3. ^{68}Ga-GP showed total rad absorbed by each organ was below the proposed annual and total limits. Radiation exposure to the whole body, blood-forming organs (red marrow and spleen), gonads (testes and ovaries), and effective dose equivalent for the proposed human single dose at 20 mCi fall below the limits of 3 rad annually and 5 rad total. The absorbed dose

in all other organs (e.g., kidneys) was below the limits of single dose of 5 rad annually and 15 rad total (Table 3). These radiation exposure values are commonly accepted as criteria for in vivo radiation safety measurement.

3.4. PET Imaging Studies. Tumors could be well visualized both in breast tumor-bearing rats and VX-2 tumor-bearing rabbits (Figures 5 and 6). From PET image ROI analysis, standard tumor uptake values (SUVs) for ^{68}Ga-GP and ^{18}F-FDG in VX-2 tumor-bearing rabbits were 3.25 and 7.04, respectively (Figures 7 and 8). PET images in tumor-bearing rats and rabbits confirmed that ^{68}Ga-GP could assess tumor uptake. PET dynamic scan showed fast tumor uptake of ^{68}Ga-GP in a New Zealand white rabbit bearing VX2 tumor (Figure 9). Furthermore, there is no intestine uptake in ^{68}Ga-GP PET imaging indicated the radioisotope labeling of ^{68}Ga-GP is stable *in vivo*.

3.5. Kinetic Study of Blood Clearance of ^{68}Ga-GP in New Zealand White Rabbit. The blood clearance of ^{68}Ga-GP showed both distribution phase and elimination phase (Figure 10(a)). The elimination phase was used to calculate
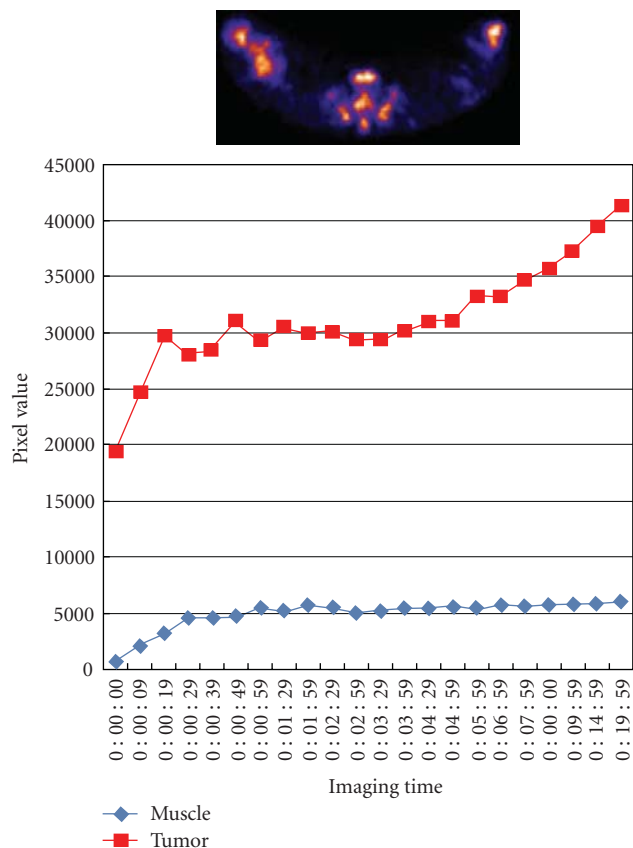
FIGURE 9: 45 Minutes dynamic tumor uptake of ^{68}Ga-GP in a New Zealand white rabbit bearing VX2 tumor. The axial view from PET-CT showed the location of tumor.

(a)

(b)

FIGURE 10: Blood clearance (a) and half-life analysis (one compartment) of ^{68}Ga showed the half-life of ^{68}Ga-GP was 1.84 hr with K value of 0.377 hr.

the half-life ($T1/2$) of ^{68}Ga-GP (Figure 10(b)). Regression line formulation ($y = -0.0018x + 0.3967$, $R^2 = 0.8375$) was estimated using Microsoft Office Excel 2003. The $T1/2$ of ^{68}Ga-GP was 1.84 hr and the elimination rate constant (k) was 0.377 hr^{-1}.

4. Discussion

Chitosan, a cationic biopolymer derived by deacetylation of chitin. Chitin and chitosan derivatives are used as excipients and drug carriers in the pharmaceutical field. For instance, films prepared using chitin or chitosan have been developed as wound dressings, oral mucoadhesive, and water-resisting adhesive by virtue of their release characteristics and adhesion. Intratumoral administration of gadopentetic acid-chitosan complex nanoparticles (approximately 430 nm in diameter) has been more effective for gadolinium neutron-capture therapy compared with a group treated with the solution. Chitin and chitosan derivatization contributed to expansion of application in drug delivery and sustained drug release [12–14]. It has been reported that chitosan could directly conjugate drugs or be modified by the introduction of thioglycolic acid (TGA) resulting in chitosan-TGA conjugates with thiol groups. Chitosan-thioglycolic acid conjugates has been found to be a promising candidate in tissue

engineering due to their physicochemical properties [15]. Despite the broadened application of chitosan derivatives, one major limitation of chitosan is lack of cellular targeting.

Previous studies have shown that glutamate peptide is a candidate of drug carrier [16, 17]. Radiolabeled glutamic acid has shown to be useful in tumor cellular imaging [18]. To optimize the intracellular uptake of chitosan derivatives, we have synthesized glutamate peptide, chitosan, and a GP copolymer. This copolymer would be ideal to conjugate the drugs with either amino or acid groups which provides an advantage over either chitosan or glutamate peptide. In addition, results from our previous in vitro cellular uptake and animal imaging studies showed that GP is a target drug carrier via glutamate transporters [10]. This targeted drug carrier may provide an advantage not only to improve drug solubility but also to overcome drug resistance during chemotherapy.

In our previous findings, ^{99m}Tc-GP was able to measure uptake differences after cells treated with paclitaxel and

uptake difference between tumor and inflammation. In vitro cellular uptake assay indicated that cellular uptake of ^{99m}Tc-GP was via glutamate transporters. In this study, we further tested the ^{68}Ga-GP imaging using PET/CT.

In summary, PET imaging studies indicated that it is feasible to use ^{68}Ga-GP to image tumors. GP has multiamino and acid groups which broaden its chemistry application.

5. Relevance

At present, there is no angiogenesis imaging agent focused on both vascular endothelial adhesiveness and cellular targets. GP interacts with vascular endothelial and cellular targets. GP also has multiple amino and carboxylic groups, which allows anticancer drug conjugate for targeted imaging and therapy. Our data indicate that ^{68}Ga-GP accumulates actively in tumors both in small and large animal models (Figures 4 and 5). The imaging data obtained from ^{68}Ga-GP not only provide an impact on improving the diagnosis of cancer but also provide a basis for internal radionuclide targeted therapy.

Acknowledgments

References

[1] F. Bertolini, M. Paolucci, F. Peccatori et al., "Angiogenic growth factors and endostatin in non-Hodgkin's lymphoma," *British Journal of Haematology*, vol. 106, no. 2, pp. 504–509, 1999.

[2] Y. Cao, "Therapeutic potentials of angiostatin in the treatment of cancer," *Haematologica*, vol. 84, no. 7, pp. 643–650, 1999.

[3] B. D. Smith, G. L. Smith, D. Carter, C. T. Sasaki, and B. G. Haffty, "Prognostic significance of vascular endothelial growth factor protein levels in oral and oropharyngeal squamous cell carcinoma," *Journal of Clinical Oncology*, vol. 18, no. 10, pp. 2046–2052, 2000.

[4] T. Mori, M. Okumura, M. Matsuura et al., "Effects of chitin and its derivatives on the proliferation and cytokine production of fibroblasts in vitro," *Biomaterials*, vol. 18, no. 13, pp. 947–951, 1997.

[5] A. Polykratis, P. Katsoris, J. Courty, and E. Papadimitriou, "Characterization of heparin affin regulatory peptide signaling in human endothelial cells," *Journal of Biological Chemistry*, vol. 280, no. 23, pp. 22454–22461, 2005.

[6] J. S. Pieper, P. B. Van Wachem, M. J. A. Van Luyn et al., "Attachment of glycosaminoglycans to collagenous matrices modulates the tissue response in rats," *Biomaterials*, vol. 21, no. 16, pp. 1689–1699, 2000.

[7] R. A. Waniewski and D. L. Martin, "Characterization of L-glutamic acid transport by glioma cells in culture: evidence for sodium-independent, chloride-dependent high affinity influx," *Journal of Neuroscience*, vol. 4, no. 9, pp. 2237–2246, 1984.

[8] C. Chenu, C. M. Serre, C. Raynal, B. Burt-Pichat, and P. D. Delmas, "Glutamate receptors are expressed by bone cells and are involved in bone resorption," *Bone*, vol. 22, no. 4, pp. 295–299, 1998.

[9] M. Béhé, G. Kluge, W. Becker, M. Gotthardt, and T. M. Behr, "Use of polyglutamic acids to reduce uptake of radiometal-labeled minigastrin in the kidneys," *Journal of Nuclear Medicine*, vol. 46, no. 6, pp. 1012–1015, 2005.

[10] I. C. Wei, N. Tsao, YA. H. Huang et al., "^{99m}Tc-glycopeptide: synthesis, biodistribution and imaging in breast tumor-bearing rodents," *Applied Radiation and Isotopes*, vol. 66, no. 3, pp. 320–331, 2008.

[11] S. Froidevaux, M. Calame-Christe, J. Schuhmacher et al., "A gallium-labeled DOTA-α-melanocyte-stimulating hormone analog for PET imaging of melanoma metastases," *Journal of Nuclear Medicine*, vol. 45, no. 1, pp. 116–123, 2004.

[12] L. Y. Wang, G. H. Ma, and Z. G. Su, "Preparation of uniform sized chitosan microspheres by membrane emulsification technique and application as a carrier of protein drug," *Journal of Controlled Release*, vol. 106, no. 1-2, pp. 62–75, 2005.

[13] M. Fujita, M. Ishihara, Y. Morimoto et al., "Efficacy of photocrosslinkable chitosan hydrogel containing fibroblast growth factor-2 in a rabbit model of chronic myocardial infarction," *Journal of Surgical Research*, vol. 126, no. 1, pp. 27–33, 2005.

[14] Y. Kato, H. Onishi, and Y. Machida, "Application of chitin and chitosan derivatives in the pharmaceutical field," *Current Pharmaceutical Biotechnology*, vol. 4, no. 5, pp. 303–309, 2003.

[15] A. Bernkop-Schnürch, M. Hornof, and D. Guggi, "Thiolated chitosans," *European Journal of Pharmaceutics and Biopharmaceutics*, vol. 57, no. 1, pp. 9–17, 2004.

[16] D. J. Yang, C. Li, S. Nikiforow et al., "Diagnostic and therapeutic potential of poly(benzyl L-glutamate)," *Journal of Pharmaceutical Sciences*, vol. 83, no. 3, pp. 326–331, 1994.

[17] W. Tansey, S. Ke, X. Y. Cao, M. J. Pasuelo, S. Wallace, and C. Li, "Synthesis and characterization of branched poly(L-glutamic acid) as a biodegradable drug carrier," *Journal of Controlled Release*, vol. 94, no. 1, pp. 39–51, 2004.

[18] R. E. Reiman, R. S. Benua, and A. S. Gelbard, "Imaging of brain tumors after administration of L-(N-13)glutamate: concise communication," *Journal of Nuclear Medicine*, vol. 23, no. 8, pp. 682–687, 1982.

Research Article

Protein Expression of Mesenchymal Stem Cells after Transfection of pcDNA3.1$^-$-hVEGF$_{165}$ by Ultrasound-Targeted Microbubble Destruction

Zhaoxia Pu,[1] Xiangdong You,[1] Qiyuan Xu,[2] Feng Gao,[2] Xiaojie Xie,[2] Hong Zhang,[3] and Wang Jian'an[2]

[1] *Department of Ultrasound, Second Affiliated Hospital, Zhejiang University College of Medicine, 88 Jiefang Road,
  Hangzhou 310009, China*
[2] *Department of Cardiology, Second Affiliated Hospital, Zhejiang University College of Medicine, 88 Jiefang Road,
  Hangzhou 310009, China*
[3] *Department of Nuclear Medicine, Second Affiliated Hospital, Zhejiang University College of Medicine,
  88 Jiefang Road, Hangzhou 310009, China*

Correspondence should be addressed to Wang Jian'an, wang_jian_an@tom.com

Ultrasound-targeted microbubble destruction (UTMD) has been proposed as a new technique for organ-specific gene transfer and drug delivery. This study was performed to investigate the effect of UTMD on marrow mesenchymal stem cells (MSCs) transfected with pcDNA3.1$^-$-hVEGF$_{165}$.pcDNA3.1$^-$-hVEGF$_{165}$ were transfected into the third passage of MSCs, with or without UTMD under different ultrasound conditions. Protein expression was quantified by hVEGF$_{165}$-ELISA kit after transfection for 24, 48, and 72 hours. UTMD-mediated transfection of MSCs yielded a significant protein expression. UTMD of mechanic index (MI) 0.6 for 90 seconds led to the highest level of protein expression.

1. Introduction

Heart disease currently remains the leading cause of death worldwide. With the development of tissue engineering, stem cell technology has been widely used and highlights the latest advances in these exciting fields [1]. Mesenchymal stem cells (MSCs) have demonstrated the ability to differentiate into cardiomyocytes, but are still limited to construct the vessels [2, 3]. Vascular endothelial growth factor (VEGF) could induce vascular endothelial cell proliferation and angiogenesis [4]. Because of its short half-life, VEGF could not maintain effective concentration in blood after injection [5]. In recent years, Ultrasound-targeted microbubble destruction (UTMD) has been proved to be a promising technique for organ-specific gene and drug delivery [6]. In this experiment, we transferred pcDNA3.1$^-$-hVEGF$_{165}$ into MSCs by UTMD and observed the effect of the protein expression.

2. Materials and Methods

2.1. Separation and Cultivation of MSCs. Our experiment was performed in the Clinical Research Center, the Second Affiliated Hospital, School of Medicine, Zhejiang University, China. Five male Sprague-Dawley rats, weighing 80–100 g, were provided by the animal center of Zhejiang University. All experiments have adhered to the National Institutes of Health guide for the care and use of laboratory animals (NIH Publications no. 8023, revised 1978). Approval from the Institutional Animal Care and Use Committee at Zhejiang University Health Science Centre was also obtained to perform the described experiments. MSCs were harvested from the bone marrow of femurs of these rats. Briefly, bone marrow cells were flushed out with 30 mL complete Dulbecco's modified Eagle's medium (DMEM, Gibco, USA) containing 10% heat-inactivated fetal bovine serum (FBS, Gibco, USA), 5 mg/mL glutamine (Gibco, USA), 100 U/mL

penicillin (Gibco, USA), and 100 U/mL streptomycin (Gibco, USA). The cells were grown in a humidified atmosphere containing 5% CO_2 and 95% O_2. The medium was replaced 24 hours later and refreshed every 2 days. Cells were subcultured according to 1 : 2 ratio when they reached approximately 80% confluence by trypsinization (0.25% trypsin, Gibco, USA). The third passage of MSCs was adopted for transfection.

2.2. Recombinant pcDNA3.1$^-$-hVEGF$_{165}$ Gene Transfer into MSCs by UTMD. The third passage of MSCs were planted into three 6-well plate (Becton Dickinson, USA) at 1.0×10^5 cells/per well and cultured for 24 hours in 37°C, 5% CO_2 conditions. Before transfection, 5 mL normal saline were added to the microbubble contrast agent SonoVue (Bracco, Italy) powder (25 mg) and thoroughly mixed for 20 seconds. 4μg/per well pcDNA3.1$^-$-hVEGF$_{165}$ recombinant (Future Biotech, China) were mixed with 10 mL lipofectamin 2000 transfection reagent (Invitrogen, USA) for 20 s [7].

In this study, all the cells were divided intothe following five groups:

(1) the blank control group: MSCs with culture fluid,

(2) the control group A: 4μg pcDNA3.1$^-$-hVEGF$_{165}$ recombinant were transfected into MSCs,

(3) the control group B: 4μg pcDNA3.1$^-$-hVEGF$_{165}$ recombinant mixed with 300μl SonoVue microbubble were transfected into MSCs,

(4) the control group C: 4μg pcDNA3.1$^-$-hVEGF$_{165}$ recombinant were transfected into MSCs by ultrasonic exposure (illustrated by the example of mechanic index (MI) 1.0 and exposure time (ET) 60 s),

(5) the UTMD group: 4μg pcDNA3.1$^-$-hVEGF$_{165}$ recombinant were transfected into MSCs by UTMD (MI 1.0, ET 60 s).

The UTMD group was also divided into three groups according to different MI and ET.

Ultrasound-targeted microbubble was ruptured as following: Acuson Sequoia 512 ultrasound's 3V2C transducer (Siemens, German) was placed on the bottom of each well plate according to the preset ultrasonic exposure condition. The ultrasound parameters were set as follows: the frequency was 4 MHz, the depth was 4 cm, MI was 0.6, 1.0, and 1.4 respectively, and ET was 30 s, 60 s, and 90 s, respectively.

MSCs cultural supernatant was collected after transfection for 24, 48, and 72 hours, respectively. Five samples were applied in each group.

2.3. Detection of VEGF$_{165}$ Protein Expression after Transfection by ELISA Quantitative Assay. hVEGF$_{165}$-ELISA kit (Jingmei, China) was used to determine VEGF$_{165}$ protein expression after transfection for 24, 48, and 72 hours according to the instructions.This was repeated five times in this experiment.

2.4. Statistical Analysis. All the parameters were expressed as mean ± standard deviation. A one-way analysis of variance

Table 1: Protein expression of VEGF$_{165}$ in mesenchymal stem cells supernatant after transfection ($n = 25$, ng/mL).

Groups	Protein expression of VEGF$_{165}$		
	24 h	48 h	72 h
(1) The blank control group	12.5 ± 1.8	12.1 ± 0.6	11.8 ± 0.1
(2) The control group A	73.1 ± 0.4	74.0 ± 1.2	70.4 ± 1.0
(3) The control group B	67.3 ± 2.1	79.4 ± 0.8	74.1 ± 1.5
(4) The control group C	63.7 ± 2.6	82.1 ± 1.7	76.3 ± 1.3
(5) The UTMD group	$218.6 \pm 0.9^*$	$269.2 \pm 2.2^*$	$199.4 \pm 2.1^*$

* $P < .05$, versus each other non-UTMD groups.
(1) The blank control group: MSCs with culture fluid.
(2) The control group A: 4μg pcDNA3.1$^-$-hVEGF$_{165}$ recombinant were transfected into MSCs.
(3) The control group B: 4μg pcDNA3.1$^-$-hVEGF$_{165}$ recombinant mixed with 300μl SonoVue microbubble were transfected into MSCs.
(4) The control group C: 4μg pcDNA3.1$^-$-hVEGF$_{165}$ recombinant were transfected into MSCs by ultrasonic exposure (illustrated by the example of Mechanic index (MI) 1.0 and exposure time (ET) 60 s).
(5) The UTMD group: 4μg pcDNA3.1$^-$-hVEGF$_{165}$ recombinant were transfected into MSCs by UTMD (MI 1.0, ET 60 s).

(ANOVA), followed by a LSD (least significant difference) test was used to compare VEGF$_{165}$ protein expression among different groups. All analyses were performed using SPSS statistical software, version 13.0 (SPSS, Inc., USA). A two-sided $P < .05$ was considered statistically significant.

3. Results

The results showed that the VEGF$_{165}$ protein expression increased at 24 hours and reached the maximum level at 48 hours, then decreased at 72 hours (Table 1). Compared with the control group, protein expression of the UTMD group was significantly increased ($P < .05$).

Table 2 also demonstrated that VEGF$_{165}$ protein level varied according to different ultrasound conditions. The group with ET 90 s and MI 0.6 showed the highest protein level at 48 hours, which has statistical significance compared with every group with ET 30 s and MI 0.6, 1.0, and 1.4, respectively ($P < .05$).

4. Discussion

The lack of suitable autologous grafts has produced a need for artificial grafts, but the patency of such grafts is limited compared to natural materials. Tissue engineering, whereby living tissue replacements can be constructed, has emerged as a solution to some of these difficulties [8]. MSCs have demonstrated the ability to differentiate into cardiomyocytes, This, in turn, is limited by the availability of MSCs to construct the vessels [9].

VEGF, a class of molecular weight of 34~45 KD glycoprotein, could induce vascular endothelial cell proliferation and angiogenesis. VEGF$_{165}$ protein-induced differentiation of MSCs directional vascular endothelial cells plays a vital role in neovascularization of ischemic tissues [10, 11]. However, because of its short half-life, VEGF could not maintain

TABLE 2: Protein expression of $VEGF_{165}$ in mesenchymal stem cells supernatant after transfection under different ultrasound conditions ($n = 25$, ng/mL).

Various ultrasound conditions		Protein expression of $VEGF_{165}$		
ET	MI	24 h	48 h	72 h
	0.6	118.2 ± 0.7	133.1 ± 0.3	112.7 ± 0.8
30 s	1.0	140.5 ± 1.1	142.0 ± 0.5	131.5 ± 0.1
	1.4	136.6 ± 0.7	154.1 ± 1.1	121.8 ± 0.9
	0.6	177.6 ± 1.2	168.8 ± 2.3	159.1 ± 0.8
60 s	1.0	218.6 ± 0.9	269.2 ± 1.2	199.4 ± 2.1
	1.4	254.6 ± 0.7	289.6 ± 3.6	249.1 ± 0.8
	0.6	$289.9 \pm 1.5^{*}$	$319.1 \pm 2.1^{*}$	$268.7 \pm 1.4^{*}$
90 s	1.0	161.2 ± 1.8	186.5 ± 0.8	151.6 ± 1.3
	1.4	$160 .0 \pm 3.5$	175.2 ± 1.6	148.2 ± 2.5

$^{*}P < .05$, versus groups with ET 30 s and MI 0.6, 1.0, and 1.4, respectively.

effective concentration in blood after injection because of rapid degradation of deoxyribonucleic acid (DNA) [12–14]. Thus, intravenous injection of plasmid DNA does not lead to detectable transfection [15]. In the present study, UTMD, a promising technique for organ-specific gene and drug delivery, was tried aiming to transfer VEGF into MSCs efficiently.

UTMD has evolved as a promising tool for organ-specific gene and drug delivery [16]. This technique has initially been developed as a method in myocardial contrast echocardiography, destroying intramyocardial microbubbles to characterize refill kinetics. When loading similar microbubbles with a bioactive substance, ultrasonic destruction of microbubbles may release the transported substance in the targeted organ [17]. Furthermore, high-amplitude oscillations of microbubbles increased capillary and cell membrane permeability and facilitated tissue and cell penetration of the released substance [18–20].

As the target cell of gene transfer, MSCs could promote expression of VEGF protein and vascularization of tissue engineering bone by transfected $VEGF_{165}$. $VEGF_{165}$ was a kind of secretary protein, whether the transfected gene could express effectively was the critical point of the present experiment.

Table 1 showed that $VEGF_{165}$ protein production increased after MSCs was transfected with $VEGF_{165}$ by UTMD. The $VEGF_{165}$ protein expression reached maximum at 48 hours and decreased later, which had statistical significance compared with all other non-UTMD group at all set moments ($P < .05$). It could be explained by three mechanisms: firstly, electron microscopy has demonstrated pore formation on cell membranes immediately after destruction of microbubbles, the pores are transient and disappeared after 24 hours [21]. Such "sonoporation" effects may help facilitating gene or drug entry into the cell. Studies on single bubbles in vitro have shown that even linear bubble oscillations are sufficient to achieve rupture of lipid membranes [22]. Secondly, sudden violent collapse of microbubbles (inertial cavitation) can produce high-velocity fluid microjets that may penetrate adjacent membranes [23]. Thirdly, inertial cavitation, which is dependent on microbubble shell composition, ultrasound frequency, pulse duration, and acoustic power, can lead to secondary shock waves, transient local high temperatures, and shear stress, all of which could potentially contribute to gene or drug delivery by UTMD [24, 25].

Table 2 showed that $VEGF_{165}$ protein level changed under different ultrasound conditions. The group with UTMD of MI 0.6 for 90 s showed the highest peak protein level at 48 hours, which has statistical significance compared with other groups with ET 30 s. Studies have confirmed that the disruption force of microbubbles is greater when the ultrasound frequency used matches the resonant frequency of microbubbles. Even low acoustic pressures can result in microbubble destruction, but higher pressures will lead to more forceful reactions [26]. However, too higher acoustic pressure will hurt the cells, this is why the $VEGF_{165}$ protein level of groups with MI 1.4, ET 90 s was lower in this study.

5. Limitations

The first limitation of this present study is that the number of samples is small. However, even with this small number of samples, we were able to reach our primary goal of investigating the protein expression of UTMD on MSCs transfected with pcDNA3.1^{-}-hVEGF$_{165}$. Secondly, the cell proliferation and angiogenesis of transfected MSCs by UTMD will not be traced, which is very important for tissue engineering. Thirdly, this study is limited in vitro. So further investigation, especially in larger animal models, is needed.

6. Conclusion

UTMD-mediated transfection of MSCs yielded a significant protein expression. UTMD of mechanic index (MI) 0.6 for 90 seconds led to the highest level of protein expression.

Acknowledgment

References

[1] K. M. Sales, H. J. Salacinski, N. Alobaid, M. Mikhail, V. Balakrishnan, and A. M. Seifalian, "Advancing vascular tissue engineering: the role of stem cell technology," *Trends in Biotechnology*, vol. 23, no. 9, pp. 461–467, 2005.

[2] J. M. Hare and S. V. Chaparro, "Cardiac regeneration and stem cell therapy," *Current Opinion in Organ Transplantation*, vol. 13, no. 5, pp. 536–542, 2008.

[3] A. Behfar, R. S. Faustino, D. K. Arrell, P. P. Dzeja, C. Perez-Terzic, and A. Terzic, "Guided stem cell cardiopoiesis: discovery and translation," *Journal of Molecular and Cellular Cardiology*, vol. 45, no. 4, pp. 523–529, 2008.

[4] H. Gerhardt, "VEGF and endothelial guidance in angiogenic sprouting," *Organogenesis*, vol. 4, no. 4, pp. 241–246, 2008.

[5] P. Douvaras, D. G. Antonatos, K. Kekou et al., "Association of VEGF gene polymorphisms with the development of heart failure in patients after myocardial infarction," *Cardiology*, vol. 114, no. 1, pp. 11–18, 2009.

[6] R. Bekeredjian, P. A. Grayburn, and R. V. Shohet, "Use of ultrasound contrast agents for gene or drug delivery in cardiovascular medicine," *Journal of the American College of Cardiology*, vol. 45, no. 3, pp. 329–335, 2005.

[7] T. Susa, T. Kato, and Y. Kato, "Reproducible transfection in the presence of carrier DNA using FuGENE6 and Lipofectamine 2000," *Molecular Biology Reports*, vol. 35, no. 3, pp. 313–319, 2008.

[8] T. Shinoka and C. Breuer, "Tissue-engineered blood vessels in pediatric cardiac surgery," *Yale Journal of Biology and Medicine*, vol. 81, no. 4, pp. 161–166, 2008.

[9] M. Siepe, P. Akhyari, A. Lichtenberg, C. Schlensak, and F. Beyersdorf, "Stem cells used for cardiovascular tissue engineering," *European Journal of Cardio-Thoracic Surgery*, vol. 34, no. 2, pp. 242–247, 2008.

[10] J. Jiang, C. Y. Fan, and B. F. Zeng, "Osteogenic differentiation effects on rat bone marrow-derived mesenchymal stromal cells by lentivirus-mediated co-transfection of human BMP2 gene and VEGF165 gene," *Biotechnology Letters*, vol. 30, no. 2, pp. 197–203, 2008.

[11] C. Q. Gao, M. Yang, L. B. Li et al., "The experimental studies on cell transplantation into chronic ischemic myocardium using mesenchymal stem cells modified by recombinant adenovirus carrying vascular endothelial growth factors 165 gene," *Zhonghua Wai Ke Za Zhi*, vol. 45, no. 14, pp. 990–993, 2007.

[12] J. J. Haigh, "Role of VEGF in organogenesis," *Organogenesis*, vol. 4, no. 4, pp. 247–256, 2008.

[13] P. E. Pestryakov and O. I. Lavrik, "Mechanisms of single-stranded DNA-binding protein functioning in cellular DNA metabolism," *Biochemistry*, vol. 73, no. 13, pp. 1388–1404, 2008.

[14] K. Kawabata, Y. Takakura, and M. Hashida, "The fate of plasmid DNA after intravenous injection in mice: involvement of scavenger receptors in its hepatic uptake," *Pharmaceutical Research*, vol. 12, no. 6, pp. 825–830, 1995.

[15] V. T. G. Chuang, U. Kragh-Hansen, and M. Otagiri, "Pharmaceutical strategies utilizing recombinant human serum albumin," *Pharmaceutical Research*, vol. 19, no. 5, pp. 569–577, 2002.

[16] P. A. Dijkmans, R. Senior, H. Becher et al., "Myocardial contrast echocardiography evolving as a clinically feasible technique for accurate, rapid, and safe assessment of myocardial perfusion. The evidence so far," *Journal of the American College of Cardiology*, vol. 48, no. 11, pp. 2168–2177, 2006.

[17] G. Korpanty, S. Chen, R. V. Shohet et al., "Targeting of VEGF-mediated angiogenesis to rat myocardium using ultrasonic destruction of microbubbles," *Gene Therapy*, vol. 12, no. 17, pp. 1305–1312, 2005.

[18] R. Bekeredjian, R. D. Kroll, E. Fein et al., "Ultrasound targeted microbubble destruction increases capillary permeability in hepatomas," *Ultrasound in Medicine and Biology*, vol. 33, no. 10, pp. 1592–1598, 2007.

[19] K. Hynynen, "Ultrasound for drug and gene delivery to the brain," *Advanced Drug Delivery Reviews*, vol. 60, no. 10, pp. 1209–1217, 2008.

[20] C. R. Mayer and R. Bekeredjian, "Ultrasonic gene and drug delivery to the cardiovascular system," *Advanced Drug Delivery Reviews*, vol. 60, no. 10, pp. 1177–1192, 2008.

[21] D. L. Miller, S. V. Pislaru, and J. F. Greenleaf, "Sonoporation: mechanical DNA delivery by ultrasonic cavitation," *Somatic Cell and Molecular Genetics*, vol. 27, no. 1-6, pp. 115–134, 2002.

[22] P. Marmottant and S. Hilgenfeldt, "Controlled vesicle deformation and lysis by single oscillating bubbles," *Nature*, vol. 423, no. 6936, pp. 153–156, 2003.

[23] E. A. Brujan, "The role of cavitation microjets in the therapeutic applications of ultrasound," *Ultrasound in Medicine and Biology*, vol. 30, no. 3, pp. 381–387, 2004.

[24] J. E. Chômas, P. Dayton, J. Alien, K. Morgan, and K. W. Ferrara, "Mechanisms of contrast agent destruction," *IEEE Transactions on Ultrasonics, Ferroelectrics, and Frequency Control*, vol. 48, no. 1, pp. 232–248, 2001.

[25] J. Wu, "Theoretical study on shear stress generated by microstreaming surrounding contrast agents attached to living cells," *Ultrasound in Medicine and Biology*, vol. 28, no. 1, pp. 125–129, 2002.

[26] S. Chen, R. V. Shohet, R. Bekeredjian, P. Frenkel, and P. A. Grayburn, "Optimization of ultrasound parameters for cardiac gene delivery of adenoviral or plasmid deoxyribonucleic acid by ultrasound-targeted microbubble destruction," *Journal of the American College of Cardiology*, vol. 42, no. 2, pp. 301–308, 2003.

Research Article

Chemiluminescent Nanomicelles for Imaging Hydrogen Peroxide and Self-Therapy in Photodynamic Therapy

Rui Chen,[1] Luzhong Zhang,[1] Jian Gao,[2] Wei Wu,[1] Yong Hu,[2] and Xiqun Jiang[1]

[1] *Laboratory of Mesoscopic Chemistry and Department of Polymer Science and Engineering,*
 College of Chemistry and Chemical Engineering, Nanjing University, Nanjing 210093, China
[2] *National Laboratory of Solid State Microstructure and Department of Material Science and Engineering,*
 Nanjing University, Nanjing 210093, China

Correspondence should be addressed to Yong Hu, hvyong@nju.edu.cn and Xiqun Jiang, jiangx@nju.edu.cn

Received 20 January 2011; Revised 18 March 2011; Accepted 24 March 2011

Academic Editor: Zhen Cheng

Hydrogen peroxide is a signal molecule of the tumor, and its overproduction makes a higher concentration in tumor tissue compared to normal tissue. Based on the fact that peroxalates can make chemiluminescence with a high efficiency in the presence of hydrogen peroxide, we developed nanomicelles composed of peroxalate ester oligomers and fluorescent dyes, called peroxalate nanomicelles (POMs), which could image hydrogen peroxide with high sensitivity and stability. The potential application of the POMs in photodynamic therapy (PDT) for cancer was also investigated. It was found that the PDT-drug-loaded POMs were sensitive to hydrogen peroxide, and the PDT drug could be stimulated by the chemiluminescence from the reaction between POMs and hydrogen peroxide, which carried on a self-therapy of the tumor without the additional laser light resource.

1. Introduction

Reactive oxygen species (ROS), a vital substance in organisms, not only involved in many signaling pathways that maintain cellular homeostasis in physiological processes [1] but also can induce severe damage in turn which is called oxidative injury [2]. Hydrogen peroxide (H_2O_2), one of the ROS, produced in cellular mitochondria, plays a major role in mediating cell growth and apoptosis [3]. In healthy organs, cells produce necessary H_2O_2 to mediate diverse physiological progresses. However, abnormal overproduction implicates the development of various pathological conditions, even severe diseases, such as cancer. Moreover, its concentration spans four orders of magnitude from 10^{-8} M in proliferation to 10^{-4} M in apoptosis [4]. Therefore, hydrogen peroxide is a very important signaling molecule acted as an intracellular indicator in the development of cancer [5].

Recently, the detection of hydrogen peroxide in vitro or in vivo has been received much interests [6–8]. By using fluorescence probe techniques, the concentration of hydrogen peroxide can be obtained through fluorescence intensity, helping us to understand the state of cells under physiological and pathological conditions [9]. Another way is peroxalate chemiluminescence (POCL) whose mechanism can be summarized in two progresses [10]. First, peroxalate derivatives can be oxidized only by hydrogen peroxide to generate a high-energy and unstable intermediate: dioxetanedione; then, the intermediate degrades to carbon dioxide as well as transfers energy to nearby molecules, such as fluorescent dye, to give a particular fluorescence [11, 12]. Using such a feature, a new type of imaging H_2O_2 is offered as reported like peroxalate polymeric nanoparticles [13]. These nanoparticles have attractive advantages beyond fluorescence probe, such as tunable wavelength emission, excellent sensitivity, and high specificity for H_2O_2, so they can be widely applied in the diagnosis of the diseases related to H_2O_2 [14]. However, a major barrier to POCL-based systems application is that peroxalate derivatives are not so stable and inclined to hydrolyze in aqueous or protic solvents [15]. Therefore, the protection of peroxalate esters from hydrolysis is the key factor to peroxalate NPs, for example, the formation of minisize organic reactor in aqueous systems through copolymer

micelles [16] or microemulsions [17]. Meanwhile, with the peroxalate esters and the fluorescent dyes together in the same phase, the energy transfer is expected to be improved [18].

Photodynamic therapy (PDT) is a new technology for cancer treatment. Photodynamic agents can be excited by laser with specific wavelength, transfer energy to the nearby oxygen, generate strong active singlet oxygen molecules. Then singlet oxygen causes microvascular acute injury, and blood vessel blockage in tumor and induces tumor cells apoptosis, achieving the purpose of local treatment [19]. However, the conventional photodynamic therapy in cancer treatment faces many problems [20]. These photodynamic drugs are hydrophobic and can only dissolve in an organic solvent, which is difficultly to be directly injected into the body. Conventional excitation laser light, ranging from 600 nm to 700 nm, cannot reach tumor site deeper than 10 mm from the skin. In addition, in the photodynamic treatment, the tumor localization must be accurately distinguished, because excitation light should only irradiate the tumor tissue, without damaging the normal organs [21]. Therefore, the general photodynamic therapy can only treat superficial tumors, limiting its clinical applications.

In this paper, a novel PDT method is developed by integrating peroxalate ester oligomers, fluorescent dyes, and photodynamic drugs simultaneously inside the PEG-PCL micelles. The hydrophobic core of PEG-PCL micelles can protect the peroxalate ester oligomer from directly contacting the water and postpone their hydrolysis. And the hydrophilic PEG shell outside the PEG-PCL micelles stabilizes these micelles in the aqueous solution, giving them long circulation in the blood, which makes them suitable to be used in biomedical field. The energy between the peroxalate and H_2O_2 reaction is effectively transferred to the fluorescent dyes within a confined space, and then dyes release the photon energy for PDT. Within the same micelle, photodynamic drugs easily get the chemiluminescence to generate active singlet oxygen molecules to kill cancer cells. Further, photodynamic drugs encapsulated inside peroxalate nanomicelles (POMs) not only improve their solubility in aqueous solution, but also can be delivered to the tumor site and increase the drug concentration inside the tumor due to the small size of POMs [22]. All can improve the effect of photodynamic therapy with the PDT drug-loaded POMs. Since the excitation is endogenous and does not require external laser light source, this inner "light stick" can be applied in PDT wherever inside the body, no matter how the tumor is deep or close to the skin. The coencapsulated fluorescent dye as a light source for a photosensitizing PDT drug is feasible [23], and intraparticle energy transfer and fluorescence photoconversion are theoretically and experimentally valid [24]. Evidence exists that the apoptosis of tumor cell mainly depends on the content of singlet oxygen, rather than that of hydrogen peroxide [25]. The presence of excess hydrogen peroxide is not only toxic to the normal tissues and cells, but also can induce a malignant tumor. It is very important to reduce the content of hydrogen peroxide and increase the singlet oxygen concentration in the tumor site. Therefore, these PDT drugs-loaded POMs are

valuable on the function that not only effectively consumes the hydrogen peroxide in the tumor site, but also transfers the H_2O_2 to singlet oxygen through the PDT method. It should be a partial solution to the shortcoming of PDT method such as the short laser wavelength and difficulty in reaching the internal tumor inside the body and have a potential application in photodynamic therapy field.

2. Materials and Methods

2.1. Materials. Methoxypolyethyleneglycol (MPEG, Mw: 2 kDa, Fluka) was dried in vacuum at $85°C$ for 4 hours before use. E-caprolactone (CL, Sigma) was dehydrated by CaH_2 overnight at room temperature and distilled under reduced pressure. Stannous octoate (Sigma) is used as received. Oxalyl chloride (Acros) was distilled under reduced pressure before use. 4-Hydroxybenzyl alcohol (Alfa Aesar), 1, 8-octanediol (Alfa Aesar), 9, 10-diphenyl anthracene (ACROS), rubrene (ACROS), rhodamine B (ACROS), mesotetraphenylporphine (TPP, ≥97%, Sterm), and aqueous hydrogen peroxide (H_2O_2, 30%, Sinopharm Chemical Reagent Co.) were used as received. All the other chemicals were of analytical grade and were used without further purification.

2.2. Synthesis of Poly(ethyleneglycol)-poly(caprolactone) (PEG-PCL) and Peroxalate Ester Oligomer. PEG-PCL was synthesized by a classical ring-opening polymerization method. Briefly, a small amount of stannous octoate (0.1% w_t/w_t) was added into a polymerization tube containing MPEG (3 g, 1.5 mmol) and CL monomer (9.3 mL). The tube was sealed off after being evacuated and then immersed in oil bath at $130°C$ for 48 hours. Then the crude polymerization product was dissolved in CH_2Cl_2 and precipitated in an excess mixture of n-hexane and ethyl (v/v : 4/1) and then filtered and redissolved in CH_2Cl_2. After concentrated with a rotary evaporator, the final product was dried in vacuum. Molecular weight of copolymer was determined by a gel permeation chromatography (GPC, Waters 515 systems) equipped with Waters 525 pump, Waters 2487 Ultraviolet absorbance Detector, and Wyatt Technology Optilab rEX refractive index detector and an STYRAGEL HR3, HR4, and HR5 (300×7.8 mm) columns in tetrahydrofuran (THF) solution. The poly-dispersity index was calculated based on polystyrene standards with molecular weights in the range from 900 to 1.74×10^6 g/mol.

Peroxalate ester oligomer was synthesized with 4-hydroxybenzyl alcohol (16 mmol), 1, 8-octanediol (2.4 mmol) and oxalyl chloride (18.3 mmol). These two kinds of dialcohol were first dissolved in dry tetrahydrofuran (THF, 10 mL), with the addition of triethylamine (40 mmol) by an injector under vacuum. The mixture was kept at $0°C$ and then added to oxalyl chloride in dry tetrahydrofuran (20 mL) protected by a nitrogen atmosphere. The reaction was kept at room temperature overnight and quenched with a saturated brine solution. The product was extracted with ethyl acetate and the combined organic layers were dried by anhydrous Na_2SO_4 over 8 hours. After concentrated under vacuum, it was isolated by precipitating in excess
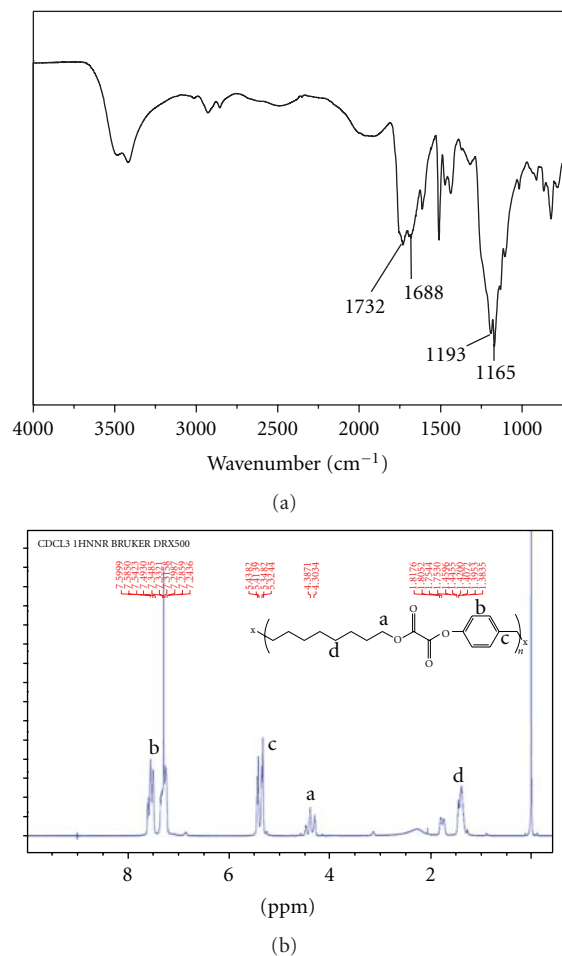
Figure 1: (a) FT-IR and (b) ^{1}H-NMR spectra of peroxalate ester oligomers.

dichloromethane/hexane (v/v : 1/1) solution, then filtered, and dried in vacuum. The chemical structure of the product was measured with FT-IR (Bruker, Vector 22) using the solid product directly and ^{1}H-NMR (Bruker DQX-300) in CDCl$_3$ solution.

2.3. Preparation of Chemiluminescent Nanomicelles.

The nanomicelles were achieved by the self-assemble block copolymers through a cosolvent evaporation method [16]. PEG-PCL (50 mg), peroxalate esters oligomer (5 mg), and the fluorescent dye rubrene (1 mg) were first dissolved in 2 mL of acetone. The mixture was added dropwise into deionized water (20 mL) to form micelles with magnetic stirring. Then the organic solvent was removed under reduced pressure at 0°C, and the resulting micelle solution was used for further experiments.

The hydrodynamic diameter and size distribution of the as-prepared micelles were determined by dynamic light scattering (DLS) using a Brookhaven BI-9000AT system (Brookhaven Instruments Corporation, USA) at a concentration of 1 mg/mL in deionized water. Morphology of these micelles was conducted on transmission electron microscopy (TEM, JEM-100S, JEOL, Japan).

2.4. Chemiluminescent Characterization of POMs.

The nanomicelles solution was used directly with a final concentration of 2.5 mg/mL in deionized water. The images of chemiluminescence produced by POMs and different concentration of hydrogen peroxide solution (in phosphate buffer pH 7.4, 0.1 M) in a 96-well plate were caught by an imaging system equipped with a −29°C CCD (EC3, UVP). And the mean density of chemiluminescence was statistical by the software. The chemiluminescent intensity of POMs and different concentration of hydrogen peroxide solution (in phosphate buffer pH 7.4, 0.1 M) were measured using a luminometer (YN FG-1, Xunjie Corporation, China) and each with three times measurements. Chemiluminescent emission spectrum of peroxalate ester oligomers (5 mg) and dyes (1 mg) in dimethyl phthalate (2 mL) with hydrogen peroxide (200 μL, 2 μM) was measured using a fluorometer spectrofluorometer (RF-5301-PC, Shimadzu) with a turn-off lamp. The stability of POMs in aqueous system was investigated by incubating them in deionized water for various time and then mixed with 0.2 μM hydrogen peroxide solution (in phosphate buffer pH 7.4, 0.1 M). The chemiluminescent intensity was subsequently measured for 100 seconds using a luminometer (YN FG-1, Xunjie Corporation, China), and the integrated areas under CL intensity curves were calculated as the value.

2.5. Preparation of TPP-Encapsulated POMs.

Mesotetraphenylporphine (TPP) was a kind of drug used in photodynamic therapy (PDT). TPP-encapsulated POMs were prepared using the same method as described above with TPP (1 mg) dissolved in acetone. The size of TPP-encapsulated POMs was also investigated by DLS. The chemiluminescence intensity of nanomicelles with TPP or without TPP was measured using a luminometer, at the same time, the influence of TPP to the CL of POMs was also observed.

2.6. The Antitumor Properties of TPP-Encapsulated POMs.

Cytotoxicity of TPP-loaded nanomicelles against two kinds of cancer cell lines was assessed by 3-(4, 5-dimethylthiazolyl-2)-2, 5-diphenyltetrazolium bromide (MTT) assay. 100 μL cells with a density around 5,000 cells/well were seeded in 96-well plate and were grown in completed media having 90% Dulbecco's Modified Eagle Media (DMEM), 10% fetal bovine serum, and 100 units/mL penicillin/streptomycin. The cells were maintained at 37°C under 5% CO$_2$ for 24 hours, then different POMs groups and H$_2$O$_2$ were added into the cultured media and incubated for another 24 hours. Cytotoxicity with or without H$_2$O$_2$-treated cells was compared in each drug group. The control cells and only H$_2$O$_2$-treated cells were also cultured under the same condition. MTT in phosphate buffer saline (PBS) was added into each well and incubated for 4 hours after the media was refreshed. Then the solution was discarded and dimethyl sulphoxide (DMSO, 150 μL) was added into the wells. The optical intensity was measured at 570 nm using microtiter plate reader. Data were expressed as an average of three times.
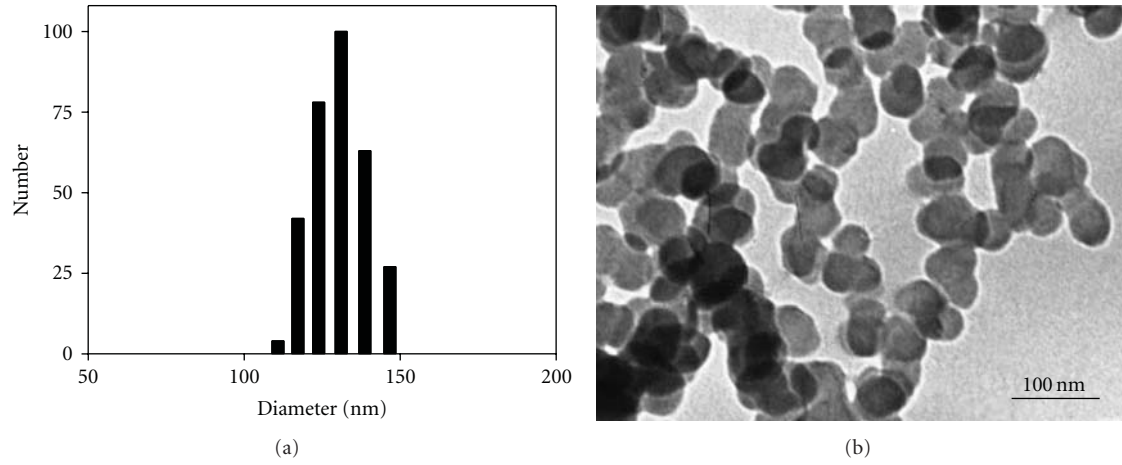
(a)

(b)

FIGURE 2: (a) Hydrodynamic diameter distribution and (b) TEM image of the nanomicelles.
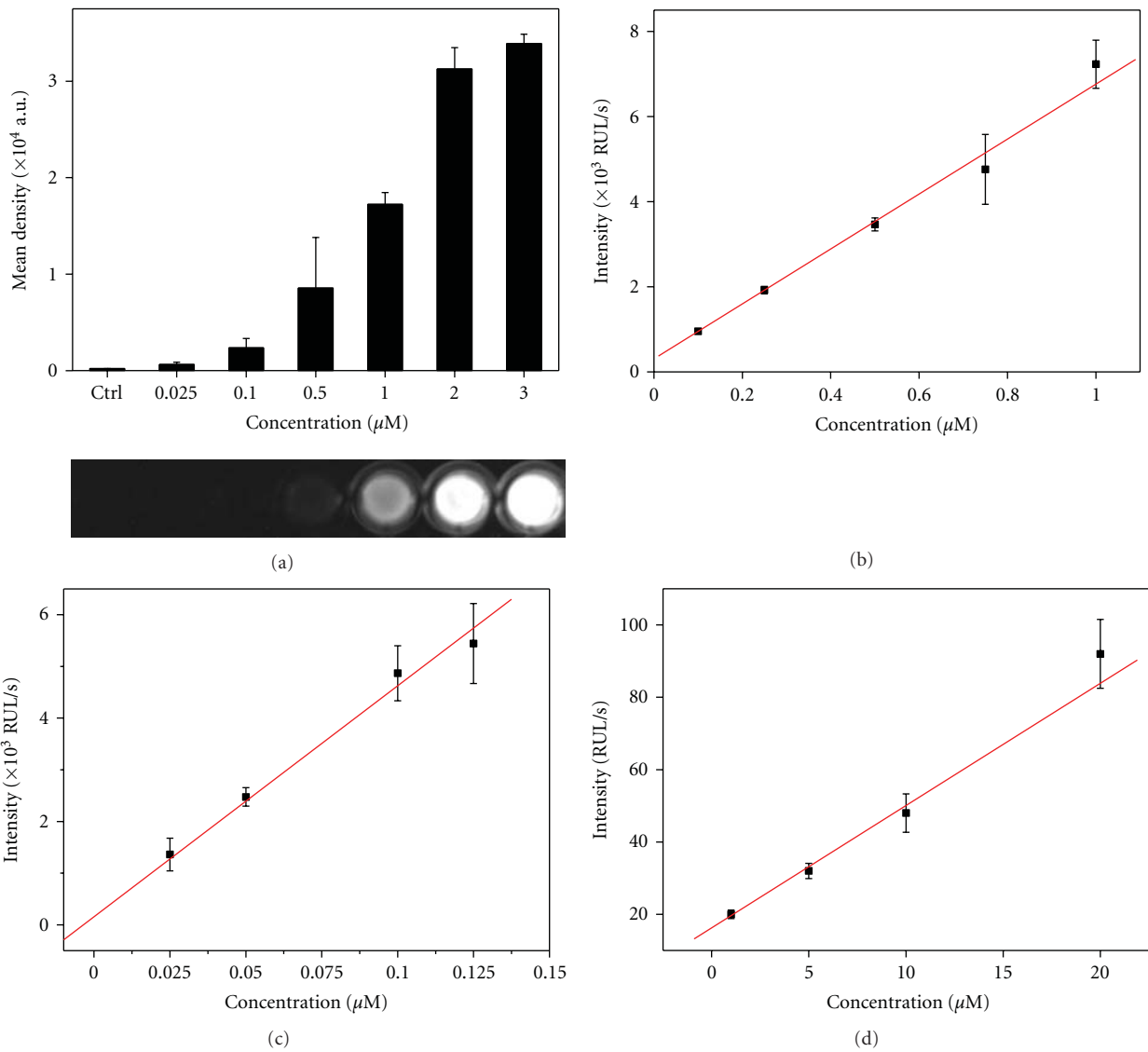

(a)

(b)

(c)

(d)

FIGURE 3: (a) Imaging of chemiluminescence produced by the POMs (2.5 mg/mL) with H_2O_2 at various concentrations; (b), (c), and (d) Correlation of the POMs (2.5 mg/mL) to various concentrations of H_2O_2 in PBS under different operating voltage (OV). (b) OV = −500 eV; (c) OV = −600 eV; (d) OV = −400 eV.
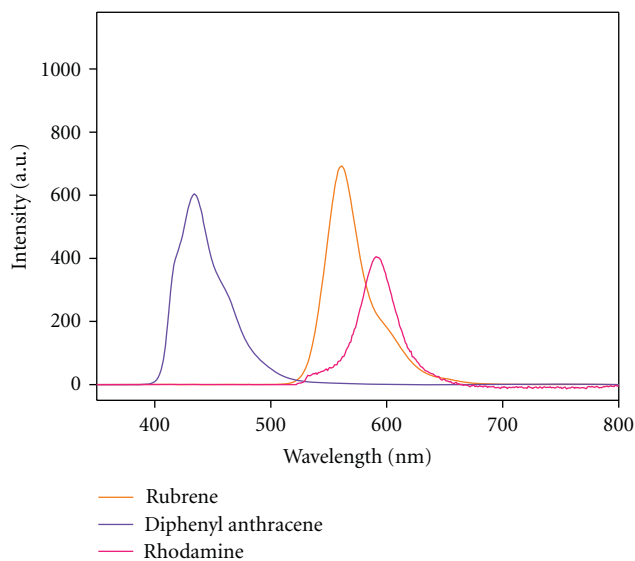
FIGURE 4: Chemiluminescence emission spectra of peroxalate ester oligomers and different dyes in dimethyl phthalate in the presence of H_2O_2.
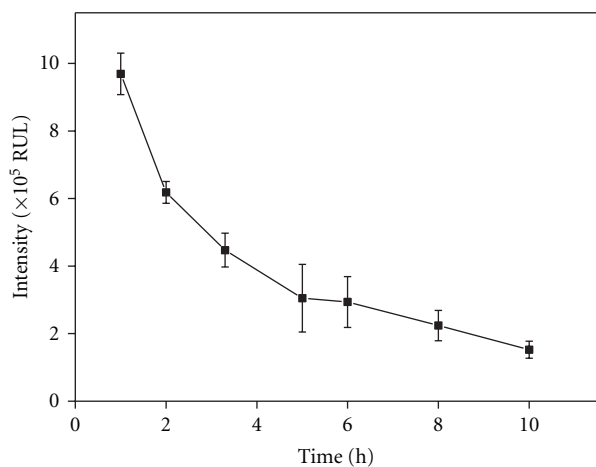

FIGURE 5: Stability of the POMs in deionized water. POMs: 2.5 mg/mL, H_2O_2: 0.2 μM, OV = -550 eV.

3. Results and Discussion

3.1. The Composition of the Nanomicelles.

The amphiphilic copolymer PEG-PCL was chosen as the scaffold of the POMs because it is biodegradable and biocompatible that had been extensively used for drug delivery [26, 27]. The hydrophilic PEG corona should enhance the biocompatibility and stability in physiologic environments, while the hydrophobic PCL cores could stabilize encapsulated peroxalate esters from water hydrolysis. In the present work, the copolymer PEG-PCL was synthesized by ring-opening polymerization, and its molecular weight was determined by GPC to be 12 kDa with polydispersity index (PI) of 1.32. Peroxalate ester oligomer was synthesized with 4-hydroxybenzyl alcohol, 1, 8-octanediol, and oxalyl chloride. The structure of product was confirmed by FT-IR and ^{1}H-NMR (Figure 1). In

FT-IR spectrum, the two groups of split peaks around 1732 cm^{-1}/1688 cm^{-1} and 1193 cm^{-1}/1165 cm^{-1} indicated the structure of mixed aromatic/aliphatic peroxalates. In ^{1}H-NMR spectrum, the characteristic resonances of 7.3 ppm (b), 5.4 ppm (c), 4.3 ppm (a), and 1.4 ppm (d) were observed, which further identified this structure. The molecular weight of peroxalate ester oligomer determined by GPC was 600 Da with PI of 1.21. Thus, it was clear that the oligomer synthesized had a trimer structure of peroxalate ester based on GPC result. During the preparation procedure of POMs, peroxalate ester oligomers together with fluorescent dyes could be totally encapsulated inside the hydrophobic core of PEG-PCL nanomicelles, which could protect the peroxalate from contacting the water and postpone the hydrolysis. The hydrophilic PEG segment would surround outside the POMs to stabilize these micelles in the aqueous solution.

3.2. The Size and Morphology of POMs.

Peroxalate ester oligomer and the fluorescent dye (rubrene) were encapsulated in the PEG-PCL copolymer micelles forming the POMs during preparation procedure. As determined by DLS, the obtained POMs had a number-weighted hydrodynamic diameter of 119 $\pm$ 0.9 nm (Figure 2(a)). The transmission electron microscopic (TEM) image manifested that these nanomicelles were spherical in outline with an average diameter of about 60 nm (Figure 2(b)), which is smaller than that from DLS because they were observed in the dry state. The small size of the nanomicelles should make them suitable for imaging hydrogen peroxide in cellular mitochondria because micelles in this size range had a higher opportunity for cell penetrating [28].

3.3. Chemiluminescence of POMs with Hydrogen Peroxide.

These obtained POMs reacting with hydrogen peroxide produced high-energy intermediate, which could chemically excite fluorescent dye to give an extent chemiluminescence. Although its intensity was too weak to be recognized by naked eye, the image of chemiluminescence could be acquired by a low-temperature CCD camera. In Figure 3(a), the chemiluminescence image of hydrogen peroxide and POMs in a 96-well plate was shown. It was clear that with the increase of the hydrogen peroxide concentration from 0.025 to 3 μM (in PBS pH = 7.4), the brighter wells could be seen. The quantitative analyses above the image confirmed that the higher hydrogen peroxide concentration was, the higher chemiluminescence intensity would be.

Meanwhile, the chemiluminescence intensity was linearly related to the concentrations of hydrogen peroxide. As shown in Figure 3(b), the chemiluminescence intensity increased linearly with the concentration of the hydrogen peroxide in the range of 0.1–1 μM, which indicated that the concentration hydrogen peroxide in the cells or organs could be quantitatively calculated according to the standard curve. Further, by changing operating voltage of luminometer, the sensitivity of the device was adjusted and adopted to cover both lower (Figure 3(c)) and higher (Figure 3(d)) concentration ranges. These results demonstrated that the POMs were quite sensitive to hydrogen peroxide and could
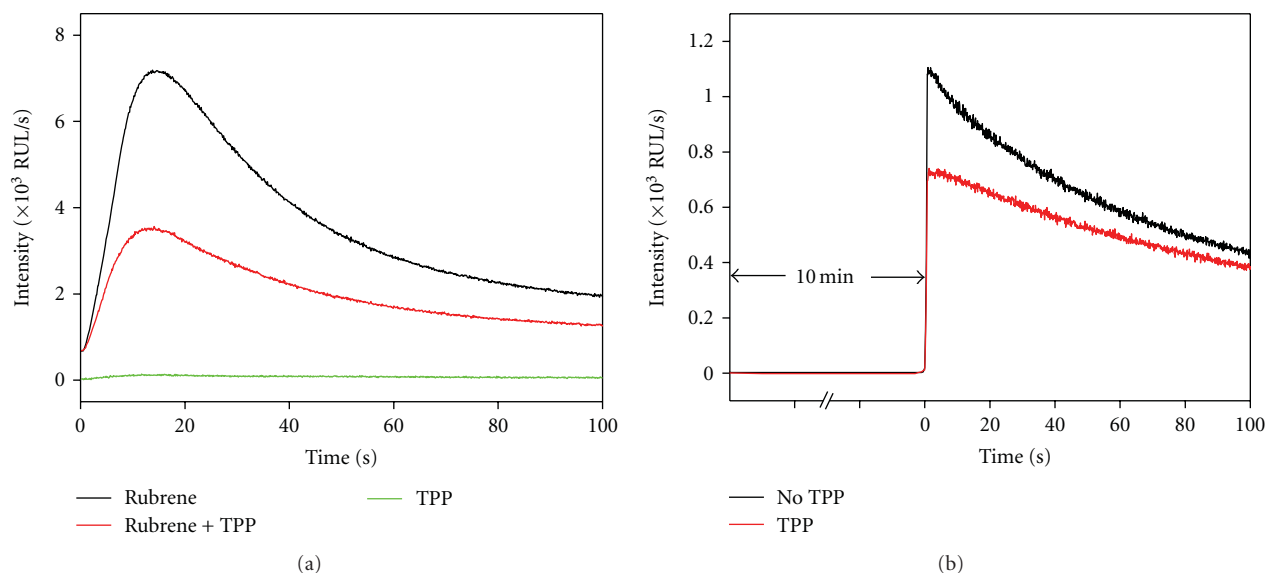
FIGURE 6: Chemiluminescence of (a) rubrene, rubrene plus TPP, and TPP-encapsulated POMs, respectively, in the presence of $0.2 \, \mu$M H_2O_2; (b) no rubrene-encapsulated POMs with and without TPP in the presence of $0.2 \, \mu$M H_2O_2, and the addition rubrene (0.2 mg) after 10 min. All concentrations of POMs were 2.5 mg/mL, OV = -550 eV.

be used to detect physiological concentration of hydrogen peroxide.

The chemical reaction between peroxalate and hydrogen peroxide formed an intermediate 1, 2-dioxetanedione which was potential to excite a variety of fluorescent dyes, suitable for a particular application. The tunable wavelength of peroxalate chemiluminescence system was investigated by encapsulating different dyes in the POMs and measuring their emission spectra. Figure 4 demonstrated that peroxalate esters oligomers could excite diphenyl anthracene, rubrene, and rhodamine in the presence of hydrogen peroxide, producing fluorescence at 430, 560, and 600 nm, respectively. The chemiluminescence emission wavelength could be readily tuned to near infrared region by using a near-infrared fluorescent dye and therefore this method can be used potentially in deep tissue imaging owing to the minimal tissue scattering and absorption to the near infrared [29].

Although the POMs have been proved a good carrier to detect the H_2O_2 in the aqueous solution, the most challenging matter of this system is the instability of peroxalate against water because of a fast hydrolysis in aqueous solutions which makes them unsuitable for physiological applications. However, the encapsulation of peroxalate esters oligomers inside the PEG-PCL micelles could protect them from water hydrolysis by providing a hydrophobic environment with low water permeability [30]. Hence, we investigated the stability of these POMs by incubating them in water for different time and measuring their chemiluminescence in the presence of hydrogen peroxide. Figure 5 demonstrated the chemiluminescence intensity from the reaction between peroxalate esters, and H_2O_2 decreased as the incubation time in water extended. The POMs had a half-life longer than 2 hours, suggesting that the POMs effectively prevented the peroxalate esters from water hydrolysis, compared to an

analogous work with a half-life of 30 min [16]. It suggested that the polymer nanomicelles effectively improved the stability of the peroxalate esters. The improved stability of the peroxalate ester oligomers should allow them to image hydrogen peroxide in physiological condition.

3.4. Characterization of the TPP-Encapsulated POMs. The photodynamic therapy agent (mesotetraphenylporphine, TPP) was encapsulated in POMs using the same method as described above. And the size of TPP-encapsulated POMs is to have similar average size with no TPP-encapsulated POMs by DLS measurement. As shown in Figure 6(a), the TPP-encapsulated POMs did not have detectable luminescence because the high-energy intermediate could not directly transfer chemical energy to TPP molecule. Although POMs could not directly excite TPP, it could stimulate rubrene for a remarkable chemiluminescence. Meanwhile, with the same concentration of POMs and rubrene, the addition of TPP weakens the fluorescence of rubrene dye, which indicated that part of energy had transferred to TPP. Rubrene played as an effective switchover for transferring chemical energy to photon energy.

In order to further verify whether TPP has absorbed the fluorescence produced by rubrene, a subtle designed experiment was carried on. According to the work reported [10], in the absence of fluorescence dyes, the high-energy intermediate dioxetanedione can maintain its energy for a while until being exposed to the dyes. In this experiment, firstly, only POMs with and without TPP were incubated in the presence of $0.2 \, \mu$M H_2O_2. No luminescence was observed in these systems as displayed in Figure 6(b). Both of these two systems had no rubrene inside them. After 10 minutes, when 0.2 mg rubrene was added into these two kinds of POMs, respectively, significant chemiluminescence signals
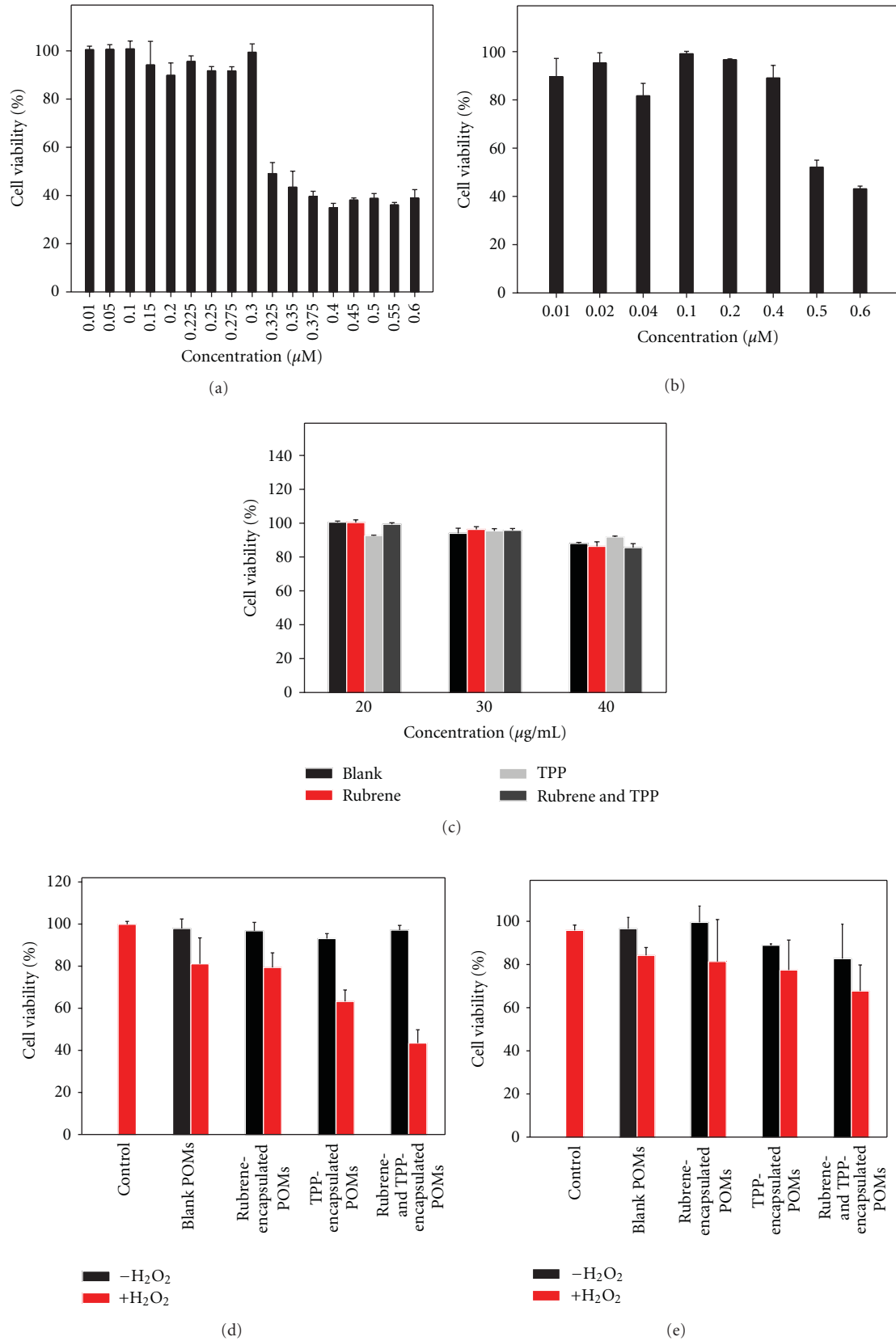
(a)

(b)

(c)

(d)

(e)

Figure 7: The cytotoxicity of H_2O_2 to (a) C6 and (b) LoVo cell lines at various concentrations in PBS (pH = 7.4); (c) the cytotoxicity of a diversity of POMs to C6 cell lines without H_2O_2. The cytotoxicity of a diversity of POMs to (d) C6 cells and (e) LoVo cells in the presence of 0.2 μM H_2O_2 or not, control means only H_2O_2 treated. All concentrations of POMs were 20 μg/mL, Rubrene 0.3 μg/mL, and TPP 2 μg/mL. Error bars indicate standard deviations from ≥3 measurements.

were observed in the systems. However, the POMs encapsulating TPP showed a reduced chemiluminescence signal compared to the blank POMs, which clearly supporting that TPP absorbed part of the energy. Therefore, part of the chemical energy from the reaction between POMs and H_2O_2 could be transformed to light energy with the help of rubrene, which indicated that the POMs and rubrene played the role of a laser light in the presence of H_2O_2. Even the chemiluminescence intensity was quite low compared with a real laser source, this system opened a new window in the PDT field because no additional laser light was needed in this system. For the traditional PDT system, external laser light was needed to excite the PPT in the tumor treatment procedure. However, restricted by its penetration depth of the laser light, only the tumor close to the skin could be killed effectively. In our system, The TPP drug was excited by the inner chemiluminescence, which avoided the use of external laser resource, consequently overcoming the problem of the depth of the tumor site. Furthermore, particles with nanosize had been proved to be accumulated in the tumor site by the EPR effect or targeting strategy [31]. So the TPP-loaded POMs may greatly improve the therapy effect compared to the traditional PDT method.

3.5. The Anticancer Properties of the TPP-Encapsulated POMs. The chemiluminescence radiation produced by the POMs in the presence of hydrogen peroxide could act as an inner light source to excite PDT drug to play curative effect. To verify the antitumor effect of the TPP-encapsulated POMs, in vitro cytotoxicity tests of the TPP-loaded POMs against C6 and LoVo cell lines were conducted. As well known, high concentration of hydrogen peroxide was cytotoxic to cells. The control experiment of cells coincubated with different concentration of hydrogen peroxide was performed, and their cytotoxicities were also evaluated by MTT assay. The results clearly showed that the critical cytotoxic concentration of hydrogen peroxide is $0.3\,\mu M$ for C6 cells (Figure 7(a)) and $0.4\,\mu M$ for LoVo cells (Figure 7(b)), respectively, helping us to choose a safe H_2O_2 concentration which was nontoxic to cells but could acquire maximum chemiluminescence. Therefore, hydrogen peroxide concentration $0.2\,\mu M$ was chosen for all the cell cytotoxicity experiments. The cytotoxicity of different kinds of POMs (e.g., with or without rubrene) was checked without hydrogen peroxide treatment (Figure 7(c)). No obvious cytotoxicity was observed at low concentration except a slight cytotoxicity at high concentration. So it seemed safe to conclude that the blank POMs have no or little cytotoxicity against the test cells. Therefore, the POMs used in the following experiment were fixed on the concentration of $20\,\mu g/mL$, and the hydrogen peroxide was the same concentration of $0.2\,\mu M$. For C6 cells, when they were treated with the POMs, in the absence of hydrogen peroxide, no or little cytotoxicity was observed in all the samples as shown in Figure 7(d). However, when hydrogen peroxide was added into the wells, an increasing cytotoxicity is observed. Furthermore, C6 cells treated with the POMs having both rubrene and TPP showed lowest cell viability compared with other groups, indicating TPP and rubrene

having a combined antitumor effect, which might resulted from the chemiluminescence-stimulated PDT effect of TPP. Similar results were also observed in the LoVo cell line cytotoxicity experiment (Figure 7(e)).

4. Conclusion

Chemiluminescent POMs were successfully developed to image tumor signal molecules: hydrogen peroxide. These POMs could improve the stability of peroxalates in aqueous system and were sensitive to low concentration of hydrogen peroxide within the physiological range. According to the linear correlation between chemiluminescent intensity and the concentration of hydrogen peroxide, a facile and robust approach for monitoring hydrogen peroxide molecules was established, which should be helpful to clinical diagnosis. When PDT drug TPP was encapsulated inside the POMs together with rubrene, the TPP-encapsulated POMs performed an anticancer property in the presence of hydrogen peroxide which was stimulated by self-produced chemiluminescence not an external laser. This system enabled us to open a new window in the PDT field without using external laser light resource to treat the malignant tumor.

Acknowledgment

References

[1] K. Rutault, C. Alderman, B. M. Chain et al., "Reactive oxygen species active human peripheral blood denditic cells," *Free Radialc Biology and Medicine*, vol. 26, no. 1-2, pp. 232–238, 1999.

[2] S. Dominici, A. Visvikis, L. Pieri et al., "Redox modulation of NF-κB nuclear translocation and DNA binding in metastatic melanoma. The role of endogenous and γ-glutamyl transferase-dependent oxidative stress," *Tumori*, vol. 89, no. 4, pp. 426–433, 2003.

[3] S. G. Rhee, "H_2O_2, a necessary evil for cell signaling," *Science*, vol. 312, no. 5782, pp. 1882–1883, 2006.

[4] M. Giorgio, M. Trinei, E. Migliaccio, and P. G. Pelicci, "Hydrogen peroxide: a metabolic by-product or a common mediator of ageing signals?" *Nature Reviews Molecular Cell Biology*, vol. 8, no. 9, pp. 722A–728A, 2007.

[5] H. Ohshima, M. Tatemichi, and T. Sawa, "Chemical basis of inflammation-induced carcinogenesis," *Archives of Biochemistry and Biophysics*, vol. 417, no. 1, pp. 3–11, 2003.

[6] E. W. Miller, A. E. Albers, A. Pralle, E. Y. Isacoff, and C. J. Chang, "Boronate-based fluorescent probes for imaging cellular hydrogen peroxide," *Journal of the American Chemical Society*, vol. 127, no. 47, pp. 16652–16659, 2005.

[7] M. C. Y. Chang, A. Pralle, E. Y. Isacoff, and C. J. Chang, "A selective, cell-permeable optical probe for hydrogen peroxide in living cells," *Journal of the American Chemical Society*, vol. 126, no. 47, pp. 15392–15393, 2004.

[8] A. E. Albers, V. S. Okreglak, and C. J. Chang, "A FRET-based approach to ratiometric fluorescence detection of hydrogen peroxide," *Journal of the American Chemical Society*, vol. 128, no. 30, pp. 9640–9641, 2006.

[9] R. W. Tsien and R. Y. Tsien, "Calcium channels, stores, and oscillations," *Annual Review of Cell Biology*, vol. 6, pp. 715–760, 1990.

[10] M. M. Rauhut, L. J. Bollyky, B. G. Roberts et al., "Chemiluminescence from reactions of electronegatively substituted aryl oxalates with hydrogen peroxide and fluorescent compounds," *Journal of the American Chemical Society*, vol. 89, no. 25, pp. 6515–6522, 1967.

[11] C. V. Stevani, S. M. Silva, and W. J. Baader, "Studies on the mechanism of the excitation step in peroxyoxalate chemiluminescence," *European Journal of Organic Chemistry*, no. 24, pp. 4037–4046, 2000.

[12] S. M. Silva, K. Wagner, D. Weiss, R. Beckert, C. V. Stevani, and W. J. Baader, "Studies on the chemiexcitation step in peroxyoxalate chemiluminescence using steroid-substituted activators," *Luminescence*, vol. 17, no. 6, pp. 362–369, 2002.

[13] D. Lee, S. Khaja, J. C. Velasquez-Castano et al., "In vivo imaging of hydrogen peroxide with chemiluminescent nanoparticles," *Nature Materials*, vol. 6, no. 10, pp. 765–769, 2007.

[14] L. Liu and R. P. Mason, "Imaging β-galactosidase activity in human tumor xenografts and transgenic mice using a chemiluminescent substrate," *PLoS ONE*, vol. 5, no. 8, Article ID e12024, 2010.

[15] S. Kim, K. Seong, O. Kim et al., "Polyoxalate nanoparticles as a biodegradable and biocompatible drug delivery vehicle," *Biomacromolecules*, vol. 11, no. 3, pp. 555–560, 2010.

[16] M. Dasari, D. Lee, V. R. Erigala, and N. Murthy, "Chemiluminescent PEG-PCL micelles for imaging hydrogen peroxide," *Journal of Biomedical Materials Research—Part A*, vol. 89, no. 3, pp. 561–566, 2009.

[17] R. B. Thompson and S. E. Shaw, "Peroxyoxalate chemiluminescence in microemulsions," *Langmuir*, vol. 4, no. 1, pp. 106–110, 1988.

[18] A. Kamyshny and S. Magdassi, "Chemiluminescence immunoassay in microemulsions," *Colloids and Surfaces B: Biointerfaces*, vol. 11, no. 5, pp. 249–254, 1998.

[19] B. C. Wilson and M. S. Patterson, "The physics, biophysics and technology of photodynamic therapy," *Physics in Medicine and Biology*, vol. 53, no. 9, pp. R61–R109, 2008.

[20] Y. N. Konan, R. Gurny, and E. Allémann, "State of the art in the delivery of photosensitizers for photodynamic therapy," *Journal of Photochemistry and Photobiology B: Biology*, vol. 66, no. 2, pp. 89–106, 2002.

[21] L. O. Cinteza, T. Y. Ohulchanskyy, Y. Sahoo, E. J. Bergey, R. K. Pandey, and P. N. Prasad, "Diacyllipid micelle-based nanocarrier for magnetically guided delivery of drugs in photodynamic therapy," *Molecular Pharmaceutics*, vol. 3, no. 4, pp. 415–423, 2006.

[22] A. Roby, S. Erdogan, and V. P. Torchilin, "Solubilization of poorly soluble PDT agent, meso-tetraphenylporphin, in plain or immunotargeted PEG-PE micelles results in dramatically improved cancer cell killing in vitro," *European Journal of Pharmaceutics and Biopharmaceutics*, vol. 62, no. 3, pp. 235–240, 2006.

[23] S. Kim, T. Y. Ohulchanskyy, H. E. Pudavar, R. K. Pandey, and P. N. Prasad, "Organically modified silica nanoparticles co-encapsulating photosensitizing drug and aggregation-enhanced two-photon absorbing fluorescent dye aggregates for two-photon photodynamic therapy," *Journal of the American Chemical Society*, vol. 129, no. 9, pp. 2669–2675, 2007.

[24] S. Kim, H. Huang, H. E. Pudavar, Y. Cui, and P. N. Prasad, "Intraparticle energy transfer and fluorescence photoconversion in nanoparticles: an optical highlighter nanoprobe for two-photon bioimaging," *Chemistry of Materials*, vol. 19, no. 23, pp. 5650–5656, 2007.

[25] S. Zhuang, J. T. Demirs, and I. E. Kochevar, "p38 mitogen-activated protein kinase mediates bid cleavage, mitochondrial dysfunction, and caspase-3 activation during apoptosis induced by singlet oxygen but not by hydrogen peroxide," *Journal of Biological Chemistry*, vol. 275, no. 34, pp. 25939–25948, 2000.

[26] M. L. Forrest, C. Y. Won, A. W. Malick, and G. S. Kwon, "In vitro release of the mTOR inhibitor rapamycin from poly(ethylene glycol)-b-poly(ε-caprolactone) micelles," *Journal of Controlled Release*, vol. 110, no. 2, pp. 370–377, 2006.

[27] H. M. Aliabadi, A. Mahmud, A. D. Sharifabadi, and A. Lavasanifar, "Micelles of methoxy poly(ethylene oxide)-b-poly(ε-caprolactone) as vehicles for the solubilization and controlled delivery of cyclosporine A," *Journal of Controlled Release*, vol. 104, no. 2, pp. 301–311, 2005.

[28] V. P. Torchilin, "PEG-based micelles as carriers of contrast agents for different imaging modalities," *Advanced Drug Delivery Reviews*, vol. 54, no. 2, pp. 235–252, 2002.

[29] C.-K. Lim, Y.-D. Lee, J. Na et al., "Chemiluminescence-generating nanoreactor formulation for near-infrared imaging of hydrogen peroxide and glucose level in vivo," *Advanced Functional Materials*, vol. 20, no. 16, pp. 2644–2648, 2010.

[30] J. M. Lin and M. Yamada, "Microheterogeneous systems of micelles and microemulsions as reaction media in chemiluminescent analysis," *Trends in Analytical Chemistry*, vol. 22, no. 2, pp. 99–107, 2003.

[31] H. Maeda, J. Wu, T. Sawa, Y. Matsumura, and K. Hori, "Tumor vascular permeability and the EPR effect in macromolecular therapeutics: a review," *Journal of Controlled Release*, vol. 65, no. 1-2, pp. 271–284, 2000.